

# Open Research Online

---

The Open University's repository of research publications and other research outputs

## Improved cranial fracture metrics for assessing the protective benefits of helmet systems

### Thesis

How to cite:

Allanson-Bailey, Lucy Sarah (2016). Improved cranial fracture metrics for assessing the protective benefits of helmet systems. PhD thesis The Open University.

For guidance on citations see [FAQs](#).

© [not recorded]

Version: Version of Record

---

Copyright and Moral Rights for the articles on this site are retained by the individual authors and/or other copyright owners. For more information on Open Research Online's [data policy](#) on reuse of materials please consult the policies page.

---

[oro.open.ac.uk](http://oro.open.ac.uk)

The Open University

**Improved cranial fracture metrics for assessing the  
protective benefits of helmet systems**

by

Lucy Sarah Allanson-Bailey MEng

Platform Sciences Division, Dstl Porton Down

March 2016

**This thesis is submitted for examination for the degree of Doctor of Philosophy to the  
Open University, in the discipline of Life and Biomedical Sciences**

Content includes material subject to © Crown copyright (2016), Dstl. This material is licensed under the terms of the Open Government Licence except where otherwise stated. To view this licence, visit <http://www.nationalarchives.gov.uk/doc/open-government-licence/version/3> or write to the Information Policy Team, The National Archives, Kew, London TW9 4DU, or email: [psi@nationalarchives.gsi.gov.uk](mailto:psi@nationalarchives.gsi.gov.uk).

## **Abstract**

Combat helmets are designed to protect the head against common battlefield threats. During defeat of high velocity bullets and fragmentation, large deformations have been shown to occur on the inside of non-metallic helmet shells. If these deformations contact the underlying head there is the potential to cause injury, termed as Behind Helmet Blunt Trauma (BHBT). A method of assessing BHBT is required to fully understand the protective capability of a helmet system. Existing methods using synthetic head models are limited in their ability to predict injury outcome as a result of a lack of available injury criteria. The aim of this study was to improve the prediction of cranial fracture outcomes associated with BHBT, focusing on the effect of impact curvature and flat face diameter.

Representative impact curvatures and flat face diameters were derived from helmet back face deformation measurements in free-air. An instrumented projectile was used to deliver a repeatable impact to a Bovine Scapula Model (BSM); the BSM being a fracture analogue for the cranium. Cranial fracture risk curves were developed using BSM fracture outcomes. These were developed for the different curvatures and flat face diameters tested, using the parameters of peak impact force, impact velocity, bone thickness considered in conjunction with impact velocity, and the Blunt Criterion (BC).

It was concluded that flat impact diameter and radius of curvature should be measured within BHBT assessment to improve the accuracy of cranial fracture prediction. To support application of the risk curves to BHBT assessment methods, it was recommended that fracture outcome should be investigated in terms of the effect of using a rigid projectile when compared to helmet deformation. BHBT assessment methods should consider how to achieve consistent and representative stand-off. Testing should also be completed on full helmet systems as opposed to flat material samples.

## **Declaration**

I declare that this thesis is composed of my own work and has been compiled by myself to conform to the submission regulations of the Open University. Instances of assistance in the course of these studies are listed below:

All practical trials undertaken at Dstl, Porton Down, were carried out alongside trained Dstl members of staff. The trials were carried out in accordance with the Dstl trials process. Under the direction of L. Allanson-Bailey, the following individuals were involved during the different phases of practical trials: Mr James Henshall, Mr Phil Homer, Dr Mark Jaffrey, Mr Gregory James, Miss Sarah Jones, Mr James Keirl, Dr Mark Laird, Mr Sam Martin, Miss Amy Pullen, Mr Brian Sainsbury, Mr Brett Seymour, Dr Jessica Ward, Miss Kathryn Waterworth, Miss Jane Weir and Mr Alex Wright.

Unless stated otherwise, Digital Image Correlation (DIC) analysis was completed by Miss Kathryn Waterworth from the Dstl Structural Dynamics team. This included the set-up, collection and analysis of HSV images in support of DIC, as required throughout the study.

Practical trials undertaken at the Army Research Laboratory (ARL) in America were completed under the direction of Dr Dixie Hisley. This work was undertaken in conjunction with L. Allanson-Bailey, supported by Dr Karin Rafaels and a dedicated trials team based at ARL. Under the direction of L. Allanson-Bailey, Mr Warren Tam extracted key measurements from the data collected during trials at ARL.

Under the direction of L. Allanson-Bailey, statistical analyses were performed by Miss Laura Craddock.

This work has not been previously submitted for a degree or any other qualification at this university or any other institution.

## **Acknowledgements**

I would like to thank Dr Jonathon David and my supervisors, Dr Martin Pearce and Dr Michael Neale, for their support and guidance throughout the project and during preparation of the manuscript.

Many thanks to all those who supported my trials work: Mr James Henshall, Mr Phil Homer, Dr Mark Jaffrey, Mr Gregory James, Miss Sarah Jones, Mr James Keirl, Dr Mark Laird, Mr Sam Martin, Miss Amy Pullen, Mr Brian Sainsbury, Mr Brett Seymour, Dr Jessica Ward, Miss Kathryn Waterworth and Mr Alex Wright. This work would not have been a success without their dedication to building bovine scapula models and working alongside me for long hours to ensure all necessary firings were completed.

I would also like to thank Miss Jane Weir for her support, and enabling me to complete this project.

Thank you to Laura Spencer for her help in obtaining and editing images to support the manuscript, as well as being a supportive friend throughout my PhD study.

Thanks must also go to Ruth Haslett, Laura Davies, Emma Egan and Lindsey Archibald, for their support throughout my research and most notably during my write up.

Finally, thank you to Matt for his unfaltering support and belief in me.

# Contents

Abstract .....	2
Declaration .....	3
Acknowledgements .....	4
Table of Figures .....	11
Table of Tables.....	15
Table of Equations .....	17
Abbreviations .....	18
Chapter 1: General Introduction.....	20
1.1 Background .....	20
1.2 Combat Helmets .....	21
1.3 BHBT Injury Risk .....	23
1.4 Helmet Assessment methods.....	24
1.5 Existing BHBT Assessment Methods .....	25
1.6 Aims .....	26
1.7 Work Structure .....	26
Chapter 2: Anatomy and Injury of the Head.....	29
2.1 Introduction .....	29
2.2 The Head .....	29
2.3 Anatomy of the Cranium .....	29
2.4 Anatomy of the Brain .....	32

2.5	Head Injuries .....	35
2.5.1	General Injury .....	35
2.5.2	Traumatic Brain Injury (TBI).....	37
2.5.3	Cranium Fracture .....	39
2.6	Summary .....	42
Chapter 3: Literature review .....		43
3.1	Introduction .....	43
3.2	Helmet BFD loading on the head .....	43
3.3	BHBT assessment methods .....	45
3.3.1	Overview .....	45
3.3.2	Biological models .....	46
3.3.3	Free-air BFD .....	51
3.3.4	Synthetic head models.....	52
3.3.5	Injury risk models .....	59
3.3.6	Limitations .....	64
3.4	Cranial fracture forces .....	65
3.4.1	Introduction .....	65
3.4.2	Factors affecting cranial fracture force .....	68
3.5	Summary .....	74
Chapter 4: Bovine scapula as a fracture analogue of the cranium .....		77
4.1	Introduction .....	77
4.2	Method.....	78

4.2.1	Validation Data .....	78
4.2.2	Bovine Scapula Models (BSMs).....	78
4.2.3	Experimental Set-Up.....	85
4.2.4	Data capture .....	88
4.2.5	Data Analysis .....	90
4.3	Results .....	93
4.3.1	Overview .....	93
4.3.2	Model validation .....	94
4.4	Discussion .....	95
4.5	Summary .....	97
Chapter 5: Quantification of helmet deformation .....		99
5.1	Introduction .....	99
5.2	Method.....	100
5.2.1	Helmet deformation data collection.....	100
5.2.2	Data Analysis .....	103
5.3	Results .....	104
5.3.1	Overview .....	104
5.3.2	Data Analysis .....	106
5.3.3	Determination of impact faces .....	109
5.4	Discussion .....	111
5.5	Summary .....	113
Chapter 6: Investigation of the effect of flat diameter and curvature on BSM fracture thresholds .....		115



6.1	Introduction .....	115
6.2	Method.....	115
6.2.1	Experimental Set-up.....	115
6.2.2	Projectile .....	117
6.2.3	BSMs.....	118
6.2.4	Testing decision processes .....	120
6.2.5	Data Collection.....	122
6.2.6	Data Analysis .....	124
6.3	Results .....	126
6.3.1	Phase 1 testing.....	126
6.3.2	Phase 2 testing.....	128
6.3.3	DIC .....	134
6.4	Discussion .....	141
6.4.1	Effect of projectile face on fracture outcome.....	141
6.4.2	BSM Target.....	143
6.4.3	Instrumented projectile.....	144
6.4.4	Force profiles .....	145
6.4.5	DIC .....	147
6.5	Summary .....	147
Chapter 7: Determination of a cranial fracture risk model .....		149
7.1	Introduction .....	149
7.2	Method.....	150

7.3	Development of cranial fracture risk models .....	152
7.3.1	Peak impact force .....	152
7.3.2	Impact velocity .....	154
7.3.3	Impact velocity & bone thickness .....	157
7.3.4	Blunt Criterion (BC) .....	161
7.4	Discussion .....	163
7.4.1	General .....	163
7.4.2	Peak impact force .....	165
7.4.3	Impact velocity .....	167
7.4.4	Impact velocity and bone thickness .....	168
7.4.5	Blunt Criterion (BC) .....	169
7.4.6	Application of the cranial fracture risk curves .....	170
7.5	Summary .....	172
Chapter 8: Conclusions and Recommendations.....		174
8.1	Skull fracture metrics for assessing BHBT .....	174
8.2	Recommendations for future research.....	176
Reference List .....		178
Appendix A: BSM Strain gauge data.....		186
Appendix B: BSM Digital Image Correlation strain data.....		190
Appendix C: Probit curve calculation script for projectile velocity .....		193
Appendix D: BSM construction post-trial statistical analysis script .....		194

Appendix E: Data for the investigation of BSM variants as a fracture analogue of the cranium.....	197
Appendix F: Helmet Deformation DIC Analysis Data .....	200
Appendix G: Post processing of projectile accelerometer data .....	204
Appendix H: Post processing of DIC analysis data .....	205
Appendix I: BSM impact data investigating a range of flat face diameters and curvatures delivered by instrumented projectile .....	206
Annex A: Dstl Bovine Scapula Model (BSM) production .....	214
Annex B: Development of an instrumented projectile.....	220

## Table of Figures

Figure 1.1: Method of ballistic threat defeat by laminate materials. ....	22
Figure 1.2: Residual deformation of a laminate helmet shell observed following defeat of multiple ballistic threats. ....	23
Figure 1.3: Process of investigation presented by focus areas required to meet the overall aims of the study. ....	28
Figure 2.1: Lateral view of the skull with the eight bone of the cranium identified. ....	30
Figure 2.2: The three major areas of the brain. ....	32
Figure 2.3: Anatomy of the brain. ....	33
Figure 2.4: The main arteries of the brain, viewed from the base of the brain. ....	34
Figure 2.5: Schematic representation of Intracranial Haemorrhage. ....	39
Figure 2.6: Simple, linear (A) and depressed, comminuted (B) flat bone fractures. ....	40
Figure 2.7: Schematic representation of simple and depressed cranial fractures. ....	40
Figure 3.1: Loading parameters determined for different impacts, based on reporting by Hisley <i>et al.</i> (2010) and Bir <i>et al.</i> (2004). ....	44
Figure 3.2: Images of synthetic head-forms designed to support Behind Helmet Blunt Trauma (BHBT) assessment methods (Table 3.2). ....	56
Figure 3.3: Cadaveric cranial fracture risk verses projectile impact force, based on the reporting of Raymond (2008). ....	61
Figure 3.4: Cadaveric cranial fracture risk verses bullet velocity, based on the reporting of Bass <i>et al.</i> (2003). ....	63
Figure 3.5: Cadaveric cranial fracture risk verses peak impact pressure on the surface of the cranium, based on the reporting of Bass <i>et al.</i> (2003). ....	63

Figure 3.6: Average peak force causing fracture of the frontal bone with bars representing the spread of data from published studies, reported by diameter of the flat circular impact face. ....	69
Figure 3.7: Average peak force causing fracture of the temporo-parietal bone with bars representing the spread of data from published studies, reported by diameter of the flat circular impact face. ....	70
Figure 3.8: Average peak force causing fracture of the frontal bone with bars representing the spread of data from published studies, reported by the inverse radius of curvature of the impact face. ....	71
Figure 4.1: Bovine skeleton (Goodrich 1885).....	79
Figure 4.2: Anatomy of the left Bovine scapula. ....	80
Figure 4.3: Impact area construction of a bovine scapula model.....	81
Figure 4.4: Side view of an Original bovine scapula model. ....	82
Figure 4.5: Impact surface (medial view) of Strain BSM construction. ....	83
Figure 4.6: Lateral view (non-impact side) of the DIC BSM construction. ....	85
Figure 4.7: The range set-up at the Dstl indoor ballistic range to investigate the use of Bovine Scapula Models as a fracture analogue of the cranium. ....	86
Figure 4.8: Cuboid frame with foam padding (red) used to house the target under investigation when determining the use of BSMs as a fracture analogue of the cranium. ..	86
Figure 4.9: Projectile used to impact the BSMs.....	88
Figure 4.10: Logistic regression analysis using two different models, where the data is subjected to separation. ....	91
Figure 5.1: UK Helmet Combat General Service Mark 6a and Combat Assault Mark 7..	101
Figure 5.2: Range set-up used by Hisley <i>et al.</i> (2010) at the ARL in Maryland USA. ....	101
Figure 5.3: Dot tattoo applied to the inner surface of a UK Helmet General Purpose Combat Assault Mark 7. ....	101

Figure 5.4: Impact point locations identified by Hisley <i>et al.</i> (2010), described as Crown, Front, Rear, Left and Right identified on a UK Helmet Combat General Service Mark 6a. ....	102
Figure 5.5: A 2D section through the location of the peak displacement of Shot #76 3D BFD. ....	103
Figure 5.6: A UK Helmet Combat Assault Mk 7 shell as it deforms to defeat a bullet threat. ....	105
Figure 5.7: Average deformation areas of two different UK Helmet Combat variants at different displacements, as BFD develops. ....	107
Figure 5.8: The deformation area of UK Helmet Combat variants at different distances of BFD development, obtained from DIC analysis and presented by shot numbers (1-5). ...	107
Figure 5.9: The average area of helmet deformation obtained from 78 impacts against two different UK Helmet Combat variants. Bars show the standard deviation of the data. ....	108
Figure 5.10: The average radius of curvature of helmet deformation obtained from 78 impacts against two different UK Helmet Combat variants. Bars show the standard deviation of the data. ....	108
Figure 5.11: Flat and curved impact faces determined from helmet BFD data in conjunction with the parameters of the projectile which the faces are to be attached to. ...	110
Figure 6.1: Range set-up for investigating the effect of flat face diameter and curvature on the fracture threshold of a cranial model. ....	117
Figure 6.2: Med-Eng Ballistic Data Acquisition System (BDAS) unit mounted within a four piece aluminium shell. ....	118
Figure 6.3: Decision process for investigation of eight different impact faces against BSM targets. ....	121
Figure 6.4: Projectile with high contrast pattern applied to the outer surface of the shell.	122
Figure 6.5: Probability of fracture with associated Confidence Intervals (CIs) as a function of projectile velocity for flat faced circular projectiles striking BSM. ....	127

Figure 6.6: Probability of fracture with associated Confidence Intervals (CIs) as a function of projectile velocity for curved projectile impact faces striking BSM. ....	127
Figure 6.7: Effect of impact diameter on the impact velocity required to cause a 50% probability of BSM fracture. ....	133
Figure 6.8: Effect of inverse radius of curvature on BSM $V_{50}$ . ....	134
Figure 6.9: Displacement curve (blue) obtained from DIC analysis using ARAMIS software and calculated force profile (red), shown within FAMOS signal analysis software. ....	135
Figure 6.10: Noise amplified within a force profile (red), which was calculated from a displacement curve (blue) of a projectile. ....	135
Figure 6.11: Depressed, detached fractures (Fracture index 4) observed to BSMs as a result of impacts from different projectile faces. ....	137
Figure 6.12: Force profiles for fracture and non-fracture outcomes for impacts with a 32 mm diameter flat projectile. ....	139
Figure 6.13: Force profile shapes observed from FAMOS (imc Measurement and Control 2011) signal analysis software. ....	140
Figure 7.1: Fracture risk models based on measures of peak impact force. ....	153
Figure 7.2: Fracture risk models based on measures of projectile velocity. ....	155
Figure 7.3: Fracture risk models for different projectile faces, developed using measures of impact velocity, bone thickness and fracture outcome. ....	158
Figure 7.4: Fracture risk models by impact velocity for different projectile faces, based on an average bone thickness of 3.7 mm for the complete dataset. ....	159
Figure 7.5: Fracture risk curves for a range of impact diameters and curvatures, based on a calculation of the BC optimised for head impacts (Hisley <i>et al.</i> 2010). ....	161

## Table of Tables

Table 3.1: Summary of literature findings relating to investigation of BHBT injury using biological models. ....	47
Table 3.2: Synthetic head-forms designed as helmet back face deformation assessment methods. ....	55
Table 3.3: Summary of literature findings relating to studies investigating impulsive impacts to the cranium. ....	66
Table 4.1: BSM fracture index reported by James <i>et al.</i> (2009). ....	90
Table 4.2: The fracture outcome by impact velocity for blunt ballistic impacts against three different BSM constructions, in conjunction with the data reported by Raymond (2008). .	94
Table 4.3: Statistical analysis outputs comparing the fracture response of three different BSM constructions (Original, Strain and DIC) to a cadaveric based model. ....	94
Table 6.1: Dimensions of representative BFD impact faces for the investigation of flat diameter and curvature effects on cranial fracture thresholds. ....	118
Table 6.2: Five day plan for manufacturing three batches of 20 BSMS. ....	120
Table 6.3: Impact velocities associated with BSM fracture for different projectile faces. .	128
Table 6.4: Findings from impacting BSMS with eight different projectile faces. ....	129
Table 6.5: Statistical analysis of BSM fracture response by different projectile faces in terms of impact velocity and bone thickness. ....	130
Table 6.6: Comparisons of probit models produced using BSM impact data against different projectile faces in terms of impact velocity and bone thickness. Evidence of a statistical difference at the 95% confidence level ( $p < 0.05$ ) has been identified for analysis considering the parameters of projectile face, bone thickness, impact velocity and fracture outcome. ....	131
Table 6.7: Parameters identified to affect BSM fracture outcome, determined through statistical analysis. ....	132



Table 7.1: Statistical comparison of fracture risk models developed using peak impact force.....	154
Table 7.2: Statistical comparison of fracture risk models developed using impact velocity data. ....	156
Table 7.3: Statistical comparison of fracture risk models developed using impact velocity, projectile and average bone thickness data. ....	160
Table 7.4: Statistical comparison of fracture risk models developed using values of the Blunt Criterion (BC). ....	162
Table 7.5: Values of residual deviance and associated degrees of freedom calculated for fracture risk curves developed using different parameters of impact. ....	166

## Table of Equations

Equation 3.1: Blunt Criterion developed by Sturdivan <i>et al.</i> (2004). .....	60
Equation 3.2: Head specific Blunt Criterion reported by Hisley <i>et al.</i> (2010) to have been developed by Sturdivan in 2005.....	60
Equation 7.1: Head specific Blunt Criterion reported by Hisley <i>et al.</i> (2010) to have been developed by Sturdivan in 2005.....	150

## Abbreviations

AEP	Allied Engineering Publication
ARL	Army Research Laboratory
BABT	Behind Armour Blunt Trauma
BC	Blunt Criterion
BDAS	Ballistic Data Acquisition System
BFD	Back Face Deformation
BHBT	Behind Helmet Blunt Trauma
BIHIM	Blunt Impact Head Injury Model
BLSH	Ballistic Load Sensing Head-form
BRGLM	Bias Reduced Generalized Linear Model
BSE	Bovine Spongiform Encephalopathy
BSM	Bovine Scapula Model
CI	Confidence Interval
CNS	Central Nervous System
CSF	CerebroSpinal Fluid
DAI	Diffuse Axonal Injury
DIC	Digital Image Correlation
DOT&E	Director Of Test and Evaluation
DSTL	Defence Science and Technology Laboratory
FE	Finite Element
FPS	Frames Per Second
FSP	Fragment Simulating Projectile
GLM	Generalized Linear Model
HHS	Human Head Surrogate
HSV	High Speed Video

HTPH	Honed Tube Pressure Housing
ISO	International Organisation for Standardisation
LED	Light Emitting Diode
MOD	Ministry of Defence
NATO	North Atlantic Treaty Organisation
NIJ	National Institute of Justice
PASS	Personal Armour Systems Symposium
PC	Personal Computer
PCB	Printed Circuit Board
PMHS	Post Mortem Human Subjects
PVDF	Polyvinylidene fluoride
STANAG	Standardization Agreement
TBI	Traumatic Brain Injury
TERP	Test, Evaluation, Research and Proof
UHMWPE	Ultra-High Molecular Weight Polyethylene
UK	United Kingdom
US	United States of America
USB	Universal Serial Bus

# Chapter 1: General Introduction

## 1.1 Background

Head injury has been a recurrent theme in the combat environment (Aarabi 1999, Carr *et al.* 2016); nearly 20% of all injuries occurring in United States (US) military operations in 2003 were sustained to the head and neck (Rustemeyer *et al.* 2007). This trend has continued within UK operations (data not shown).

UK combat helmets are designed to protect the head against non-ballistic impact such as bumps, in addition to the common battlefield threats of bullets and fragmentation from devices such as grenades and Improvised Explosive devices (IEDs) (Abbott *et al.* 1997, STANAG-2902 2004, Wallace *et al.* 2012). Current protection against ballistic projectiles has been achieved by using non-metallic composite materials in the helmet construction, resulting in lighter helmets than the previous metal systems (Abbott *et al.* 1997, Lindemulder *et al.* 1998, Sowry 1998). However, these composite helmet solutions inherently deform more than metal systems as part of the mechanism in which projectiles are stopped from causing direct injury to the helmet user (Abbott *et al.* 1997, Cheeseman *et al.* 2003, Evans-Pughe 2014, Lucuta *et al.* 2014). This increased deformation may occur to such an extent as to contact the underlying head, resulting in severe injury, termed as Behind Helmet Blunt Trauma (BHBT) (Freitas *et al.* 2010).

There are no reported occurrences of BHBT in recent combat operations (Carr *et al.* 2016). However, a future desire for lighter helmet systems, using composite material technology to achieve improved ballistic performance (Sowry 1998, Evans-Pughe 2014), may increase the likelihood of BHBT.

There is considerable uncertainty over the associated risk of BHBT head injury, highlighting the requirement for a BHBT assessment method to help understand the scale of the problem.

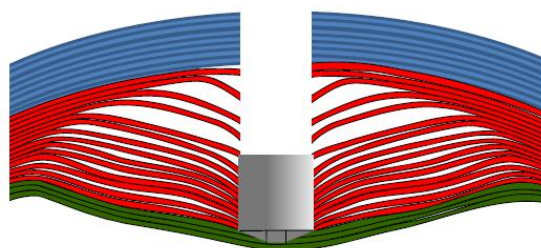
Nationally and internationally recognised combat helmet test methods have started to consider the helmet Back Face Deformation (BFD) effects as part of the pass/fail criteria (CSA-TC-Z613 2008, National Research Council 2014, STANAG AEP 2920 2015). However, methods using a clay backing to measure indentation (NIJ 0106.01 1981, MPS DOI-MTD-03/010 2003, STANAG AEP 2920 2015) have no scientific evidence on which to associate injurious limits with the helmet deformation measured (National Research Council 2014).

Helmet BFD assessments have included the use of instrumented synthetic head-forms (CSA-TC-Z613 2008, Barnes-Warden *et al.* 2013, Neale *et al.* 2013); measurements of peak force are collected, and related to a probability of cranial fracture. However, the injury metric has been determined from a limited number of studies, investigating specific helmets or materials (Sarron *et al.* 2000, Bass *et al.* 2003, 2004, Freitas *et al.* 2010). Therefore, the aim of this study was to improve the understanding of injury metrics capable of predicting BHBT, for application within BHBT assessment methods.

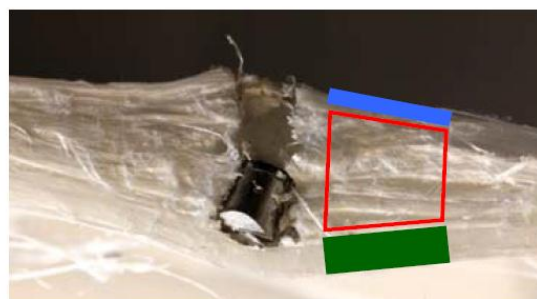
## **1.2 Combat Helmets**

Combat helmets consist of a harness system, a liner, and an outer shell. The harness system is used to maintain the outer shell on the head through the use of straps and padding (DE&S 2010). In conjunction with the liner, the harness distributes the load over the head if an impact to the outer shell occurs (Evans-Pughe 2014). The thickness of the liner and harness system fills the gap between the surface of the head and the outer shell. This gap is known as the stand-off distance. An air gap may also form part of the stand-off depending on the specific location of the harness and overall helmet design. The role of the outer shell is to distribute load providing bump protection and prevent penetration and perforation of the head by projectiles. The protection provided to the head relies on the complete combat helmet system.

Current UK combat helmet shells are constructed of composite materials such as aramids and polyethylene (Evans-Pughe 2014). The shell is formed by compressing numerous layers of the composite material within a resin, forming a laminate structure (Evans-Pughe 2014). Figure 1.1 shows the process by which a laminate material defeats a ballistic threat such as a high velocity ( $300\text{-}1000\text{ m}\cdot\text{s}^{-1}$ ) fragment or bullet (Lucuta *et al.* 2014). On contact with the helmet shell the projectile initially cuts through the outer layers of the shell structure before the material starts to delaminate, and the remaining layers stretch until the projectile comes to rest (Cheeseman *et al.* 2003, Evans-Pughe 2014, Lucuta *et al.* 2014). The projectile is stopped within the layers of the shell construction, termed ‘penetration’ (Lindemulder *et al.* 1998). During defeat of a ballistic threat, deformation can be observed on the back face of the helmet shell. Resultant deformation, similar to that pictured in Figure 1.2, can be seen post impact. As the BFD forms, Hisley *et al.* (2010) observed variation in the area, curvature and velocity of the deforming shell surface.



a) Schematic



b) Test result

**Figure 1.1: Method of ballistic threat defeat by laminate materials.**

**Fragment Simulating Projectile (FSP) (grey) impact area with: shear cutting zone (blue), delamination zone (red), and stretched layers (green), represented schematically (a) and in physical testing (b). Reproduced with the permission of Lucuta *et al.* (2014).**

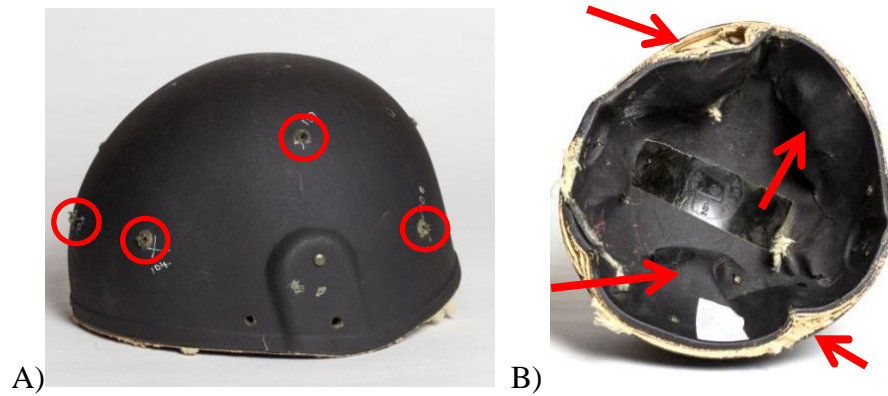


**Figure 1.2: Residual deformation of a laminate helmet shell observed following defeat of multiple ballistic threats. A) External shell view with entry points visible (highlighted by the red circles). B) Internal view with residual deformations and areas of delamination indicated by the red arrows.**

When compared to steel helmets, composite materials show a reduction in mass and an increased resistance to perforation<sup>1</sup> from ballistic threats (Evans-Pughe 2014, Shadrake 2014). There is an enduring interest to look at lighter composite materials with greater resistance to perforation in future helmet designs (Lindemulder *et al.* 1998, Sowry 1998, Evans-Pughe 2014). Although the principal concern is stopping the threat hitting the head, the resulting BFD may still have the potential to cause Traumatic Brain Injury (TBI).

### **1.3 BHBT Injury Risk**

BHBT investigations have explored both local (such as cranial fracture) and global (acceleration of the whole head) injury potential (Sarron *et al.* 2000, Bass *et al.* 2003, 2004, Freitas *et al.* 2010). During a BHBT event, Bass *et al.* (2003) identified that the global acceleration of the head was below the levels reported to cause accelerative injury; however, serious injury was seen at the BFD impact location in the form of cranial fracture, likely to be associated with underlying brain injury.

Models capable of assessing the mechanical response of biological tissues have been used to assess the injuries associated with BHBT (Sarron *et al.* 2000, Bass *et al.* 2003, 2004,

---

<sup>1</sup> Perforation is the term used to describe a projectile passing through a material and exiting out of the other side.



Freitas *et al.* 2010). These have focused on an accurate representation or use of actual craniums, identifying bone fracture on a macroscopic level. Injury to the brain is challenging to measure outside of in-vivo studies (Liu *et al.* 2012); therefore fracture of the cranium has been the main measured outcome. It is assumed that injury severity to the brain is likely to be increased should the cranium be compromised.

Differences in injury outcomes have been observed due to helmet material, bullet type, stand-off and the presence of any padding (Sarron *et al.* 2004, Liu *et al.* 2012, Freitas *et al.* 2014). Therefore, appropriate and accurate helmet assessment methods are required to assess the risk of BHBT.

## **1.4 Helmet Assessment methods**

Where military helmet assessment methods were previously focused on the ability of a helmet shell to provide bump protection and stop perforation of ballistic threats (NIJ 0106.01 1981, HP White laboratories 1995, STANAG-2920 2003), awareness of the risk of BHBT has led to the inclusion of helmet BFD assessment (CSA-TC-Z613 2008, National Research Council 2014, STANAG AEP 2920 2015). Helmets are placed onto synthetic models with clay inserts. This was originally to assess the protective capability of a backed helmet system; these clay models are now used to obtain a measure of helmet BFD in terms of displacement into the clay (MPS DOI-MTD-03/010 2003, National Research Council 2014, STANAG AEP 2920 2015). However, without scientific evidence to support head injury prediction based on displacement into clay (National Research Council 2014), in addition to the challenges of moulding and conditioning the clay (Anctil *et al.* 2008), alternative methods for assessing BHBT have been sought.

## 1.5 Existing BHBT Assessment Methods

A number of BHBT assessment methods have been proposed using metal head-forms to repeatedly collect dynamic force or pressure data from helmet BFD (Bass *et al.* 2002, Anctil *et al.* 2008, Watson *et al.* 2008, Bolduc *et al.* 2010, Barnes-Warden *et al.* 2013). The method proposed by Anctil *et al.* (2008) has been considered by the Canadian Standards Association (CSA-TC-Z613 2008); a similar method was described by Bolduc *et al.* (2010) to the North Atlantic Treaty Organisation Standardisation Agency (STANAG) in support of the next revision of STANAG AEP 2920 (2015). Associated injury prediction is achieved by comparing the measured forces against a statistical model of force verses probability of cranial fracture (Anctil *et al.* 2005, Bolduc *et al.* 2010). One of these statistical models is derived from a total of nine cranial fracture outcomes from cadaveric impacts, using a single bullet type and helmet system (Bass *et al.* 2002, Anctil *et al.* 2005)

Existing injury criteria based on cranial fracture have measured the localised impact as peak force or pressure experienced by the bone, but there has been no other consideration of the BFD such as the shape or velocity of the impact (Bass *et al.* 2003, Sarron *et al.* 2004, Freitas *et al.* 2010).

Previous experimentation has shown cranial bone to respond differently to impact size and shape, loading velocity and rate, position, and biological variation (Nahum *et al.* 1968, Hodgson *et al.* 1970, Schneider *et al.* 1972, Wilber 1974, Allsop *et al.* 1991, Yoganandan *et al.* 1995, Delye *et al.* 2007, Hansen *et al.* 2008, Motherway *et al.* 2009). In addition, testing has already shown variations in the helmet BFD as a result of impacting different helmet materials in different locations, with different projectiles, and where helmets are also mounted differently (Sarron *et al.* 2000, Sarron *et al.* 2004, Anctil *et al.* 2006, Keown *et al.* 2006, Watson *et al.* 2008, Hisley *et al.* 2010).

An increased understanding of cranial fracture outcome as a result of the parameters associated with BFD impact, such as curvature and area, would enhance the ability to predict cranial fracture associated with BHBT. These improved injury criteria could support existing physical head forms, and inform improved test methodologies for the assessment of BHBT. This would ensure the protection level and risks associated with wearing a particular helmet system are quantified. Where the protection afforded by a helmet can be accurately assessed, lighter helmets could then be developed. Lighter helmets would reduce the weight burden on the user, enabling them to be more agile, with the potential to undertake an increased work load prior to fatigue.

## **1.6 Aims**

The overarching aim of this work was to improve understanding of the injury metrics that can be used to predict cranial fracture outcome, in support of the assessment of BHBT. This was investigated through the effect of loading area and curvature on cranial fracture response. Use of this knowledge to develop an improved injury criterion to support the assessment methodology of BHBT, was a key outcome.

## **1.7 Work Structure**

Due to the complex nature of cranial fracture injury and BHBT, a number of topics were investigated to inform the study. Figure 1.3 shows the work undertaken and how this was linked within the overall structure of the investigation.

Understanding the anatomy of the head, combined with an overview of how injury can occur (Chapter 2) was the first step in understanding the importance of the structures of the head and how the cranium fractures. A review of the literature followed (Chapter 3) to investigate the potential loading of helmet BFD onto the head. This included investigation of existing BHBT assessment methodologies, with supporting injury criteria. Further

investigation was required to develop the understanding of cranial fracture risk associated with BHBT.

The next stage was to develop a suitable test methodology for investigating cranial fracture, whilst maintaining links to existing data. A cranial fracture model was identified (Chapter 4) to enable large scale testing, in conjunction with production of a system for delivering a simplified BHBT impact (Chapter 5). The findings of this work were then applied within a complex trial methodology to investigate the effect of varying curvatures and flat face diameters on fracture outcome (Chapter 6). Part of this work was to compare the findings of the trial to other experimental data, determining the relationship between the model outputs and cadaveric head impacts. Following this the trial findings were used to develop cranial fracture risk curves (Chapter 7), specifically to support BHBT test methodologies. Finally, the conclusions and recommendations of the complete work package were determined (Chapter 8).

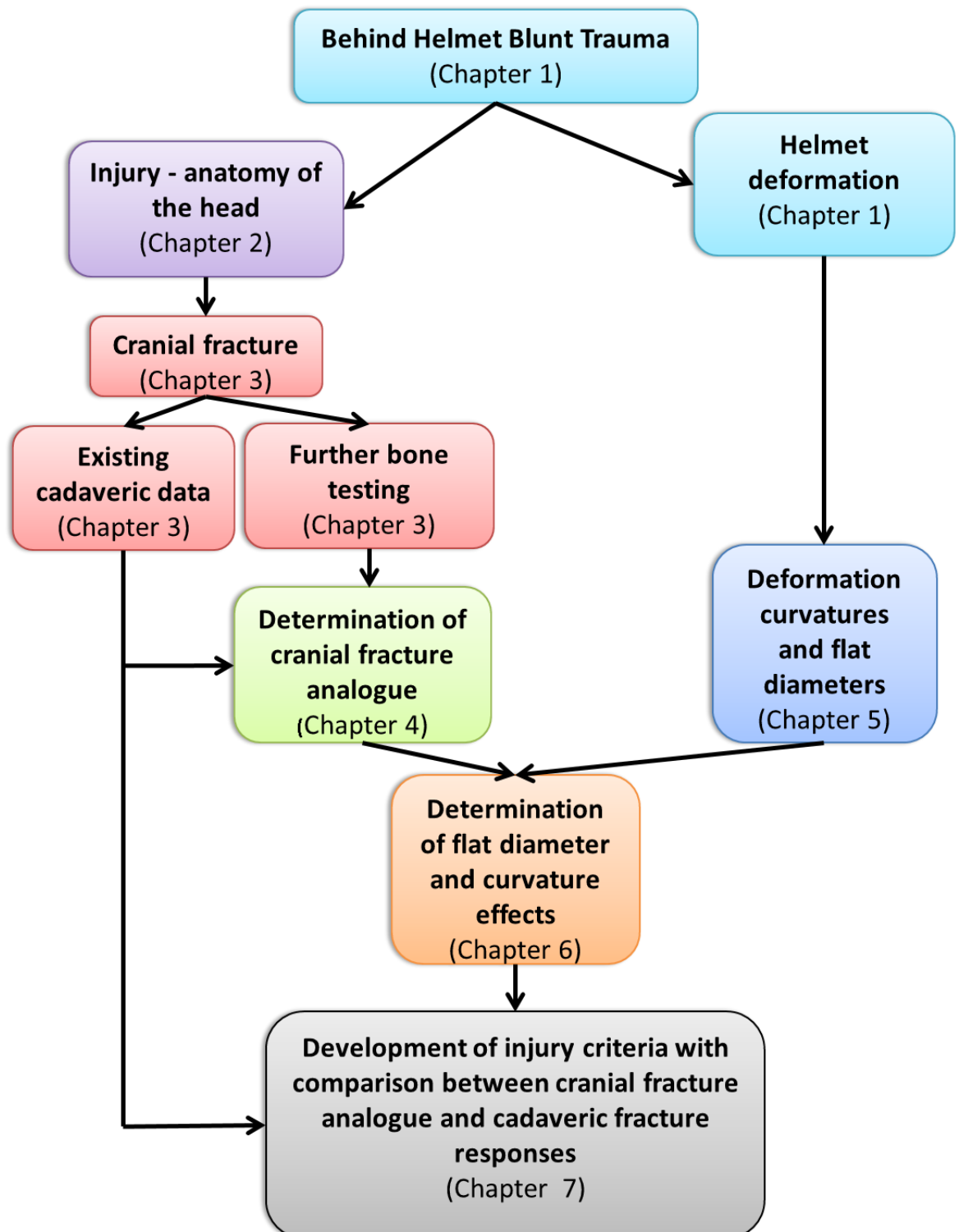


Figure 1.3: Process of investigation presented by focus areas required to meet the overall aims of the study.

# **Chapter 2: Anatomy and Injury of the Head**

## **2.1 Introduction**

In order to understand how injury to the head can occur and determine the severity of such injuries, the anatomy of the head needs to be understood. Therefore, the aim of this chapter was to determine the structures of the head and their importance in terms of protection, leading on to how the protection can be breached and the associated injury outcomes.

## **2.2 The Head**

The bones in the head are collectively known as the skull, which consists of the neurocranium and the face (Strachan 1993, Moore *et al.* 1999, Medical-Dictionary (2003)). The cranium describes the neurocranium without the mandible. The cranium contains the brain, whilst the face supports the organs associated with sight, hearing, smell and taste (Gray 1973, Strachan 1993, Moore *et al.* 1999).

The adult head weighs between 3-5 kg (Walker *et al.* 1973, Raymond 2008). Combat helmets cover and protect the cranium. Consequently, the cranium and underlying structures are the principal focus for the remaining sections of this chapter.

## **2.3 Anatomy of the Cranium**

The bones of the cranium form a closed, protective shell around the brain. This is formed of eight bones joined together by immovable joints or sutures (Gray 1973, Tortora *et al.* 1990, Strachan 1993, Cheng *et al.* 1998, Moore *et al.* 1999, Medical-Dictionary 2003). The cranium consists of the frontal, occipital, sphenoid and ethmoid bones. There are also the paired parietal and temporal bones, located on both sides of the cranium (Figure 2.1) (Gray 1973, Tortora *et al.* 1990, Strachan 1993, Cheng *et al.* 1998, Moore *et al.* 1999, Medical-Dictionary 2003).

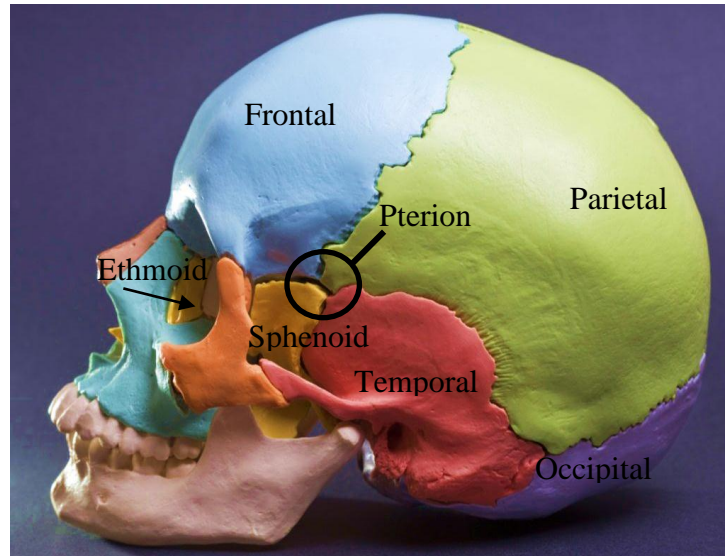


**Figure 2.1: Lateral view of the skull with the eight bone of the cranium identified.**

© Copyright Leafalive. Image purchased from Dreamstime.com and used under the royalty-free license agreement.

Each bone is constructed of external and internal layers or tables (Tortora *et al.* 1990, Moore *et al.* 1999). The outer layers are formed of compact, cortical bone. These are separated from each other by a layer of spongy trabecular bone, forming the inner table (Gray 1973, Tortora *et al.* 1990, Moore *et al.* 1999). Both the inner and outer surfaces of the bones are covered with a layer of periosteum, a thin membrane.

The individual bones comprising the cranium are described as flat bones. This is because the outer cortical layers are more or less parallel (Tortora *et al.* 1990, Moore *et al.* 1999). However, the bones are not uniform. Each bone has a unique curvature and variation in thickness, typically ranging from 2-13 mm (Oldendorf *et al.* 1960, Tubbs *et al.* 2005, Delye *et al.* 2007). The frontal bone (Figure 2.1) for example contains hollowed out pockets or sinuses (Gray 1973, Bo *et al.* 1980). In contrast, the occiput is a thick structure containing grooves for venous sinuses. The bones forming the base of the cranium contain numerous apertures through which the vessels and cranial nerves traverse (Gray 1973, Tortora *et al.* 1990, Cheng *et al.* 1998).

The lateral aspect of the cranium deserves separate attention. At the point where the antero-inferior corner of the parietal bone meets the sphenoid bone is a region called the pterion (Figure 2.1) (Gray 1973, Moore *et al.* 1999). This area is of particular interest; not only is the bone thin here being typically only a couple of millimeters, it also overlies the anterior division of the middle meningeal vessels. Therefore, this region is susceptible to haemorrhage following violent insult to the cranium (Moore *et al.* 1999).

The outer surface of the cranium is covered by layers of soft tissue, collectively termed the scalp (Bo *et al.* 1980, Moore *et al.* 1999). The scalp typically has a thickness between 2-12 mm, and consists of five layers (Oldendorf *et al.* 1960, Delye *et al.* 2007, Raymond 2008). Starting at the outer most layer, the scalp consists of:

- Skin;
- Connective Tissue formed of a vascular, fibro-fatty layer;
- Aponeurosis, a tendinous sheet;
- Loose areolar connective tissue, a further connective tissue loosely binding the aponeurosis to the underlying periosteum; and,
- Periosteum forming the outer lining of the cranium bones (Gray 1973, Bo *et al.* 1980, Tortora *et al.* 1990, Moore *et al.* 1999).

The skin, connective tissue and aponeurosis layers are tightly bound together, and move as one unit (Gray 1973, Bo *et al.* 1980, Moore *et al.* 1999). The loose areolar connective tissue enables the outer three layers to move across the surface of the cranium. The deepest layer of the periosteum is bound to the bones of the cranium and is continuous with the fibrous tissues in the cranial sutures (Bo *et al.* 1980, Moore *et al.* 1999).



## 2.4 Anatomy of the Brain

The human brain weighs approximately 1.45 kg (Gray 1973, Tortora *et al.* 1990, Cheng *et al.* 1998, Medical-Dictionary 2003). It can be divided into three major parts: forebrain, midbrain and hindbrain. The division of the Forebrain, Midbrain and Hindbrain can be seen in Figure 2.2. In addition, the brain contains ventricles, meninges and a complex vascular supply.

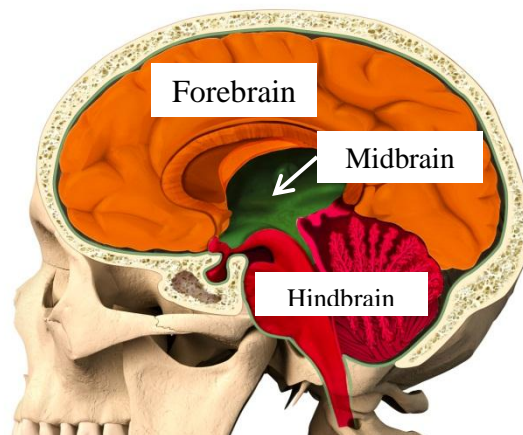


**Figure 2.2: The three major areas of the brain.**

**Original image © Copyright Leonello Calvetti. Image purchased from Dreamstime.com and used under the royalty-free license agreement.**

The forebrain consists of the hypothalamus, the thalamus and the cerebrum (Gray 1973). The cerebrum is the largest part of the brain and consists of two cerebral hemispheres. Each hemisphere has a number of folds or gyri, separated by fissures or sulci. This gives the brain its characteristic appearance of multiple folds, and divides the hemispheres into lobes (Figure 2.3). The lobes are named after the bones to which they are adjacent – frontal, parietal, temporal, etc. (Tortora *et al.* 1990, Cheng *et al.* 1998, Medical-Dictionary 2003). The lobes are responsible for higher functional human activity including memory, thought, creativity, intelligence, speech, sensation and voluntary motion (Tortora *et al.* 1990).

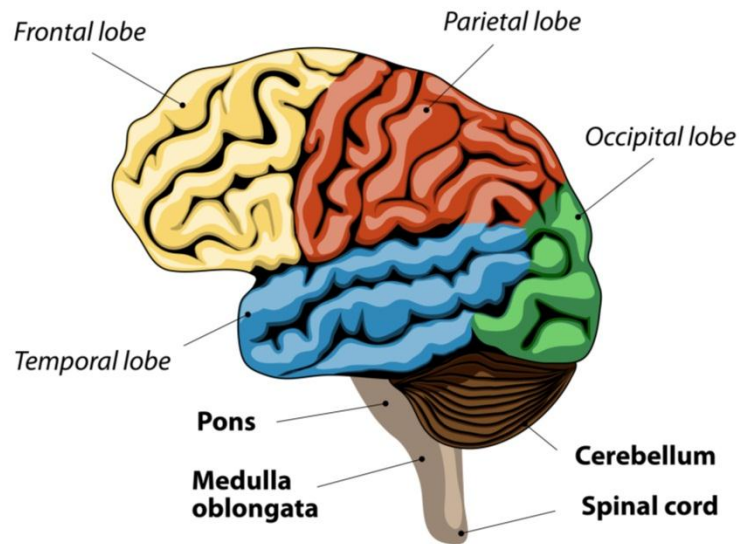


**Figure 2.3: Anatomy of the brain.**

© Copyright Designua. Image purchased from Dreamstime.com and used under the royalty-free license agreement.

The midbrain is closely associated with motor system pathways (Tortora *et al.* 1990), and is the narrowest part of the brain. It contains the cerebral aqueduct (aqueduct of Sylvius), which is linked with the ventricles. These are four ‘hollow’ areas of the brain in which CerebroSpinal Fluid (CSF) circulates (Tortora *et al.* 1990, Cheng *et al.* 1998, Moore *et al.* 1999). CSF functions to bathe the entire Central Nervous System (CNS). It allows for excretion of waste from nervous tissue. However, it is also thought to afford protection from injury through effects of buoyancy and buffering from impact (Tortora *et al.* 1990, Cheng *et al.* 1998, Widmaier *et al.* 2004).

The medulla oblongata, pons and cerebellum comprise the hindbrain (Figure 2.3) (Gray 1973, Medical-Dictionary 2003). The medulla oblongata and pons, along with the midbrain comprise a functional unit called the brainstem (Tortora *et al.* 1990, Widmaier *et al.* 2004). It is through the brainstem that all motor and sensory pathways travel, connecting the spinal cord to the higher brain structures, forming the CNS (Tortora *et al.* 1990).

The brain and the spinal cord are surrounded by three layers of membranes known as the meninges. This consists of the dura mater (most external), the arachnoid mater, and the pia mater (most internal) (Gray 1973, Bo *et al.* 1980, Tortora *et al.* 1990, Cheng *et al.* 1998, Widmaier *et al.* 2004). The primary function of these layers is to protect and support the CNS (Widmaier *et al.* 2004).

The brain has a dual blood supply incorporating two carotid and two vertebral arteries (Gray 1973, Bo *et al.* 1980, Strachan 1993). All four are linked within the brain to form a ring of feeding vessels known as the Circle of Willis (Figure 2.4) (Bo *et al.* 1980, Tortora *et al.* 1990, Strachan 1993, Cheng *et al.* 1998). At rest, blood flow to the brain is on average approximately 750 mL/per minute (Ganong 2005). A complex regulatory system comprising both physical and hormonal features ensures that cerebral blood flow is maintained (Tortora *et al.* 1990).

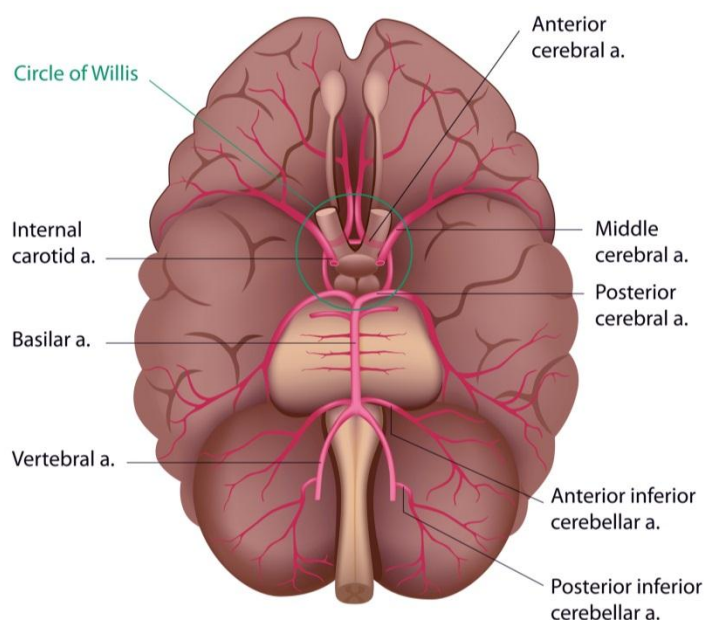


**Figure 2.4: The main arteries of the brain, viewed from the base of the brain.**

© Copyright Alila07. Image purchased from Dreamstime.com and used under the royalty-free license agreement.

Whilst blood is vital to the metabolic function of the brain, a highly selective barrier separates the brain from the contents of the vessels. This ensures that only essential

nutrition for the brain passes across (Tortora *et al.* 1990, Widmaier *et al.* 2004, Ganong 2005). This 'blood brain barrier' is clinically significant as it plays an important role in the prevention of infection (Tortora *et al.* 1990, Widmaier *et al.* 2004, Ganong 2005).

Protection to the brain is afforded mechanically by the bony encasement of the cranium, with an element of support and protection thought to be provided from the CSF (Tortora *et al.* 1990, Moore *et al.* 1999). The brain is 'suspended' within the cranium by numerous vascular structures, nerve roots and fine fibrous connections, collectively called the arachnoid trabeculae (Ganong 2005).

## **2.5 Head Injuries**

### **2.5.1 General Injury**

During violent acceleration of the head the brain may move relative to the cranium, making it vulnerable to shearing forces (Cantu 1995, Bullock *et al.* 1997). However, it is thought that in some cases these shearing effects are reduced by the relative motion of the arachnoid mater against the dura, the action of the trabeculae and some cushioning of the CSF (Tortora *et al.* 1990, Ganong 2005).

Injury to the brain will occur if impact energy is great enough to overcome the bony support of the cranium, penetrating the brain, or the acceleration applied to the head is great enough to negate the support discussed, resulting in haemorrhage and/or axonal injury (Ganong 2005).

#### **2.5.1.1 Penetrating Head Injury**

Penetrating injury is described as a breach of the dura, resulting in breaching of the physical barriers between the exterior and the cranial contents. Injury of this type is predominantly caused by objects with a presented area of less than 6.5 cm<sup>2</sup> (Melvin *et al.*

1968) and in most cases, common battlefield threats such as bullets or fragmentation would be significantly smaller than this (Abbott *et al.* 1997).

The extent of neural insult is related to: the physical properties of the object penetrating the cranium, the energy imparted by that object in the head, its path through the brain and the extent of ‘secondary’ damage, such as bone fracture fragments being pushed into brain tissue (Maynard *et al.* 1997, Moore *et al.* 1999).

Penetrating injury will not only cause primary destruction of the tissues, such as cerebral lacerations and haemorrhage in the object’s path, but also subsequent secondary damage due to insult to the delicate homeostasis of the brain environment (Maynard *et al.* 1997, Moore *et al.* 1999). Penetrating injury caused by projectiles with a large transfer of momentum are likely to result in both focused wounding and more global acceleration injuries (Maynard *et al.* 1997). However, small ballistic projectiles such as fragments and bullets have a high velocity, small surface area and low mass. These are capable of causing penetrating wounding, with minimal global acceleration of the head as the momentum transferred will be low (Maynard *et al.* 1997). Therefore injuries caused by small ballistic projectiles will be focused on the localised effects.

#### **2.5.1.2 Blunt Head Injury**

Loading distributed over an area of more than 6.5 cm<sup>2</sup> can be considered as a blunt impact (Melvin *et al.* 1968). Contact and acceleration are the two phenomena used to explain the principal neuropathological features of blunt head injury (Bullock *et al.* 1997); contact results in effects such as lacerations to the scalp, cranial fracture and bleeding (Bullock *et al.* 1997). The scalp layer has been identified as an important factor in reducing the severity of blunt injury to the underlying cranium and brain (Tedeschi 1977, Cantu 1995, Raymond *et al.* 2008). Acceleration results in relative movement of the brain within the cranium causing pressure gradients and strains throughout the brain (Bullock *et al.* 1997).

## **2.5.2 Traumatic Brain Injury (TBI)**

### **2.5.2.1 Overview**

Bleeding and/or Diffuse Axonal Injury (DAI) can be caused by a direct blow to the head (which may or may not penetrate the cranium), or rapid acceleration-deceleration of the head (Bullock *et al.* 1997, Moore *et al.* 1999).

A second phase of injury may become apparent hours or days after the initial traumatic event. This is associated with a malfunction in cerebral blood flow due to the initial injury, affecting the homeostasis of the brain and as such the internal environment begins to fail; this can ultimately result in death (Cantu 1995). Whilst the initial impact injury may be focused with identifiable wounding, often the damage is much more widespread and centred around the response of the brain tissue to movement within the cranium (Cantu 1995, Moore *et al.* 1999). Such injuries range from concussion through to DAI (Moore *et al.* 1999).

### **2.5.2.2 Haemorrhage**

Bleeding within the cranium may occur following violent injury to the head (Cantu 1995). The nature and location of this bleeding is related to the type of injury and the underlying state of the brain (Cantu 1995). Although this is all encompassed as intra-cranial haemorrhage or bleeding within the cranium, those causing potentially damaging effects on the brain may be defined as:

- Extradural or Epidural Haematoma, found between the dura mater and the inner aspect of the cranium (Figure 2.5). This is commonly associated with a blow to the head in conjunction with acute traumatic head injury (Cantu 1995, Moore *et al.* 1999). It is frequently associated with a tear in the artery supplying the dura, caused

by fracture of the temporal bone (Cantu 1995). Typically a brief loss of consciousness occurs (Moore *et al.* 1999);

- Subdural Haematoma occurs between the dura and arachnoid mater, creating a subdural space (Figure 2.5) (Cantu 1995, Moore *et al.* 1999). More common than extradural haematomas, it forms following an insult to veins rather than arteries, as seen with extradural bleeds (Moore *et al.* 1999). As opposed to fracture and arterial tear, the bleeds are associated with shearing forces of acceleration/deceleration and rotation, leading to tears in bridging veins (Cantu 1995);
- Subarachnoid Haematoma is bleeding within the area between the arachnoid and pia mater (Moore *et al.* 1999).
- Intracerebral Haematoma occurs in the substance of the brain itself, below all the layers of the meninges (Figure 2.5) and it may be referred to as a contusion. These arise from tissue tears in areas where the brain has moved relative to the overlying cranium or from direct impact with the cranium itself. Due to the nature of the motion of the brain suspended within the buoyant field of the CSF, a direct blow or marked acceleration-deceleration of the head may result in the brain becoming contused not only at the point of initial impact, but also on the opposite side of the brain to the injury. This is due to a ‘lag-phase’ in the movement of the brain relative to the cranium, which results in the brain region directly opposite the opposing force colliding with the cranium at this point causing damage: the coup – contre coup phenomenon (Cantu 1995).

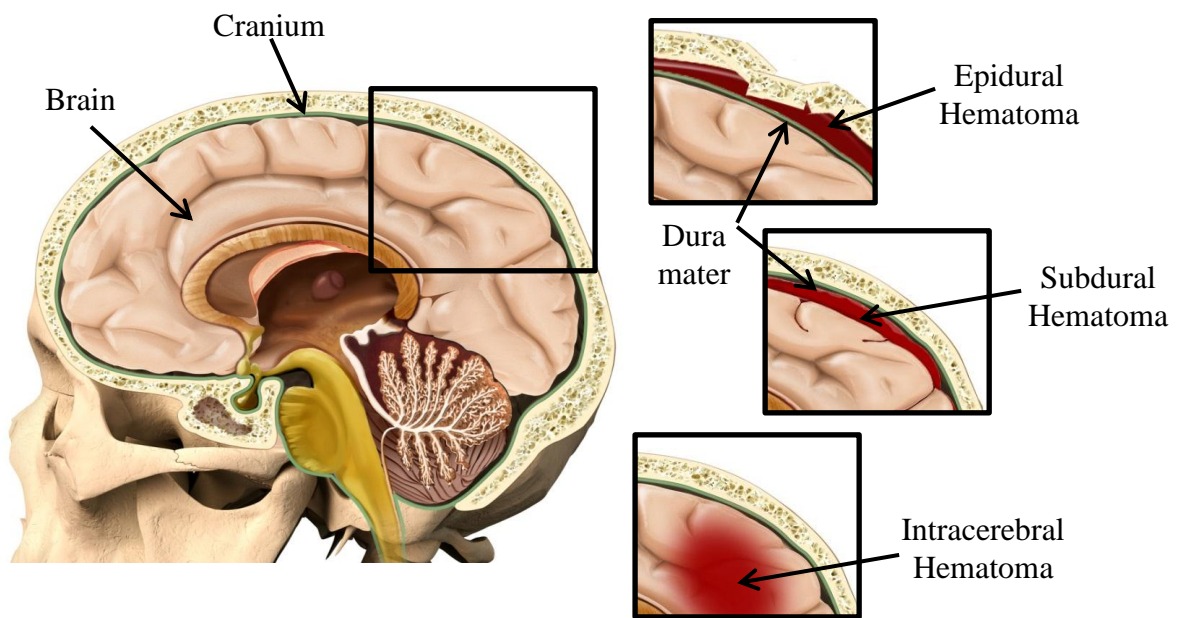


Figure 2.5: Schematic representation of Intracranial Haemorrhage.

Main image © Copyright Leonello Calvetti. Image purchased from Dreamstime.com and used under the royalty-free license agreement.

### 2.5.2.3 Diffuse Axonal Injury

This is a common cause for significant morbidity following head injury associated with acceleration and deceleration (Moore *et al.* 1999). Sudden exposure of the brain to violent acceleration and deceleration causes rotational shearing forces to be exerted on neural tissue. These forces are most marked in regions of the brain where tissue density gradients are greatest and causes trauma to the brain cells known as axons (Lewis 2006).

## 2.5.3 Cranium Fracture

### 2.5.3.1 Types

Fractures of the cranium may be roughly differentiated by the pattern of the fracture, the region in which they occur and any breach of the overlying skin (Moritz 1943). Hence the pattern of cranium fractures may be termed as:

- Linear (Figure 2.6A and Figure 2.7), where the fracture pattern forms a simple line radiating away from the point of impact (Moritz 1943, Moore *et al.* 1999); or,



- Depressed (Figure 2.6B and Figure 2.7), described when the fracture pattern involves one or more bony fragments being pushed into the brain, with potential effects on the underlying tissue (Moritz 1943, Moore *et al.* 1999).

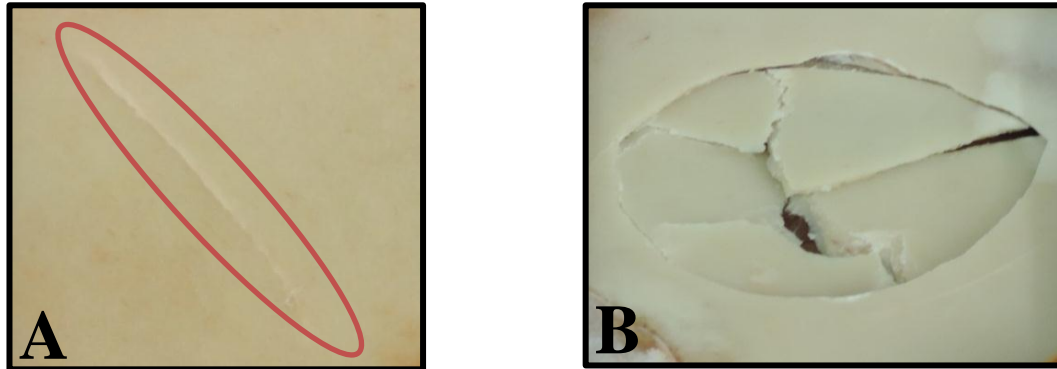


Figure 2.6: Simple, linear (A) and depressed, comminuted (B) flat bone fractures.

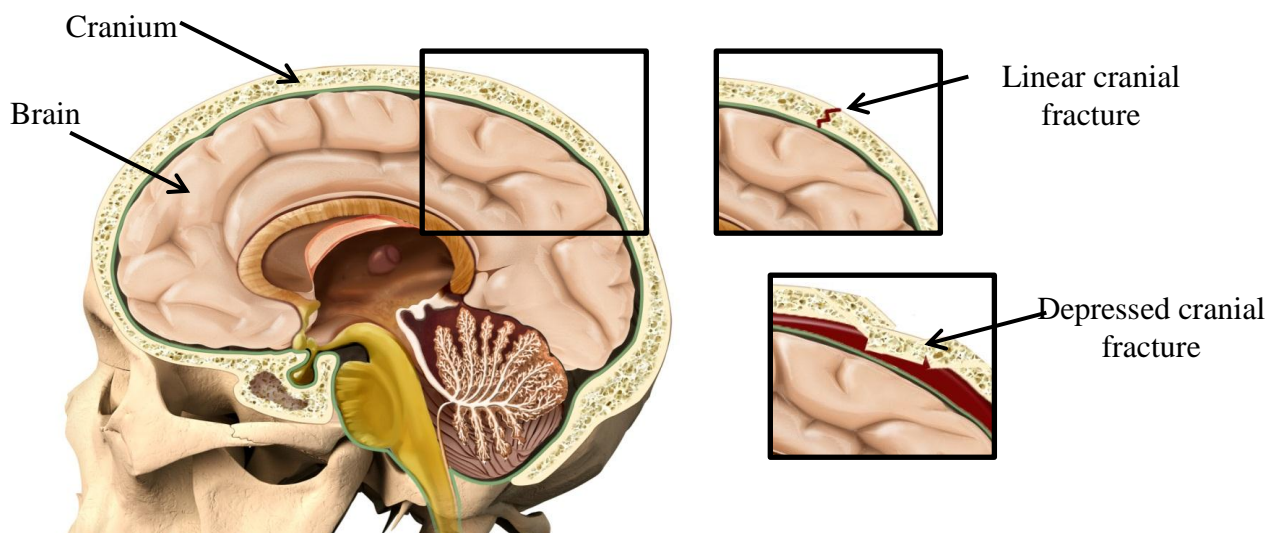


Figure 2.7: Schematic representation of simple and depressed cranial fractures.

Main image © Copyright Leonello Calvetti. Image purchased from Dreamstime.com and used under the royalty-free license agreement.

Fracture types may be further defined in terms of the resulting bone fragmentation:

- Simple, involving a single fracture line with the identification of two main fracture fragments (Moritz 1943) (Figure 2.6A); and,
- Multi-fragmentary or ‘comminuted’ where a number of fracture lines exist with multiple pieces of fracture fragments identified (Moritz 1943, Moore *et al.* 1999) (Figure 2.6B).

Finally, if the fracture is associated with perforation of the overlying skin, the above fractures may be further defined as:

- Open, where the skin over the fracture has been perforated, contacting the deeper structures and often exposing the underlying tissues (Medical-Dictionary 2003); and,
- Closed, documenting that the skin over the fracture has remained intact.

#### **2.5.3.2 Effect of Loading Rate**

To cause fracture, energy must be transmitted to the bone and this loading may be either static or dynamic. When a load is applied over a time greater than 200 milliseconds it is determined as static, and causes crushing as multiple linear fractures develop during absorption of the energy applied (Lewis 2006).

More commonly, loading is dynamic, determined by a rapidly applied impact to the head (Lewis 2006). A dynamic or impulsive impact causes localised deformation beneath the impact site, possibly leading to penetration (Lewis 2006). Localised bending of the cranium produces compressive strain on the outer table and tensile strain on the inner table (Lewis 2006). Bone is stronger in compression than tension, hence the inner table fractures first (Moritz 1943, Lewis 2006). The resulting fracture will be due to the magnitude of

impact and location, in addition to the area which the force is distributed over the cranium (Melvin *et al.* 1968).

### **2.5.3.3 Area of impact**

Melvin *et al.* (1968) identified different fracture types to occur to the frontal bone depending on the area of the impactor used. Penetration fractures are localised, cutting through or fracturing a plug of bone material, whilst comminuted depressed fractures are produced by bending of an area of bone, caused by an impactor with an area between 6.5 cm<sup>2</sup> and 13 cm<sup>2</sup> (Melvin *et al.* 1968). Impact areas greater than 13 cm<sup>2</sup> were observed to cause linear fractures remote from the site of contact (Melvin *et al.* 1968).

## **2.6 Summary**

The head is a complex region, susceptible to potentially severe injury. There is variability between the bones of the cranium in terms of thickness and geometry, in addition to differences in the underlying structures such as vessels and brain tissue. In order to understand the injury risks associated with BHBT, these variations may need to be considered.

Injuries to the head result from two main causes, contact at the site of impact and acceleration/deceleration due to global movement of the head. Contact injuries such as helmet deformation impacting the head commonly result in localised damage to the soft tissues of the scalp in conjunction with fracture of the underlying cranium. Therefore, these structures should be considered when investigating injury outcomes for impacts from helmet BFD.

Loading area and rate affect the type and severity of cranial fractures. Therefore, the parameters of impact area and rate must be representative of helmet BFD impacts when investigating injury outcomes associated with BHBT.

## **Chapter 3: Literature review**

### **3.1 Introduction**

A review of the literature was carried out to determine the current understanding associated with the loading conditions of helmet BFD on the head. In conjunction, the methods available for assessing the risk of head injury as a result of impact from helmet BFD were also reviewed. This focused on the prediction of injury outcomes, identifying areas where further investigation would be beneficial.

As part of this review, a range of cadaveric impact data was investigated. This was explored to determine whether existing information could inform the testing required to improve the prediction of head injury associated with BHBT.

### **3.2 Helmet BFD loading on the head**

The head can be injured under a range of loading conditions (Bir *et al.* 2004, Hisley *et al.* 2010) (Figure 3.1). Projectiles travelling at high velocities, with a small mass and contact area (i.e. bullets and fragments) will typically cause penetration injuries on impact with the head (Maynard *et al.* 1997, Bir *et al.* 2004). As the mass and contact area of a projectile increases and the velocity decreases, the injuries caused will change from perforation or penetration with minimal global motion, to acceleration/deceleration injuries associated with blunt impacts (Figure 3.1).

Blunt ballistic impacts caused by less-lethal impact rounds and baseballs or cricket balls, typically involve contact with an object of mass 20 to 110 g, travelling at velocities between  $20 \text{ m}\cdot\text{s}^{-1}$  and  $115 \text{ m}\cdot\text{s}^{-1}$  (Figure 3.1). Blunt ballistic loading has been shown to cause localised injury to the head; this commonly results in cranial fracture, with limited

injury observed as a result of global motion or acceleration of the head (Bass *et al.* 2003, Raymond 2008).

As a result of conducting 15 impacts on laminate helmet shells, Hisley *et al.* (2010) estimated helmet BFD to have an effective dynamic mass of between 20-30 g, a peak velocity between 30-40 m·s<sup>-1</sup> and a projected surface area up to 100 cm<sup>2</sup>. This was determined for a single helmet and bullet combination, at a stand-off representative of when the BFD would effectively strike the head. From these findings, helmet BFD appears to be representative of the blunt ballistic impact conditions detailed in Figure 3.1.

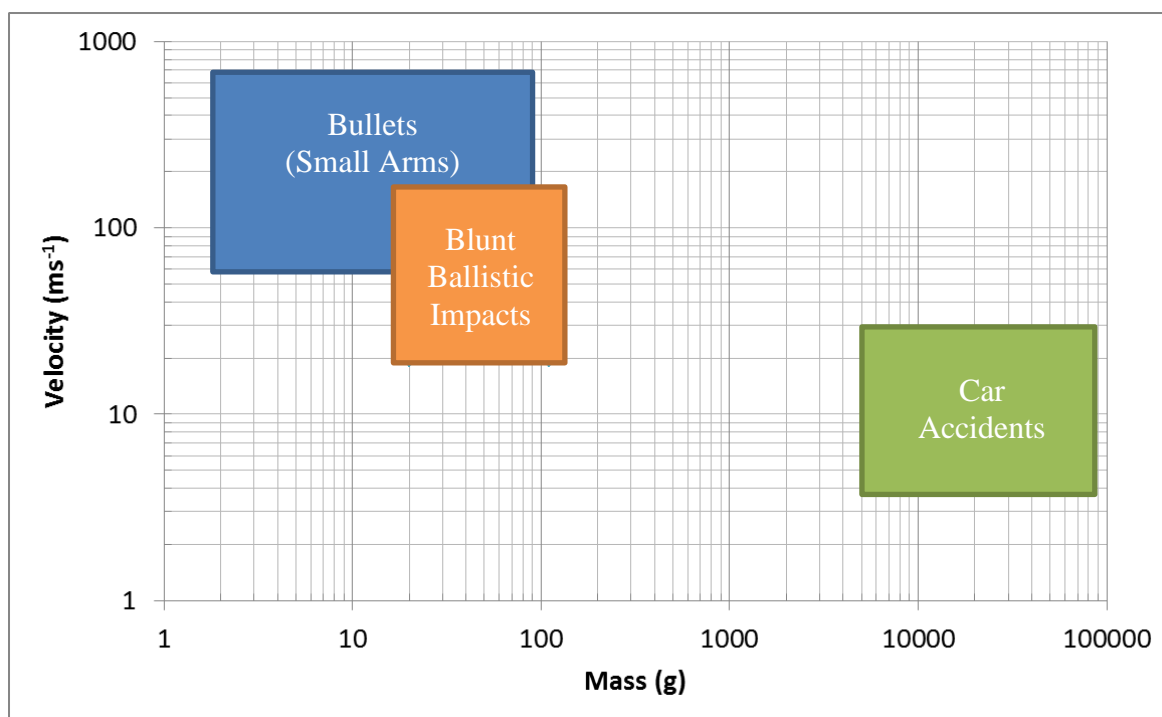


Figure 3.1: Loading parameters determined for different impacts, based on reporting by Hisley *et al.* (2010) and Bir *et al.* (2004).

In terms of the shape of impact, observation of helmet BFD by Hisley *et al.* (2010) and Sarron *et al.* (2000) reported a bell shape, increasing in radius of curvature and area over time. However, the change in shape and force distribution once contact has been made with the head is not well characterised. This is due to challenges with visualising the BFD when there is a head underlying the helmet. Instrumenting the helmet shell or using x-ray

imaging (Bass *et al.* 2003, Freitas *et al.* 2014) may be viable techniques for measuring the BFD, but these are currently indicative at best.

### **3.3 BHT assessment methods**

#### **3.3.1 Overview**

A variety of methods have been used to assess the risk of head injury from BFD, identified within the following categories:

- Biological models, consisting of complete cadaveric specimens, isolated skulls with synthetic components and animal models. These could be described as frangible models as they break;
- Free-air BFD, investigating the deformation surface of the helmet to obtain quantitative data which can be related to injury risk; and,
- Synthetic head models, non-frangible systems which can provide comparison between impacts in terms of the magnitude of sensor outputs.

The frangible nature of biological models means they cannot be used for repeated studies. They suffer reproducibility issues due to biological variation, and are not cost effective. However, they provide the most representative means of assessing injury risk. These methods can be used for helmet assessment whilst also developing an understanding of injury risk; mathematical injury risk models can be produced from biological test data (Bass *et al.* 2003, Raymond *et al.* 2008).

The free-air and synthetic model methods can be used to provide comparison between different helmet BFD impacts in terms of impact parameters such as peak force and surface velocity. However, a prediction of injury risk can only be achieved by applying the instrumentation outputs to a mathematical injury risk model.

### 3.3.2 Biological models

A number of investigations have been undertaken using biologically based targets to develop an understanding of BHBT injury potential. Complete cadaveric heads (Bass *et al.* 2003, Sarron *et al.* 2004), isolated skulls (Sarron *et al.* 2000), skulls combined with synthetic materials (Sarron *et al.* 2004, Freitas *et al.* 2014) and animals (Liu *et al.* 2012) have been used to investigate the injurious effects of deforming helmet armour impacting underlying tissues. Some of these investigations have placed a complete helmet system on the biological model (Bass *et al.* 2003, Freitas *et al.* 2014), whilst others produced BFD in flat armour plates to cause damage to the underlying biological model (Sarron *et al.* 2000, 2004, Liu *et al.* 2012). A summary of these investigations is presented in Table 3.1.

The injuries associated with BHBT were found to include damage to the scalp (Bass *et al.* 2003, Sarron *et al.* 2004); circular lacerations were observed at the site of impact. Cranial fractures were also reported (Sarron *et al.* 2000, Bass *et al.* 2003, Sarron *et al.* 2004, Freitas *et al.* 2010, Freitas *et al.* 2014); linear fractures were observed to radiate from and around the point of impact, with the most severe cases resulting in comminuted fractures at the impact site. Bass *et al.* (2003) also reported the presence of dural contusions due to the dura coming away from the bone at the impact site. However, the full effect of these contusions on the brain is unknown. Where brain tissue was included, the injurious effects were not reported due to the inability of the tissues to respond in the same way as live tissues (Bass *et al.* 2003, Sarron *et al.* 2004). It is understood that the material properties of the brain tissues change very rapidly following death. In addition, after thawing, the brain tissue was reported to be in an advanced state of decomposition due to the freezing and thawing process. This reduced the appearance of any injuries. Therefore, living tissues would be required to fully assess injury to brain tissue (Bass *et al.* 2003).

Reference	Target		No. Targets	Projectile	Projectile Velocity (m·s <sup>-1</sup> )	Stand-off* (mm)	Stand-off content	Results		Findings
	Biological Specimen and Condition	Protective Material covering Specimen (cm)						Input Loading Measurements	Biological Response Data	
Bass <i>et al.</i> (2003)	Fresh/frozen Cadavers	Ultra High Weight Polyethelene (UHWPE) helmet	9	9 mm bullet	405 - 459	13	Air	Projectile velocity Flash x-ray (Observation of BFD contact area)	Global accelerations Neck forces and motion Intracranial pressure and strain Skull impact force and strain Acoustic fracture detection	Skull fractures occurred due to impact in 5 subjects, neck response not sufficient to cause injury.
Freitas <i>et al.</i> (2010)	Human head surrogate (Refreshed human craniums)	Combat helmet	>4	9 mm bullet	410 - 444	Not measured, dependant on helmet fit	Air or Padding <sup>o</sup>	Projectile velocity Flash x-ray (observation of BFD contact area)	Intracranial pressure Skull fracture Cranial strain Head/helmet acceleration	Development and verification of Human Head Surrogate (HHS), increased injury severity with air backed BFD.
				4 gram Right Circled Cylinder	466 - 492					
Freitas <i>et al.</i> (2014)	Human head surrogate (Refreshed human craniums)	Combat helmet	<70	4 gram Right Circled Cylinder	437 - 480	20	Air or Padding <sup>o</sup>	Projectile velocity Flash x-ray (observation of BFD contact area)	Intracranial pressure Skull fracture Cranial strain Head/helmet acceleration	Further verification of HHS - range of injury outcomes for different threat , helmet and padding combinations.
		Combat helmet with applique		9 mm bullet	428 - 438					
				7.62 x 39 bullet	715 - 719					
				7.62 x 51 bullet	843 - 851					
Liu <i>et al.</i> (2012)	Anethetized Pigs	Aramid plate (20 x 15 x 9)	24	9 mm bullet	279 - 297	12	Foam padding	Projectile velocity	Intracranial pressure	Correlation between intracranial pressure waveforms and different ballistic impact velocities.
Sarron <i>et al.</i> (2000)	Dry skulls	Aluminium plate (1.2 thick)	30	Spherical steel ball	381 - 443	10	Air	Projectile velocity	Intracranial pressure Contact force Acoustic fracture detection Macroscopic analysis of fractures and soft tissue injury Radiographs	Permanet cone displacement of the aluminium plate was observed, higher contact pressures were not statistically different across the different regions of impact, requirement for consideration of aramid and/or composite materials and consideration of a skin/scalp layer.
Sarron <i>et al.</i> (2004)	Dry skulls	Polyethelene plate (0.9 thick)	21	9 mm bullet	405 - 416	12 - 15	Air	Projectile velocity Residual BFD	Intracranial pressure Contact force Macroscopic analysis of fractures	Plate type influenced level of injury and intracranial pressure, air gap reduced the intracranial pressure, polyethylene plates failed for all cadaveric impacts, a stand-off greater than 12mm advised from dry skull impacts.
	Fresh Cadavers	Aluminium plate (1.2 thick) Aramid plate (1.0 thick) Polyethylene plate (0.9 thick)	9			0 - 8		Projectile velocity	Intracranial pressure Residual force and momentum Macroscopic analysis of fractures and soft tissue injury Radiographs	

\* Stand-off is the gap between the rear of the protective material and the surface of the head.

<sup>o</sup> Depending on the harness system in terms of any padding included to improve comfort and fit for the user, the stand-off across different areas of the helmet shell will vary between air gaps and padding.

**Table 3.1: Summary of literature findings relating to investigation of BHBT injury using biological models.**



In an effort to assess the potential for brain injury as a result of raised intracranial pressure or bulk stress, intracranial pressures were measured in all of the investigations (Table 3.1). However, Bass *et al.* (2003) did not report on the measures obtained. Equally, where intracranial pressures were reported, they were not consistently documented in conjunction with other injuries. Therefore, it makes it very challenging to use existing data to determine if there is a relationship between intracranial pressure, brain injury and cranial fracture. In the highest cases, Sarron *et al.* (2004) reported pressures over 1000 kPa, whilst Liu *et al.* (2012) reported pressures around 750 kPa for high impact velocities; Freitas *et al.* (2014) documented pressures up to 255 kPa. These all exceed 235 kPa, determined by Zhang *et al.* (2004) as the threshold for severe traumatic brain injury as a result of focused impacts. Therefore, the BHBT tests would suggest severe brain injury to be caused in conjunction with scalp and cranial damage. However, intracranial pressures are dependent on the material properties and geometry of the tissues (Liu *et al.* 2012). Therefore, the intracranial pressures measured in these studies may not be directly comparable to the response of living human brain tissue.

In an effort to understand the potential for global acceleration injuries to the head and neck, Bass *et al.* (2003) and Sarron *et al.* (2004) measured the movement of the head. Bass measured the acceleration of the head and forces in the neck, whilst Sarron reported on a residual force, calculated from the acceleration of a pendulum arm on which the head was mounted. Based on findings extrapolated from the automotive environment, Bass reported the acceleration of the head and forces in the neck to be below levels expected to cause injury. Sarron was in agreement that the global motion was below injurious levels. Therefore, BHBT assessments of current helmet materials have determined the injuries associated with BHBT to be predominantly localised, rather than being caused by global acceleration of the head.

Within the investigations using biological models, a range of parameters have been investigated in terms of their effect on injury outcome. Bass *et al.* (2003), Liu *et al.* (2012) and Sarron *et al.* (2000) investigated the effect of changing projectile velocity, with all other aspects of their test methods remaining consistent. In all cases, it was found that an increase in projectile velocity resulted in a more severe injury outcome. For higher projectile velocities Bass *et al.* (2003) and Sarron *et al.* (2000) reported higher contact forces with increased fracture severity and increased intracranial pressures, which Liu *et al.* (2012) also reported. Therefore, as would be expected, it can be concluded that projectile velocity affects the loading that the BFD causes to the underlying head.

The effect of varying stand-off and the content of the stand-off has been investigated by Sarron *et al.* (2004) and Freitas *et al.* (2014) respectively. Sarron *et al.* (2004) found that increasing the stand-off reduced the intracranial pressure and fracture severity whilst Freitas *et al.* (2014) found that for the same stand-off, the inclusion of padding had the same effect. Therefore, the stand-off and content of the stand-off affects the loading of the helmet BFD onto the underlying head.

Different helmet materials were tested within the studies by Freitas *et al.* (2014) and Sarron *et al.* (2004). However, Freitas *et al.* (2014) also varied the projectile, therefore differences in the injuries sustained cannot be solely attributed to changes in the helmet material. Sarron *et al.* (2004) used the same projectile against three different helmet materials, each of a different thickness. For comparable stand-offs and bullet velocities, the material tested was reported to influence the injury severity and intracranial pressure. Sarron *et al.* (2004) reported that the greater the deformation of the material the larger the contact area with the underlying head, resulting in more severe fractures and larger intracranial pressures. Overall it was concluded that the material under test affects the injury outcome (Sarron *et al.* 2004), indicating variability in the BFD loading to the

underlying head, due to the response of the material to impact. This highlights the importance of testing different helmet systems to assess the risk of BHBT.

Freitas *et al.* (2014) found, when fired at the same protective material, different projectiles caused different levels of injury as a result of the helmet BFD. However, the velocities of the projectiles also varied. Therefore, the different injury severities observed between different projectile impacts cannot be directly attributed to the change in projectile; as previously determined, the velocity would have had an effect.

Bass *et al.* (2003) and Freitas *et al.* (2010), (2014) used flash x-ray to observe the interaction of the helmet BFD and the head. Detailed measurement of the interaction was not reported, most likely due to the challenges of obtaining accurate data from the x-ray images. In addition, where helmet systems are being assessed for their protective capability against realistic bullet velocities, injury outcome is the primary focus. Therefore, the challenges with measuring the helmet deformation on contact with the head were not addressed. However, a detailed understanding of the parameters associated with the BFD such as surface velocity and curvature would enable the development of injury risk models associated with the parameters of loading. These risk models could then be applied to any impact rather than only being relevant to a specific test set-up.

When conducting investigations using biological models, it is important to consider that human testing is bound by regulations, the Human Tissue Act (2004) in the UK and the Code of Federal Regulations, Protection of Human Subjects in the US (2009). For the testing of cadaveric specimens, individuals and institutions require licences to practise and study proposals must undergo an ethical review (Human Tissue Act 2004, Protection of Human Subjects 2009). It is these handling restrictions on cadaveric specimens which led Freitas *et al.* (2010) to develop surrogate human head models. There are other issues such as supply and minimising specimen numbers. This has led others to develop alternative

assessment methods without the use of any biological materials (Bass *et al.* 2000, Anctil *et al.* 2005, Hisley *et al.* 2010). However, the injury outcomes obtained from cadaveric investigations are essential to relating measures of BFD impact to injury risk.

### 3.3.3 Free-air BFD

Hisley *et al.* (2010) used Digital Image Correlation (DIC)<sup>2</sup> to capture the free-air BFD of the helmet as a means of assessing BHBT. The method was used to quantify the surface of the helmet deformation in terms of velocity, area and shape. This method can be used to assess the effect of shot location (front, side, rear etc.), threat type (fragments and bullets), threat velocity, helmet material and shape on the severity of helmet BFD.

Hisley *et al.* (2010) used the BFD characteristics measured using DIC to estimate values of the energy based Blunt Criterion (BC) (section 3.3.5), which could then be used to make conservative estimates of the risk of head injury.

In cases where the helmet is not perforated, this method can only provide an understanding of the helmet BFD at the initial point of contact with the head, determined by the stand-off selected. Without a backing, the interaction between the deforming helmet shell and an underlying head post-contact cannot be investigated.

The main limitation of this approach is that it does not consider the presence of a backing (i.e. the head) and the effect this may have on the BFD. Testing undertaken within Dstl has shown that where a helmet material was able to defeat a threat in free-air, the presence of a backing caused the threat to perforate the protective material (M. Neale, personal communication). This would have caused a penetrating injury to the head rather than BHBT type injuries. Therefore, the free-air BFD measured using DIC might not be

---

<sup>2</sup> DIC is a non-contact, digital technique, using high speed video images from two cameras to produce a three-dimensional representation of a surface moving over time. This is achieved using software containing complex algorithms to map points on the surface and their relationship to one another.

representative of the backed material response. Where perforation is assumed as the worst case outcome, this assessment method may over-estimate the protective capability of a helmet system against ballistic threats.

### **3.3.4 Synthetic head models**

A number of synthetic head models have been designed, enabling multiple assessments to be undertaken without the legalities and variability associated with biological models.

Initially, when assessing helmet resistance to perforation, synthetic head-forms consisting of metal structures with metal witness plates or clay inserts were used to back the helmet shell (NIJ 0106.01 1981, HP White laboratories 1995, MPS DOI-MTD-03/010 2003, STANAG-2920 2003). When impacting the helmet, the permanent deformation of the clay provided a measurement of the peak BFD (HP White laboratories 1995, MPS DOI-MTD-03/010 2003). Irrespective of the deformation measured, perforation of the helmet shell remained the focus for assessment using the HP White (0401.01B) test method. However, the Metropolitan Police Service (DOI-MTD 03/10) helmet test method stipulated any perforation of the helmet shell or a deformation of the clay exceeding an arbitrary value of 50 mm to be a test failure. This highlights an understanding that even without perforation, the resultant deformation could cause serious injury to the underlying head.

Due to the increased awareness of BHBT, more recent versions of combat helmet test standards have also included assessment methods for measuring helmet BFD, and assigning pass/fail criteria based on measured effects of BFDs (CSA-TC-Z613 2008, STANAG AEP 2920 2015). STANAG 2920 (2015) and the US Director of Test and Evaluation (DOT&E) has mandated the use of existing metal head-forms with clay inserts to obtain measures of clay deformation. The DOT&E states the clay deformation must not exceed 16.0 mm on crown, right, and left side locations of the helmet, with a maximum deformation of 25.4 mm for the front and rear locations (National Research Council 2014);

these deformation limits are for a single bullet type (9 mm). However, there appears to be no scientific basis for the limits (National Research Council 2014).

STANAG 2920 directs all pass/fail criteria limits to be set by the National Authority (NA); this may be due to different authorities accepting different levels of injury risk. However, the lack of any guidance suggests a limited understanding of injury potential as a measure of deformation into clay. In particular, there is no reporting to suggest helmet deformations in clay have been compared to the BHBT injury assessments discussed in section 3.3.2. This shows that the potential for BHBT to occur is understood; however, the ability to accurately predict injury outcomes is limited.

More complex models have been developed to enable the collection of data using a range of sensor systems. These can provide a probability of injury risk based on the findings of the biological testing. One of these systems, the Ballistic Load Sensing Headform (BLSH) (Anctil *et al.* 2005), has been incorporated into the Canadian Standards Association (CSA) technical committee (Z613) test method; inclusion of the head model has also been proposed for the next version of STANAG 2920 (Bolduc *et al.* 2010). This further supports an awareness of the potential for injury from helmet BFD impacts, and hence there is a requirement to ensure helmets are appropriately assessed.

Liu *et al.* (2012) developed a synthetic pig head model made of polymer materials for investigation of intracranial pressures alongside in-vivo studies (section 3.3.2). The intention was to validate the synthetic model to remove the need for further in-vivo testing. However, similarly to the biological assessment methods, Liu *et al.* (2012) found differences in pressure measures as a result of the material properties. Even if the model was developed to optimise the pressure measurements, a pig head model would not lend itself to testing complete helmet systems.

Within the published literature, the majority of synthetic head models used to assess BHBT have focused on measuring the localised impact to the surface of the head, using off-the-shelf sensor systems mounted in a metal head shape (Anctil *et al.* 2008, Watson *et al.* 2008, Barnes-Warden *et al.* 2013). In terms of the BFD loading the surface of the head, force and contact pressure can be recorded using sensors systems (Anctil *et al.* 2005). Five synthetic head models have been identified (Table 3.2 and Figure 3.2), with impact force being the most common measurement. These head models have been investigated further to determine the impact parameters collected, and therefore the information available to support the prediction of injury outcomes.

The design for three of the synthetic head models (Table 3.2 and Figure 3.2) has evolved from existing head-forms, namely the Hybrid III (Backaitis *et al.* 1994) and the International Organisation Standardisation (ISO) size J head-form. Instrumentation capable of measuring head impact has been incorporated into these head-forms (Anctil *et al.* 2008, Bolduc 2009, Neale *et al.* 2013). The benefit of using existing head-forms is that they are defined shapes and sizes in addition to being representative of the mean of the population they are based on.

Of the five synthetic models (Table 3.2 and Figure 3.2), three have included a nape in the design; the BLSH, the Blunt Impact Head Injury Model (BIHIM) and the instrumented head-form developed by the Metropolitan Police. The nape is important for securing helmets on the head; therefore, the fit of the helmet will be more accurate and secure with a nape section. Un-representative mounting will affect the stand-off, as previously discussed, this will affect the BFD impact and hence the potential injury outcome. Therefore, the fit of the helmet on a head model is an important aspect of the assessment method.

Reference	Model name	Head Shape	Neck representation	Scalp representation	Instrumentation	Instrumentation location(s) on headform	Injury risk model	Image
Bolduc <i>et al.</i> (2000) reported by Bass <i>et al.</i> (2002)	Modified Hybrid III	50th Percentile Hybrid III No nape	Hybrid III	Hybrid III rubber skin	Polyvinylidene fluoride (PVDF) stress gauges	One of: left, right, front and rear	Peak Impact Pressure to determine skull fracture risk, based on Bass <i>et al.</i> (2003)	Figure 3.2 A
					Tri-axial accelerometer	Near headform centre of gravity	Peak acceleration (400 g injury threshold from WSTC*)	
Anctil <i>et al.</i> (2008)	Blunt Load Sensing Headform (BLSH)	International Organisation for Standardisation (ISO)-size J headform No nape	Hybrid III	Rubber pad	7 Piezoelectric quartz load cells	One of: left, right, front and rear	Peak Impact force to determine skull fracture risk, extrapolated from Bass <i>et al.</i> (2003)	Figure 3.2 B
Watson <i>et al.</i> (2008)	Aluminium headform	Capsule extended on one end to represent the face No nape	Hybrid III	None	9031A Kistler force transducer	Rear	Not reported	Figure 3.2 C
					Zephyr Film sensor	Variable, reported on front	Not reported	
					Tri-axial accelerometer	Inside head-form	Peak acceleration (400 g injury threshold from WSTC*)	
Barnes-Warden <i>et al.</i> (2013)	Instrumented headform	Average head size including ears, nose, mouth and chin Includes nape	Solid neck extended from average head size	Not documented	PCB dynamic force sensor	Front, right, back, left and crown	Aligned to Anctil <i>et al.</i> (2008) (Peak Impact force to determine skull fracture risk, extrapolated from Bass <i>et al.</i> (2003))	Figure 3.2 D
Neale <i>et al.</i> (2013)	Blunt Impact Head Injury Model (BIHIM)	International Organisation for Standardisation (ISO)-size J headform Includes nape	Hybrid III	Rubber pad	Variable, currently 7 Piezoelectric quartz load cells	Variable	Peak Impact force to determine skull fracture risk, based on Raymond (2008)	Figure 3.2 E

\* WSTC - Wayne State Tolerance Curve (Lissner *et al.* 1960), predicting injury risk from global acceleration of the head.

**Table 3.2: Synthetic head-forms designed as helmet back face deformation assessment methods.**



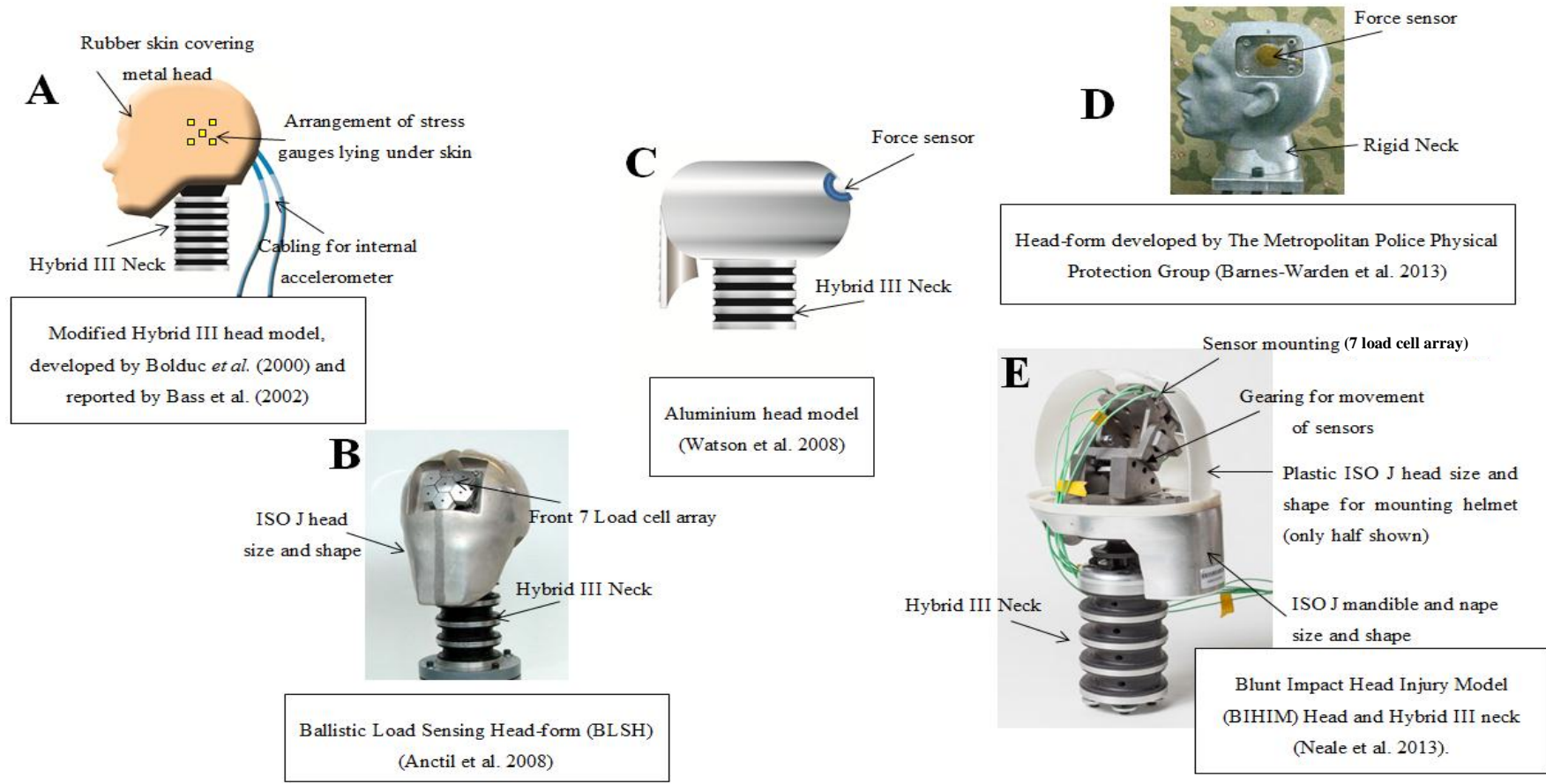


Figure 3.2: Images of synthetic head-forms designed to support Behind Helmet Blunt Trauma (BHBT) assessment methods (Table 3.2).

Image B © Copyright Biokinetics Ltd. (2008), Image reproduced with permission from B. Ancil (Biokinetics Ltd.). Image D © Crown Copyright (2013), Metropolitan police. Image reproduced with permission from J. Barnes-Warden (MET Police).

The face is not of interest when assessing BHBT, hence four of the synthetic head-forms feature only a simple representation of the face, with a chin to aid fit of the helmet under test (Table 3.2 and Figure 3.2). The system developed by Barnes-Warden *et al.* (2013) includes more detailed facial features. This is only because the model was based on a full head scan of an individual, but provides the ability to assess helmet coverage in addition to BHBT.

Each head model has been developed to be used in conjunction with a neck (Table 3.2 and Figure 3.2). The systems have predominantly used a Hybrid III neck (Backaitis *et al.* 1994), designed for frontal impacts in the automotive environment and formed of metal rings supported by sections of rubber. The neck provides support to the head and allows the head to move as a result of impact. This means the global movement of the head can be observed. However, the Hybrid III neck has not been validated for side or rear impacts, or in terms of its response under blunt ballistic loading to the head. Therefore its response may not be representative, but allows some comparison of the movement of the head. Barnes-Warden *et al.* (2013) opted for a rigid neck, keeping the head model and instrumentation as simple as possible. This limits the ability to observe any global movement of the head. However, this may not be an issue as Bass *et al.* (2003) concluded from cadaveric testing that neck injuries would be unlikely from BHBT loading conditions.

Measurement of impact force has focused on the use of load sensors to collect the force profile and extract the peak force measured (Table 3.2 and Figure 3.2). Polyvinylidene fluoride (PVDF) stress gauges were used by Bolduc (2009) and also applied within biological investigations by Bass *et al.* (2003). However, comparison of PVDF film sensors to load cells by Anctil *et al.* (2004), identified load cells to provide the best correlation between applied force and load measured. The key reason for this was due to challenges associated with achieving calibration and identifying degradation of the PVDF sensors. Alternatively, the load cells were robust with clearly defined calibration methods.

Load cells are a common measurement system reported to be used within synthetic BHBT assessment models (Table 3.2 and Figure 3.2). Load cells have either been used as part of an array or in isolation to determine the loading from BFD. In both cases the loading response was only reported in terms of the peak force measured. Anctil *et al.* (2008) and Neale *et al.* (2013) used sensor arrays, providing a measurement area of approximately 6 cm<sup>2</sup>. Single load cells have been used by Watson and Barnes-Warden, limiting the sensor area to approximately 2 cm<sup>2</sup>. To measure the peak force, the force over the area of the helmet BFD contacting the head should be measured. Systems with a single load sensor therefore assume that the BFD will be centrally located over the load sensor.

The location of sensors is also variable between the models. Predominantly the sensors are located in one or more of the following discrete positions: front, rear, crown, left and right sides. To enable movement of the sensor system, the BIHIM (Neale *et al.* 2013) was developed with the sensors mounted on a multi-part gearing system. The aim of this system was to enable assessment of a wider range of different areas of the helmet.

Three of the five head-models are reported to have a layer of silicon rubber over the load sensors, providing representation of the scalp. Raymond (2008) determined the BLSH with a rubber pad to have a similar loading response to cadaveric impacts. Therefore, in a similar response to the scalp, the rubber layer compresses, distributing the load over the sensors.

These synthetic assessment methods can be used in isolation to differentiate between impact forces caused by helmet BFD impacts; higher forces can be assumed to indicate an increased likelihood of injury. However, combining the measures from the synthetic models with an injury risk curve can provide predictions of injury outcome. This has been a common approach in the automotive environment (Backaitis *et al.* 1994). Application of

this approach within the assessment of BHBT provides a definitive measure of the protection provided by a helmet system.

### **3.3.5 Injury risk models**

Cranial fracture risk models, which have been applied to BFD assessment methods, have predominantly been developed from data obtained in three cadaveric investigations. Two investigations were focused on less-lethal blunt ballistic impacts (Sturdivan *et al.* 2004, Raymond 2008), and the third by Bass *et al.* (2003), directly investigated BHBT.

An energy based risk model, the Blunt Criterion (BC), was originally reported by Sturdivan *et al.* (2004) for less-than-lethal projectile impacts to the chest and abdomen. The BC was used by Hisley *et al.* (2010) to predict cranial fracture risks from helmet BFDs obtained using DIC. It was also identified as having a good correlation to cranial fracture outcome for blunt ballistic loading associated with impacts representative of less-lethal weapons, completed by Raymond (2008). However, the BC calculations applied by Hisley *et al.* and Raymond differ. Raymond used the formula (Equation 3.1) available in the open literature (Sturdivan *et al.* 2004), applying the BC developed for the chest and abdomen directly to the head. Hisley *et al.* (2010) had access to a draft report by Sturdivan (2005), not available in the open literature, explicitly reporting on the development of the original BC to produce an '*Injury criteria for blunt impacts to the head*' (Equation 3.2). However, there was no clear explanation of how the head impact criterion was derived by Sturdivan.

In both versions, the BC used the thickness of the cranium, diameter of a flat circular impactor and impact energy to provide a prediction of the injury outcomes (Sturdivan *et al.* 2004, Hisley *et al.* 2010). Both versions assume constant properties for the scalp and cranium. The version developed by Sturdivan *et al.* (2004) and used by Raymond (2008) (Equation 3.1), includes a function of mass that is omitted in the more recent reporting by Hisley *et al.* (2010) (Equation 3.2). In addition, Raymond used scalp and cranial thickness

together in centimeters, whilst the revised head criteria used only the cranial thickness, measured in millimeters.

$$BC = \ln \frac{E}{M^{1/3}TD}$$

**Equation 3.1: Blunt Criterion developed by Sturdivan *et al.* (2004).**

**E is impact energy (J), M is the mass of the target struck (kg), D is the diameter of the flat circular projectile (cm) and T is the combined thickness of the scalp and cranium at the impact point (cm).**

$$BC = \ln \frac{E}{TD}$$

**Equation 3.2: Head specific Blunt Criterion reported by Hisley *et al.* (2010) to have been developed by Sturdivan in 2005.**

**E is impact energy (J), D is the diameter of the flat circular projectile (cm) and T is the thickness of the cranium at the impact point (mm).**

In both calculations, the BC considers diameter of a flat impactor, highlighting that the area is expected to affect the injury outcome. However, curved impact surfaces such as those associated with BFD (Hisley *et al.* 2010), are not considered. In addition, although the energy available for a BFD surface has been estimated (Hisley *et al.* 2010), the interaction of the deforming helmet shell with the head, and hence how much energy is actually transferred has not been considered; the criterion was originally developed for rigid projectiles and not helmet BFD.

Raymond (2008) found the BC to be a good predictor of fracture outcome. This is most likely due to its consideration of a range of parameters associated with the impact and the target, rather than considering only a single parameter. However, as previously reported (section 3.3.2), the velocity, mass and shape of helmet BFD has not been quantified in terms of BHBT injury potential. Therefore, it would be beneficial to investigate these parameters in relation to BHBT to determine their effect on injury outcome. This could

then be used to determine whether one of the BC calculations could be used to predict injury outcome for BHBT.

In addition to the BC, Raymond (2008) investigated peak impact force against fracture outcome; peak impact force was determined as an adequate predictor of cranial fracture outcome. As a result, an injury risk model based on a total of fourteen impacts, seven causing fracture of the temporo-parietal region, was produced for peak impact force (Figure 3.3) (Raymond 2008). The impact force was calculated from projectile deceleration, providing the peak force applied to the head. However, Raymond acknowledged that the model was based on a small data set, with further information required to improve the statistical power and the associated confidence limits of the model. It was also identified that there were three potential versions of the peak force risk curve developed by Raymond; the presented risk curve could not be reproduced from the raw data, and the curve and mathematical formula for the curve did also not align. Therefore, when making any comparisons to this study, the raw data should be used to avoid misinterpretation of the results.

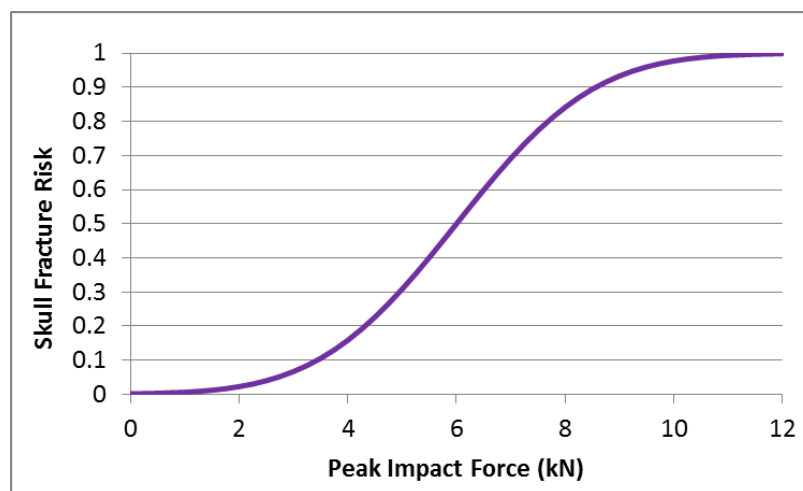


**Figure 3.3: Cadaveric cranial fracture risk versus projectile impact force, based on the reporting of Raymond (2008).**

**This figure is based on the reproduction of the parametric risk curve presented in Raymond (2008) as figure 6.2.**

Due to the synergies identified between less-lethal impacts and BFD loading (section 3.2), Bolduc *et al.* (2010) advised use of Raymond's BC based risk curve to support BHBHT assessments. Alternatively, Neale *et al.* (2013) directly applied force measures from the BIHIM (Table 3.2 and Figure 3.2) to the cranial fracture risk curve developed by Raymond (Figure 3.3). The BIHIM response was determined to be comparable to Raymond's data, providing a prediction of skull fracture outcome from force data collected by the BIHIM.

Bass *et al.* (2003) and Sarron *et al.* (2004) reported use of their biological data to develop injury risk curves, using fracture versus no fracture outcomes to develop cranial fracture risk models for bullet velocity or impact pressure. Sarron *et al.* (2004) used data from 18 impacts on dry skull based surrogates to develop probit curves for the probability of causing a significant fracture due to impact pressure. A significant fracture was determined as a comminuted fracture with a minimum area of 3 cm<sup>2</sup> and, impact pressure was measured using a 0.09 cm<sup>2</sup> pressure sensor. However, the dry skull model was not reported to be validated against the complete cadaveric response. Therefore, the cranial fracture risk curve should be validated before applying the findings to alternative test methods.

Bass *et al.* (2003) derived two cranial fracture risk models using the data obtained from cadaveric investigations (section 3.3.2). In both cases the models were based on nine data points obtained from investigating a single helmet and bullet system. Therefore, these risk models can only be accurately applied to testing associated with the same bullet and helmet system. One model presented cranial fracture in terms of bullet muzzle velocity (Figure 3.4), the other using peak impact pressure measured on the surface of the cranium (Figure 3.5). A 50% risk of cranial fracture was calculated for a bullet impacting the helmet at 437.0 m·s<sup>-1</sup>, associated with a peak impact pressure of 51.2 MPa (Bass *et al.* 2003).

Anctil *et al.* (2005) transferred the Bass *et al.* (2003) cranial fracture risk model, developed for initial muzzle velocity (Figure 3.4), to the outputs of the BLSH (Table 3.2 and Figure

3.2), by investigating the same test methodology as Bass *et al.* but mounting the helmet on the BLSH instead of a cadaveric specimen. Impacts of the same bullet types at similar muzzle velocities, against the same helmet systems, were used to determine the corresponding BLSH load cell outputs, producing a cranial fracture risk curve in terms of peak force measured.

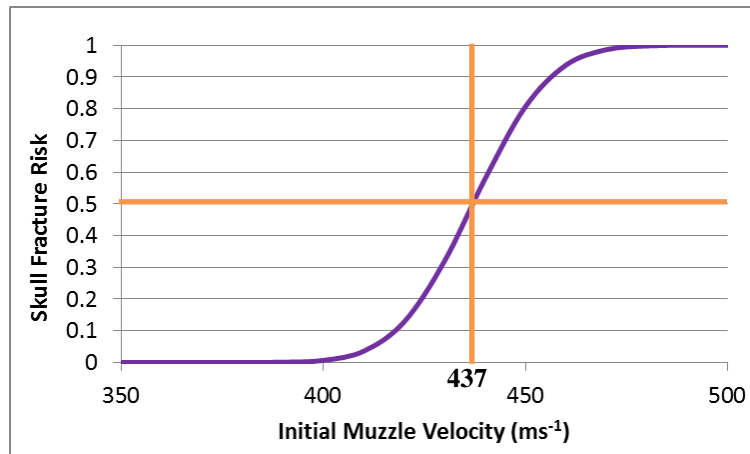


Figure 3.4: Cadaveric cranial fracture risk versus bullet velocity, based on the reporting of Bass *et al.* (2003).

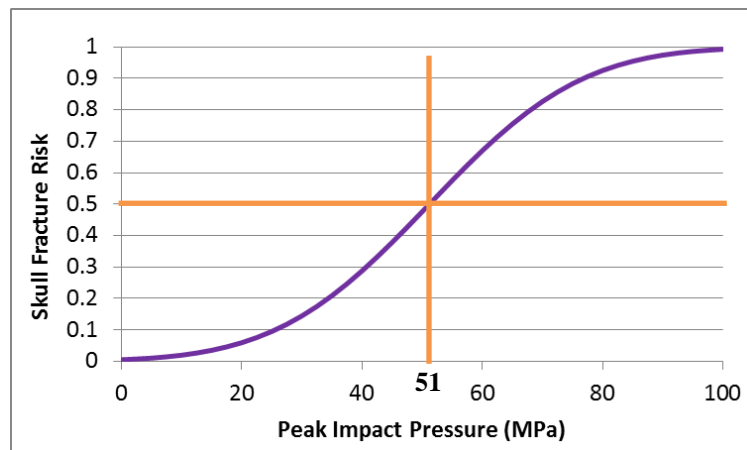


Figure 3.5: Cadaveric cranial fracture risk versus peak impact pressure on the surface of the cranium, based on the reporting of Bass *et al.* (2003).

Similarly, Bass *et al.* (2003) used a transfer function to apply the peak impact pressure cranial fracture risk curve (Figure 3.5) to the modified Hybrid III head model (Table 3.2 and Figure 3.2). Therefore, methods for predicting the injurious effects of helmet BFD impacts are available to support helmet assessments. However, they are based on specific



helmet and bullet systems, limiting the ability to apply these risk curves to different helmet assessments.

### **3.3.6 Limitations**

Injury severity has been shown to vary due to the helmet material, projectile type and velocity, stand-off and any padding within the stand-off. However, the interaction between the helmet BFD and the underlying head has not been measured beyond contact pressure or force on the surface of the cranium. Therefore, the variation in injury outcomes has not been considered in terms of specific changes in the deformation such as velocity and shape of the deforming helmet surface.

The BC considers the diameter of the impact to have a measurable effect on fracture outcome under blunt ballistic loading conditions. However, none of the BHBT assessment methods have measured the impact area or curvature of the helmet BFD. Therefore, it would be valuable to investigate whether flat impact diameter could be measured in conjunction with impact peak impact force to achieve a more accurate prediction of cranial fracture outcome associated with BHBT.

Investigation of fracture thresholds obtained for unprotected heads against a range of impact shapes and sizes may provide an understanding of the effects on cranial fracture outcome. When considering head injuries, Melvin *et al.* (1968) and Lewis (2006) identified that loading rate and area of impact have an effect on the type of cranial fracture caused. Data obtained to aid understanding of cranial fracture thresholds under loadings associated with car accidents and some bullet investigations are unlikely to be directly comparable to blunt ballistic impacts. However, the data may be extrapolated to hypothesise the effects that specific changes, such as increasing impact area, may have on fracture thresholds of the cranium under blunt ballistic loading. Therefore, it is reasonable to consider other head impact studies.

Investigation of cranial fracture studies reporting measures of impact force would enable extrapolation of the findings to the blunt ballistic impacts undertaken by Raymond (2008). In addition, where force is the primary data output, any findings may be applied to existing BHBT assessment methods capable of collecting force measures.

### **3.4 Cranial fracture forces**

#### **3.4.1 Introduction**

A range of studies have been undertaken investigating the fracture thresholds of cranial bone (Allsop *et al.* 2001, Yoganandan *et al.* 2004, Motherway *et al.* 2009). Sixteen studies investigating impulsive impacts to areas of the cranium have been identified from the literature (Table 3.3). These have been selected to enable comparison of fracture forces caused by impacts from a range of flat and curved faces. Additional studies have been omitted due to a lack of information regarding individual impacts such as specimen details and impact velocity (Wilber 1974), or duplication of data points within reporting; the papers published by Gadd *et al.* (1968) and Nahum *et al.* (1968) appear to contain the same data points. Therefore, to avoid repetition of the data, only the work by Nahum *et al.* (1968) is considered within this review.

A number of different investigations have been carried out to obtain fracture forces for impacts to the cranium (Table 3.3). In addition to the inherent variation of the biological targets such as bone thickness, head mass and scalp thickness, the investigations have used a range of different impact methods. These have included drop towers, pendulums and projectiles. The impact method has also influenced the mounting of the target, such as being guided in fall to rigidly fixed in a vice. When comparing the available data, it is worth considering that the impact and mounting method are likely to have had an effect on the fracture outcomes observed.

Reference	Cadaveric/ Skull Samples	Position	Mounting	Impact method	Impact object shape	Dimensions (cm)	Impact Mass (kg)	Force Range (Tolerance) (kN)	Velocity Range (ms <sup>-1</sup> )
Allsop <i>et al.</i> (1988)	15	Frontal	None (guided fall)	Drop tower	Semicircular rod	1.0 rad x 2.0 dia x 23.0	14.5	2.2 - 6.5	3.0 - 4.2
Allsop <i>et al.</i> (1991)	20	Temporoparietal	None (guided fall)	Drop tower	Flat surfaced cylinder	2.5 diameter	10.6	2.5 - 10.0	2.7
	11	Parietal				Flat rectangular		10.0 x 5.0	12.0
Crawford (2009)	5	Frontal	Inversely suspended	Projectile	Flat surfaced cylinder	3.8 diameter	0.103	4.4 - 9.4	5.12 - 31.5
Delye <i>et al.</i> (2007)	18	Frontal	Inversely attached to pendulum arm	Pendulum	Flat surfaced cylinder	7.0 diameter	28.9 - 48.3	5.9 - 14.3	3.4 - 7.0
Hodgson <i>et al.</i> (1970)	7	Frontal	None (guided fall)	Drop tower	Cylinder	2.5 rad x 16.5	4.5	4.2 - 7.3	2.7 - 3.5
	5					0.8 rad x 16.5		3.1 - 7.1	
Hodgson <i>et al.</i> (1971)	20	Frontal	None (guided fall)	Free fall	Flat surfaced cylinder	20.3 rad	Specimen head	6.5 - 9.4	2.2 - 3.8
						Curved		7.6 rad	4.3 - 8.0
								2.5 rad	4.1 - 5.1
									5.1 - 10.9
Nahum <i>et al.</i> (1968)	10	Frontal Temporoparietal	Lying on rigid surface	Drop tower	Flat surfaced cylinder	2.9 diameter	~7.0	2.8 - 6.7 (4.0) 1.7 - 5.9 (2.0)	~7.0
Nusholtz <i>et al.</i> (1993)	9	Frontal	Inversely attached to pendulum arm	Pendulum & Ballistic impact device	Flat surfaced cylinder	15.0 diameter	25-65	2.6 - 9.1	3.5 - 5
Ono <i>et al.</i> (1993)	7	Frontal	None (guided fall)	Free fall	Flat rectangular	12.0 x 8.0	Specimen head	8.3 - 14.7	3.7 - 7.0
	8	Occipital						8.1 - 19.1	
Patrick <i>et al.</i> (1993)	4	Frontal	Attached to body, seating support	Sled	Flat surfaced cylinder	15.0 diameter	Specimen head & component of full cadaver	4.0	4.5 - 8.7
Raymond <i>et al.</i> (2008)	7	Temporoparietal	Inversely suspended	Projectile	Flat surfaced cylinder	3.8 diameter	0.103	3.4 - 6.2 (2.3)	19.5 - 35.2
Schneider <i>et al.</i> (1972)	17	Frontal	Lying on rigid surface with polyurethane supports	Drop tower	Flat surfaced cylinder	2.9 diameter	3.12	1.4 - 9.9 (4.0)	16 - 19.7
		Temporoparietal					1.50 - 3.15	2.1 - 5.2 (2.0)	5 - 6.0
Stalnaker <i>et al.</i> (1993)	15	Frontal	Seated cadaver, stabilisation with wax cords	Pneumatic cannon	Flat surfaced cylinder	15.2 diameter	10	6.6	
		Temporoparietal						7.2 - 9.6	
		Occipital						9.6	
Verschueren <i>et al.</i> (2007)	4	Frontal	Inversely attached to pendulum arm	Pendulum	Flat surfaced cylinder	7.0 diameter	14.3 (Arm)		5.3 - 6.9
Viano <i>et al.</i> 2004	4	Frontal	Rigidly inverted	Projectile	Flat surfaced cylinder	3.7 diameter	0.025 - 0.035	4.1	33 - 69
Yoganandan <i>et al.</i> (1995)	3	Varied	Rigid in vice	Loaded piston	Hemispherical	4.8 rad	Unknown	8.8 - 14.0	7.1 - 8.0

**Table 3.3: Summary of literature findings relating to studies investigating impulsive impacts to the cranium.**

The impact faces tested have included a wide range of sizes and shapes from a flat rectangle of 10 by 5 cm (Allsop *et al.* 1991) to a curved face of 2.5 cm radius (Hodgson *et al.* 1970, Hodgson *et al.* 1971). Due to the curvature of the cranium, it would be expected that beyond a limit of approximately a 7 cm flat diameter, the impact surface would extend beyond the contact surface of the cranium. Therefore, any further increases in impact diameter would not be expected to affect the cranial fracture threshold as the contact area between the cranium and impact face would cease to increase.

The impactors are documented to have masses between 0.1 kg and 65 kg, impacting at velocities ranging between  $2.7 \text{ m}\cdot\text{s}^{-1}$  to  $69 \text{ m}\cdot\text{s}^{-1}$  (Table 3.3). These variables are likely to affect cranial fracture outcome, affecting the energy imparted to the cranium on impact. Therefore, it may not be possible to use the available data to quantify the effects of impact area and curvature in isolation.

Testing of the cranium has focused on the regions with the largest areas of flatter bones, the frontal and temporoparietal (Gray 1973, Moore *et al.* 1999). These two regions account for a large proportion of the cranial vault, and enable consideration of variation in bone thickness (section 2.2). Therefore, the available data may support different fracture thresholds for different regions of the cranium. These could be applied within BHBT assessment methods to improve the accuracy of the injury prediction.

Within the published data (Table 3.3), fracture forces between 2.2 kN and 14.7 kN have been reported for dynamic impacts on the frontal bone; an average fracture force of 6.3 kN was calculated from the available data. Fracture forces for the temporoparietal region were reported between 1.7 kN and 10 kN, with an average of 5.7 kN calculated from the available data (Table 3.3). However, some of this data was obtained following multiple impacts to the same specimen (Hodgson *et al.* 1970, Ono *et al.* 1993), with no consideration of cumulative effects such as microscopic cracks occurring prior to fracture

being identified on a macroscopic level. This may limit the comparisons which can be made between the different datasets.

### **3.4.2 Factors affecting cranial fracture force**

#### **3.4.2.1 Impact size and shape**

A range of surfaces have been used to impact the cranium (Table 3.3). Most of the impactors were reported to be aluminium, and formed from a single uniform shape. However, Allsop *et al.* (1991) also used a set of 8 rectangular segments to act as a single rectangular impact face. Melvin *et al.* (1968), Hodgson *et al.* (1970), Wilber (1974), Slobodnik (1982), Allsop *et al.* (1991), and Byers (2008), all reported area or radius of impact to have an effect on the fracture response of the cranium; the smaller the radius or area of impactor, the lower the force required to cause cranial fracture. However, none of the investigations reported quantification of the relationship, only that there appeared to be one.

The data associated with the literature (Table 3.3) has been combined in an effort to quantify the effect of curvature and/or flat diameter on cranial fracture force. It is understood that the variation between test methodologies may limit the conclusions that can be drawn.

The fracture forces relating to impacts to the frontal bone, achieved using flat circular impact faces of varying diameter, have been compared (Figure 3.6). The average fracture force has been calculated for each individual dataset, with the bars representing the range of fracture forces observed. Average force measures collected for impact diameters below 8 cm, in addition to the fracture data reported by Patrick *et al.* (1993), follow a trend of increasing impact diameter associated with increasing fracture force (Figure 3.6). Based on the average impact forces calculated, the relationship is potentially linear.

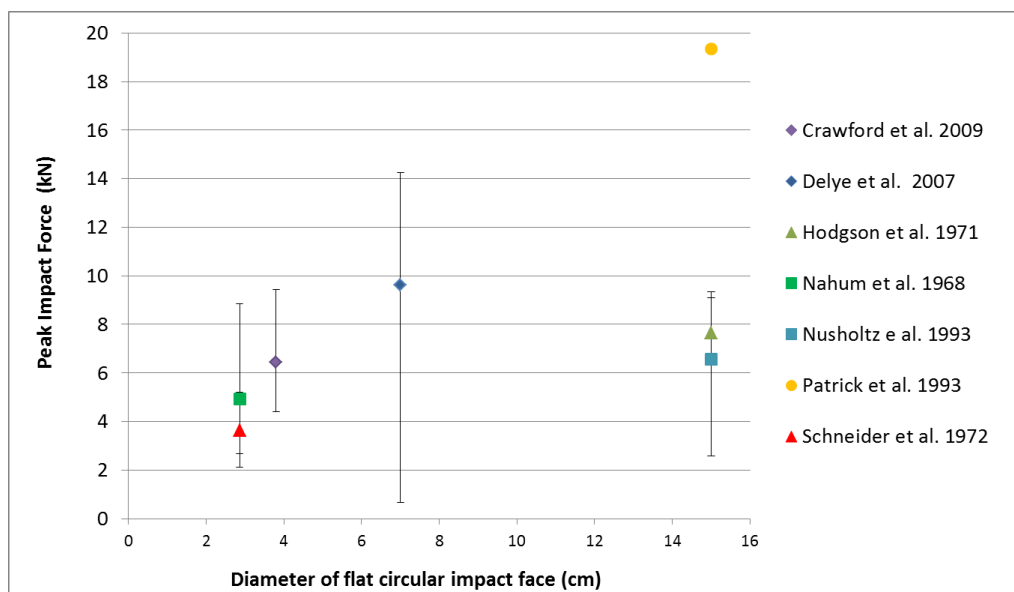


**Figure 3.6: Average peak force causing fracture of the frontal bone with bars representing the spread of data from published studies, reported by diameter of the flat circular impact face.**

Based on the linear trend observed in the other data, the fracture forces obtained by Hodgson *et al.* (1971) and Nusholtz *et al.* (1993) are lower than would be expected for an impactor of 15 cm diameter. These lower fracture forces may be due to conducting multiple impacts on the same specimens until fracture was observed on a macroscopic level. The data reported by Delye *et al.* (2007) was also obtained from multiple impacts to the same specimens, which may be the reason why such a wide spread of fracture forces were measured. Additionally, the change in the trend (Figure 3.6) may be due to the impactor diameter exceeding the limit of contact for the curvature of the cranium; beyond this limit it would be expected that the impactor area no-longer affected the fracture threshold. This limit may have been reached in the studies by Hodgson *et al.* (1971) and Nusholtz *et al.* (1993). However this does not explain the high forces measured by Patrick *et al.* (1993). The variability in the data obtained using a 15 cm diameter impact surface may be due to the differences in test methods; Patrick *et al.* (1993) used a full cadaver placed on a sled, whilst Hodgson *et al.* (1971) and Nusholtz *et al.* (1993) tested isolated heads. The mounting methods may have affected the force measured.

Fracture forces for flat circular impacts were also investigated for the temporoparietal region (Figure 3.7). Impactors with a diameter less than 4 cm show a reduction in fracture force as the diameter of the impactor increases (Figure 3.7). This is converse to the findings for impacts against the frontal bone and the reported trend within additional reporting (Melvin *et al.* 1968, Allsop *et al.* 1988, Byers 2008) and may be due to variation in the test methods. There is insufficient data for impact faces with a diameter greater than 4 cm to determine if the observed trend continues with larger diameter flat impact faces (Figure 3.7).

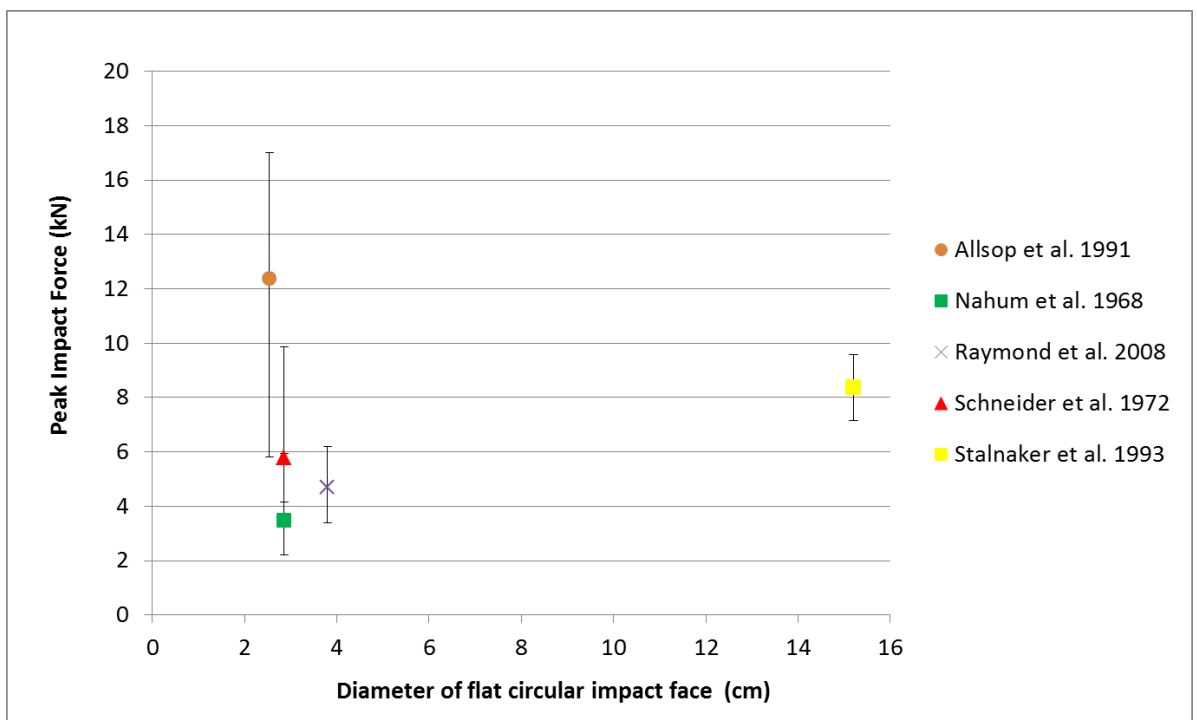


**Figure 3.7: Average peak force causing fracture of the temporo-parietal bone with bars representing the spread of data from published studies, reported by diameter of the flat circular impact face.**

Published fracture force measures for curved impactor faces against the frontal bone were also considered (Figure 3.8). Similarly to the previous data comparisons, the average fracture forces are presented with bars used to show the full range of fracture forces obtained. For simplicity, only the flat impact face data reported by Hodgson *et al.* (1971)

was included for comparison. To include the flat surface (infinite radius of curvature) impacts, the faces were plotted by the inverse of the radius of curvature.

A linear trend of decreasing fracture force with increased curvature is reflected for data associated with inverse impact curvatures below  $0.2 \text{ cm}^{-1}$  (Figure 3.8). However, this data was all reported by Hodgson *et al.* (1971) and the relationship does not appear to continue throughout the complete dataset (Figure 3.8). Based on the available data, there does not appear to be a clear relationship between peak impact force and impact curvature for cranial fracture outcomes.

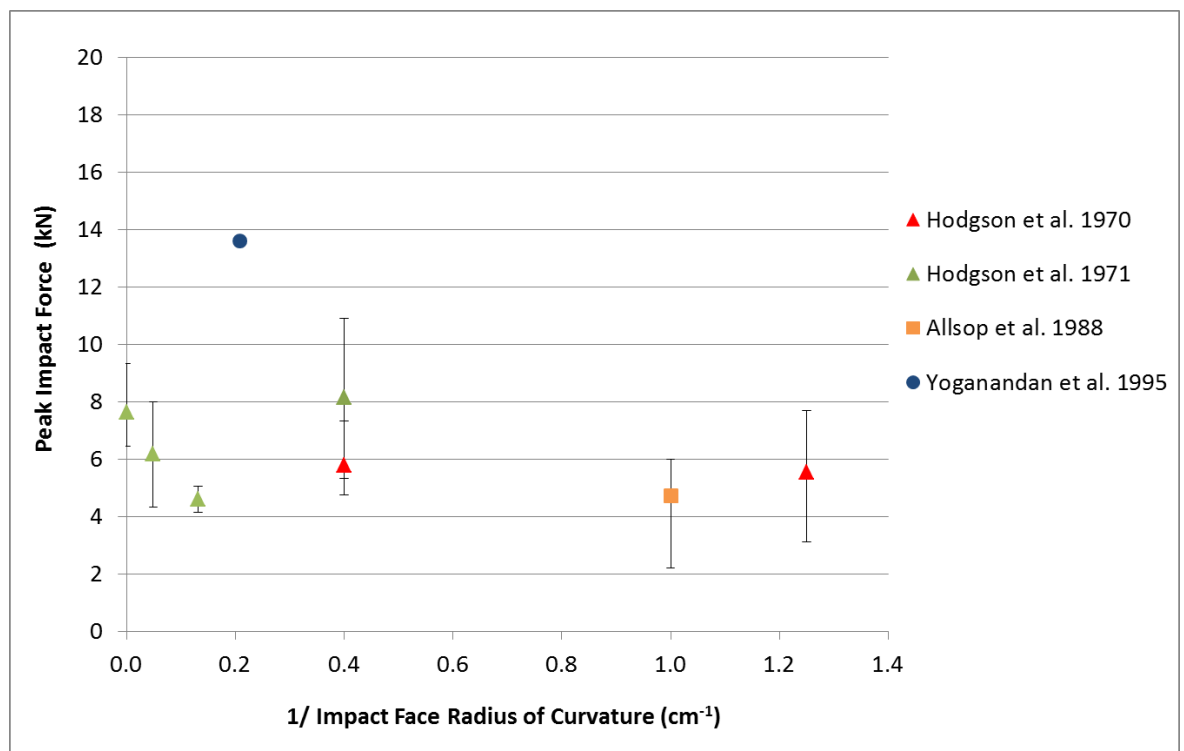


**Figure 3.8: Average peak force causing fracture of the frontal bone with bars representing the spread of data from published studies, reported by the inverse radius of curvature of the impact face.**

Overall, studies investigating the effect of flat diameter and curvature on cranial fracture thresholds have also varied other test parameters, so it is challenging to quantify the effect of flat diameter or curvature. Variability across experimental methods limits the conclusions which can be drawn from combining datasets across a range of different investigations. However, from the information available, curvature and flat diameter do



appear to have an effect on the force required to fracture the cranium. This is as much as a 100% difference between some impact faces. In terms of predicting cranial fracture outcome from measurements of helmet BFD, this could have a substantial effect on the accuracy of the predictions and hence the protective capability determined for a helmet. Therefore, further investigation is required to quantify the effect for application within BHBT cranial fracture risk models.

#### **3.4.2.2 Target construction**

The force required to break a cranium covered by scalp tissue has been reported to be ten times greater than bare cranium fracture forces (Cantu 1995). Nahum *et al.* (1968) and Raymond *et al.* (2008) also identified soft tissue thickness to play an important role in energy absorption, affecting cranial fracture. For impacts against seven cadaveric specimens, using a solid projectile (103.3 g) with a flat circular impact face of 38 mm diameter and maximum velocities of  $35 \text{ m}\cdot\text{s}^{-1}$ , Raymond *et al.* (2008) found that 7 mm of scalp was the threshold between fracture and non-fracture of the underlying cranium. Soft tissue effects must therefore be considered during impact testing or potentially controlled to enable the investigation of other variables.

It has been concluded that specimen age, head mass, gender and bone mineral content do not affect cranial fracture forces (Allsop *et al.* 1991, Raymond 2008). However, bone thickness at the impact site has been determined as a factor affecting the force required to cause fracture (Yoganandan *et al.* 2004, Delye *et al.* 2007). Therefore investigations into cranial fracture should consider the thickness of the bone under test when determining the potential fracture risk.

### **3.4.2.3 Target preparation**

Ono *et al.* (1993) was the only study (Table 3.3) to use dry skulls, all of the other investigations used hydrated cadaver specimens. For the literature identified, differences between the experimental methods limit the conclusions which can be drawn regarding the effect of using dry or hydrated skulls. However, differences have been found between the testing of dry and hydrated bone specimens in other studies; bone dried at room temperature has greater tensile strength (Taylor *et al.* 1997, Nyman *et al.* 2006). Therefore, to achieve representative fracture outcomes, hydrated bone should be used in experimental testing. In terms of the treatment of the tissues, testing has shown that there was no significant difference between testing on embalmed and fresh cadaveric heads (Nahum *et al.* 1968, Yoganandan *et al.* 2004).

### **3.4.2.4 Target mounting**

The cranial fracture studies have used a range of different methods for mounting the specimen under test (Table 3.3). Injuries associated with BHBT are localised, with minimal acceleration of the head (section 3.3.2). Therefore, forces causing localised cranial fracture are of primary interest, with less consideration of the global movement of the head.

The method of mounting the target can affect the localised impact received. Gadd *et al.* (1968) found that, for the same impact condition, there was a twenty to thirty percent increase in measured impact force when the head was rigidly supported compared to when a more freely supported system was used. The loading used by Nahum *et al.* (1968) is not comparable to helmet BHBT; the method used an impactor with a mass up to seven times greater than that expected to be associated with BHBT. However, the results show that the mounting of a target should be considered when comparing the available data or undertaking further experimental studies with the intention of comparing datasets.

### 3.4.2.5 Loading rate

Factors affecting the loading rate include mass, velocity, shape and stiffness of the impactor, combined with the method of mounting and the target system itself (Nahum *et al.* 1968, Schneider *et al.* 1972, Delye *et al.* 2007). The majority of studies (Table 3.3) do not provide a detailed understanding of the loading rate. Therefore, the effect of impact rate cannot be investigated from the selected literature. However, the testing by Yoganandan *et al.* (1995), subjecting cranial bone to quasistatic and dynamic loading, identified rate to be a significant factor in fracture outcome; nearly double the force (from 6.4 kN to 11.9 kN) was required to cause fracture when the loading rate was increased from a maintained velocity of  $0.002 \text{ m}\cdot\text{s}^{-1}$  to over  $7.0 \text{ m}\cdot\text{s}^{-1}$ . Nahum *et al.* (1968) also reported that bone strength is greater when the rate of loading is increased. Therefore, to ensure representative fracture outcomes, loading rates associated with BHBT should be considered when investigating related cranial fracture outcomes.

## 3.5 Summary

Loading of the head due to helmet BFD is similar to blunt ballistic impacts (Bir *et al.* 2004, Hisley *et al.* 2010). In the case of free-air helmet BFD, the impact is bell shaped with a projected area below  $100 \text{ cm}^2$ , calculated as having a mass between 20 to 110 grams travelling at a velocity between 20 to  $115 \text{ m}\cdot\text{s}^{-1}$  (Hisley *et al.* 2010).

Several BHBT assessment methods have been developed using a range of models and techniques (Sarron *et al.* 2004, Anctil *et al.* 2008, Hisley *et al.* 2010). Investigations using biological models have shown that severe injuries can be caused by impacts from helmet BFD. The injuries can be observed on a macroscopic scale, predominately identified as localised fracture of the cranium, combined with damage to the soft tissues at the point of

impact (Bass *et al.* 2003, Sarron *et al.* 2004). However, measurement of the helmet BFD causing injury has been limited to measurement of the impact pressure at the site of impact.

Additional assessment methods have used synthetic head models to capture information relating to the helmet BFD impacting the head. The majority of helmet test standards are focused around the use of clay within a synthetic head-form, obtaining only a peak deformation depth of the helmet BFD (HP White laboratories 1995, MPS DOI-MTD-03/010 2003, STANAG AEP 2920 2015). However, there is limited information to support the prediction of head injury from peak deformation into clay (National Research Council 2014). In addition, clay is not representative of the cranium and scalp, affecting the interaction with the helmet BFD and hence the resultant deformation observed.

Alternative synthetic models have been developed, using sensors embedded in a metal head-form to assess the protective benefits of helmets (Anctil *et al.* 2008, Watson *et al.* 2008, Neale *et al.* 2013). Similarly to the biological methods, these instrumented head forms are only capable of collecting impact pressure or force relating to the loading of the helmet BFD onto the head. DIC assessment (Hisley *et al.* 2010) is the only method where a range of measurements have been obtained from the deforming surface of the helmet.

Injury risk curves have been developed which are focused on cranial fracture outcome based on a single impact parameter (Sarron *et al.* 2000, Bass *et al.* 2003). The BC has also been applied to BHBT assessment (Bolduc *et al.* 2010, Hisley *et al.* 2010), considering the impact parameters of velocity, mass and flat diameter. However, helmet BFD is bell shaped (Hisley *et al.* 2010); the effect of impact curvature has not been considered within any of the existing injury risk curves. Therefore, the effect of impact curvature and flat diameter on cranial fracture force is required to support improved injury risk prediction associated with the assessment of BHBT.

Fracture investigations outside of BHBT assessments have reported impact area and curvature as having a substantial effect on the fracture threshold of the cranium (Melvin *et al.* 1968, Nahum *et al.* 1968, Schneider *et al.* 1972, Bass *et al.* 2003, Byers 2008). However, the relationships between these parameters have not been quantified (Hodgson *et al.* 1971, Sarron *et al.* 2004). There is some evidence of a linear relationship of increasing fracture forces for flat impactors with larger impact diameters. Variability between test methods has limited the ability to quantify the relationships by combining existing datasets. However, there do appear to be differences of up to 100% (4kN) in fracture forces for changes in inverse radius of curvature of less than  $0.2 \text{ cm}^{-1}$ . Therefore, further investigation of cranial fracture outcome as a result of different impact curvatures and flat diameters is required to support the assessment of BHBT.

# **Chapter 4: Bovine scapula as a fracture analogue of the cranium**

## **4.1 Introduction**

To investigate the effects of impact curvature and flat diameter on cranial fracture thresholds a representative fracture model is required. Cadaveric specimens would be the most representative models. However, there are a number of limitations associated with the use of cadaveric specimens such as licencing, low specimen numbers and specimens being generally older than the population of interest (section 3.3.2). Therefore, work was carried out to investigate the applicability of using an alternative cranium fracture model. Any model will have its own limitations, most likely to be associated with the differences in geometry and material properties when compared to the item they are intended to represent. Therefore, alternative models require validation against the most representative data, which typically comes from cadaveric investigations.

An alternative cranial fracture model to cadaveric specimens was identified within Dstl, where researchers combined bovine scapula with layers of gelatin and chamois leather to form a Bovine Scapula Model (BSM) (reviewed by James *et al.* (2009)). However, there have been changes to bovine scapula supply since the development of the model. Therefore, the aim of this chapter was to determine the suitability of the currently available BSM as a cranial fracture model. In addition to Dstl's original design, two additional modifications to the BSM were investigated to determine whether an alternative BSM could offer an improved analogue of cranial fracture when compared to existing cadaveric data.

## **4.2 Method**

### **4.2.1 Validation Data**

Review of the literature (section 3.4) found that Raymond (2008) and Crawford (2008) carried out work investigating cranial fracture using a projectile of 103.3 g, fired at velocities around  $35 \text{ m}\cdot\text{s}^{-1}$ ; loading conditions comparable to those that cause BHBT (section 3.2). Replication of the test method used by Raymond and Crawford would enable the fracture response of the BSM to be directly compared to cadaveric responses. This could better establish the BSM as a fracture analogue of the cranium.

The data reported by Crawford (2008) used five particularly small head specimens, with three having masses below 3.0 kg; head masses were reported, on average, between 3 kg and 5 kg (section 2.2). Crawford reported the specimens to be representative of a 5<sup>th</sup> percentile female, which is unlikely to be representative of the UK military population at risk from BHBT. In addition, Crawford measured lower fracture forces for the frontal bone when compared to Raymond's fracture forces for the temporo-parietal region (Raymond 2008). These are converse findings to other cranial fracture studies reported in the literature (section 3.4.1). Also, the data reported by Crawford did not contain measures of bone thickness. Therefore, the comparisons which could be made between the Crawford and alternative cranial fracture model data were limited. As a result, only the data reported by Raymond was used to further validate the BSM.

### **4.2.2 Bovine Scapula Models (BSMs)**

#### **4.2.2.1 Origin of the BSM**

In terms of the similarity of the bovine scapula (Figure 4.1) to specific bones of the cranium, Taylor *et al.* (1997) found an area within the subscapula fossa (Figure 4.2) to

have a similar thickness and geometry to the temporal-parietal region of the cranium (Section 2.3). This is determined as the impact area of the scapula. Subsequent mechanical tension and compression testing confirmed similar mechanical properties associated with the impact area, or central third of the subscapula fossa, to those of the temporal-parietal region (Taylor *et al.* 1997, Arnold *et al.* 1999).

Initial testing was uniaxial, investigating small samples of bone cut from the scapula and tested at low rates. This was very different to the bilateral loading of BHBT onto a large bone structure of varying thickness. However, James *et al.* (2009) used the BSM to investigate blunt ballistic impacts, identifying similar fracture patterns to those reported by Raymond (2008). Therefore, the BSM may be a suitable fracture analogue for the cranium under blunt ballistic loading.

In addition, bovine scapulae are a waste product of cattle slaughter houses. This makes them readily available and affordable, and therefore an accessible resource for large scale investigations.

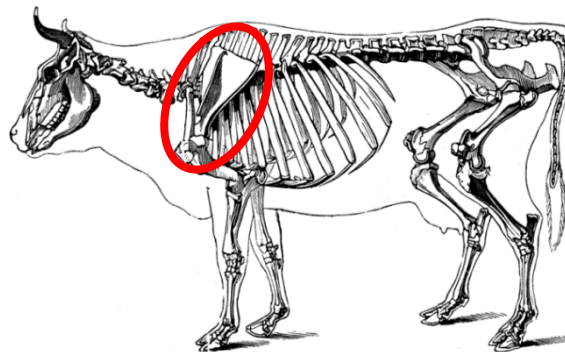


**Figure 4.1: Bovine skeleton (Goodrich 1885).**

**The left scapula is highlighted with the lateral surface containing the spinae visible.**

**© Copyright FCIT (2015), permission for use obtained under ClipArt ETC free classroom license.**



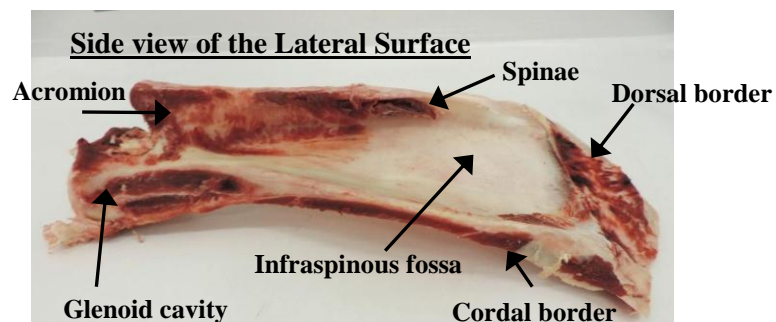
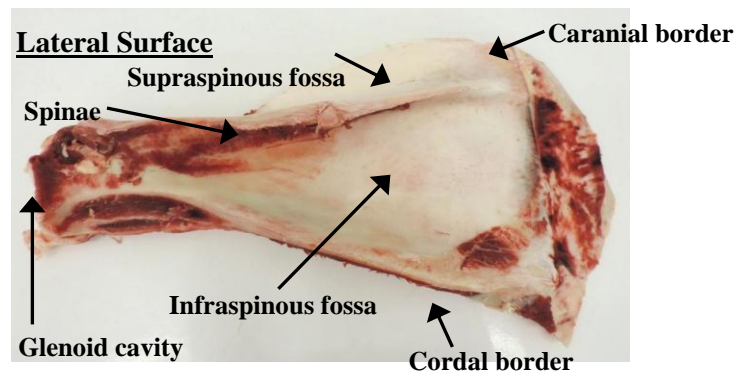
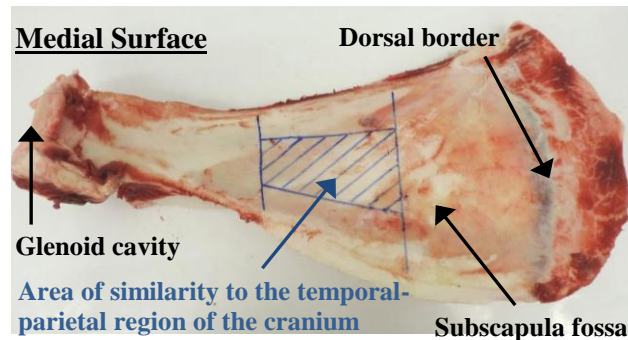


**Figure 4.2: Anatomy of the left Bovine scapula.**

The shaded region within the subscapula fossa was identified as having similarity to the temporal-parietal region of the cranium. Anatomical labelling derived from Budras *et al.* (2003).

Since Taylor *et al.* (1997) identified the bovine scapula as a potential cranial fracture model, there have been changes to the maturity of the bones available. In the late eighties, the outbreak of Bovine Spongiform Encephalopathy (BSE) resulted in all cattle (for food use) being slaughtered at 30 months old or less (Food Standards Agency 2005). Since November 2005, cattle over 30 months could be sold as food if tested negative for BSE (Food Standards Agency 2005). Therefore, scapula may be obtained from a wider range of cattle ages compared to those tested by Taylor *et al.* (1997). It is important to consider that

the development of the bone may be affected; older cattle are likely to have scapula of increased thickness and therefore higher strength than the scapula tested by Taylor *et al.* (1997). This may affect the suitability of the BSM as a cranial fracture model for the impact rates of interest, hence the requirement to test and validate the BSM using currently available scapulae.

Over 66 BSMs were constructed and tested in this work, investigating at least 22 BSMs for each of three construction methods. Based on previous work using the BSM, 22 tests per group or variable was expected to provide sufficient statistical power for determining differences in fracture thresholds (S. Holden, personal communication).

#### 4.2.2.2 BSM impact area construction

Initial BSM construction was consistent for all models, using steps one to six of the Dstl Bovine Scapula Model Construction, detailed in Annex A. All models had two layers of chamois leather and a 10 mm thick layer of 20% ballistic gelatin over the impact area (Figure 4.3).

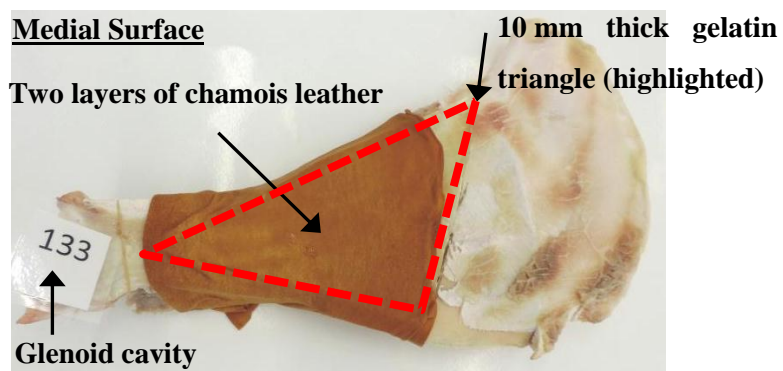


Figure 4.3: Impact area construction of a bovine scapula model.

Two layers of gelatin soaked chamois leather combined with 10 mm thick 20% ballistic gelatin, to form representation of the scalp over the impact area.

The construction was very similar to the Dstl BSM construction previously reported by James *et al.* (2009). Modifications were made to the original production method to reduce

the number of gelatin slices and chamois leathers required. These changes were made to optimise the use of the available resources. Further details of these modifications are reported within Annex A. The changes were not likely to have a substantial effect on the response of the BSM.

Following production of the scalp layers, three different BSM constructions were produced: Original BSM, Strain BSM and DIC BSM.

#### 4.2.2.3 Original BSM construction

In addition to the impact area construction, the Original BSM (Figure 4.4) followed the Dstl BSM production method reported in the work by James *et al.* (2009) (Annex A). BSMs were produced with a backing of 20% ballistic gelatin. The gelatin had a thickness between 30 and 60 mm (step 7 of Annex A); the thickness varied between models due to the manufacturing process and irregular shape of the scapulae. A total of 22 Original BSM models were tested.

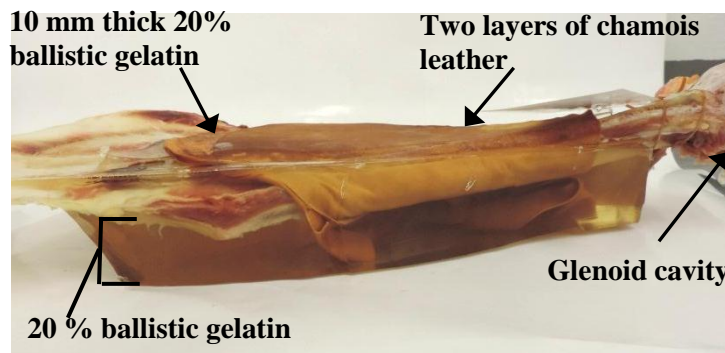


Figure 4.4: Side view of an Original bovine scapula model.

On the lateral surface (un-impacted side) of the bone, the 30 to 60 mm thickness of 20% ballistic gelatin can be seen.

#### 4.2.2.4 Strain BSM construction

A second construction method called Strain BSM, was identical to the Original BSM with the exception that strain gauges were attached to the surfaces of the bone (Figure 4.5A).

The purpose of this construction was to determine whether the addition of strain gauges affected the fracture response of the BSM.

Raymond (2008) previously applied tri-axial strain gauges to the surface of the cranium. Therefore, three Vishay type 062UR tri-axial rosette strain gauges were mounted on the impact site (Figure 4.5B), in the same configuration as used by Raymond (2008). Glue was used for attachment prior to sealing with wax to protect the gauges from moisture. Attachment of the gauges was completed before the gelatin and chamois layers were applied over the impact area (Step 6 Annex A).

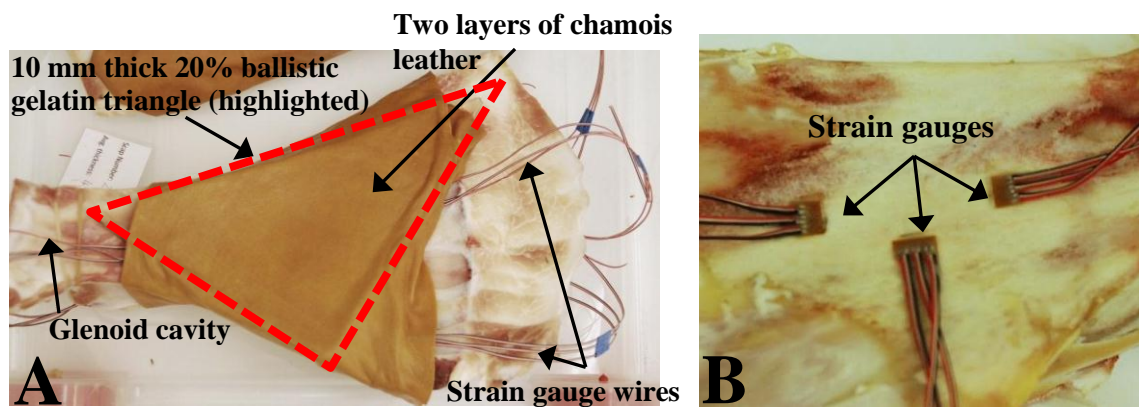


**Figure 4.5: Impact surface (medial view) of Strain BSM construction.**

External surface of the model (A), with tri-axial rosette strain gauges attached to the surface(s) of the bone (B).

A total of 22 Strain BSMs were tested. Half of these had an additional three strain gauges attached to the lateral (non-impact) surface of the bone, directly under those on the medial (impact) surface. Strain measures were not reported by Raymond in sufficient detail to enable comparison with the strain measures obtained from the Strain BSM. Therefore, the addition of the gauges was purely to determine their effect on fracture response of the BSM. Due to significant resource requirements associated with purchase and attachment of the gauges, strain data was collected (Appendix A) to support investigations into bovine scapula fracture mechanics.

#### 4.2.2.5 DIC BSM construction

DIC BSMs were the same construction as the Original BSM, with the exception that the 20% ballistic gelatin backing was omitted. Therefore, the lateral (non-impact) surface of the scapula could be observed throughout impact.

The focus of this work was on the fracture response of the DIC BSM. However, it was determined that application of a high contrast dot tattoo on the lateral bone surface (Figure 4.6) would enable strain measures to be obtained using a non-contact optical technique called Digital Image Correlation (DIC).

DIC is a technique that uses complex mathematical algorithms applied to HSV video images to provide quantitative information relating to a surface (McCormick *et al.* 2010). Outputs include velocity, displacement and in-plane strain measurements of the imaged surface. In order to calculate this information the software requires images of a high contrast pattern moving in space. Using a high contrast dot tattoo, DIC may provide information relating to bone fracture metrics.

A total of 25 DIC BSMs were tested; ten had only the high contrast dot pattern whilst the remaining 15 also had three strain gauges of the same type as the Strain BSMs, attached to the medial (impact) bone surface. Six of the strain gauged DIC BSMs also had three strain gauges attached to the lateral (non-impact) bone surface. The strain gauges were attached using the method and orientations as reported for the Strain BSMs. This construction could enable comparison between strain measures collected by gauges and DIC. There was insufficient information relating to cadaveric strain measures to enable use of this data with respect to comparing the BSM fracture response; however the information was collected to optimise the outputs from the study within other applications. The method, analysis and results from the strain gauge and DIC outputs are reported in Appendices A and B respectively.

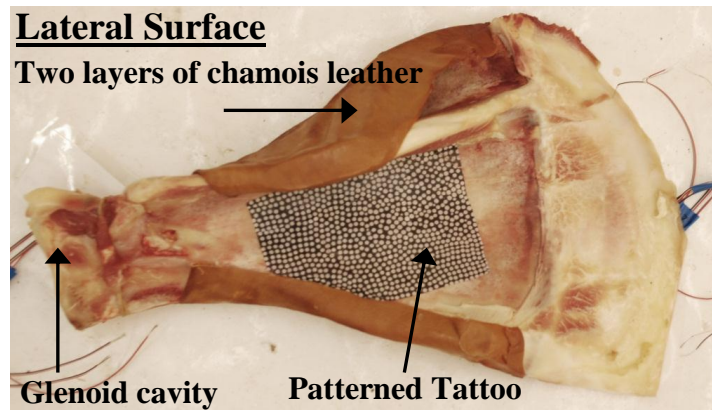


**Figure 4.6: Lateral view (non-impact side) of the DIC BSM construction.**

Strain gauges were applied to the medial (impact) bone surface prior to scalp construction, with a high contrast dot tattoo applied to the lateral surface of the bone.

### **4.2.3 Experimental Set-Up**

Ballistic testing of the BSMs was undertaken at the indoor ballistic range at Dstl Porton Down. The experimental set-up (Figure 4.7) was based on the set-up of the cadaveric testing carried out by Raymond (2008). The key differences between the set-ups were the BSM target instead of a cadaveric head and use of an un-tethered projectile, compared to Raymond's tethered system.

A compressed air firing system called the Dstl Honed Tube Pressure Housing (HTPH)<sup>3</sup> was used to fire a hollow aluminium projectile. Prior to impact, each BSM was weighed using D. Brash and Sons Ltd scales, accurate to  $\pm 1$  g. The BSM target was then positioned at a distance of 1.6 m from the muzzle, or barrel end, to enable enough space for the inclusion of velocity capture screens.

---

<sup>3</sup> Within the Dstl indoor range facility Wasp tracking system, the HTPH was number 92.

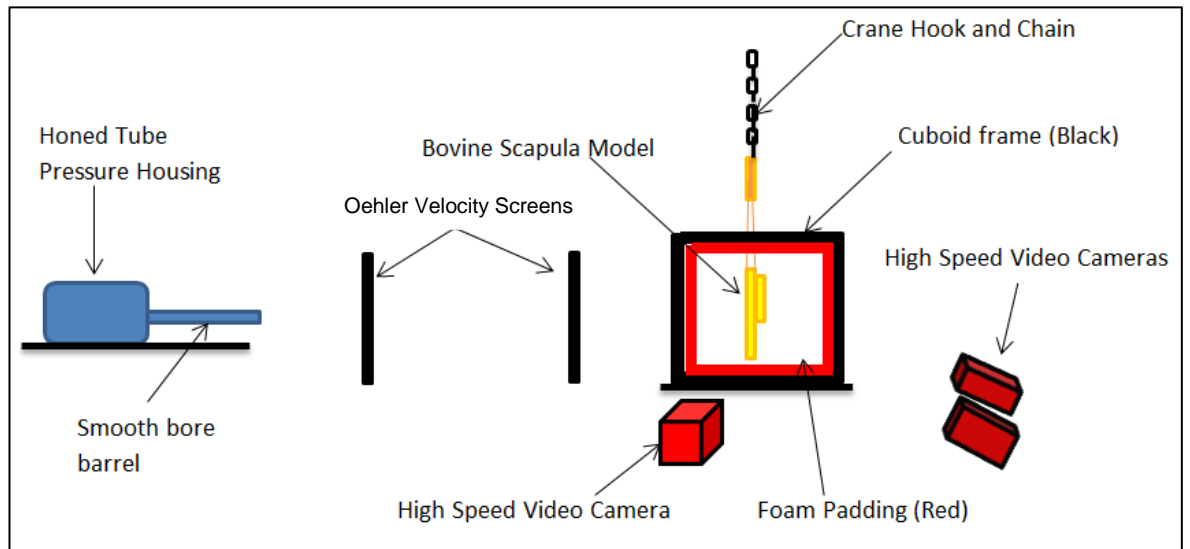


**Figure 4.7: The range set-up at the Dstl indoor ballistic range to investigate the use of Bovine Scapula Models as a fracture analogue of the cranium.**

The BSM was suspended in a string cradle within a padded cuboid frame of side 63 cm. The two sides perpendicular to the direction of the projectile were covered with transparent Perspex, enabling observation of the impact. The remaining sides and exposed sections of the frame were covered with foam in an effort to contain and protect the projectile during ricochet (Figure 4.8).

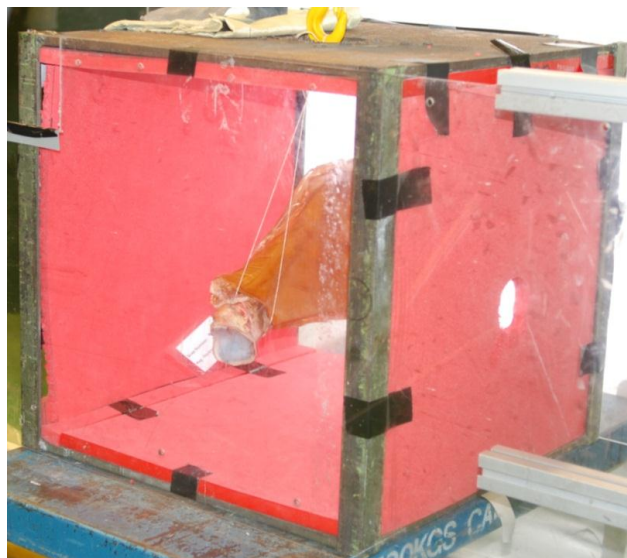


**Figure 4.8: Cuboid frame with foam padding (red) used to house the target under investigation when determining the use of BSMs as a fracture analogue of the cranium.**

Following impact the BSM was examined, cutting away the layers of chamois leather and gelatin to expose the bone, and determine the fracture outcome.

#### **4.2.3.1 Firing System**

The projectile was fired using the HTPH and a 40 mm diameter smooth bore proof barrel<sup>4</sup>. An obturator<sup>5</sup> was fitted behind the projectile to improve fit and achieve repeatable projectile velocities. Finally, a compressed air cartridge (Airmunition SN04663) was used as the energy source to propel the projectile, enabling projectile velocities in the range of 13 to 75 m·s<sup>-1</sup>.

#### **4.2.3.2 Projectile**

Raymond (2008) used an aluminium projectile of 103.1 g, with a uniaxial accelerometer attached to the rear of a flat circular impact face of 38 mm diameter. Data collection was achieved via a tether, attached to the rear of the projectile. However, limitations identified with using a tethered system such as failure of the cables and associated data loss, led to the development of an un-tethered system to support this work (Annex B).

The un-tethered aluminium projectile had a flat circular impact face of 38 mm diameter, a length of 74 mm and a weight of 99.0 ±0.1 g (Figure 4.9). It was not possible to increase the mass to the 103.1 g used by Raymond; there were insufficient resources to manufacture an appropriately weighted system. Additionally, the inclusion of any mass which could become unconstrained may have caused uncontrolled yawing and/or an undefined impact. Therefore, the mass was determined to be adequate, remaining within the scope of blunt ballistic impacts and being consistent across all firings.

---

<sup>4</sup> Within the Dstl indoor range facility Wasp tracking system, the proof barrel was number 117.

<sup>5</sup> An obturator is a plastic device placed behind the projectile (in front of the air cartridge), which expands under the force of the compressed air to fit the barrel. Therefore, the majority of the air pressure is transferred to moving the projectile as less is able to escape down the sides of the barrel around the projectile.



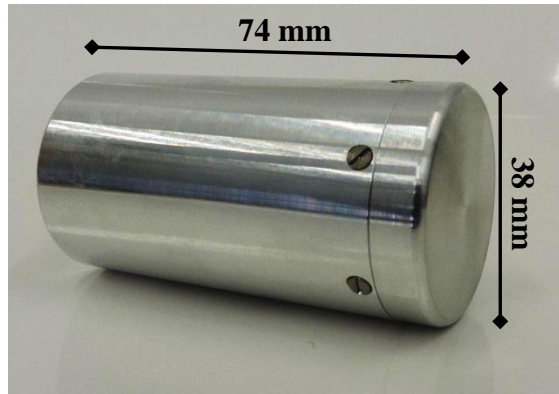


**Figure 4.9: Projectile used to impact the BSMs.**

Unfortunately development of the instrumented projectile (Annex B) was not completed at the time of testing. Therefore, the projectile did not contain any instrumentation; there was no measure of impact force. This resulted in comparisons between BSM and cadaveric fracture responses being limited to measures of impact velocity and fracture outcome. The projectile was however designed to enable the impact face to be changed, although a 38 mm diameter flat impactor was used for all firings in this testing.

#### **4.2.4 Data capture**

##### **4.2.4.1 Projectile Velocity**

To collect the projectile velocity, two Model 57 Photoelectric Oehler velocity screens of 0.92 m by 0.46 m were placed 0.50 m apart between the muzzle and target. The screens were triggered by the projectile passing through an infra-red beam, using the time taken to pass the distance between the two screens to calculate a velocity. Considering the errors associated with the time step, light gate response and actual measured velocity, the maximum error associated with the system was calculated as 0.45%. This was calculated as  $\pm 0.23 \text{ m}\cdot\text{s}^{-1}$  based on a projectile velocity of  $51.59 \text{ m}\cdot\text{s}^{-1}$ .

Post impact, the projectile velocity was combined with the BSM fracture outcome. The data was then fitted to a probit model (Finney 1952) within the statistics program R (R

Core Team 2012). Probit analysis was undertaken using an analysis method previously developed for ballistic material testing (Appendix C). The binary outputs were determined as perforation (1) or fracture for this study, and penetration (0) when no fracture occurred. This initial analysis was used to inform the velocity of the following impact. This analysis also enabled a value of the  $V_{50}$ <sup>6</sup> to be calculated for each BSM construction.

#### **4.2.4.2 High Speed Video**

A Photron SA5 Mono HSV camera was used to observe the flight of the projectile and the interaction between the BSM and projectile during impact (Figure 4.7). Images were collected at 20,000 frames per second (fps), using a 0.05 m lens focused at a distance of 1.1 m. These were determined to be the appropriate settings based on the field of view required to observe the projectile impacting the BSM.

#### **4.2.4.3 Bone fracture**

Raymond (2008) described cadaveric specimen fractures in clinical terms, reporting outcomes of ‘none’ or ‘depressed, comminuted’ fractures. Collection of the type of fracture observed may be useful to understanding cranial fracture thresholds for different fracture severities, where each type of fracture may be associated with a different impact force. Therefore, a scoring method with the ability to identify the different fractures was applied within this work.

The scoring system reported by James *et al.* (2009) (Table 4.1) was used to record BSM fracture occurrence and severity. It was similar to the fracture classifications used within other cadaveric studies by Nahum *et al.* (1968) and Schneider *et al.* (1972), and contains descriptions which could be applied to the findings of Raymond (2008).

---

<sup>6</sup>  $V_{50}$  is the velocity where there is determined to be a 50% probability that the target will fracture.

Description	Score
No fracture (on macroscopic investigation only)	1
Linear fracture	2
Depressed intact fracture	3
Depressed detached fracture	4
Total fracture (complete destruction of the area)	5

**Table 4.1: BSM fracture index reported by James *et al.* (2009).**

## 4.2.5 Data Analysis

### 4.2.5.1 Statistical methods

Rather than directly comparing the individual impact responses, the BSM and cadaveric data points were fitted to a probit model to enable comparison between the fracture risk models. Due to the variability of biological targets and projectile velocity, this method was identified as the most appropriate for comparing the BSM fracture responses.

Probit analysis was undertaken using a bias reduced generalized linear model (brglm) (Kosmidis 2013) within the statistics program R (R Core Team 2012) (Appendix D). The brglm was selected as it reduces the problem of separation within data, leading to a more accurate result when compared to other Generalized Linear Model (GLM) analysis methods (Figure 4.10) (Ellis *et al.* 2013). Separation occurs when only two outcomes are possible and these are separated around a particular stimulus threshold (Kosmidis *et al.* 2010). Where separation is present in a dataset, use of GLMs causes non-finite standard errors. However, using the brglm reduces this problem. The brglm is able to represent a wider range of responses.

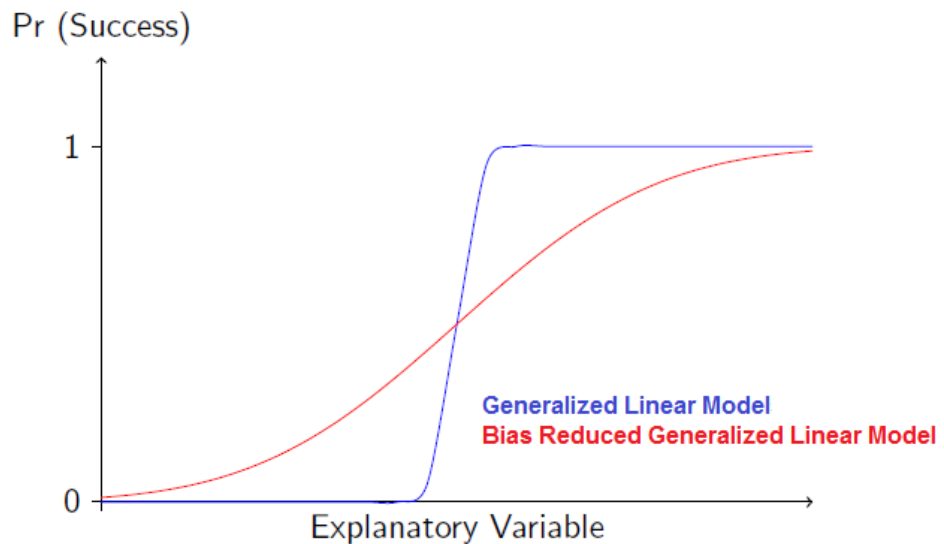


**Figure 4.10: Logistic regression analysis using two different models, where the data is subjected to separation.**

Separation is likely to occur within this dataset where fracture (1) and no fracture (0) are the two outcomes, and fracture is likely to occur in all data points beyond a particular threshold, such as an impact velocity. Similarly, no fractures (0) are likely to occur below this threshold. Therefore, the brglm is the most appropriate statistical method for conducting logistic regression on BSM fracture outcome data.

Using probit modelling within R (R Core Team 2012) statistical software enables a broader set of parameters to be investigated together, exploring their effect on the fracture outcome. The parameters are tested for interactions, giving an overall more accurate model fit when compared to conventional methods which investigate isolated parameters. If a number of the parameters affecting a dataset are investigated together then there is increased power in the test, and misleading results obtained from investigating individual parameters are avoided (Kosmidis 2013).

Within this analysis, three probit models based on the impact data for the BSM constructions (Original, Strain and DIC) were compared to a probit model fitted to the cadaveric data collected by Raymond (2008). The null hypothesis was that there was no difference between the fracture responses of the BSM constructions when compared to the

cadaveric based fracture model. The differences between each construction method and the cadaveric data were compared by a p value; this is a measure of the probability of obtaining a result equal to, or more extreme than, what was actually observed, assuming the hypothesis under test is true (Clarke *et al.* 2004). The significance level, or threshold value, determined with a 95% confidence that the null hypothesis could be rejected was associated with a p value of less than 0.05 and denoted by \*. A 99% confidence level or p value of less than 0.01 was denoted by \*\*, and a 99.9% confidence level was associated with p values below 0.001 (\*\*\*).

A step-wise process was used to explore the parameters of impact velocity, bone thickness, mass and fracture outcome associated with the three BSM constructions and cadaveric data (L. Craddock, personal communication). Interactions between these parameters were also explored to determine the factors affecting fracture outcome. Any parameters and interactions determined not to have an effect on the fracture outcome, p value >0.05 were then removed, and the process was re-run to investigate the strength of the significant parameters in more detail.

Between each run of the model, a statistical test was used to determine how the fit of the data to the model had been affected by the reduction. Where the fit of the data was not determined to be statistically different, the model continued to be reduced sequentially. A final fit was determined as the point when any further reduction of the data within the model caused a significant reduction in the fit of the data (L. Craddock, personal communication).

When the final fit of the model was determined, the factors having the largest effect on fracture outcome remained. This method was used to ensure a number of parameters and interactions were considered, with refinement to determine the statistically significant parameters.

## 4.3 Results

### 4.3.1 Overview

A total of 69 BSMs were impacted with the projectile, at velocities ranging between  $22 \text{ m}\cdot\text{s}^{-1}$  and  $52 \text{ m}\cdot\text{s}^{-1}$ . Using the HSV images, all of the impacts were observed to be perpendicular to the BSM under test. Fractures, recorded across all levels of the BSM fracture index (2-5), were found in 42 of the models.

Individual shot data is documented in Appendix E. Table 4.2 presents the high level findings by construction method, including the  $V_{50}$  and associated 95% confidence limits obtained from the isolated probit analysis of impact velocity during testing.

The average scapula bone thicknesses were either 4.4 mm or 4.5 mm across the three BSM constructions (Table 4.2). The average masses varied due to the construction method used; the DIC BSMs were the lightest of the three construction groups, with an average mass of 1.8 kg as they did not have a gelatin backing like the Original and Strain BSMs. The variability between the Original (4.3 kg) and Strain BSM (3.9 kg) construction masses was likely to be due to a combination of the original mass of the scapulae and the volume of gelatin applied to the rear surface of the models. Although the backing was produced using the same method, on average the Original BSMs may have had more gelatin applied than the Strain BSMs.

Using the measure of  $V_{50}$ , the DIC BSMs were associated with impact velocities of at least  $5 \text{ m}\cdot\text{s}^{-1}$  (13%) slower than the Original and Strain BSM constructions. Therefore, the inclusion of a gelatin backing increases the  $V_{50}$ . The DIC BSM construction also had the highest uncertainty in terms of the 95% confidence limit associated with the  $V_{50}$ . This was more than double the 95% confidence limits calculated for the Original and Strain BSMs (Table 4.2).

Group	Total number of models	No. 3 strain gauge models	No. 6 strain gauge models	Min. bone thickness (mm)	Max. bone thickness (mm)	Avg. bone thickness (mm)	Min. mass (kg)	Max. mass (kg)	Avg. mass (kg)	No. models fractured	V <sub>50</sub> (m·s <sup>-1</sup> )	95% Confidence Limit at the V <sub>50</sub> (m·s <sup>-1</sup> )
Original	22	0	0	2.8	6.4	4.4	3.6	5.9	4.3	12	43.5	±2.2
Strain	22	14	8	2.9	6.4	4.4	3.4	4.5	3.9	14	40.6	±1.9
DIC	25	9	6	2.8	6.7	4.5	1.3	2.3	1.8	16	35.4	±1.9
Raymond	14	14	0	3.5	6.3	4.8	3	4.3	3.4	7	26.7	± 7.4

Table 4.2: The fracture outcome by impact velocity for blunt ballistic impacts against three different BSM constructions, in conjunction with the data reported by Raymond (2008).

### 4.3.2 Model validation

Using the cadaveric data reported by Raymond (2008) to form the baseline model, statistical differences in the fracture response of the three BSM constructions were investigated (Table 4.3). The statistical model considered the parameters of model mass, bone thickness, impact velocity and fracture outcome. At the 95% confidence level, a p value of less than 0.05 shows evidence of a statistical difference between the probit models developed using the BSM datasets and the cadaveric data based model.

BSM construction	p value	Significance at 95% confidence level (p<0.05)
Original BSM	0.057	
Strain BSM	0.034	*
DIC BSM	0.004	**

Table 4.3: Statistical analysis outputs comparing the fracture response of three different BSM constructions (Original, Strain and DIC) to a cadaveric based model.

The analysis considered model type, model mass, bone thickness, impact velocity, and fracture outcome. A significant difference at the 95% confidence level (p<0.05) is denoted by the presence of a star, with the increasing number of stars showing a stronger level of significance.

The final model fit (Table 4.3) found that in statistical terms there was ‘no evidence at the 95% confidence level (p<0.05)’ for a difference between the fracture risk curves developed using the Original BSM and Raymond (2008) cadaveric datasets (p=0.057) (Table 4.3). At

the 99% confidence level ( $p < 0.01$ ), there is statistical evidence that there is a difference between the Original BSM and Raymond (2008) cadaveric datasets ( $p = 0.057$ ) (Table 4.3). However, the statistical difference between these datasets is less than the differences determined for the Strain and DIC BSM datasets; there was evidence at the 95% confidence level ( $p < 0.05$ ) that Strain ( $p = 0.034$ ) and DIC ( $p = 0.004$ ) BSMs had a statistically different fracture response to the cadaveric based model.

#### **4.4 Discussion**

Three different BSM constructions were investigated. The Original BSM construction was statistically determined to have the most similar fracture response to the cadaveric heads impacted by Raymond (2008). This similarity was identified in terms of the model masses and bone thickness, in conjunction with the impact velocities and fracture outcomes.

The Strain BSM construction provided the most similar instrumentation set-up to the cadaveric head impacts completed by Raymond (2008). However, the Strain BSM fracture response was identified as being statistically different (at the 95% confidence level) to the fracture response based on Raymond's cadaveric dataset. The Strain BSMs had a lower average mass (3.9 kg) compared to the Original BSMs (4.3 kg); therefore, the lower masses of the Strain BSMs may have resulted in their fracture at lower impact velocities.

The DIC BSM based probit model was found to be the least representative of the fracture risk model based on Raymond's cadaveric data. This is most likely due to the group being on average almost 60% lighter than the Original and Strain BSMs.

When only considering the parameters of impact velocity and fracture outcome, to cause a 50% probability of fracture the Original BSMs ( $V_{50}$  of  $43.5 \text{ m}\cdot\text{s}^{-1}$ ) required a 64% higher impact velocity when compared to the cadaveric heads tested by Raymond ( $V_{50}$  of  $26.6 \text{ m}\cdot\text{s}^{-1}$ ). In addition, the Strain and DIC BSM constructions were associated with  $V_{50}$



values of  $40.6 \text{ m}\cdot\text{s}^{-1}$  and  $35.4 \text{ m}\cdot\text{s}^{-1}$  respectively. These values would suggest the DIC BSM to be most closely aligned to the cadaveric response; however, this is not the case when a multi-parameter logistical regression model was applied. This highlights the importance of considering a number of parameters associated with an impact event. This is particularly important when testing models with inherent biological variability, all of the variable parameters are considered. A simplified statistical model would have resulted in misinterpretation of the data.

Of the three BSM datasets, the DIC BSM dataset had the largest 95% confidence interval associated with the calculation of its  $V_{50}$  at  $\pm 4.8 \text{ m}\cdot\text{s}^{-1}$ . This is more than double the confidence limits calculated for the Original ( $\pm 2.2 \text{ m}\cdot\text{s}^{-1}$ ) and Strain BSMs ( $\pm 1.9 \text{ m}\cdot\text{s}^{-1}$ ), and is potentially due to there being three slight variations in construction of no strain gauges, three strain gauges and six strain gauges. This variability may have affected the fracture outcomes. However, there is insufficient data relating to each variation to conduct a detailed analysis.

In order to develop the understanding of cranial fracture force thresholds, impact force data is required. Ideally the projectile would have been instrumented to enable the calculation of force data for comparison, in conjunction with velocity, to the cadaveric data collected by Raymond (2008). The inclusion of force data would have enabled an additional parameter for comparison between the BSM and cadaveric data. However, when the projectile and target characteristics are similar, impact force will be related to impact velocity. Therefore it is likely that the relationships identified for impact velocity in this study will be similar to the fracture responses based on peak force measures.

Using the cadaveric data obtained by Raymond (2008) to validate BSM based cranial fracture risk curves requires a similar projectile to be used to maintain consistency across investigations. Therefore, a comparable projectile in terms of material and shape was used.

However, the mass was nearly 4% (4 g) lower than the system used by Raymond. The 4 g difference between the projectiles used in the cadaveric and BSM studies will have affected the fracture outcomes observed. This does not affect the comparisons between the different BSM constructions. However, a heavier projectile will have a higher momentum and energy when fired at the same velocity as a lighter projectile. Therefore if the BSMs had been impacted with a 103.1 g projectile it is likely that they would have fractured at a lower velocity. This could have led to a more similar fracture response to the cadaveric study, when compared to the response found in this testing. However, even a 10% reduction ( $4.4 \text{ m}\cdot\text{s}^{-1}$ ) in impact velocity would not be enough to align the Original BSM  $V_{50}$  ( $43.5 \text{ m}\cdot\text{s}^{-1}$ ) with the cadaveric fracture response ( $V_{50}$  of  $26.6 \text{ m}\cdot\text{s}^{-1}$ ).

Each BSM construction type contained a range of bone thicknesses and masses. The scapula bones had inherent biological variation in size, thickness and mass, similar to the variations seen in the cadaveric specimens used by Raymond (2008). However, variability in cattle slaughter age will affect the development of the bone and hence its mechanical properties, potentially affecting the overall fracture response of different batches of scapula. This will be dependent on the animals available for slaughter at the time of obtaining the scapula. Therefore each test series undertaken using BSMs should validate the fracture response using comparable cadaveric data.

## **4.5 Summary**

To determine a fracture analogue of the cranium, three different BSM constructions were tested under blunt ballistic impact conditions. The impacts were comparable to cadaveric head testing carried out by Raymond (2008). A BSM construction of a scapula backed with 20% ballistic gelatin and combined with scalp representation using chamois leathers and 10 mm of gelatin (denoted as Original BSM), has been statistically determined as providing a representative fracture response to cadaveric head impact data. This

comparison was made by applying the data within a multi-parameter logistical regression model. It has been determined that the BSM could be used as a potential fracture analogue of the cranium to develop theories on cranial fracture response and outcomes associated with BHBT cranial fracture risk.

Where different batches of scapula may vary in fracture response, it is recommended that future BSMs studies include a group comparable to cadaveric testing. This will enable determination of the relationship between the two models for each test series, and hence the applicability of the BSM findings to cranial fracture outcomes.

## Chapter 5: Quantification of helmet deformation

### 5.1 Introduction

The effects of impact curvature and flat diameter on cranial fracture response have been identified for investigation. This is to provide improved predictions of cranial fracture outcomes associated with the assessment BHBT. Therefore helmet BFD should be quantified to determine representative curvatures and flat diameters which may impact the head. These could then be used to investigate their effect on cranial fracture thresholds using the BSM.

When there is a head model underlying the BFD, reporting suggests that it is challenging to observe the helmet BFD (Bass *et al.* 2003, Freitas *et al.* 2014). However, BFD in free air has been quantified using DIC analysis (Hisley *et al.* 2010). The DIC technique provides an understanding of the shape and size of helmet deformation as it develops, although it is understood that the BFD will change as it interacts with the head; Bass *et al.* (2003) and Freitas *et al.* (2014) used x-ray imaging to observe the BFD conforming to the head. However, the DIC data could be used to understand the shape and area of helmet deformation in air (without any padding lining the helmet shell). This would be representative of BFD until the deformation makes contact with the underlying head.

A number of factors that are directly related to the helmet BFD have been determined to affect BHBT. These factors include bullet type and velocity (Freitas *et al.* 2014), in addition to the protective material tested and its stand-off from the underlying head (Sarron *et al.* 2004). Padding within the stand-off was also determined to affect the resulting BHBT (Merkle *et al.* 2010). This may affect the shape of the helmet BFD in addition to varying the distribution and rate of loading onto the underlying head. Investigations into thoracic BBT have used a projectile to represent the armour deformation (Arborelius *et al.* 2012),

overcoming the variability of using a bullet and armour system. This approach could also be taken for helmet BFD, where the DIC measures could be applied to a projectile. The projectile could then be used to enhance the understanding of cranial fracture thresholds associated with BHBT. Through the use of Raymond's data, Bolduc *et al.* (2010) have already highlighted acceptance of using projectile based cranial fracture thresholds to support BHBT assessments.

The projectile used by Raymond (2008) has already been used to develop a cranial fracture model (Chapter 4). This system could be modified to deliver a range of representative helmet BFD impacts. Therefore, the aim of this work was to determine representative curvatures and flat diameters for helmet BFD. This information was required to design projectile faces that could then be used to investigate cranial fracture thresholds under blunt ballistic loading conditions.

## **5.2 Method**

### **5.2.1 Helmet deformation data collection**

Impact testing of UK combat helmets was undertaken in collaboration with the Army Research Laboratory (ARL), in Maryland USA. UK Helmet Combat General Service Mark 6a and Helmet Combat Assault Mark 7 variants (Figure 5.1) were obtained for testing due to their wide use within the UK Military. The test set-up (Figure 5.2) was consistent with that reported by Hisley *et al.* (2010).

Prior to testing, all of the internal components of the helmet systems (padding, liner and harness) were removed and any paint on the internal surface of the helmet shell was removed by sanding. The internal surface of the helmet shells were then covered with a randomised pattern ink tattoo (Figure 5.3).

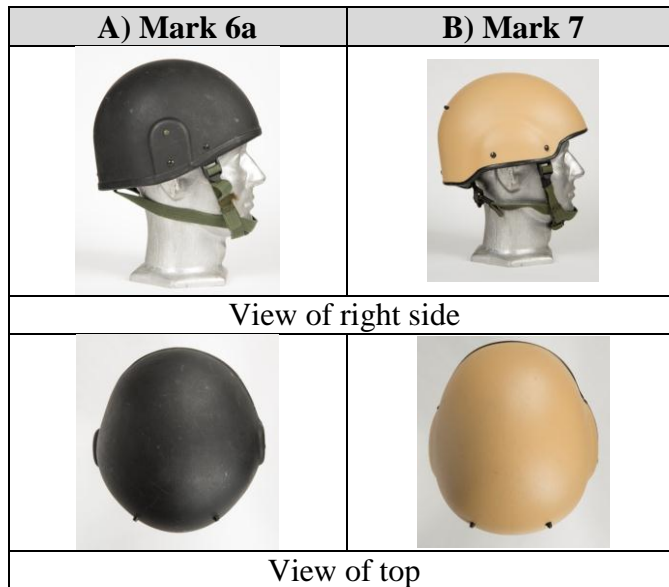


Figure 5.1: UK Helmet Combat General Service Mark 6a and Combat Assault Mark 7.

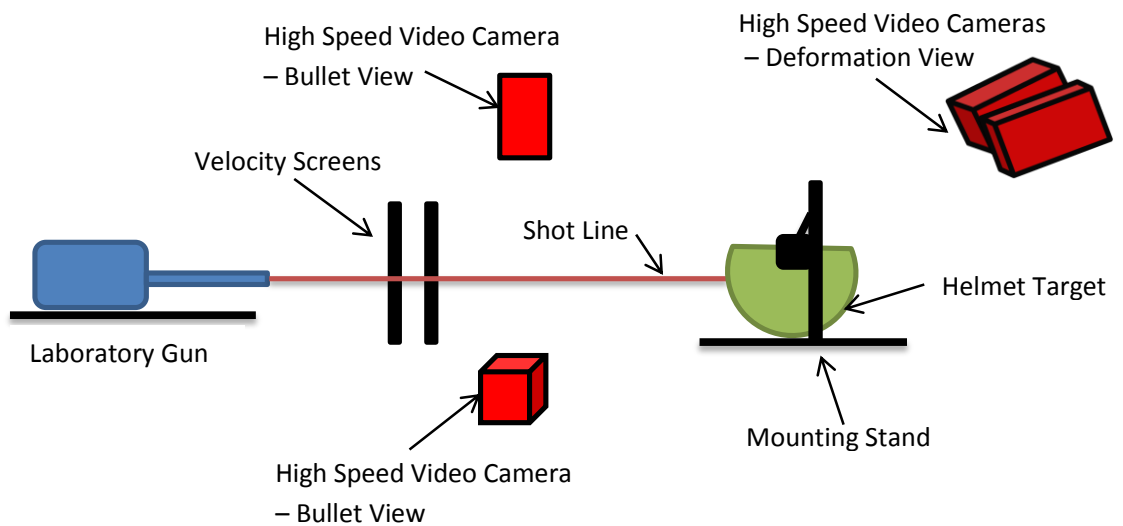
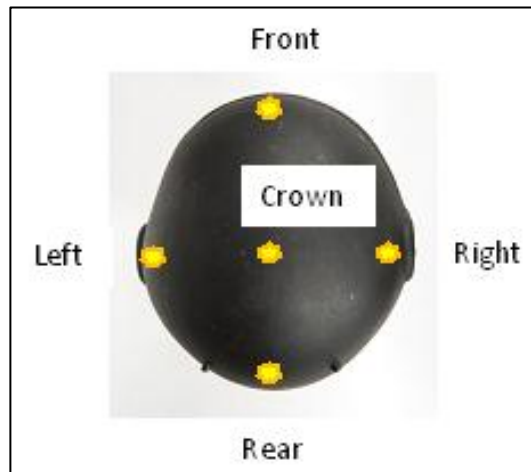


Figure 5.2: Range set-up used by Hisley *et al.* (2010) at the ARL in Maryland USA.



Figure 5.3: Dot tattoo applied to the inner surface of a UK Helmet General Purpose Combat Assault Mark 7.

A laboratory weapon was used to fire a single bullet type at representative muzzle velocities, measured using light gates. Each helmet was tested in five predefined locations (Figure 5.4). On impact with the helmet, the BFD was observed using two HSV cameras. These HSV images were then used by ARL to conduct 3D DIC analysis for each shot, using ARAMIS software v6.1 (GOM Optical measurement techniques 2009).



**Figure 5.4: Impact point locations identified by Hisley *et al.* (2010), described as Crown, Front, Rear, Left and Right identified on a UK Helmet Combat General Service Mark 6a.**

On completion of testing, each measured helmet deformation was presented within a 2D plot. These plots showed peak displacement from the original surface of the shell and the peak velocity of the deformation surface. The deformations were also sectioned across the peak displacement to obtain 2D plots of the peak deformation forming over time (Figure 5.5).

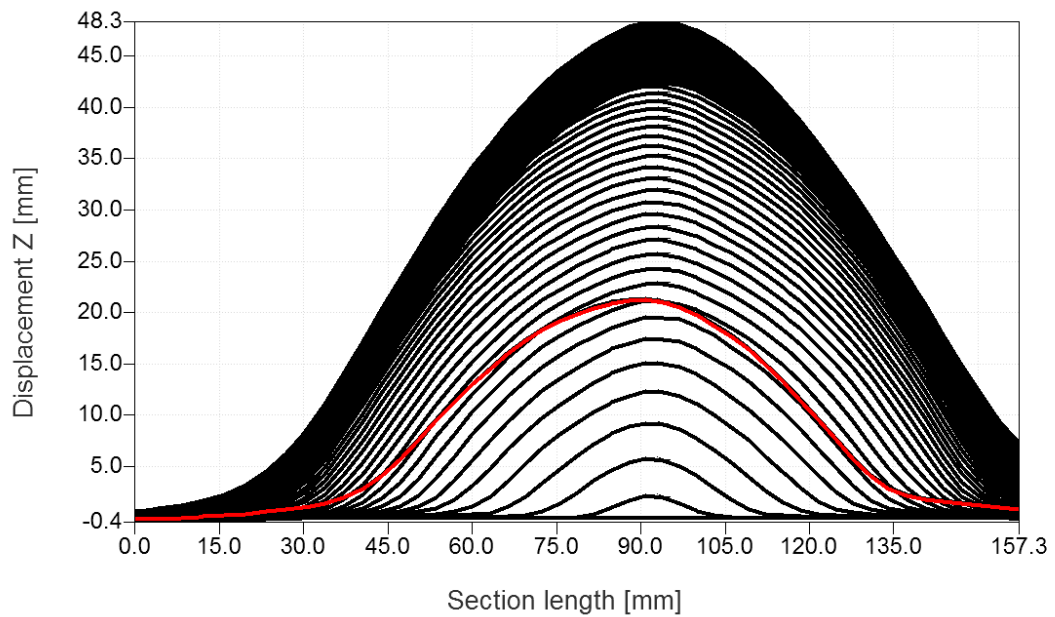


**Figure 5.5: A 2D section through the location of the peak displacement of Shot #76 3D BFD.**

Each black line corresponds to a point in time as the displacement developed to a peak. The time intervals between each line were the same (20  $\mu$ s), showing the reduction in the gap and hence the decrease in velocity as the deformation expanded to the peak. The red line indicates the residual deformation of the surface post impact.

Image exported from post processing analysis by ARL (USA Government, permission for use kindly given), using ARAMIS post processing software (GOM Optical measurement techniques 2009).

## 5.2.2 Data Analysis

Each displacement profile was investigated. The DIC was advanced frame-by-frame until the peak displacement reached a 5 mm increment. As the displacement developed, measurements of the area<sup>7</sup>, velocity and radius of curvatures were taken at each 5 mm increment up to a maximum displacement of 50 mm. At 50 mm from the helmet shell the majority of impacts had reached their maximum deformation.

The deformations were generally symmetrical in shape. Therefore the radius of curvature was determined at the peak displacement, across a single 2D section of the deformation. This provided an understanding of the shell deformation over time, and enabled

---

<sup>7</sup> Area determined as the 2D surface of the helmet shell affected by the deformation.



determination of the BFD at a range of displacements. This provided outputs to inform the design of impact faces for application on a rigid projectile.

## **5.3 Results**

### **5.3.1 Overview**

A total of 16 UK Combat Helmet shells (ten Helmet Combat General Service Mark 6a and six Helmet Combat Assault Mark 7 variants) were impacted, resulting in a data-set of 80 shell deformations. The bullet velocity, impact location, shot number, and HSV images of each deformation were collected.

DIC analysis was undertaken on each impact. During some deformations, layers of material came apart over the surface being measured. This limited the ability of the DIC analysis to provide quantitative results, and affected the data which could be obtained for two deformations. Therefore, a total of 78 shell deformations were provided by ARL.

The maximum BFD displacement ranged from a depth of 37 to 58 mm. This peak occurred between 640 and 2040  $\mu\text{s}$  after the start of the surface deformation. The deforming surface of the helmet shells were observed to be moving at a maximum velocity between 153 and 234  $\text{m}\cdot\text{s}^{-1}$ , occurring between 40 and 80  $\mu\text{s}$  after the initiation of the deformation. The velocity of the surface reduced as the deformation area continued to increase, as shown for a single impact in Figure 5.6.

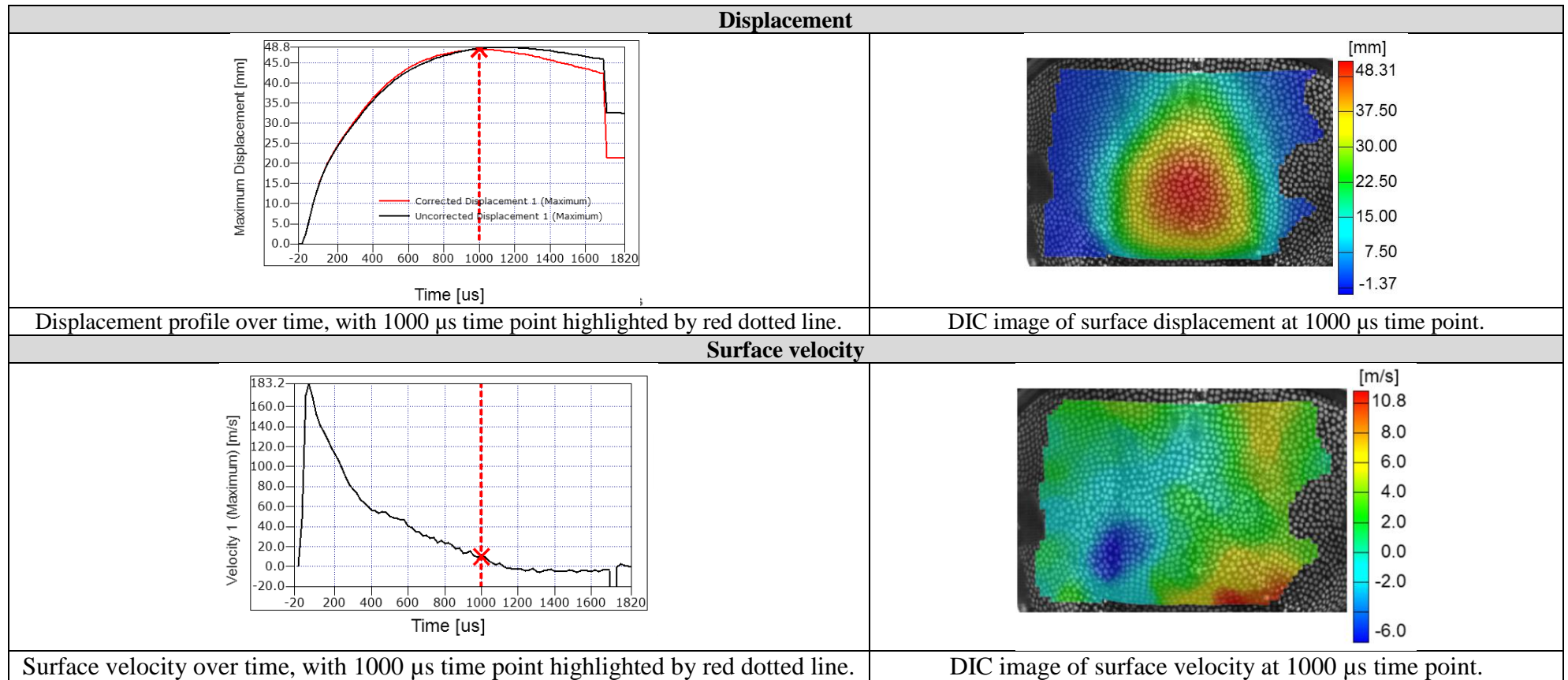


Figure 5.6: A UK Helmet Combat Assault Mk 7 shell as it deforms to defeat a bullet threat.

Velocity and displacement profiles of shot #76 at 1000  $\mu$ s. The corrected displacement, shown by the continuous red line in the top left hand image, has accounted for any movement of the whole helmet shell. Therefore, the red line shows the displacement of only the BFD. Images exported from post processing analysis by ARL (US Government, permission for use kindly given), using ARAMIS software (GOM Optical measurement techniques 2009).

### 5.3.2 Data Analysis

The details of each impact are given in Appendix F, including deformation area, maximum velocity and radius of curvature for the first three 5 mm increments, from 5 mm to 15 mm of displacement. These 5 mm increments are determined to be representative of the stand-off levels expected when wearing the helmets tested.

Area of deformation and average radius of curvature were highly variable (Appendix F). For deformation area, the measurements showed differences over  $5.0 \times 10^3 \text{ mm}^2$  (35%) at the peak displacement. Similarly, the radius of curvatures varied by up to 104 mm (78%) at the peak displacement. Therefore, to enable investigation of any potential differences in deformation due to shot number and helmet variant, the deformations were combined to calculate average values of deformation area and curvature.

For each 5 mm increment of displacement, no differences were observed between average deformation area as a result of the helmet variant (Figure 5.7) or shot number (Figure 5.8). However, in the final stages of deformation, different shapes were observed. This was as a result of interactions with the shell edge and geometry effects, with changes in the geometry being particularly noticeable at the ear sections. These effects were not investigated further as the cross sectional shapes remained generally bell shaped with a curved leading edge (Figure 5.5). This bell shape was consistent across all locations of impact and between the two different helmet variants. In addition, the displacement at which the deformation was affected was much greater than any level of stand-off likely to be maintained by the wearer. Therefore, the shell edge and geometry effects were not important in terms of the aim of this study.

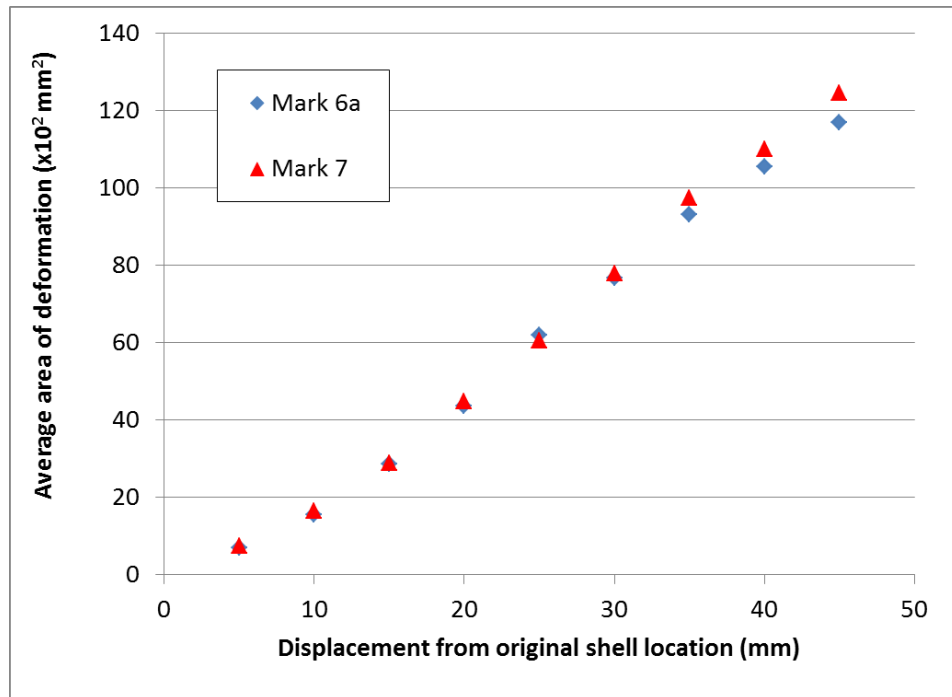


Figure 5.7: Average deformation areas of two different UK Helmet Combat variants at different displacements, as BFD develops.

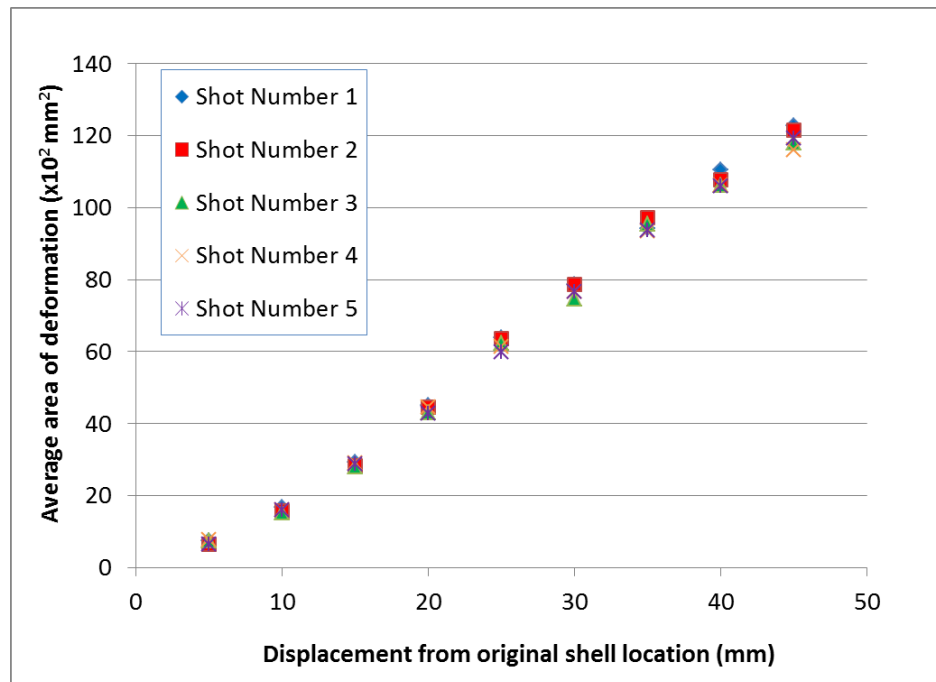


Figure 5.8: The deformation area of UK Helmet Combat variants at different distances of BFD development, obtained from DIC analysis and presented by shot numbers (1-5).

Using all 78 impacts, an average area (Figure 5.9) and radius of curvature (Figure 5.10) was calculated for each 5 mm increase in deformation displacement. The averages are presented along with the standard deviation to highlight the variability observed within testing.

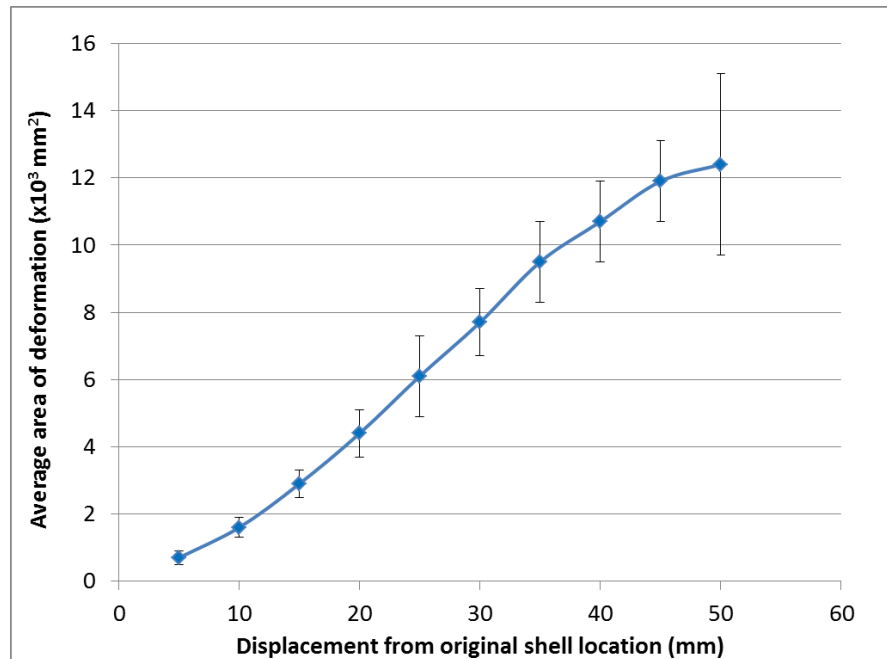


Figure 5.9: The average area of helmet deformation obtained from 78 impacts against two different UK Helmet Combat variants. Bars show the standard deviation of the data.

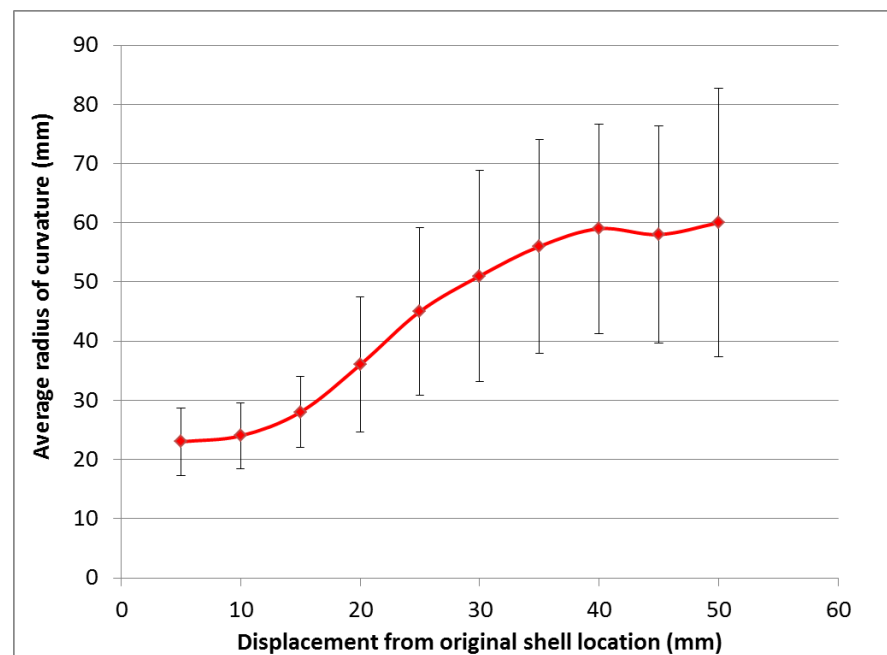


Figure 5.10: The average radius of curvature of helmet deformation obtained from 78 impacts against two different UK Helmet Combat variants. Bars show the standard deviation of the data.

### 5.3.3 Determination of impact faces

The areas and curvatures of BFD were used to design a variety of projectile faces which could be used to assess BHBT (Figure 5.11). The projectile design was comparable to the system used by Raymond (2008), in the investigation of a cadaveric cranial fracture response. Full details of the projectile development are provided in Annex B. The projectile had a maximum diameter of 38 mm throughout its length. Therefore, due to projectile design and the firing mechanism the impact face had a maximum diameter of 38 mm. Although this enabled direct comparison to the cadaveric data reported by Raymond, it meant that additional flat face diameters had to be less than 38 mm.

To quantify any relationship between impact diameter and fracture outcome, data was required for a minimum of three different impact faces. Improved confidence would be achieved through the investigation of a larger number of different projectile faces. Therefore, a total of four flat faces were designed; an area of  $1.1 \times 10^3 \text{ mm}^2$  (38 mm diameter) and three smaller areas of 0.8, 0.5 and  $0.3 \times 10^3 \text{ mm}^2$ , relating to flat face diameters of 32 mm, 26 mm and 20 mm respectively. Due to restriction of the projectile diameter, the flat faces were only representative of the smallest areas determined from the BFD measures (Figure 5.9). However, the DIC analysis showed that these diameters could be relevant to helmet BFD impacts for small displacements.

Measures of the BFD radius of curvatures were used to determine four curved faces (Figure 5.11), spanning a large proportion of the curvatures identified through DIC analysis (Figure 5.10). To maintain the projectile diameter at 38 mm, the smallest achievable radius was determined as a hemisphere of 19 mm radius. The largest radius of curvature used was 50 mm. This was not the largest curvature observed from the DIC analysis (Figure 5.10) but was chosen to give 4 projectiles with a reasonably small and consistent change in curvature. Additionally, a 50 mm radius of curvature was comparable

with cadaveric testing planned at ARL (K. Rafaels, personal communication), although there are differences in the diameter of the projectiles, which may limit the comparisons which can be made.









Impact Face	Diameter (mm)	Radius of Curvature (mm)	Impact Surface Area ( $\times 10^2 \text{ mm}^2$ )	Image
1	38	$\infty$	11.3	
2	32	$\infty$	8.0	
3	26	$\infty$	5.3	
4	20	$\infty$	3.1	
5	38	19	22.7	
6	38	30	14.7	
7	38	40	13.8	
8	38	50	14.1	

Figure 5.11: Flat and curved impact faces determined from helmet BFD data in conjunction with the parameters of the projectile which the faces are to be attached to.

## 5.4 Discussion

Collaboration with Hisley et al. (2010) enabled collection of quantitative data relating to the dynamic deformation of UK combat helmets. More than one helmet shell shape was considered, ensuring the findings were not specific to a single helmet. However, only a single projectile and impact velocity were investigated. In addition, the two helmet variants showed very similar BFD responses (Figure 5.7), most likely due to their similar material construction. Therefore, it may be beneficial to impact helmets of different material constructions with different projectiles at different velocities, using the same test method, to determine the different profiles. This would ensure that studies undertaken using the results were applicable to any helmet BFD.

Testing was conducted at a representative bullet impact velocity and it was identified that repeated shots on a single helmet did not affect the deformation shape or area measured (Figure 5.8). However, this was up to a maximum of 5 shots, any increase may have limited the usability of the results due to pre-existing shell damage.

There are several errors associated with the measurements obtained using DIC analysis. These include the accuracy of the ARAMIS software algorithms and measurement of the deformation post analysis. For example, a peak deformation of 37 mm occurred over a time of 640  $\mu$ s. With the HSV collecting images at 50,000 frames per second, 32 frames of data were collected. Assuming consistent development, the deformation increased by up to 1.2 mm per frame. However, the displacement of interest was at 5 mm increments of displacement. Therefore, if the displacement of interest was not captured in an isolated frame, it may vary up to  $\pm 0.6$  mm. This would be dependent on the frame chosen to analyse. The measurements of area and radius of curvature were then affected by human error. This was determined to be approximately  $\pm 1.0$  mm. Further errors are likely to be present within the GOM software processing. However, these could not be defined.



Therefore, it was not possible to quantify all of the errors associated with the DIC analysis. However it is likely that the values of BFD are representative. This is based on the use of a recognised test method (Hisley *et al.* 2010) and ensuring consistency between shots.

The BFD measures were used to develop impact faces for a 38 mm diameter projectile. The full range of areas and curvatures obtained through DIC analysis could not be represented due to limitations on the projectile diameter. Therefore, there may be a future requirement to expand the range of projectile faces. The data obtained within this study is available to support this development.

A range of flat-circular diameters and curvatures have been determined. These can be used to investigate the effects of curvature and flat diameter on cranial fracture thresholds. The two smallest diameter flat faces of 20 and 26 mm have areas of 0.3 and 0.5 x10<sup>3</sup> mm<sup>2</sup> respectively. These are considerably less than the average areas measured from the helmet BFDs (Figure 5.9). However, the area contacting the head is likely to be less than the area of deformation measured. This is due to the bell shape of the deformation. In addition, based on the spread of the data, the small areas are relevant to some deformations at 5 mm and will be relevant to the first 4 mm of deformation for other BFDs. This will be representative for cases of minimal distance between the head and helmet shell. Alternatively, the areas may be representative of BFD associated with helmets of different constructions to those tested in this work.

Similarly, the hemispherical face of 19 mm radius of curvature was smaller than the average measured curvatures. However, it was the smallest radius possible within the design constraints of the projectile and it provided the most extreme curvature to the flat faced 38 mm diameter. Looking at the spread of the data (Figure 5.10), the 19 mm curvature represents some of the smallest measures for the helmets tested, and it may also

be applicable to different helmet constructions and small distances between the head and helmet shell.

Testing was focused on achieving penetration of the helmet shells, and testing was therefore optimised to ensure perforation did not occur. However, alternative testing undertaken at Dstl has observed that contact of BFD with a backing surface can promote perforation of the armour (M. Neale, personal communication). In these cases a penetrating injury would occur instead of a blunt ballistic impact. Therefore, the measures of BFD obtained may not be representative of the response of a backed helmet. However, the challenges of capturing helmet deformation with a backing in place were the initial reason for using free-air measurements. With this in mind, the BFD areas and curvatures have been determined as representative. Therefore, the projectile faces are suitable to investigate cranial fracture response due to blunt ballistic impact associated with BHBT.

Within the literature (Section 3.4.2.1), flat impact faces of 20, 26 and 32 mm in diameter and curved faces of 19, 30 and 40 mm radius of curvature have not been investigated in terms of cranial fracture thresholds. Therefore, investigation of these impacts also has the potential to enhance the understanding of cranial fracture outcomes within the wider research community, beyond those interested in the assessment of BHBT.

## **5.5 Summary**

Using DIC analysis, helmet BFD for a given helmet, projectile and impact velocity have been measured to have an average area of  $0.7 \times 10^3 \text{ mm}^2$  at a peak displacement of 5 mm. This average area has been found to increase to  $12.0 \times 10^3 \text{ mm}^2$  at a maximum displacement of 50 mm. Similarly, at a peak displacement of 5 mm, average radius of curvature has been calculated at 23 mm, increasing up to an average of 60 mm at a maximum displacement of 50 mm. In conjunction with projectile design requirements, this information has informed

the shapes of eight impact faces; four flat-circular faces of 38, 32, 26 and 20 mm diameters, and four curved faces of 19, 30, 40 and 50 mm radius of curvature.

Testing of a 38 mm flat impact face will enable comparison to existing cadaveric data, essential for validation purposes. Investigation of the full range of impact faces would enable differences in cranial fracture thresholds to be determined and quantified. This information could enhance the understanding of cranial fracture outcomes within the wider research community and support the development of cranial fracture risk models associated with BHBT.

# **Chapter 6: Investigation of the effect of flat diameter and curvature on BSM fracture thresholds**

## **6.1 Introduction**

The literature review of existing BHBT assessment methods and associated cranial fracture risk models has identified that the effects of BFD shape, specifically in terms of curvature, have not been investigated. A range of representative helmet deformation curvatures and areas have been identified within section 5.3.3. The areas are represented by flat impact faces of varying diameter. Investigation of the effect of these flat diameters and curvatures on cranial fracture thresholds would support the development of cranial fracture risk models associated with blunt ballistic impacts from helmet BFD.

The aim of this work was to use an instrumented projectile to deliver a range of impacts, representative of helmet deformation, to BSM targets. The Original BSM has been identified as a fracture analogue for the cranium (Chapter 4). This would provide data to determine the effect of flat diameter and curvature of impact on cranial fracture thresholds to inform cranial fracture risk models associated with BHBT.

## **6.2 Method**

### **6.2.1 Experimental Set-up**

Testing was undertaken in the Dstl Building 390 South Indoor Test, Evaluation, Research and Proof (TERP) range. Over the four week duration of the trial the chamber had a temperature in the range of 16.3-19.4 °C, a humidity between 43-54 RH and an air pressure of 976-1009 mbar; as recorded using a Fisher Scientific Traceable unit (SN130753635).

The test set-up was comparable to that used by Raymond (2008) and detailed as part of the determination of a cranial fracture analogue (Section 4.2.3). The range set-up included a compressed air firing system, HSV instrumentation and a BSM target suspended in a protective frame (Figure 6.1); however, the previously used Oehler velocity screens were replaced with an MSI (Type 858-001AS/A) light gate and detector. This light gate was used to trigger a single HSV camera (Photron Fast Cam SA-Z 2100K-M-18G, SN10202402020) with a 105 mm lens. The camera was positioned to record projectile impact with the BSM target in addition to a number of pre-impact images, recording at a rate of 120,000 fps.

The Original BSMs were constructed using the method previously reported in section 4.2.2.3, and suspended in a string cradle. The BSM targets were suspended within a foam padded cuboid frame (section 4.2.3). Transparent Perspex was used to cover two sides of the frame, enabling the target surface to be well lit using spot lights and HSV images to be collected, whilst containing the projectile and target post impact.

The air cartridge pressure was typically set to 60 psi to achieve projectile velocities in the desired range. As the projectile was only able to collect 62.4 ms of data, the distance between the barrel and the target ( $0.42 \pm 0.01$  m) needed to be reduced when compared to the test set-up detailed in section 4.2.3. Hence, the removal of the Oehler velocity screens system. However, the distance was reduced to a level which still enabled the projectile to be imaged in free flight prior to impact for velocity calculation. Additionally, this distance ensured the barrel-end remained outside of the target box, limiting any potential ricochet damage to the projectile.

Post impact the BSM was examined and dissected to expose the bone for identification of the fracture outcome. Depending on the fracture outcome, the next impact was completed

at a velocity determined to support the collection of equal numbers of fracture and non-fracture outcomes.

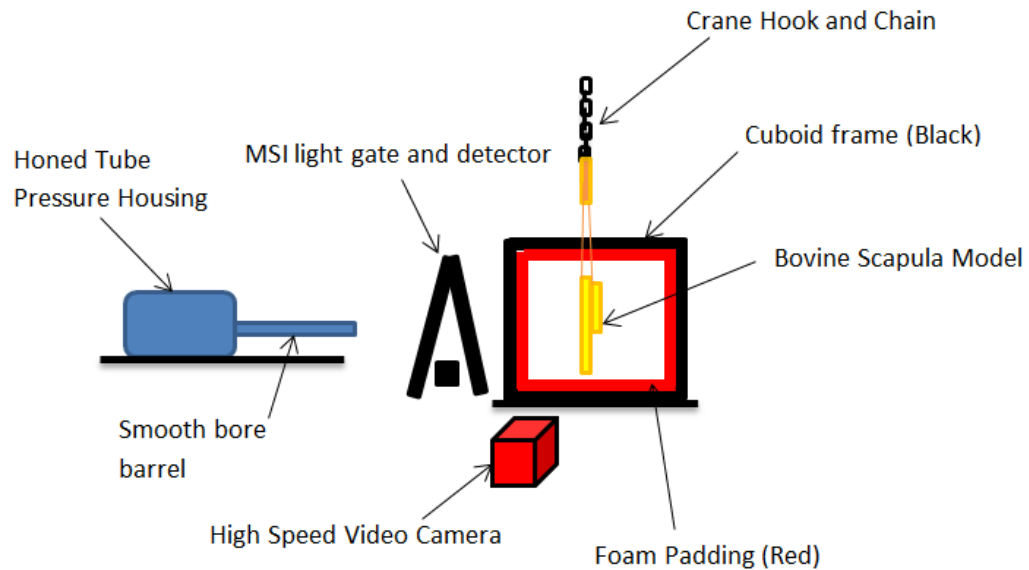


**Figure 6.1: Range set-up for investigating the effect of flat face diameter and curvature on the fracture threshold of a cranial model.**

## 6.2.2 Projectile

An un-tethered instrumented projectile with an aluminium shell was used for all impacts. The projectile contained a Med-Eng Ballistic Data Acquisition System (BDAS), including an accelerometer for collection of the projectile acceleration (Figure 6.2). A full description of the projectile design is given in Annex B.

Due to the limits of durability associated with the BDAS, four projectiles were used in this study. The projectile masses (including the BDAS) were in the range of  $104.5 \pm 1.7$  grams, dependant on the impact face tested. The four units used in this study were serial numbers 3357, 3358, 5023 and 5024. In addition, a projectile which did not contain any instrumentation was used to check the experimental set-up.



**Figure 6.2: Med-Eng Ballistic Data Acquisition System (BDAS) unit mounted within a four piece aluminium shell.**

As described in section 5.3.3, eight different impact faces (Table 6.1) were used to investigate the effects of flat diameter and curvature on BSM fracture response.

Impact Face (Test Group)	Diameter (mm)	Radius of curvature (mm)
1	38	$\infty$
2	32	$\infty$
3	26	$\infty$
4	20	$\infty$
5	38	19
6	38	30
7	38	40
8	38	50

**Table 6.1: Dimensions of representative BFD impact faces for the investigation of flat diameter and curvature effects on cranial fracture thresholds.**

An ink pad was used to apply ink to the impact face of the projectile prior to firing. Transfer of the ink to the chamois leather of the BSM enabled identification of the location of impact.

### 6.2.3 BSMs

Recent research into statistical methods associated with probit analysis has identified that confidence limits can be reduced by approximately 60% when data collection is increased from 20 to 40 tests (L. Craddock, personal communication). However, the relative gain

identified from increasing a dataset from 30 to 40 data points is minimal compared to the relative gain observed by increasing a dataset from 20 to 30 points. Therefore 30 data points was considered acceptable and would be collected for each of the eight impact faces under test. Therefore, a total of 240 Original BSMs were required to complete this study. In order to allow for any pre-existing damage or otherwise unsuitable samples, a total of 260 bovine scapulae were purchased from a local butcher<sup>8</sup>. The scapulae were obtained from cattle between 12-18 months old. Any scapulas with pre-existing damage such as fractures due to the butchering process were discarded.

The Original BSMs were manufactured in batches of 20, using the same method and construction as detailed in Annex A. Each batch took three consecutive days to construct, and production had to fit within a 5 day week. This resulted in the production of three batches over the five day period (Table 6.2). A period of 20 days was required to complete all 240 impacts.

The BSMs were impacted on the same day as they were removed from the moulds and weighed. Although every effort was made to sufficiently back the scapulae with gelatin, in some cases pockets of air were identified behind the rear surface of the bone. Pockets of air occurred due the irregular shape of the scapula combined with the method of moulding the backing. These models were removed from testing as the potential effect on fracture outcome could not be quantified.

---

<sup>8</sup> R. Owton Butchers, Burnetts Lane, Southampton, UK.



Activity	Day 1	Day 2	Day 3	Day 4	Day 5
- Rehydrate scapulae - Mould 10mm slices - Remove excess soft tissue - Measure bone thickness and label model	<b>Batch 1</b>	<b>Batch 2</b>	<b>Batch 3</b>		
- Apply scalp representation over impact area - Mould backing		<b>Batch 1</b>	<b>Batch 2</b>	<b>Batch 3</b>	
- Remove from mould and separate models - Weigh each BSM - Impact BSMs			<b>Batch 1</b>	<b>Batch 2</b>	<b>Batch 3</b>

**Table 6.2: Five day plan for manufacturing three batches of 20 BSMS.**

#### **6.2.4 Testing decision processes**

A decision process (Figure 6.3) was applied to the study to ensure only meaningful tests were carried out and resources were not wasted. Evaluation of the impact faces at the extremes of diameter and curvature was initially undertaken, i.e.:

- 38 mm diameter flat face (largest flat);
- 20 mm diameter flat face (smallest flat); and,
- 19 mm radius of curvature (hemispherical).

A probit analysis was applied to the impact velocities and associated fracture outcomes to produce fracture risk models. These models and their associated 95% confidence limits were compared. If there was any gap between the 95% confidence limits then it was assumed that there was sufficient difference between the fracture outcomes to warrant further investigation of the effect of impact curvature and/or flat diameter. Where this was the case, the intermediate impact faces were tested to provide increased resolution when quantifying the effect of flat face diameter and curvature of impact on BSM fracture thresholds.

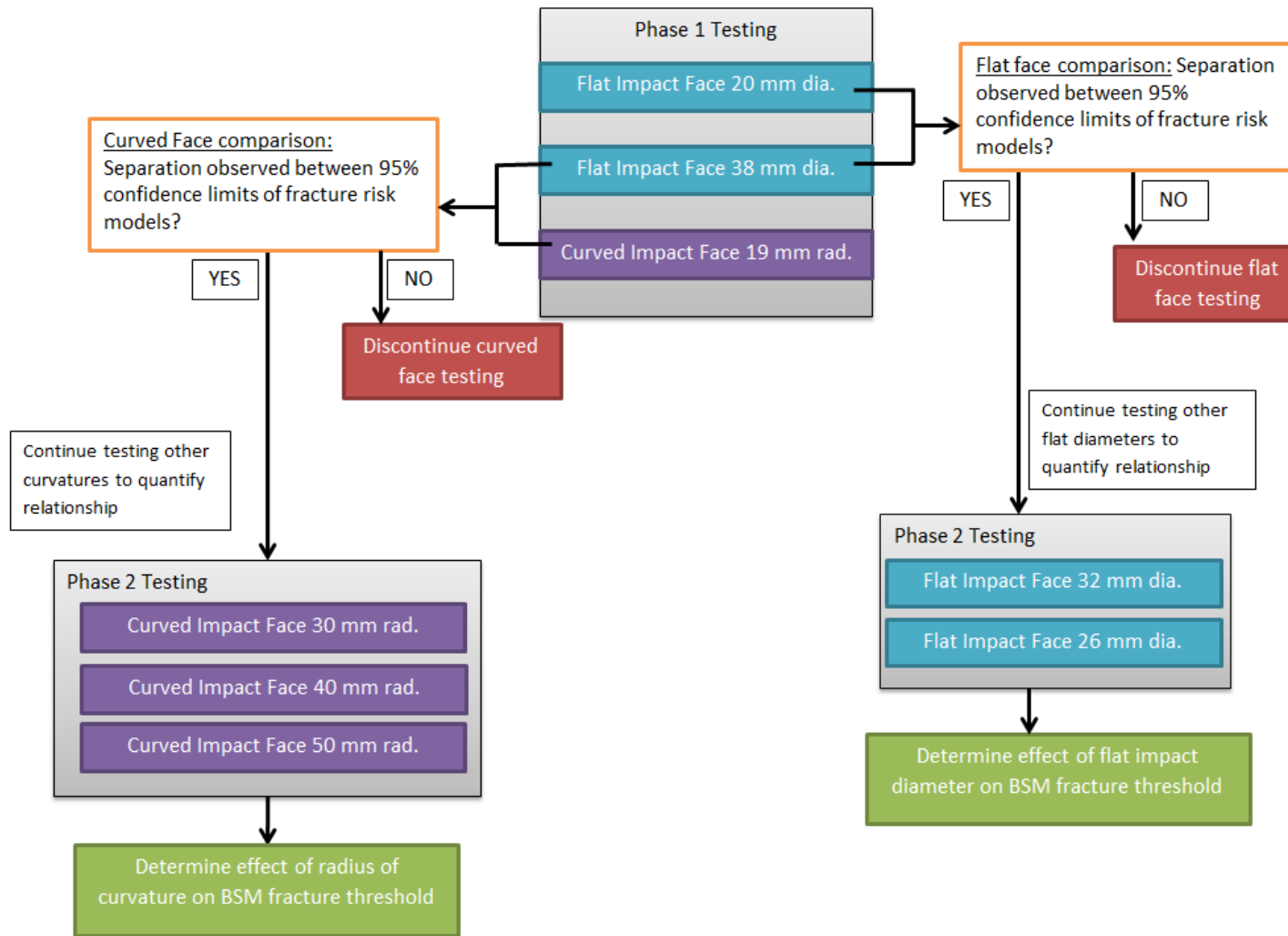


Figure 6.3: Decision process for investigation of eight different impact faces against BSM targets.

## 6.2.5 Data Collection

### 6.2.5.1 Projectile displacement

Force data can be calculated from acceleration, derived from double differentiation of projectile displacement over time. Therefore, the projectile was covered with a high contrast pattern (Figure 6.4) to enable quantification of the displacement through 2D DIC post processing analysis. The peak force measures calculated from the DIC and BDAS data were compared to determine whether DIC could be used to provide accurate force measures should the BDAS fail, or as an alternative to the instrumented projectile to obtain impact parameters in future investigations.



Figure 6.4: Projectile with high contrast pattern applied to the outer surface of the shell.

### 6.2.5.2 Projectile velocity

Projectile velocity was calculated from the HSV camera images. This was achieved by using a calibrated image of the area in front of the BSM target to measure the projectile position at two points in time. Calibration was achieved using a meter rule within the field of view to identify the actual distance travelled in relation to the image pixel size. The errors associated with frame rate and image calibration were combined to determine a 10% maximum error in velocity measurement. However, this HSV method has previously been empirically compared to projectile velocities obtained using a light gate system (0.45%

calculated error) (G. James, personal communication). There was less than a 10% difference between the two methods of measuring velocities. Therefore, the human error associated with the HSV based measurement appears to be lower than expected. The HSV method of velocity measurement applied within this study is likely to determine projectile velocities with a maximum error of 5%.

#### **6.2.5.3 Fracture Classification**

Investigation of each BSM post impact was undertaken by visual inspection of the impact area. Once the external surface had been photographed, the 10 mm thick gelatin and chamois layers were removed to expose the impacted area of bone. A visual inspection of the bone was made and a fracture classification assigned using the same scale reported in section 4.2.4.3. Due to the flat homogeneous nature of the impact area and the removal of the gelatin, it was unlikely that any fractures detectable by the unaided human eye would have gone unnoticed. In some cases the backing gelatin was also removed to investigate the fracture pattern in more detail, to inform the fracture classifications. To ensure consistency across all the tests, the fracture classification was determined in consultation between members of the trials team.

#### **6.2.5.4 Impact Acceleration**

Within the instrumented projectiles, each BDAS contained a uniaxial PCB Piezotronics accelerometer, with a range of  $\pm 21,000$  g. Acceleration data was collected at a rate of 103.4 kHz for an event of 6448 samples. Filtering of the data was achieved within the system using a 4-pole anti-aliasing Bessel filter with a cut-off frequency of 15 kHz.

Pre and post firing, each projectile was connected to the BDAS Data Retrieval Program (version 10.0.27211) on a Windows-based PC. This enabled data capture parameters to be set and data to be downloaded. A trigger level of  $9.8 \times 10^3 \text{ m}\cdot\text{s}^{-2}$  (1000 g) was used for all

firings. Any offset observed in the accelerometer reading was adjusted to achieve an acceleration measure of  $0 \text{ m}\cdot\text{s}^{-2}$  at rest. Acceleration and time data was exported post impact in .csv format before the projectile was re-set for the next firing.

In terms of accuracy, the BDAS system was reported to have a non-linearity of  $\pm 1\%$  and an accuracy of  $\pm 1\%$  of the full scale. This corresponds to an error of  $\pm 2.1 \times 10^3 \text{ m}\cdot\text{s}^{-2}$ . Therefore, peak force calculations based on the acceleration measures of the heaviest projectile will have a maximum error of  $\pm 220 \text{ N}$ . However, the forces calculated within this investigation were in the order of kN. Therefore, the effect on any findings is likely to result in maximum errors between 11% and 3% for peak forces of 2 kN and 7 kN respectively.

## **6.2.6 Data Analysis**

### **6.2.6.1 BDAS**

The acceleration data for each impact was processed using a FAMOS (imc Measurement and Control 2011) signal analysis software script (Appendix G). As part of this processing the data was filtered with a 4300 Hz cut-off frequency. The filtering applied to the acceleration data was the same as Raymond (2008) used for cadaveric testing. Therefore the data can be compared.

Using the acceleration and mass of the projectile, peak force was calculated. Peak acceleration, peak force and time to peak force were recorded for each impact.

### **6.2.6.2 Two-dimensional DIC**

The HSV images were imported into ARAMIS (GOM Optical measurement techniques 2011) DIC software for processing. Analysis of the images provided a displacement over time profile for the projectile during each impact. The deceleration profile of the projectile

was calculated by double differentiation of the displacement-time curve. This process was achieved within FAMOS signal analysis software, where a filter of 4300 Hz cut-off frequency was also applied to the data (Appendix H). The acceleration data was then used with the projectile mass to calculate the impact force. Peak force was recorded for each impact to enable comparison with the BDAS force measures.

### **6.2.6.3 Statistical Methods**

The *brglm* (Kosmidis *et al.* 2010) was used to conduct a probit analysis of the experimental data. As reported in the BSM construction study in Chapter 4, the *brglm* provides a number of benefits over other probit analysis methods. Therefore this model was used within R statistical software (R Core Team 2012) to analyse the BSM fracture outcomes. Statistical analysis was initially undertaken during testing. Probit analysis (Finney 1952) was conducted after each impact, using the impact velocity and fracture outcome for the test data associated with the same impact face. The calculated  $V_{50}$  and 95% confidence limits were used to inform the next impact velocity; impact velocities were focused around the  $V_{50}$  whilst attempting to obtain equal numbers of fracture and non-fracture outcomes. Extreme impact velocities were also tested to expand the range of velocities tested.

On completion of testing, the *brglm* (Kosmidis 2013) was used within R statistical software (R Core Team 2012) to conduct a probit analysis on all the data obtained for the different projectile faces. The parameters of projectile face, impact velocity, peak impact force, bone thickness and BSM mass were investigated in terms of fracture outcome. Similarly to the analysis reported in chapter 4, a step-wise approach was used to determine the factors affecting fracture outcome.

Finally, comparison of the peak force measures calculated from the DIC and BDAS data was carried out using a Welch two sample t-test (Welch 1947) within R statistics software. The Welch two sample t-test is an appropriate t-test for comparing two sets of data with

different ranges, identified as having un-equal variance (Welch 1947). This analysis was undertaken to determine whether DIC could provide a suitable alternative for assessing impact force. Use of DIC instead of the instrumented projectile could simplify the firing process and enable use of a wider range of projectile sizes and masses in future investigations.

## **6.3 Results**

### **6.3.1 Phase 1 testing**

Initial testing used the three extreme projectile faces to impact 87 BSMs. The remaining 3 of the desired 90 BSMs were removed from the study due to air bubbles between the lateral (non-impact) surface of the scapula and the backing gelatin. Separate probit analyses produced a probability of fracture curve as a function of the impact velocity for each projectile face tested (Figure 6.5 and Figure 6.6).

The shape and gradient was similar for the three curves. Therefore the probability of fracture varied in a similar way, around a threshold value of impact velocity. However, the threshold velocity at which fractures occurred was different (Table 6.3). The probit models showed that the 20 mm diameter flat impact face caused a 50% probability of fracture at a velocity of  $20.8 \text{ m}\cdot\text{s}^{-1}$  (Table 6.3). This was 33% slower than the impact velocity calculated from the 38 mm diameter flat impact data ( $29.8 \text{ m}\cdot\text{s}^{-1}$ ). Similarly, there was a 36% difference determined between the  $V_{50}$  values calculated for the 38 mm flat ( $29.8 \text{ m}\cdot\text{s}^{-1}$ ) and 19 mm radius of curvature ( $19.1 \text{ m}\cdot\text{s}^{-1}$ ) probit models (Table 6.3).

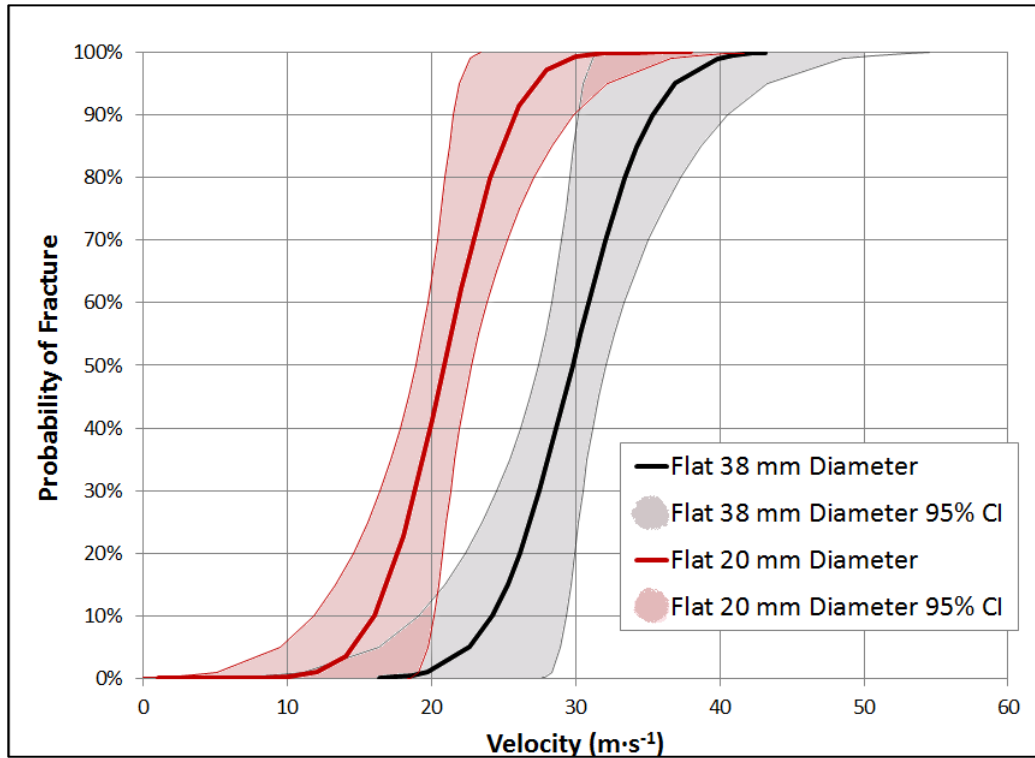


Figure 6.5: Probability of fracture with associated Confidence Intervals (CIs) as a function of projectile velocity for flat faced circular projectiles striking BSM.

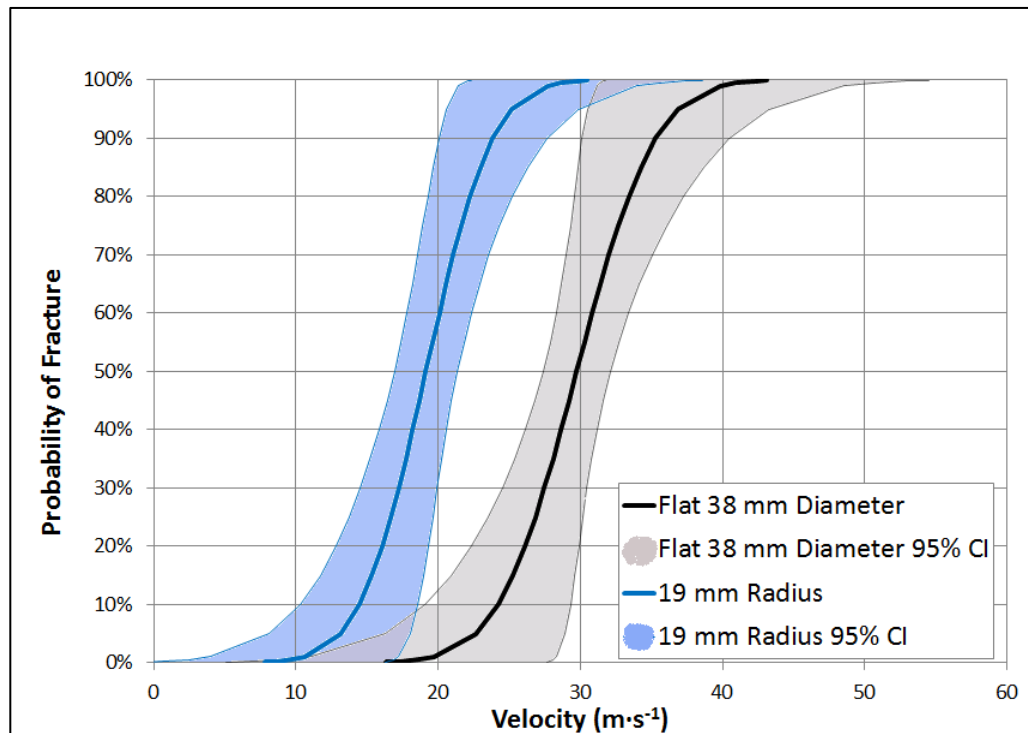


Figure 6.6: Probability of fracture with associated Confidence Intervals (CIs) as a function of projectile velocity for curved projectile impact faces striking BSM.



Projectile face	Impact velocity for 50% probability of fracture (m·s <sup>-1</sup> )	95% Confidence Interval (± m·s <sup>-1</sup> )
38 mm diameter flat	29.8	2.3
20 mm diameter flat	20.8	2.2
19mm radius of curvature	19.1	2.2

**Table 6.3: Impact velocities associated with BSM fracture for different projectile faces.**

The 95% Confidence Intervals (CIs) showed a similar pattern across the three probit curves (Figure 6.5 and Figure 6.6), showing that the fit of the data to the brglm was similar across the three datasets. The difference observed between the probit models and associated 95% confidence intervals highlighted that the projectile faces had caused a change in the impact velocities, affecting fracture of the BSMs. Therefore, in line with the testing schedule given in section 6.2.4, the remaining five projectile faces were tested. The aim was to obtain greater resolution in the data to support the quantification of the effects of flat diameter and curvature on BSM fracture outcome.

## 6.3.2 Phase 2 testing

### 6.3.2.1 Effect of projectile face on BSM fracture outcome

A total of 234 BSMs were impacted with instrumented projectiles fitted with one of the eight different impact faces. Not all of the test groups contained the desired 30 impacts (a total of 240 tests) due to some BSMs having air bubbles behind the impact area of the bone. As previously discussed, these models were omitted from testing.

The instrumented projectile successfully collected impact acceleration for 224 of the 234 BSM impacts; the remaining 10 tests were not collected due to intermittent or catastrophic failure of the BDAS. The 2D DIC analysis was not able to provide accurate peak force measures for the tests associated with BDAS failure.

The result of each individual BSM impact is documented in Appendix I. BSMs tested with the same projectile face were grouped together and used to calculate average measures of BSM mass, and bone thickness (Table 6.4). Approximately half of the BSMs tested within each group resulted in a fracture outcome. Across the groups, the BSM targets that were tested had an average target area thickness of  $3.7 \pm 0.2$  mm (5% variability) and an average mass of  $4.35 \pm 0.35$  kg (8% variability). In terms of biological variation, they were considered to be sufficiently similar to enable comparisons across the groups.

Projectile Face (mm)	Projectile Mass (g)	Total BSMs Tested	Number of Fracture Outcomes	Avg. Bone Thickness (mm)	Avg. BSM Mass (Kg)	V <sub>50</sub> (m·s <sup>-1</sup> )	95% Confidence Limit (m·s <sup>-1</sup> )
Flat 38 diameter	104.9	28	14	3.8	4.0	29.8	2.3
Flat 32 diameter	103.9	30	13	3.6	4.4	27.3	1.8
Flat 26 diameter	102.8	29	15	3.9	4.5	23.9	3.1
Flat 20 diameter	104.5	30	16	3.7	4.4	20.8	2.2
19 radius of curvature	105.8	29	16	3.7	4.2	19.1	2.2
30 radius of curvature	106.1	28	13	3.5	4.7	22.5	2.6
40 radius of curvature	103.7	30	15	3.5	4.4	30.2	2.1
50 radius of curvature	103.9	30	16	3.8	4.3	27.5	3.1

**Table 6.4: Findings from impacting BSMs with eight different projectile faces.**

Details of how the bone thickness and mass of each BSM were measured can be found in Annex A.

### 6.3.2.2 Significance of impact diameter and curvature on BSM fracture outcome

The parameters of projectile face, BSM mass, bone thickness, impact velocity, peak force and fracture outcome for all 234 BSMs were collectively analysed using the brglm. Impact velocity and peak force showed such a strong relationship to each other that it masked the other interactions within the data. Therefore an initial analysis was undertaken to investigate the parameters of projectile face, BSM mass, bone thickness, impact velocity, and fracture outcome.

At the 95% confidence level ( $p < 0.05$ ), BSM mass was not identified to affect fracture outcome within this dataset ( $p = 0.46$ ). This is likely to be due to the similarity between the

BSMs and across the groups. Therefore the initial statistical analysis was re-run, investing the dataset for statistical differences due to projectile face, bone thickness, impact velocity and fracture outcome only. A second analysis was undertaken to investigate the effect of peak force. The parameters of projectile face, bone thickness, and fracture outcome were also considered in conjunction with peak force. In both analyses, the probit model associated with the 38 mm projectile face was used as a baseline for comparison with the models developed for the other seven projectile faces.

At the 95% confidence level ( $p < 0.05$ ) there was evidence that the probit models based on the 26 and 20 mm flat diameter projectile data were different to the 38 mm flat diameter probit model (Table 6.5). Similarly, there was evidence of a difference between the 19 and 30 mm radius of curvature faces when compared to the 38 mm flat diameter model (Table 6.5). Conversely, at the 95% confidence level ( $p < 0.05$ ) there was no evidence of a statistical difference between the probit models based on the 32 mm flat diameter, 40 and 50 mm radius of curvature faces compared to the 38 mm flat diameter probit model (Table 6.5).

<b>Projectile Face</b>	<b>p value</b>	<b>Evidence of significance at the 95% confidence level (<math>p &lt; 0.05</math>)</b>
Flat circular 32 mm diameter	0.260	
Flat circular 26 mm diameter	0.001	**
Flat circular 20 mm diameter	0.000	***
19 mm radius of curvature	0.000	***
30 mm radius of curvature	0.005	**
40 mm radius of curvature	0.573	
50 mm radius of curvature	0.148	

**Table 6.5: Statistical analysis of BSM fracture response by different projectile faces in terms of impact velocity and bone thickness.**

The analysis considered the parameters of projectile face, bone thickness, impact velocity and fracture outcome. The outputs are a comparison to a probit model based on a 38 mm flat faced diameter dataset. Evidence of a significant difference at the 95% confidence level ( $p < 0.05$ ) is identified by a \*, with greater significance shown by an increasing number.

The relationships between each of the projectile face datasets were investigated through a series of pairwise comparisons. This was undertaken to determine the significance of the differences observed across the complete dataset. The models associated with the 20 mm diameter and 19 mm radius of curvature projectiles showed evidence of statistically significant differences with the larger diameter and curvature projectile faces (Table 6.6). Based on the differences observed between the models based on the 19 mm radius of curvature and the 38 mm flat diameter and 40 mm radius of curvature datasets (Table 6.5 and Table 6.6), it would be expected that the 19 mm radius of curvature would also be statistically different to the 50 mm radius of curvature. However, there is no evidence of a statistically significant difference between these two projectile faces ( $p=0.171$ ).

<b>Projectile faces compared</b>	<b>p value</b>
20 mm diameter and 32 mm diameter	0.008
20 mm diameter and 40 mm radius of curvature	0.002
20 mm diameter and 50 mm radius of curvature	0.031
19 mm radius of curvature and 40 mm radius of curvature	0.015

**Table 6.6: Comparisons of probit models produced using BSM impact data against different projectile faces in terms of impact velocity and bone thickness. Evidence of a statistical difference at the 95% confidence level ( $p<0.05$ ) has been identified for analysis considering the parameters of projectile face, bone thickness, impact velocity and fracture outcome.**

Across the eight projectile faces tested there was also statistical evidence that the parameters of impact velocity, bone thickness and impact force affected individual BSM fracture outcomes (Table 6.7). A relationship between impact velocity and bone thickness was determined in terms of fracture outcome; BSMs with very thin bones were likely to fracture at the lowest velocities used. Alternatively, the BSMs with the thickest bones only fractured if a high impact velocity was used. These parameters were expected to affect fracture outcome based on engineering principles and review of the literature associated with investigations into cranial fracture thresholds (section 3.4.2.2).

Peak impact force was determined as a key parameter affecting BSM fracture outcome (Table 6.7). However, at the same impact velocity, higher forces were recorded for non-fracture outcomes when compared to fracture outcomes. For example, when using the 50 mm radius of curvature projectile, impact velocities of approximately  $24 \text{ m}\cdot\text{s}^{-1}$  were associated with a peak force of 4.3 kN for a non-fracture outcome when compared to a peak force of 2.6 kN for a fracture outcome. This was observed across all of the projectiles tested, and could suggest a statistical relationship of decreasing probability of fracture when impact force is increased. This is converse to the actual physical relationship that the probability of fracture increases as the impact force increases. Therefore it was determined that fracture predictions based on the force data were not appropriate to quantify the effect of impact face diameter and curvature on cranial fracture outcome.

Parameter	p value	Evidence of significance at the 95% confidence level ( $p < 0.05$ )
Impact velocity	0.000	***
Avg. Bone Thickness	0.002	**
Impact velocity & Avg. Bone Thickness	0.037	*
Peak Impact Force	0.000	***

**Table 6.7: Parameters identified to affect BSM fracture outcome, determined through statistical analysis.**

Evidence of a significant difference at the 95% confidence level ( $p < 0.05$ ) is identified by a \*, with greater significance shown by an increasing number. This analysis considered the parameters of impact velocity, projectile mass, model mass, bone thickness, peak impact force and fracture outcome to determine whether factors other than projectile face had an effect on the fracture response of the BSM,

### **6.3.2.3 Quantification of projectile diameter and curvature effects on BSM fracture outcome**

The effects of flat diameter and curvature on fracture outcome were quantified separately. Using the probit analysis, a  $V_{50}$  was obtained for each of the projectile faces tested. The 95% confidence limits associated with each  $V_{50}$  were also included. This provided a measure of the uncertainty associated with each  $V_{50}$ . The velocities were then plotted

against either the flat diameter (Figure 6.7) or the inverse radius of curvature (Figure 6.8). Reporting by inverse curvatures enabled the inclusion of the flat faced 38 mm diameter projectile within a suitable scale.

A linear relationship was identified between flat impact diameter and  $V_{50}$  (Figure 6.7). The equation associated with the relationship could be used to predict the  $V_{50}$  for a range of flat circular diameters. This will be most reliable within the range of the diameters tested, becoming increasingly unreliable as it is extrapolated.

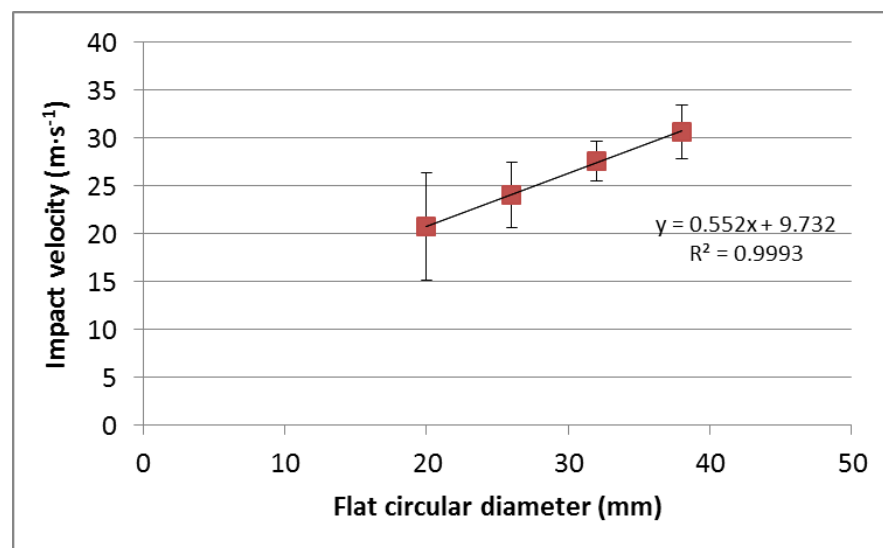


**Figure 6.7: Effect of impact diameter on the impact velocity required to cause a 50% probability of BSM fracture. Data obtained using a flat faced aluminium projectile with a mass of approximately 103 g. The 95% confidence limits are presented for each projectile diameter tested. The black line with associated equation and  $R^2$  value represents a linear relationship within the data.**

For the  $V_{50}$  values associated with the inverse radius of curvatures (Figure 6.8), the relationship also appears to be linear. However, the  $R^2$  value of 0.88 and hence fit of the data is not as good as the linear relationship for comparing fracture outcomes associated with flat circular diameter projectiles (Figure 6.7), with an  $R^2$  value of 0.99. In particular, the data for a curvature of 40 mm radius appears to be higher than expected for the linear relationship identified.

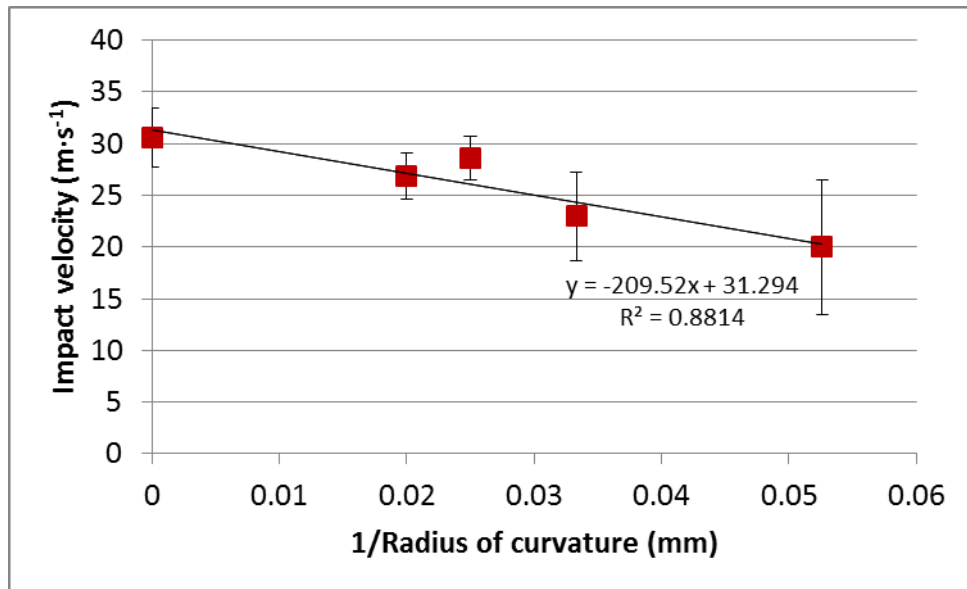


**Figure 6.8: Effect of inverse radius of curvature on BSM  $V_{50}$ .**

Data obtained using an aluminium projectile with a mass of approximately 103 g. The 95% confidence limits are presented for each impact curvature tested. The blue dotted line represents a potential bilinear relationship within the data.

### 6.3.3 DIC

DIC analysis was possible for 217 of the 234 firings; the remaining 17 firings were associated with HSV images which could not be analysed using DIC due to shadowing of the projectile by the BSM. In these cases the larger fin of the scapula either blocked the view of the projectile or the light required to adequately see the projectile on impact.

The displacement time curves were used to calculate the peak force of the projectile (Figure 6.9). In some cases it was challenging to identify the peak force from the processed DIC data due to the noise in the displacement time curve being amplified through double differentiation (Figure 6.10).

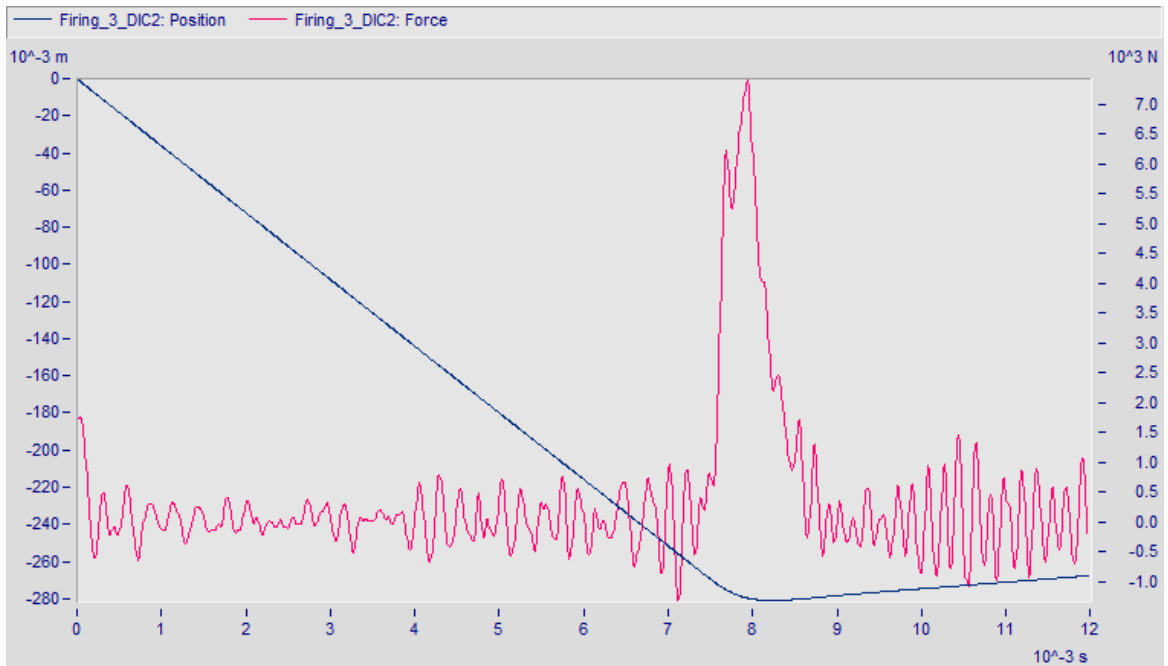


**Figure 6.9: Displacement curve (blue) obtained from DIC analysis using ARAMIS software and calculated force profile (red), shown within FAMOS signal analysis software.**

**Firing #3 against BSM #5 using a 38 mm diameter flat circular projectile face.**

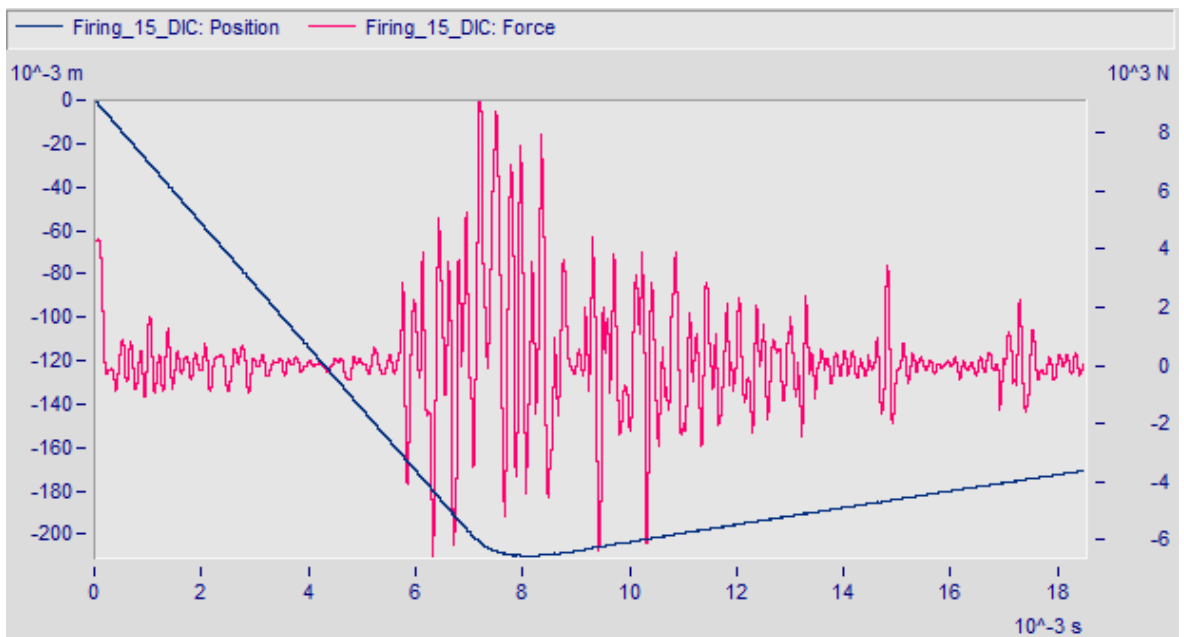


**Figure 6.10: Noise amplified within a force profile (red), which was calculated from a displacement curve (blue) of a projectile.**

**Firing #15 against BSM #7 using a 38 mm diameter flat circular projectile face. The displacement curve was obtained from DIC analysis using ARAMIS software, and the force profile was calculated within FAMOS signal analysis software. The figure is extract from FAMOS.**



The peak forces obtained from DIC analysis were in the range of 1.0 kN to 15.4 kN, with a mean of 5.3 kN. However, there was an outlier, calculated at 51 kN, due to noise in the displacement curve at the time of impact. It is unlikely that the 51 kN value is representative. Therefore, it was not considered further.







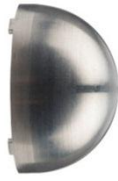
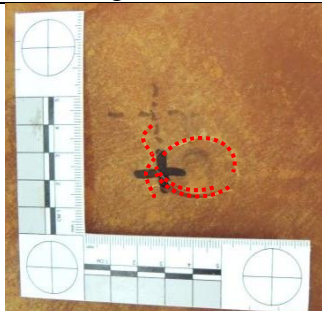
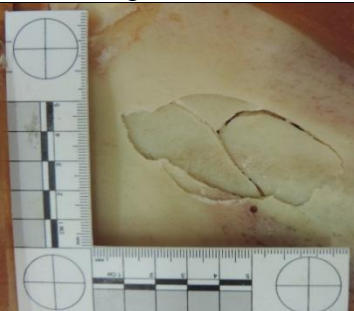
Calculation of peak force from the BDAS acceleration measures produced a range of forces from 1.7 kN to 9.5 kN with mean of 4.4 kN. The DIC method of calculating peak force produced a wider range of peak force values compared to forces calculated from the BDAS accelerometer. Application of the Welch Two-Sample t-test identified that there was evidence at the 95% confidence level ( $p < 0.05$ ) of a statistical difference between determining peak force using DIC and the BDAS projectile ( $p = 0.011$ ). The force measures obtained by the two different methods did not correlate to each other.

In comparison to the post processing and noise amplification associated with the DIC method, the BDAS provides a direct measure of acceleration using a calibrated accelerometer. Therefore, the accelerations obtained from the BDAS were used to calculate impact force for each BSM impact.

#### **6.3.3.1 Fracture Outcome**

Examination of the BSMs post impact determined the fracture outcome and level of severity. For the same fracture classification, different patterns of fracture and damage to the chamois and gelatin layers were observed due to the impact face of the projectile (Figure 6.11). Impacts causing a depressed, detached fracture (fracture index 4) showed no visible lacerations to the chamois leather when using the 38 mm diameter flat projectile face; however, the 20 mm diameter flat face impacts caused cutting of an arc around the edge of the impact face, whilst the hemispherical face caused star like damage (Figure 6.11). The 32 mm diameter and 50 mm radius of curvature faces produced impact patterns aligned with the 38 mm diameter flat face. There was a gradual transition to the patterns

observed for the smallest flat diameter (20 mm) and curvature (19 mm radius) as the projectile faces decreased in diameter and radius of curvature. Damage to the chamois leathers and underlying gelatin generally only occurred in association with fracture outcomes. In non-fracture outcomes, ink transferred from the projectile to the outer chamois leather was often the only evidence of an impact.

Projectile Face	Impact Surface	Fracture Pattern
 <p data-bbox="357 882 620 913">38 mm diameter flat</p>	 <p data-bbox="772 882 1007 913">Firing # BSM #12</p>	 <p data-bbox="1171 882 1406 913">Firing # BSM #12</p>
 <p data-bbox="357 1229 620 1261">20 mm diameter flat</p>	 <p data-bbox="772 1229 1007 1261">Firing # BSM #67</p>	 <p data-bbox="1171 1229 1406 1261">Firing # BSM #67</p>
 <p data-bbox="320 1581 663 1612">19 mm radius of curvature</p>	 <p data-bbox="772 1581 1007 1612">Firing # BSM #37</p>	 <p data-bbox="1171 1581 1406 1612">Firing # BSM #37</p>

**Figure 6.11: Depressed, detached fractures (Fracture index 4) observed to BSMs as a result of impacts from different projectile faces.**

The black cross was used for alignment pre-impact. The actual impact location was identified by the black ink circle, transferred from the projectile face. The red dotted lines highlight laceration of the chamois layers.

Observation of depressed, detached fractures caused by the different projectiles (Figure 6.11) has shown that fractures due to impacts from the 20 mm diameter flat and 19 mm

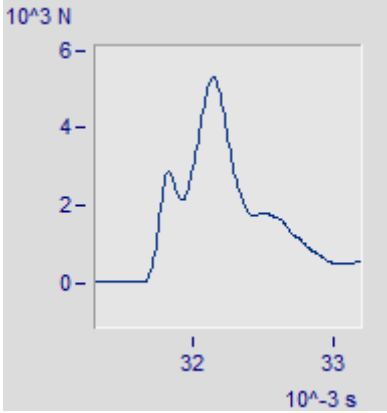
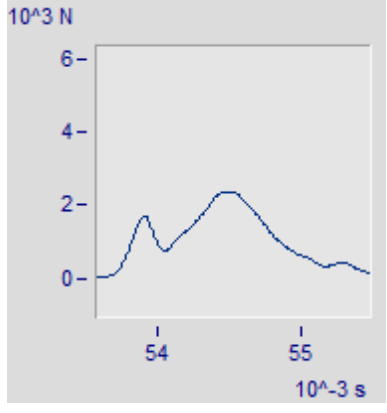
radius of curvature faces radiate from a central point; this is due to the smaller contact area of these projectile faces, and hence a more focused application of force. The fracture patterns associated with the 38 mm radius of curvature impact were less clearly defined, as a result of the increased area over which the force was applied.

In terms of the total fracture area, the depressed, detached fractures caused by the 38 mm diameter flat faced projectile were generally elliptical in shape (Figure 6.11). This was due to anisotropy in the scapula. Conversely, the 20 mm diameter flat and 19 mm radius of curvature faces caused more irregular shaped fractures.

The pitch and yaw of the projectile was not measured within this study, however, yaw of the projectile could be observed within some of the HSV images. The vast majority of impacts were observed to be normal to the BSM surface (233 of the 234 impacts). This is likely to be due to the small distance of free air flight between the end of the gun barrel and the target. In the one case, the projectile yaw was approximately 30 degrees, occurring at a projectile velocity of  $14.7 \text{ m}\cdot\text{s}^{-1}$  (firing #140); this was associated with a non-fracture outcome (Appendix I). Overall, in this study it was considered unlikely that yaw of the projectile affected the fracture outcomes.

#### **6.3.3.2 Impact force profiles**

Peak force was calculated from the impact acceleration profile to enable comparison to the cadaveric data reported by Raymond (2008). However, irrespective of whether fractures occurred or not (Figure 6.12), variation in the complete force profiles could be seen between the different projectile faces (Figure 6.13). The force profile was expected to have a smaller initial peak as the projectile contacted the chamois leather and compressed the gelatin, prior to a larger peak produced by the resistance of the bone. However, this pattern was not consistent across the different groups (Figure 6.13).

Fracture Outcome	Non-fracture Outcome
 <p>The graph shows force in <math>10^3</math> N on the y-axis (0 to 6) and time in <math>10^{-3}</math> s on the x-axis. The x-axis has markers at 32 and 33. The force profile shows an initial peak of approximately 3 at 32 ms, followed by a much larger peak of approximately 5.5 at 33 ms, then a gradual decay.</p>	 <p>The graph shows force in <math>10^3</math> N on the y-axis (0 to 6) and time in <math>10^{-3}</math> s on the x-axis. The x-axis has markers at 54 and 55. The force profile shows a peak of approximately 1.8 at 54 ms, followed by a larger peak of approximately 2.5 at 55 ms, then a gradual decay.</p>
<p>Flat 32 mm diameter (Firing #157 BSM #142 velocity <math>28.6 \text{ m}\cdot\text{s}^{-1}</math>)</p>	<p>Flat 32 mm diameter (Firing #159 BSM #146 velocity <math>13.8 \text{ m}\cdot\text{s}^{-1}</math>)</p>

**Figure 6.12: Force profiles for fracture and non-fracture outcomes for impacts with a 32 mm diameter flat projectile.**

The signals are observed within FAMOS (imc Measurement and Control 2011) signal analysis software. All x-axes are in  $\times 10^{-3}$  s and the y-axes in  $\times 10^3$  N.

Impacts from the 38 mm flat circular face and the 50 mm radius of curvature showed the expected pattern of an initial peak followed by a much larger peak (Figure 6.13). However, as the impact face became smaller in diameter (in the case of flat) or had a smaller radius of curvature, the force profile showed a third peak occurring after the largest peak (Figure 6.13). As this third peak increased, the first peak appeared to reduce and was not present in the 20 mm diameter flat face or the 19 mm radius of curvature impacts (Figure 6.13).

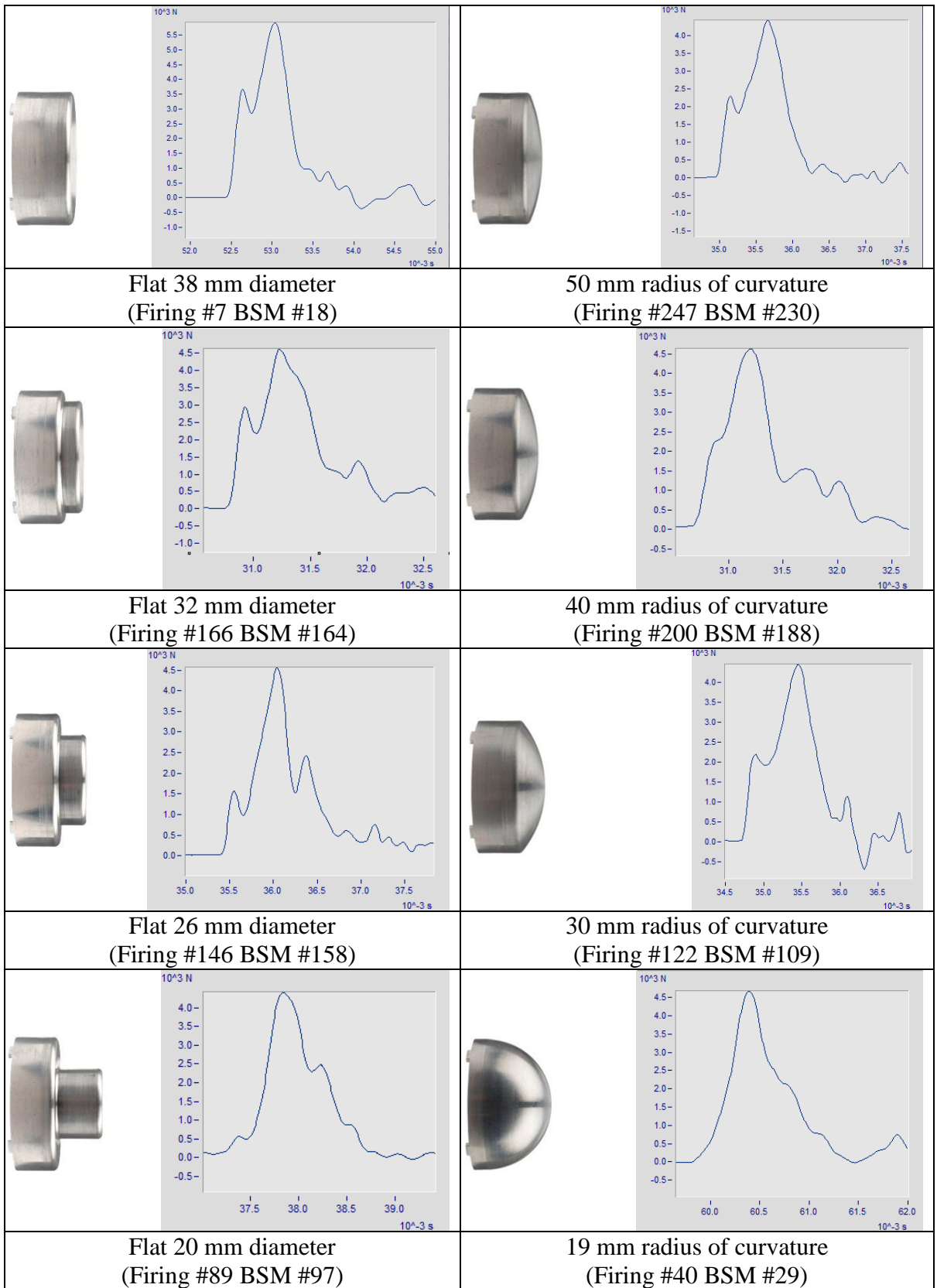


Figure 6.13: Force profile shapes observed from FAMOS (imc Measurement and Control 2011) signal analysis software.

The profiles correspond to different projectile faces used to impact BSM targets. The profiles are representative of the projectile used, irrespective of the occurrence of a fracture. All x-axes are in  $\times 10^{-3}$  s and the y-axes in  $\times 10^3$  N.

## **6.4 Discussion**

### **6.4.1 Effect of projectile face on fracture outcome**

Curvature and flat impact diameter were found to have an effect on BSM fracture outcome and, would appear to be important factors to consider in accurately predicting cranial fracture outcomes. For the range of projectiles tested,  $V_{50}$  showed a linear relationship as the best fit for flat projectile diameter and inverse radius of projectile curvature.

These relationships can be used to obtain  $V_{50}$  values associated with a range of projectile diameters or curvatures; interpolation and extrapolation can provide the expected fracture response for impact diameters and curvatures beyond those tested in this study. However, there are limits to how far the relationships can be extrapolated; at the lower end of the scale, it would be expected that the relationship would become non-linear as the impact moves away from the diameters associated with blunt impact (section 2.5.1.1). Therefore, the curve is unlikely to be applicable beyond this limit. It is also unlikely that the relationship can be extrapolated beyond a certain upper limit, dependent on the shape and area of the bone under test. Where the projectile impact face extends beyond the contact area of the bone, increases in the diameter would no longer affect the contact area between the bone and the projectile. Therefore, as the projectile diameter extends beyond this limit, the fracture response of the bone is unlikely to change. This would be shown by the linear relationship plateauing at larger flat diameters. This expected limit does not appear to have been reached within the BSM study; further testing with larger projectile faces would be needed to determine the limit for impacting BSMs. However, the limit is expected to vary for impacts to different regions of the head due to the varying curvatures of the cranium.

Similarities were found between the fracture responses associated with the 38 mm diameter flat projectile face and the curved projectiles of a 40 mm radius and greater. This

relationship may suggest that fracture risk curves developed using flat projectiles could also be relevant to curved impacts of a 40 mm radius of curvature or more. However, the projectiles were tested against an approximately flat area of bone. The interaction between the projectile face and the bone geometry is likely to affect the fracture response. Therefore further investigation would be required to determine if the relationships are applicable to curved areas of bone such as the frontal and occipital regions.

Similarities between BSM fracture responses were found between the flat face diameters and corresponding curvature tests, for example the smallest diameter flat (20 mm) and smallest radius of curvature (19 mm), or the second smallest faces of 26 mm diameter flat and 30 mm radius of curvature. It was considered that the similarities are likely to be due to the contact area rather than the shape of the projectile. However this cannot be investigated from the data as there was no method for measuring the area of the curved faces engaging with the BSM at any particular point in time. The only information available is that the 19 mm radius of curvature would have the largest surface area. However, the proportion of the face contacting the bone would be expected to be much less than the surface area; any curve impacting an approximately flat surface would suggest a point loading. Therefore the fracture response calculated for each projectile face cannot be compared by surface area as this is unlikely to be a representative measure of the contact area.

The fracture responses of the BSMs were statistically different at the 95% confidence limit for the tests using the 19 mm radius of curvature when compared to the 40 mm radius of curvature and 38 mm diameter flat (infinite radius of curvature) projectiles. However, there was no statistical difference at the 95% confidence limit determined between the fracture responses associated with the 19 mm radius of curvature and 50 mm radius of curvature model. This is converse to the expected outcome. Based on the pattern observed for the  $V_{50}$  values (Figure 6.8), the BSMs tested with the 50 mm radius of curvature fractured at lower

impact velocities than would have been expected. Alternatively, the data for the 40 mm radius of curvature appeared to be higher than expected for the linear relationship identified. The reason for this variability is unclear. The BSMs tested were not different to the BSMs used to test the other impact faces; average bone thickness, average BSM mass and the projectile mass were all comparable to the other projectiles tested. Therefore it is assumed that the deviation is due to the interaction of a number of variables affecting the individual BSM outcomes. The tests using the 50 mm and 40 mm radius of curvature projectiles could be repeated to determine whether the results are an anomaly. However, based on the findings for the other projectile faces, further data is unlikely to change the overarching relationships determined between BSM fracture response and projectile curvature.

#### **6.4.2 BSM Target**

Bovine scapulae were obtained in a single batch, limiting variability in cattle age and butchering processes across the targets. There was no selection process applied during production or testing. However, the variability of the BSMs tested was similar for each different projectile. Therefore the differences observed to fracture outcome are due to the projectile faces and not the natural variability of the BSMs.

As BSMs with an inadequate gelatin backing were removed from testing, some projectile faces were not tested against the desired 30 BSMs. However, the lowest number of data points for a single impact face was 28. This was double the cadaveric dataset of 14 impacts obtained by Raymond (2008). Therefore, the BSM datasets have increased statistical power when compared to Raymond's dataset, resulting in increased confidence that the BSM findings reflect the expected fracture outcomes.

Based on macroscopic examination the BSM fracture outcomes were identified across the full scale of severity. The overall length and width of the fracture areas was similar for



individual projectile faces; this was also consistent across all of the different impact faces tested. The similarity in overall dimensions of the fractured area may be due to the maximum diameter of the projectile being 38 mm. Alternatively, the fracture area may be due to the geometry of the bone; the impact area is surrounded by bone of increasing thickness, so the failure may be due to the transition to thicker bone.

Increased granularity of the fracture outcome was obtained when compared to the fracture outcomes reported by Raymond (2008). Therefore, investigation of the force and velocity measures compared to the fracture severity may provide additional information relating to cranial fracture thresholds. Based on the literature reviewed within section 3.4, this has not been investigated previously. However, the fracture severities were not investigated further, falling outside of the scope of this study.

All of the BSMs had a 10 mm thick layer of gelatin and two layers of chamois leather over the impact area. This provided some representation of scalp tissue. The damage observed to the gelatin and chamois leather layers varied depending on the projectile face (Figure 6.11). The 20 mm diameter and 19 mm radius of curvature faces had a cutting effect on the chamois layers, which was not observed for the 38 mm diameter flat impacts for the same fracture severity. It is expected that the chamois and gelatin layers play a role in the absorption of impact energy. Raymond (2008) identified the thickness of the scalp to affect the fracture outcome within cadaveric testing. Further work would be required to fully understand the role of scalp thickness in cranial fracture outcome.

### **6.4.3 Instrumented projectile**

Due to the individual construction of the projectiles their masses varied by  $\pm 1.7$  g (1.6%). This was due to variations in the quantity of wiring and glue used to mount the instrumentation in the housing, and small differences between the mass of the faces under

test. The variability in mass was controlled as far as possible within resourcing limits, machining the impact faces to control the mass of the complete projectile.

The calculation of peak force considers the mass of the projectile therefore, the peak force measures are comparable for the different projectiles. However, the  $V_{50}$  values may have been affected due to the energy of the projectile being proportional to its mass. Although, to achieve the same projectile energy for a mass varying by 1.6%, the difference in impact velocity would not need to be more than 1% in this study. Therefore, the relationships identified using impact velocities are likely to be representative.

Beyond the current study, the instrumented projectile system could be used in a range of other applications. For example, model calibration could be achieved by producing correlations between parameters such as force calculated from the projectile and force measured in the model. Additionally, the internal BDAS could be transferred into an alternative casing to support the assessment of other impacts, such as those from less-lethal impact rounds. Equally, if projectile housings akin to the material types, mass and responses of helmet BFD could be developed, this would allow interactions with an underlying head model to be defined. The aim of this would be to develop a better understanding of the response of the helmet material when contacting the head.

#### **6.4.4 Force profiles**

Different force profiles were observed for the different projectile faces tested. There was similarity between the range of flat diameters and curvatures tested, although there were differences between the largest and smallest projectile faces. This was principally the presence of an additional peak within the force profile either prior to or after the main impact

In cases where the flat circular diameters were less than the 38 mm diameter of the projectile, an additional third peak may be caused by impact of the widest part of the projectile contacting the target after the smaller face. This would cause a third smaller peak to occur after the main peak, representative of the time taken for the full projectile diameter to impact the BSM after the initial contact. However, this explanation cannot be applied to the curved faces as each curvature spanned the full projectile diameter (38 mm), but the same additional peak has been observed.

Alternatively, the additional peak could be due to the projectile interacting with the gelatin on the back of the BSM; where the gelatin would provide resistance to the projectile and cause a small peak in deceleration after the main peak caused by contacting the bone. However, this would only apply when the bone was fractured and would be likely to occur in all fractures. This was not the case.

Further investigation of the root causes of the different force profiles fell outside of the scope of this study. In order to understand the cause of the differing profiles the interaction between the projectile and target would need to be investigated further. Ideally the force profile would need to be synchronised to the HSV in addition to measures of strain and acoustic sensors to better understand the specific timings associated with each impact event.

Where it is not possible to directly measure impact diameter and/or curvature within a BHBT assessment method, it may be possible to differentiate between impacts based on differences in the profiles of the sensor signals. This would provide an alternative method to enable consideration of flat diameter and curvature effects within BHBT assessment. Although associated with high uncertainty, a prediction of BSM fracture response could also be determined if the impact was comparable to this study.

### **6.4.5 DIC**

The development of the instrumented projectile was a challenging process and failures during the trial affected the data which could be captured. Therefore an alternative method of calculating force data using DIC was sought should any limitations of the instrumented projectile become insurmountable.

Unfortunately there were also limitations with the 2D DIC method of calculating peak force measures: post processing took a considerable amount of time, and if the illumination of the projectile was not optimised on a firing then the HSV images were too dark to enable DIC analysis to be completed. Where the HSV images were suitable for DIC analysis, the process of differentiating the displacement curve amplified any errors, producing a very noisy signal. Therefore, it was difficult to determine the peak of interest. Due to these factors, the peak force measures obtained by DIC analysis did not correlate with the calibrated accelerometer within the BDAS. As a result, the peak force for each impact was calculated using the BDAS acceleration data.

This method of using DIC may be explored further in future studies due to the potential to collect impact parameters from any projectile, without the need for instrumenting the projectile itself. It may be the case that the HSV images could be optimised by improving the illumination of the projectile. The resolution of the images could also be increased to improve the displacement profile obtained.

## **6.5 Summary**

This work aimed to investigate the effect of different projectile faces on BSM fracture thresholds. Under blunt ballistic loading, flat face diameter and curvature have been identified as having a significant effect (at the 95% confidence level) on the fracture

outcome of BSMs. Differences in force profile, fracture pattern and damage to the chamois layers have also been found due to the flat face diameter and curvature of the impact face.

A linear relationship has been found as the best fit for BSM fracture response to impacts with a flat faced projectile and prediction of  $V_{50}$ ; where a 47% (18/38) reduction in flat projectile diameter has resulted in a 30% (9.0/29.8) reduction in  $V_{50}$ . For curved projectiles, a linear relationship was identified between inverse radius of curvature and  $V_{50}$  prediction.

To better predict fracture outcome from blunt ballistic impacts, flat face diameter and curvature of an impact should be measured in conjunction with peak force, impact velocity and bone thickness.

## Chapter 7: Determination of a cranial fracture risk model

### 7.1 Introduction

Projectile diameter and curvature have been found to have a statistically significant effect on BSM fracture thresholds, which has been quantified, as reported in section 6.3.2.3. In order to use this understanding to support the prediction of cranial fracture outcomes within BHBT assessment methods, cranial fracture risk curves must be developed. Therefore, the aim of this work was to use the BSM data (Appendix I) to develop fracture risk curves for varying impact face curvatures and flat face diameters. The data reported by Raymond (2008) was available to develop a comparable cranial fracture risk curve, providing validation of the BSM risk curve developed using the 38 mm diameter flat faced projectile.

A risk curve showing the effect of flat diameter or curvature in conjunction with peak impact force is required to support data collection from existing BHBT assessment methods (Bolduc *et al.* 2010, Barnes-Warden *et al.* 2013, Neale *et al.* 2013).

In conjunction with projectile face and peak force, the parameters of impact velocity and impact velocity in conjunction with bone thickness were also determined to be factors affecting fracture outcome (Section 6.3.2.2). Therefore, all of these parameters should be considered when predicting fracture outcomes. In addition, application of the data within existing criteria, such as the BC applied to helmet BFD by Hisley *et al.* (2010), may provide further insight into the suitability of the criterion within the assessment of BHBT.

Calculation of the BC was reported within the review of existing cranial fracture assessment methods (Section 3.3.5). The original BC developed by Sturdivan *et al.* (2004) was not applicable to the BSM data as it included a function of the cube-root of total body mass ( $M^{1/3}$ ), enabling scaling between different models or specimens; this is not applicable

to the BSM as they are not a scaled equivalent of a human head. Hisley *et al.* (2010) reported an alternative calculation of the BC where this function for target mass has been removed. Also, the BC was developed for predicting soft tissue injury. Although the parameters affecting bone fracture outcome may be similar, it is unlikely that the interactions will be the same. The more recent BC (Equation 7.1) is also not specific to cranial fracture outcome; however, Hisley implied fracture was considered in its development. Therefore, this method of calculating BC was applied to the BSM (Appendix I) and cadaveric (Raymond 2008) datasets.

$$BC = \ln \frac{E}{TD}$$

**Equation 7.1: Head specific Blunt Criterion reported by Hisley *et al.* (2010) to have been developed by Sturdivan in 2005.**

***E* is impact energy (J), *D* is the diameter of the flat circular projectile (cm) and *T* is the thickness of the cranium at the impact point (mm).**

## 7.2 Method

Probit analysis was undertaken using the using the `brglm` (Kosmidis 2013), providing a more accurate risk curve when compared to other previously used GLM analyses (Section 4.2.5.1). The `brglm` is based on a parametric distribution<sup>9</sup>, and was selected over a non-parametric<sup>10</sup> method due to the improved estimations at the extremes of the model. Statistical models based on parametric or non-parametric distributions are likely to return slightly different injury risk outcomes (Kent *et al.* 2004). This is due to the way the model is fitted to the data. When compared to parametric models based on the same data, non-parametric models have been shown to underestimate injury risk at the low end of the scale and overestimate it at the high end in some cases, (Kent *et al.* 2004).

---

<sup>9</sup> A parametric test makes assumptions about the parameters of the population distribution.

<sup>10</sup> Non-parametric tests make no assumptions about the parameters of the population distribution.

The BSM and cadaveric data points were combined into a single dataset, which was then fitted to the brglm probit model. In terms of the BC, a value of BC was calculated (Equation 7.1) from the information associated with each isolated impact prior to the values being combined within a single dataset, which was in turn fitted to the brglm.

A residual deviance, with an associated number of degrees of freedom, was calculated for each group of risk curves. Residual deviance is a measure of the fit of the dataset to the brglm; a lower value is associated with an improved fit. Residual deviance will vary due to experimental set-up and data, therefore there is no threshold defined for a good or bad fit. However, residual deviance can provide a way of comparing the fit of different models using the same dataset, where the lowest value is associated with a model which provides the best representation of the data. The degrees of freedom indicate how many independent random variables or relationships are present within the model; the lower the value the simpler the model. Comparison of the residual deviance and associated degrees of freedom for the risk curves developed for each different parameter was used to identify which measures are best able to predict fracture outcomes.

Through use of the brglm and analysis of the combined dataset, the slope of the probit curves was forced to a common value for all of the curves displayed. Statistical differences were calculated between the individual risk curves associated with each parameter. All of the risk curves were compared to the 38 mm diameter flat projectile BSM risk curve. The null hypothesis being that there was no difference between the risk curves. A 95% confidence that that null hypothesis could be rejected was associated with a p value of less than 0.05. These comparisons were primarily to validate the BSM fracture risk curve, investigating the statistical relationship between the 38 mm diameter flat projectile impacts for the cadaveric and comparative BSM fracture risk models. An understanding of the statistical importance of using different curves to predict cranial fracture outcome was also obtained.



## 7.3 Development of cranial fracture risk models

### 7.3.1 Peak impact force

Peak force measures calculated from projectile acceleration were used within the brglm to produce cranial fracture risk curves for the different projectile faces (Figure 7.1). The residual deviance of the curves was 310 on 228 degrees of freedom. This was the highest residual deviance reported across the fracture risk curves developed. The risk curves all have some probability of fracture when no force is applied. This is clearly not a true reflection of the risk.

At a peak impact force of 2.8 kN, the 20 mm flat diameter or 19 mm radius of curvature risk curves show a 50% probability of fracture (Figure 7.1). This is a higher probability of fracture risk than any of the other risk curves; the next curve is the 30 mm radius of curvature associated with a 35% probability of fracture at the 2.8 kN peak impact force. The models based on the 20 mm diameter flat and 19 mm radius of curvature tests overlay each other. This shows that for a given force, the probability of fracture from these two projectiles is the same.

The 26 mm diameter flat and 50 mm radius of curvature models also show the same fracture response across the range of probabilities of fracture (Figure 7.1). In general, as the radius of curvature increases the force required to cause fracture also increases. Therefore, the 50 mm radius of curvature risk curve is expected to be positioned between the risk curves for the 40 mm radius of curvature and the 38 mm diameter flat face. The 50 mm radius of curvature risk curve is actually positioned between the 30 mm radius of curvature and 40 mm radius of curvature. Therefore, the 50 mm radius of curvature fracture risk model does not follow the expected trend for the curvatures tested, as previously highlighted in section 6.3.2.3.

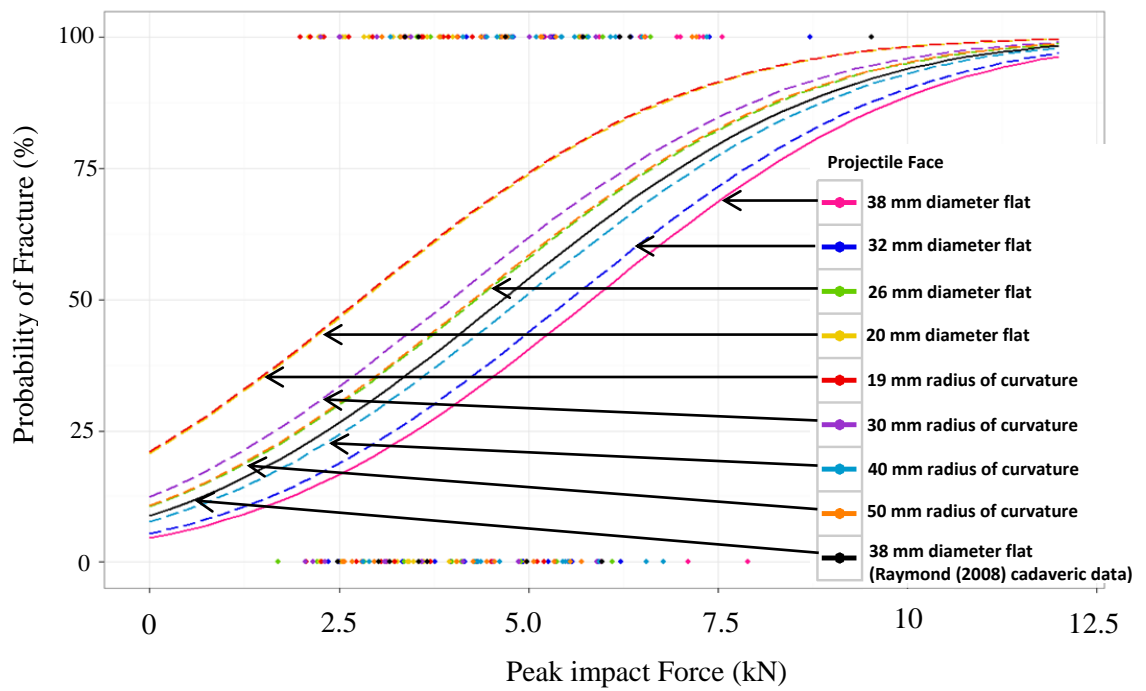


**Figure 7.1: Fracture risk models based on measures of peak impact force.**

A range of impact diameters and curvatures are presented. The curves are based on data obtained from BSM testing, unless stated otherwise. The solid lines highlight comparable risk curves based on 38 mm diameter flat impacts for BSM and cadaveric models.

At the 95% confidence level there is no evidence of a statistical difference between the models based on 38 mm diameter flat face cadaveric (Raymond 2008) and BSM data (Table 7.1). This suggests the BSM provides a representative cranial fracture response when considering peak impact force measures. However, as a result of the small number of cadaveric tests available there are higher uncertainties associated with the fit of the Raymond data when compared to the BSM data. This is the reason why there is no statistical difference although clear differences can be seen between the risk curves (Figure 7.1).

Model	p value
Flat circular 32 mm diameter projectile vs BSM	1.000
Flat circular 26 mm diameter projectile vs BSM	0.951
Flat circular 20 mm diameter projectile vs BSM	0.377
19 mm radius of curvature projectile vs BSM	0.397
30 mm radius of curvature projectile vs BSM	0.893
40 mm radius of curvature projectile vs BSM	0.998
50 mm radius of curvature projectile vs BSM	0.939
Flat circular 38 mm diameter projectile vs cadaver	0.998

**Table 7.1: Statistical comparison of fracture risk models developed using peak impact force.**

The models consider the parameters of projectile face, fracture outcome and peak impact force. Each model is compared to the risk model based on the 38 mm flat faced diameter projectile vs BSM dataset.

At the 95% confidence level ( $p < 0.05$ ) there is no evidence of a statistical difference between the 38 mm diameter flat model and the 19 mm radius of curvature ( $p = 0.397$ ) or 20 mm diameter flat ( $p = 0.397$ ) models (Table 7.1). However, for an impact force of 5 kN, there is a 35% difference in probability of cranial fracture between an impact of 38 mm flat diameter and the 20 mm flat diameter or 19 mm radius of curvature impact. The statistical findings are due to the inclusion of Raymond's data. However, the large gap between the curves suggests that even though the differences are not statistically significant, force should be measured in conjunction with impact diameter or radius of curvature to obtain a more accurate prediction of cranial fracture probability than peak force alone.

### **7.3.2 Impact velocity**

Impact velocity was used to develop fracture models (Figure 7.2) associated with a residual deviance of 241 on 238 degrees of freedom. The models are divided into three main groups. In terms of the distribution of the curves, they align with the findings reported in section 6.3.2.2; the four largest flat and curved faces require higher velocities to cause fracture. Equally, the models developed for the two smallest faces predict a similar

probability of fracture; the curves almost overlay each other and are both associated with a 50% probability of fracture of approximately  $20 \text{ m}\cdot\text{s}^{-1}$ . In addition, the models associated with the 26 mm diameter flat and 30 mm radius of curvature projectiles are associated with a 50% probability of fracture at  $24 \text{ m}\cdot\text{s}^{-1}$  and  $23 \text{ m}\cdot\text{s}^{-1}$  respectively, highlighting their similarity. These risk curves fall between the two groups of extreme projectile faces tested.

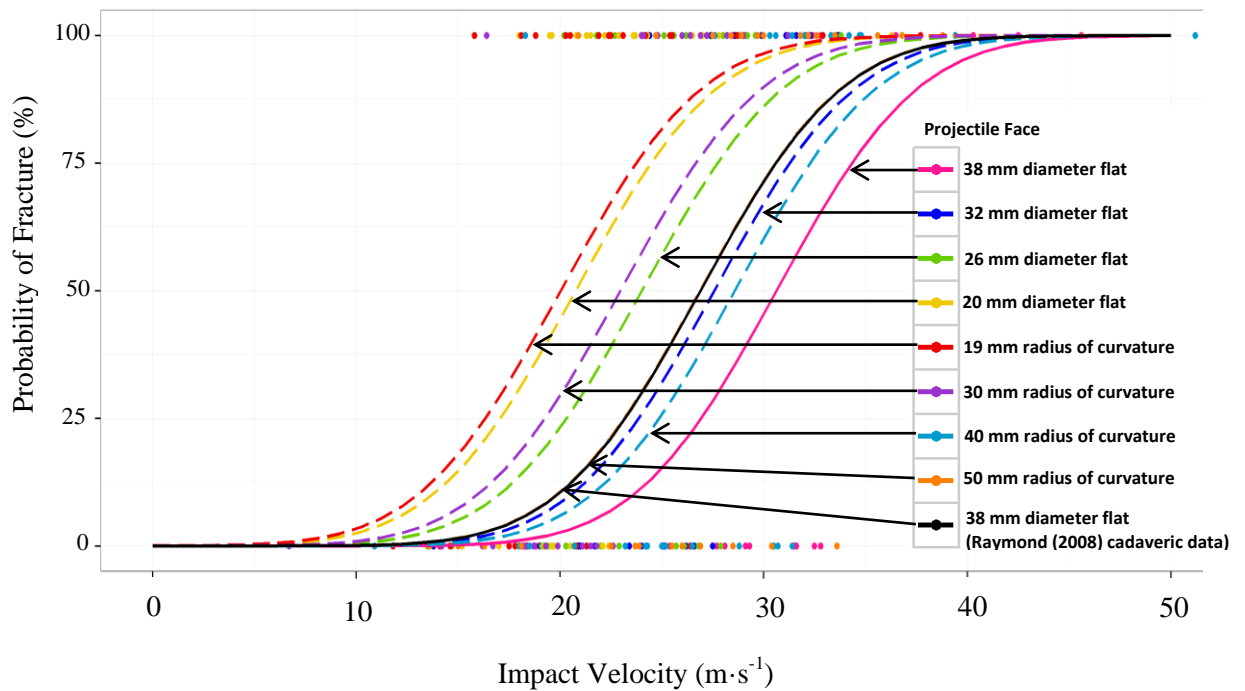


**Figure 7.2: Fracture risk models based on measures of projectile velocity.**

A range of impact diameters and curvatures are presented. The curves are based on data obtained from BSM testing, unless stated otherwise. The solid lines highlight comparable risk curves based on 38 mm diameter flat impacts for BSM and cadaveric models. The 50 mm radius of curvature risk curve has the same probability of fracture as the 38 mm flat diameter cadaveric based curve, and hence it is hidden.

The cadaveric based fracture risk curve aligns with the BSM 50 mm radius of curvature model. These models were grouped with the 32 and 38 mm diameter flat and the 40 mm radius of curvature faces, and showed no evidence of a statistical difference at the 95% confidence level ( $p < 0.05$ ) (Table 7.2). The cadaveric data was obtained using a 38 mm diameter flat faced projectile. Therefore it was expected that there would be no evidence of

a statistical difference between the cadaveric and 38 mm diameter BSM fracture risk curves, as identified.

Model	p value	Evidence of significance at the 95% confidence level (p<0.05)
Flat circular 32 mm diameter projectile vs BSM	0.880	
Flat circular 26 mm diameter projectile vs BSM	0.060	
Flat circular 20 mm diameter projectile vs BSM	0.000	***
19 mm radius of curvature projectile vs BSM	0.000	***
30 mm radius of curvature projectile vs BSM	0.020	*
40 mm radius of curvature projectile vs BSM	0.990	
50 mm radius of curvature projectile vs BSM	0.700	
Flat circular 38 mm diameter projectile vs cadaver	0.940	

**Table 7.2: Statistical comparison of fracture risk models developed using impact velocity data.**

The analysis has considered the parameters of projectile face, fracture outcome and impact velocity only. The models are compared to a model based on a 38 mm flat faced diameter projectile vs BSM dataset. Evidence of a significant difference at the 95% confidence level (p<0.05) is identified by a \*, with greater significance shown by an increasing number.

At an impact velocity of  $30 \text{ m}\cdot\text{s}^{-1}$ , there is approximately a 50% difference in probability of fracture between the risk curve developed using the 38 mm diameter flat projectile (approximately 45% probability of fracture), and the 19 mm radius of curvature risk curve (approximately 95% probability of fracture). This is supported by evidence of a statistical difference between the two fracture risk curves at the 99.9% (p<0.001) confidence level (Figure 7.2). Similarly, at the same impact velocity ( $30 \text{ m}\cdot\text{s}^{-1}$ ) there is also approximately a 50% difference in probability of fracture between the risk curves developed using the 20 mm diameter flat projectile (approximately 95% probability of fracture), and the 38 mm flat diameter (approximately 45% probability of fracture) projectiles. Therefore, when using impact velocity, the flat diameter and/or curvature of the impact should be considered when predicting cranial fracture outcome.

### **7.3.3 Impact velocity & bone thickness**

Values of bone thickness were considered with impact velocity and fracture outcome to develop fracture risk curves for each of the projectile faces and the cadaveric data. The resulting risk curves were plotted in three dimensions, presenting the effects of impact velocity and bone thickness on fracture outcome (Figure 7.3). The residual deviance associated with these risk curves was calculated at 170 on 237 degrees of freedom.

Within the tests for each projectile face, the BSMs and cadaveric specimens did not have the same range of thicknesses. This is reflected by variations along the thickness axis in the 3D plots (Figure 7.3). Also, the statistical models do not all pass through the origin, or zero, of all the axes; this is unrepresentative of the actual response. Therefore, for some projectile faces, the risk of fracture may be overestimated for small thicknesses impacted at low velocities.

Due to the increased complexity of the risk curves, it is difficult to compare across the datasets. Therefore, the curves (Figure 7.3) have been sectioned at a bone thickness of 3.7 mm, the average bone thickness for the combined data (cadaveric and BSM tests). This has essentially normalised the data, enabling production of a two dimensional plot showing the different curves for each projectile face in terms of projectile velocity (Figure 7.4).

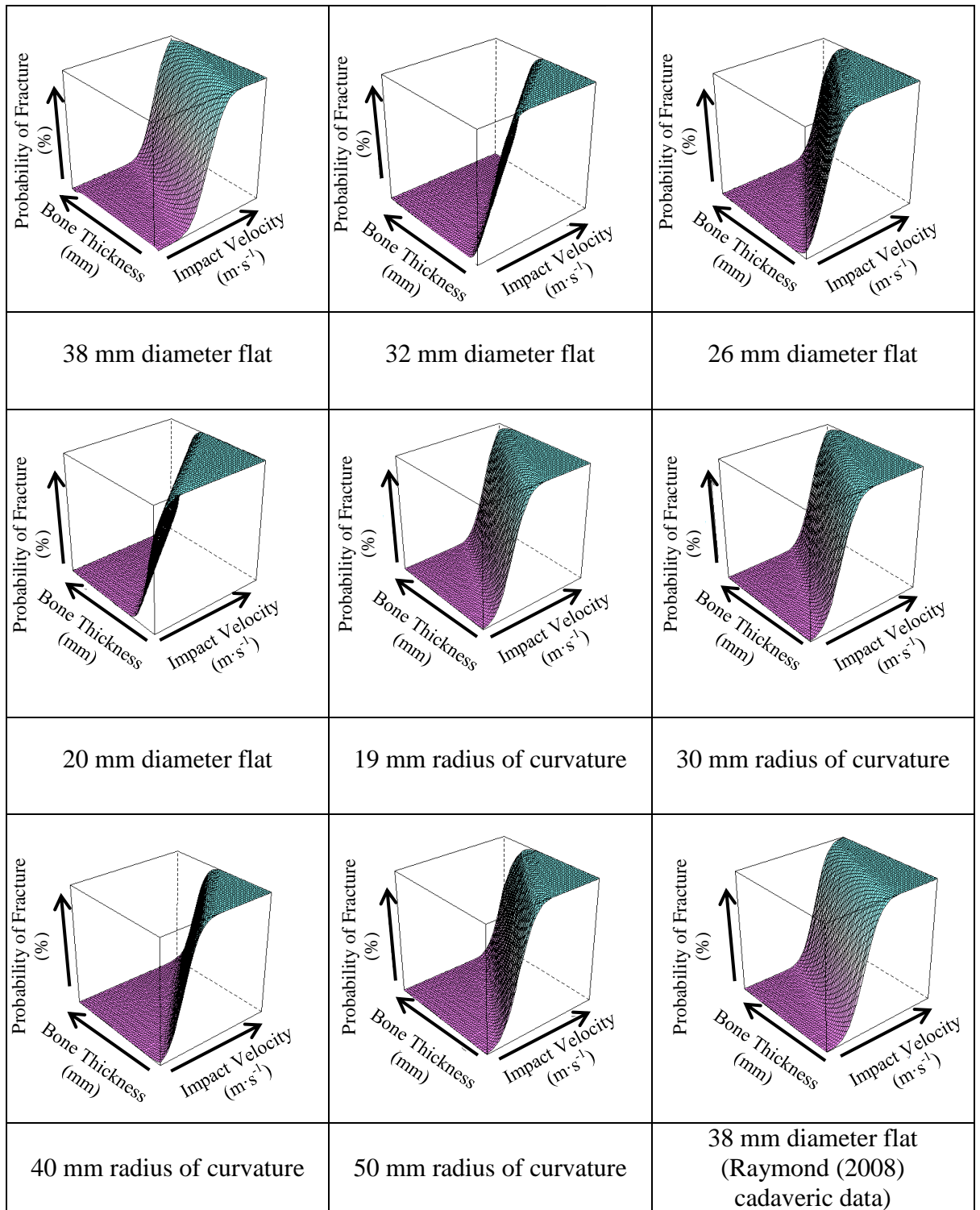


Figure 7.3: Fracture risk models for different projectile faces, developed using measures of impact velocity, bone thickness and fracture outcome.

A range of impact diameters and curvatures are presented. The curves are based on data obtained from BSM testing, unless stated otherwise. The analysis has considered the parameters of projectile face, bone thickness, impact velocity and fracture outcome. The axes are the same scale within each risk curve; probability of fracture ranges from 0 to 100%, bone thickness ranges from 1 to 8 mm and impact velocity ranges from 0 to 50 m·s<sup>-1</sup>.

The 2D BSM impact velocity and bone thickness models shows similar groupings to the models which considered impact velocity in isolation (Section 7.3.2). However, the position of the curves has varied due to consideration of the bone thickness. This is due to differences in average bone thickness for the tests associated with a single projectile face. In general, groups with an average bone thickness lower than that for the whole dataset (<3.7 mm) will shift to the right of the velocity scale, relative to the position when velocity is considered in isolation. Similarly, data associated with a larger average bone thickness than the combined dataset (>3.7 mm) shift to the left of the scale.

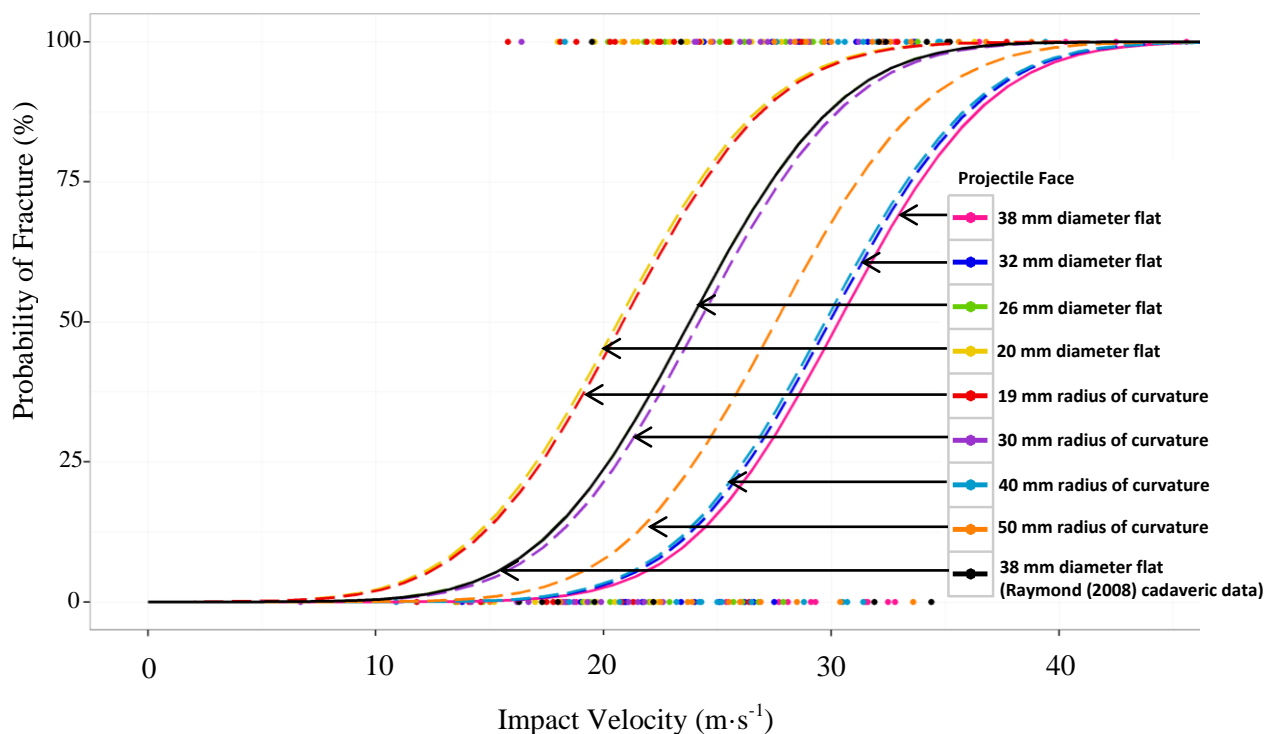


Figure 7.4: Fracture risk models by impact velocity for different projectile faces, based on an average bone thickness of 3.7 mm for the complete dataset.

The curves represent a section through three-dimensional risk curves developed using measures of impact velocity, bone thickness and fracture outcome. The curves are based on data obtained from BSM testing, unless stated otherwise. The 26 mm diameter flat curvature risk curve has the same probability of fracture as the 38 mm flat diameter cadaveric based curve, and hence it is hidden.



The model based on the 38 mm flat faced cadaveric data (Raymond 2008) has fitted to the same model as the BSM 26 mm flat diameter impacts, with a 50% probability of fracture occurring at  $24 \text{ m}\cdot\text{s}^{-1}$  (Figure 7.4). It was expected that the cadaveric model would align with the 38 mm flat faced BSM data (50% probability of fracture at  $31 \text{ m}\cdot\text{s}^{-1}$ ) due to use of the same projectile face.

At the 95% confidence level ( $p < 0.05$ ), the difference between the BSM and cadaveric models for the same impact diameter falls short of statistical significance ( $p = 0.061$ ) (Table 7.3). However, a difference can be seen between the fracture risk curves; the 50% probability of fracture is  $31 \text{ m}\cdot\text{s}^{-1}$  for the BSM data compared to only  $24 \text{ m}\cdot\text{s}^{-1}$  for the cadaveric risk curve. The difference is greater than that observed when impact velocity was considered in isolation (Figure 7.2). This increased difference is due to the cadaveric data having an average bone thickness of 4.8 mm (Raymond 2008) compared to the 3.7 mm average bone thickness calculated for the combined cadaveric and BSMs dataset.

<b>Model</b>	<b>p value</b>	<b>Evidence of significance at the 95% confidence level (<math>p &lt; 0.05</math>)</b>
Flat circular 32 mm diameter projectile vs BSM	0.996	
Flat circular 26 mm diameter projectile vs BSM	0.066	
Flat circular 20 mm diameter projectile vs BSM	0.002	**
19 mm radius of curvature projectile vs BSM	0.009	**
30 mm radius of curvature projectile vs BSM	0.168	
40 mm radius of curvature projectile vs BSM	1.000	
50 mm radius of curvature projectile vs BSM	0.933	
Flat circular 38 mm diameter projectile vs cadaver	0.064	

**Table 7.3: Statistical comparison of fracture risk models developed using impact velocity, projectile and average bone thickness data.**

The analysis has considered the parameters of projectile face, bone thickness, impact velocity and fracture outcome. The models are compared to a model based on a 38 mm flat faced diameter projectile vs BSM dataset. Evidence of a significant difference at the 95% confidence level ( $p < 0.05$ ) is identified by a \*, with greater significance shown by an increasing number.

### 7.3.4 Blunt Criterion (BC)

The BC based risk curves (Figure 7.5) have a residual deviance of 170 on 238 degrees of freedom. Calculation of the BC has focused each dataset around a defined fracture threshold, shown by the steep gradient of the BC based risk models.

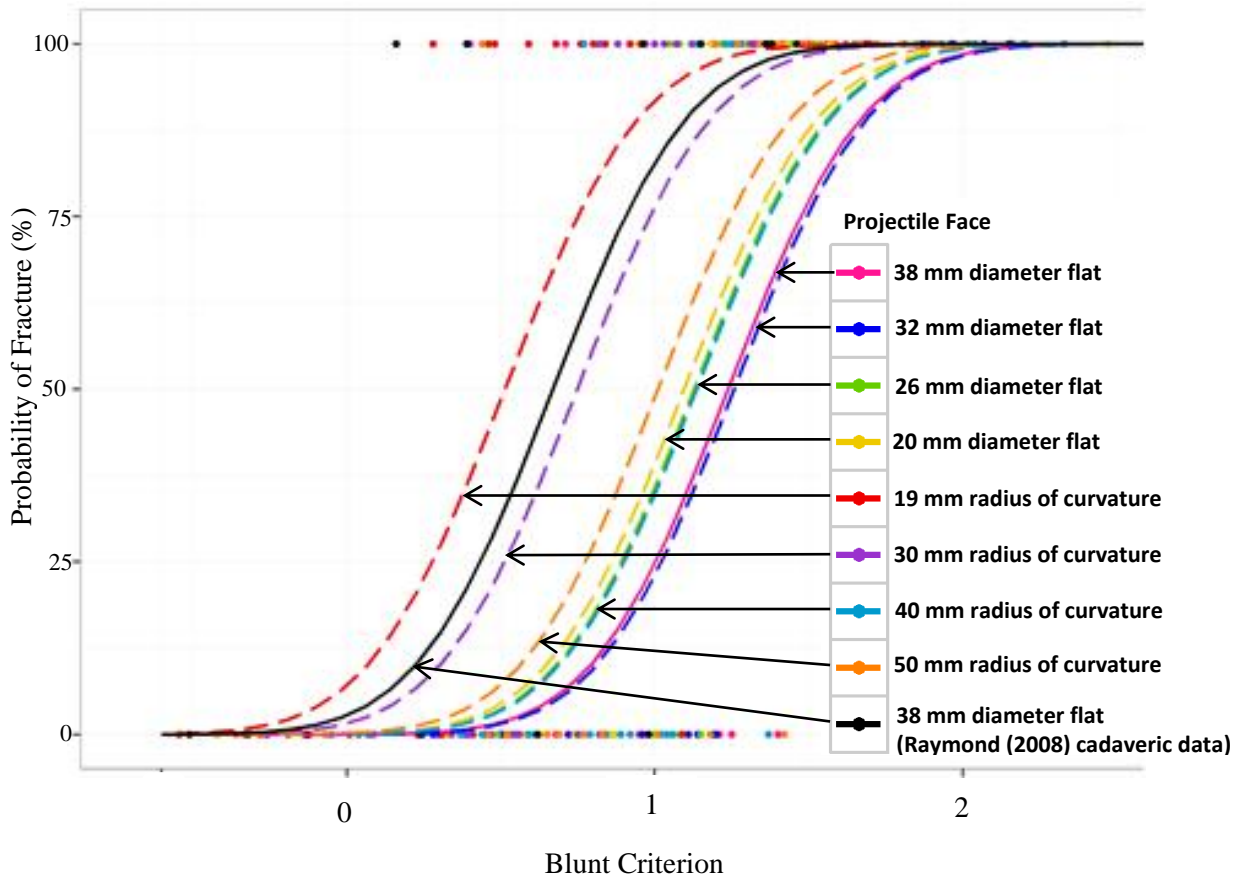


**Figure 7.5:** Fracture risk curves for a range of impact diameters and curvatures, based on a calculation of the BC optimised for head impacts (Hisley *et al.* 2010).

A range of impact diameters and curvatures are presented. The curves are based on data obtained from BSM testing, unless stated otherwise. The solid lines highlight comparable risk curves based on 38 mm diameter flat impacts for BSM and cadaveric models.

The curves fitted to the flat face BC values (Figure 7.5) are highly grouped with a 50% probability of fracture occurring between a BC of 1.1 and 1.3. Also associated with this group are the models associated with the 40 and 50 mm radius of curvature tests. At the 95% confidence level ( $p < 0.05$ ) there was no evidence of a statistical difference between these six risk curves (Table 7.4). This was expected since BC is a function of the projectile

diameter. Therefore a single risk curve should be sufficient to represent all of the flat impact faces.

Model	p value	Evidence of significance at the 95% confidence level (p<0.05)
Flat circular 32 mm diameter projectile vs BSM	1.000	
Flat circular 26 mm diameter projectile vs BSM	0.997	
Flat circular 20 mm diameter projectile vs BSM	0.988	
19 mm radius of curvature projectile vs BSM	0.001	**
30 mm radius of curvature projectile vs BSM	0.049	*
40 mm radius of curvature projectile vs BSM	0.999	
50 mm radius of curvature projectile vs BSM	0.865	
Flat circular 38 mm diameter projectile vs cadaver	0.147	

**Table 7.4: Statistical comparison of fracture risk models developed using values of the Blunt Criterion (BC).**

The analysis has considered the parameters of projectile face, the BC and fracture outcome. The models are compared to a model based on a 38 mm flat faced diameter projectile vs BSM dataset. Evidence of a significant difference at the 95% confidence level (p<0.05) is identified by a \*, with greater significance shown by an increasing number.

Differences can be seen between this main group and the cadaveric, 19 and 30 mm radius of curvature models. At the 95% confidence level (p<0.05) there was no evidence of a statistical difference (Table 7.4) between the 38 mm diameter flat BSM model and the cadaveric based BC model (p=0.147). However, there is evidence of a statistically significant difference between the 38 mm diameter flat and the 30 mm radius of curvature BSM curves (p=0.049); these curves have a smaller difference when compared to the 38 mm diameter flat cadaveric and BSM curves. Therefore, a statistical difference would be expected when comparing the Raymond (2008) and 38 mm diameter flat BSM risk curves. However, there is a lack of statistical power associated with Raymond's data as a result of the small number of tests undertaken.

There is a clear difference between the cadaveric based curve and the BSM 38 mm diameter flat projectile curve; the cadaveric based curve is associated with a 50% probability of fracture at a BC of 0.6, compared to a BC of 1.2 for the BSM based curve. This difference is unexpected as both tests used a 38 mm diameter flat projectile. The difference was most likely due to variability in bone thicknesses; where all other parameters are comparable, larger bone thicknesses would have resulted in a lower BC value.

There is statistical evidence that the 19 (p=0.001) and 30 mm radius of curvature (p=0.049) risk curves are different to the 38 mm diameter BSM curve (Table 7.4). This was expected as the BC only considers projectile diameter. Therefore, a diameter of 38 mm was used to calculate BC values for all of the curved projectile tests. However, the BSM fracture responses were different as a result of different projectile curvatures. Hence, the curved projectile risk curves do not align with the flat projectiles.

## **7.4 Discussion**

### **7.4.1 General**

BSM data has been used to develop a number of fracture risk curves for impacts of different diameters and curvatures. Cadaveric data was included within the same analysis to understand the ability of the BSM risk curves to predict cranial fracture outcomes. This approach was taken as the statistical methods applied to a dataset will affect the injury models produced (Kent *et al.* 2004). Raymond (2008) did not use the brglm or R statistics software. Therefore, the original cranial fracture risk models reported by Raymond could not be used for direct comparison with the BSM based models; the raw cadaveric data was applied within the same statistical analysis as the BSM data to enable a direct comparison.

The fracture models had different maximum gradients dependant on whether the parameter was peak force, impact velocity, the BC or impact velocity in conjunction with bone thickness. However, for each individual parameter, the gradients were consistent across the range of models. This was due to the gradients being forced to a common value through use of the brglm. Therefore, for a single parameter, differences between the curves could be described with a simple translation of the model along the x-axis.

For some parameters there was evidence of a significant difference between the smallest curved (19 mm radius of curvature) and flat diameter (20 mm) BSM based models, when compared to the 38 mm flat diameter BSM based model. This finding further supports the findings of section 6.4.5; impact curvature and flat diameter affect the fracture response of the cranium and should be considered when predicting fracture outcomes. Flat diameter and impact curvature should therefore be measured by BHBT assessment methods to better predict cranial fracture risk.

Fracture responses for a 38 mm diameter flat impact were available for both BSMs and cadaveric specimens. Although the models based on this data were previously determined to be statistically similar (Section 4.), the cadaveric models consistently showed a higher probability of fracture than the comparable BSM models for a single stimuli value. Therefore, higher peak impact forces and projectile velocities were required to cause fracture of the BSM, compared to the cadaveric specimens. This was irrespective of the measurement used to predict fracture. This suggests the models based on BSM data may under-estimate the likelihood of fracture of the cranium. However, Raymond (2008) only considered the temporo-parietal region of the cranium. Regions with a higher fracture response, such as the frontal bone, may be more closely aligned to the BSM.

A better prediction of fracture risk to the temporo-parietal region may be achieved by translating the BSM risk models. Initially, the 38 mm flat circular model could be off-set to

overlay the cadaveric risk curve. The other BSM models could then be off-set by the same translation. This assumes that the cranial fracture response to the different projectiles would be the same as that identified using the BSM. Validation of this approach could be improved with further cadaveric data. The understanding of cranial fracture response could be enhanced by conducting cadaveric tests using a 19 mm radius of curvature projectile, to determine a cadaveric response for the extreme projectile faces. This data could be used to produce probit models for comparison with the 19 mm radius of curvature BSM models. Therefore, the BSM fracture responses could be appropriately aligned at the two extremes of the projectile faces. Raymond (2008) conducted the original cadaveric testing at Wayne State University. In order to ensure consistency of experimental methods, it was deemed to be appropriate to enlist the expertise at the University to conduct this additional cadaveric investigation. A study has commenced with this aim but has not completed at the time of reporting.

For all of the parameters used to develop risk curves, there was no evidence of a statistically significant difference between the models based on the comparable cadaveric and BSM data. Therefore the BSM has been identified to be statistically representative of cranial fracture response when considering the parameters of peak force, impact velocity, impact velocity in conjunction with bone thickness and the BC. However, differences between the curves were observed, with the greatest differences associated with the parameters of impact velocity in conjunction with bone thickness and the BC. Further validation of the data to establish whether these differences are significant would be beneficial prior to using the fracture risk models to predict cranial fracture outcomes.

#### **7.4.2 Peak impact force**

The intention of this work was to develop cranial fracture risk curves based on impact force, and peak impact force was calculated within the BSM study to support this.

However, the fracture risk models developed using peak force measures (Figure 7.1) appear to overestimate fracture outcome at lower impact forces and are associated with a higher residual deviance than the other parameters investigated (Table 7.5). This suggests that models based on alternative parameters such as impact velocity or calculation of criterion such as the BC are needed to better predict cranial fracture outcome.

Parameter	Residual Deviance	Degrees of Freedom
Peak force	310	228
Impact velocity	241	238
Impact velocity & bone thickness	170	237
Blunt Criterion (BC)	170	238

**Table 7.5: Values of residual deviance and associated degrees of freedom calculated for fracture risk curves developed using different parameters of impact.**

When developing injury risk curves, Kent *et al.* (2004) reported that it was important to consider data censoring and the use of parametric or non-parametric models. Data censoring is the term used to describe whether an outcome (i.e. bone fracture) occurred exactly at the value of the stimulus (i.e. impact velocity or peak impact force) measured. If the outcome occurs at the measured value of the stimuli the data is termed to be ‘uncensored’. If however, the outcome has occurred but it is unknown whether the same outcome would have occurred at a lower value of the stimuli, then the data is termed as ‘left censored’ - the unknown stimulus value lies to the left of the measured stimuli. Conversely, where the unknown value of the stimulus lies on the right of the measured point, the data is termed ‘right-censored’. The parameters of peak impact force and impact velocity associated with the BSM data were assumed to be doubly censored. This means fracture outcomes were assumed to be left censored and non-fracture outcomes were assumed to be right censored. Risk models based on censored datasets require failure and non-failure outcomes as the model is focused around the transition from failure to non-failure. Hence, the risk models have been developed using the fracture and non-fracture

outcomes associated with the BSM and cadaveric datasets. However, this may not be appropriate for the peak force data.

It is worth considering that the investigation of BSM fracture outcomes by peak impact force found, for impacts of the same velocity, higher forces were calculated when no fracture occurred (Section 6.3.2.2). When this data is applied within statistical analysis, the output suggests an inverse relationship between impact force and fracture outcome; this is unrealistic.

A statistical inverse relationship can be an indication of a combination of censored and uncensored data (Kent *et al.* 2004). Raymond (2008) proposed cranial fracture force data to be uncensored. By using timing data it was reported that peak force occurred at the same time as peak strain, which occurs immediately prior to fracture. Once fractured the bone was unable to transfer any load, causing a rapid decrease of the strain and force measures. However, Allsop *et al.* (1988) reported that in some cases of cranial fracture the peak force occurred after fracture. This suggests that in this case, peak force measures are left censored for fracture outcomes. Therefore, to confirm whether peak force fracture data is censored or uncensored, further investigation would be required. Determination of the data censoring would help to determine appropriate methods for developing risk models using peak force measures; this may improve the fit or residual deviance of the models.

### **7.4.3 Impact velocity**

Impact velocity data is clearly doubly censored; there is an unknown increase in velocity required to cause fracture in the non-fracture cases. Therefore, these data points are right censored. Equally, for fracture outcomes it is unknown whether a lower velocity would have caused the same outcome. The data associated with measures of impact velocity have therefore been treated appropriately by using the brglm. This may explain why these models are a better fit to the data than those associated with the peak force data.



The relationships between the impact velocity fracture risk curves are aligned with the relationships identified in section 6.3.2.3; a linear relationship for flat projectile faces and potentially a bilinear relationship for the inverse radius of curvatures. The relationships were developed using the  $V_{50}$ . However, the curves are parallel to one another, and therefore the same relationships can be applied for any probability of fracture. The full models and individual probability relationships could be used to interpolate and extrapolate beyond the projectile faces tested. However, as discussed in section 6.4.1, there are limits to the range of projectiles over which the extrapolation can be applied.

#### **7.4.4 Impact velocity and bone thickness**

When bone thickness was considered alongside the impact velocity, the residual deviance was calculated as 170, compared to a value of 241 when bone thickness was omitted (Table 7.5). Therefore, an improved model fit was determined when bone thickness was included with impact velocity. This suggests that the models are better able to predict the risk of fracture. This was as expected based on the BSM data (section 6.3.2.2) and review of the literature (section 3.4.2.2); bone thickness is a key parameter affecting fracture outcome. However, despite the lower residual deviance, the differences between the curves was associated with a reduced statistical significance when compared to those associated with the isolated parameter of impact velocity; additional data is most likely needed to account for the consideration of an extra variable.

At the average bone thickness for the dataset (3.7 mm), the fracture risk curves presented by impact velocity (Figure 7.4) all have the same gradient, and a simple translation could be used to map between the curves. However, when the 3D risk curves are considered (Figure 7.3), it looks unlikely that the different curves can be related by a simple translation for the full range of bone thicknesses and impact velocities. Therefore, individual curves are required to provide an accurate prediction of fracture risk.

#### **7.4.5 Blunt Criterion (BC)**

In addition to the mass of the projectile, calculation of the BC includes the parameters of impact velocity, flat diameter of the impact and bone thickness. These are all parameters identified to affect fracture outcome through statistical analysis of the BSM data in section 6.3.2.2. These are the same parameters considered within the risk curves developed using impact velocity in conjunction with bone thickness. As the residual deviance of the two groups of risk curves are the same (170), it would suggest that any variability in the mass of the projectiles has had a negligible effect on the fracture response associated with each of the different projectiles tested.

The flat diameter BSM data approximately converged to a single fracture risk curve, suggesting that the consideration of impact diameter within the calculation of the BC is treated appropriately. However, the calculation does not consider impact curvature, which was highlighted by a statistical difference determined for the curves associated with the 19 and 30 mm radii of curvature. Therefore, if the intention is to use BC for curved impacts, further development would be recommended.

Application of the BC to determine cranial fracture risk curves has highlighted that the BSMs generally have thinner bone thicknesses when compared to the cranium specimens tested. This is shown by a greater difference between the cadaveric and 38 mm flat diameter BSM risk curves when compared to the other groups of risk curves developed. When compared to the risk curves associated with the parameters of peak force and impact velocity in isolation, a large difference was also seen when bone thickness was considered in conjunction with impact velocity. Bone thickness has been determined to affect fracture outcome, where a thinner bone is more likely to fracture than a thicker one for the same impact velocity. Therefore, it would be expected that the BSMs would have fractured at lower velocities than the cadaveric specimens. However, this is not the case; BSMs appear

to fracture at higher velocities, although the difference is not statistically significant. Any increased resistance to fracture of the BSMs may be due to the layer of gelatin and chamois leathers over the impact area. Investigation of the gelatin and chamois layers would enable its influence on the bone fracture response to be determined. It is possible that a reduction in the thickness of these layers may make the BSM and cadaveric responses more similar. This also highlights that scalp thickness may need to be included in the BC calculation.

#### **7.4.6 Application of the cranial fracture risk curves**

Successful application of the fracture risk curves calculated here can only be achieved if an assessment method can differentiate between different impact curvatures and flat diameters. This could be achieved either by directly measuring the shape or by using variations in sensor profiles to identify the shape (Section 6.3.3.2).

Current synthetic models cannot measure impact curvature (Section 3.2), but some systems could give an indication of the impact diameter. The synthetic systems developed by Anctil *et al.* (2008) and Neale *et al.* (2013) have an array of load sensors; the number of sensors recording an impact force will provide some indication of the contact diameter. However, the width and number of the load sensors will limit how accurately the diameter can be determined. In the sensor arrays used by Anctil *et al.* (2008) and Neale *et al.* (2013), a central sensor of approximately 20 mm diameter is surrounded by a ring of 6 further sensors of the same size. Therefore, for a central impact the diameter can only be identified as above or below 20 mm. A reduction in sensor size, with an increase in the number of sensor rings and hence sensors would provide improved measurement of impact diameter.

Differences in the force profiles collected by load sensors may be the only way to obtain an indication of both impact curvature and diameter from current synthetic model assessment methods. The force profiles presented in section 6.3.3.2 illustrate that it may be possible to determine the impact curvature or diameter by this method. This method may be applied to

systems that have one load sensor, such as the synthetic models developed by Barnes-Warden *et al.* (2013) and Watson *et al.* (2008).

Where existing BHBT assessment methods do not have the capability to measure impact diameter or curvature, it may be appropriate to use the fracture risk curves based on the 19 mm radius of curvature BSM data. These risk curves are associated with the highest risk of fracture and appear to be representative of the worst case impacts from helmet BFD.

In order to apply the BC or impact velocity in conjunction with bone thickness curves it would be necessary to determine thicknesses of the cranium for the population at risk. However, it would be challenging to obtain these measurements because of the need for x-ray exposure. In addition, current assessment methods using synthetic head models have not reported the ability to measure the mass or impact velocity of helmet BFD. Therefore, only force based criteria could be directly applied to existing BHBT assessment methods using synthetic head models.

The instrumented projectile(s) could be used to assess the ability of a synthetic head model to measure impact curvature and diameter. The fracture risk curves developed using peak force and impact velocity could also be applied to synthetic head-models by using the instrumented projectile(s). This could be achieved by impacting a model with the different projectiles, at a range of velocities. Peak force could be calculated from the projectile, or impact velocity could be measured, to align sensor outputs with the cranial fracture risk curves. However, the peak force risk curves appear to over-estimate the probability of fracture, as previously discussed. Further investigation of peak force measures is required to confirm the associated data censoring.

Alternatively, the risk curves could be applied to the free-air BFD assessment method reported by Hisley *et al.* (2010). The DIC analysis could be extended to measure the curvature of the BFD as well as the diameter. Hisley has already shown that the existing

BC formula can be applied to free-air measurements. However, to fully utilise the additional data, the BC would need further development to include impact curvature. Finally, the calculation of the BC using DIC could also be improved by determining thicknesses of the cranium for the population at risk. Alternatively, the impact velocity risk curves could be applied to the free-air BFD assessment method reported by Hisley *et al.* (2010); measures of velocity and curvature of helmet BFD could be obtained using the DIC method, applying the risk curves to predict fracture occurrence of the cranium.

The projectile faces used in this study were determined from BFD profiles. However, it is important to consider that development of helmet BFD may be affected by the underlying head, as discussed in section 3.3.3. Therefore, the fracture risk curves may not be representative in terms of the protective capability of the helmet system. Equally, the relationship between impacts caused by a rigid projectile and helmet BFD has not been investigated. Previous studies have observed the BFD to conform to the head (Bass *et al.* 2003, Freitas *et al.* 2014). This may spread the load over a wider area and reduce the risk of fracture. Therefore, when compared to BFD, use of a rigid projectile may over-estimate the likelihood of fracture.

## **7.5 Summary**

Data obtained from BSM impacts has been used to develop a number of fracture risk models. Using the parameters of peak impact force, the BC, impact velocity and bone thickness, the models predict the effect of impact diameter and curvature on fracture outcome.

It is important to consider that most of the fracture risk curves have been developed using BSM data and not human skulls. A cadaveric based model has been included for comparison with an equivalent BSM curve; however, in all cases these comparisons showed the BSM based model underestimated the probability of cranial fracture.

Validation of the BSM findings could be improved by conducting further cadaveric investigations to provide fracture responses for the different projectile faces. Alternatively, different regions of the cranium could be tested. In both cases the data could be used to develop cranial fracture risk models that could be used for additional comparisons to the BSM based fracture risk curves.

The aim of this work was to support existing BHBT assessment methods with improved cranial fracture risk curves. In order to make a meaningful assessment, methods must be able to differentiate between different impact curvatures and flat diameters. Where BHBT assessment methods are not able to measure impact curvature and flat diameter, the fracture risk curve based on impacts from a 19 mm radius of curvature could be used to predict fracture outcome. This is considered as the worst case impact curvature.

Following consideration of the fracture risk curves in terms of residual deviance, comparability between BSM and cadaveric models, data censoring and the method of application, BHBT assessment methods should where possible measure the mass and velocity of the helmet BFD and the thickness of the underlying skull in addition to the curvature and flat diameter of the BFD on impact with the underlying head. This information would provide the best prediction of cranial fracture outcome.

In all cases, the fracture risk curves should not be applied to methods for assessing BHBT without considering the limitations of the risk curves and the assessment method. The fracture risk models have been developed using BSMs and a rigid projectile. Therefore, the risk curves may not be appropriate to cranial fracture outcomes and a deformable helmet. However, use of a fracture analogue for the cranium and a rigid projectile was the best technique available in order to conduct such an extensive and controlled study.

## Chapter 8: Conclusions and Recommendations

### 8.1 Skull fracture metrics for assessing BHBT

During the defeat of high velocity bullets by non-metallic helmets, large deformations have been shown to occur on the inside of the helmet shell (Lucuta *et al.* 2014). If these deformations contact the underlying head of the helmet user there is the potential to cause injury, termed as BHBT (Bass *et al.* 2003, Sarron *et al.* 2004). A method of assessing BHBT is required to fully understand the protective capability of a helmet system. Existing methods have used biological (Bass *et al.* 2003, Sarron *et al.* 2004) and synthetic models (Anctil *et al.* 2005, Freitas *et al.* 2010) to gather information relating to impact from helmet BFD. However, the effects of impact curvature and area on skull fracture outcome have not been considered. Therefore, the aim of this work was to improve BHBT assessment methods by understanding the injury metrics that can be used to predict cranial fracture outcomes, focusing on the effects of impact curvature and flat face diameter.

Through the use of DIC to measure helmet deformation, it has been shown that as a helmet deforms, the curvature, area and surface velocity of the deformation varies. Therefore, in agreement with Sarron *et al.* (2004), the level of displacement will affect the parameters of the deformation. This should be considered when testing and using combat helmet systems. In addition, the geometry of the helmet has been shown to have an effect on the resulting deformation. Therefore, assessment of flat panels of a helmet material may not provide a representative deformation shape, and hence lead to an inaccurate prediction of cranial impact. It is concluded that full helmet systems should be used for the assessment of BHBT, unless a relationship between flat panel BFD and curved surface BFD can be developed.

This study has shown that the BSM is a suitable alternative to cadaveric specimens for assessing the risk of cranial fracture. Therefore, the BSM could be used to support further investigation of fracture outcomes for the cranium.

Existing cranial fracture risk curves for BHBT rely on the measurement of a single impact parameter of peak force (Anctil *et al.* 2005, Neale *et al.* 2012). However, this work has concluded that in isolation, peak force is a poor predictor of skull fracture outcome. This study has concluded that impact velocity is better than peak force for predicting cranial fracture outcome from a blunt ballistic impact. The curvature and flat diameter of the strike face have also been determined to affect cranial fracture outcome. Therefore, BHBT assessment methods should include instrumentation capable of measuring the curvature, flat diameter and surface velocity of the helmet deformation on impact with an underlying head.

This study has produced fracture risk curves which could be used to predict cranial fracture outcome. These can be applied where the parameters of impact curvature and flat diameter are measured in conjunction with impact force, velocity and/or bone thickness. Risk curves using peak force have been produced to support existing assessment methods; although peak force is not an ideal measurement, the curves could be applied to enhance existing assessment methods.

The fracture risk curves have been developed using at least double the number of data points reported by Bass *et al.* (2003) and Raymond (2008). Therefore, it is concluded that the fracture risk curves produced within this work have increased statistical power and reduced confidence limits when compared to previously reported fracture risk curves. However, it is important to consider the limitations associated with these skull fracture risk curves. In particular, it would be expected that helmet BFD will conform to the head (Bass *et al.* 2003, Freitas *et al.* 2014). Although the projectile shapes used in this study are



representative of helmet BFD, the interaction between the head and helmet material during actual BFD impact has not been investigated. Therefore, the impacts and associated cranial fracture risk models are likely to over-estimate fracture outcomes for similar impacts from helmet BFD.

## **8.2 Recommendations for future research**

The fracture risk curves developed using peak force values over-estimate the probability of fracture when no force is applied. Data censoring was identified as a potential reason for this inaccuracy. However, there is insufficient information available to relate cranial bone fracture timings with force application. Further investigation into the timings associated with peak impact force and fracture would confirm the censoring associated with peak force measures. This could be achieved by using force measures from a projectile and a microphone to capture fracture, both aligned to a common time base. The information obtained could ensure the appropriate statistical methods were applied to peak force data. This would provide a definitive understanding of the suitability of peak force as a predictor of cranial fracture under blunt ballistic loading.

The BC already considers diameter of flat impacts within its calculation. However, further development would be advised if the BC is to be applied to impacts from curved faces. Data from a wider range of impact faces would be required to support this development. If this could be achieved, there is the potential to produce a single fracture risk curve which would be applicable to a range of impact face shapes.

Scalp thickness was not considered within this study. However, previous work has identified scalp thickness to play a part in fracture outcome (Raymond 2008), although the effect has not been quantified. Therefore, further investigation into the effect of scalp thickness is required to support further development of cranial fracture risk curves.

Fracture thresholds have been focused on the temporo-parietal region of the cranium. If there is a desire to develop fracture risk curves for the other regions of the skull then it is recommended that a similar approach to this study is taken; test group sizes of 20 data points should be considered as an absolute minimum.

It is recommended that further validation of the BSM data is undertaken. Cadaveric data should be generated for comparison with the extreme radius of curvature (hemispherical projectile) BSM fracture risk model. This would enable the relationship between the BSM and cadaveric risk models to be more fully understood.

To apply the cranial fracture risk models to assess BHBT, the assessment method would need to be capable of measuring the impact diameter and curvature. This could be achieved directly by instrumentation or potentially inferred from the signal profiles obtained. Where these measurements cannot be obtained, it is recommended that the fracture risks curves developed using the most severe impact, the 19 mm radius of curvature, are applied to existing BHBT assessment methods. This would enable prediction of the worse-case fracture outcome using measures of peak force.

Based on the findings of this study it is recommended that BHBT assessment methods measure deformation curvature and/or flat diameter as part of the data collected. Ideally the parameters of peak force, helmet BFD velocity and helmet BFD mass would also be measured. Methods using helmets placed on a head-form should also determine a consistent method for achieving and measuring stand-off. This stand-off should be representative of how the helmet would be worn.

## Reference List

- Aarabi, B. (1999). History of the Management of Craniocerebral Wounds. . Missile Wounds of the Head and Neck. K. H. Aarabi B, Dagi TF, George ED, Levy ML, eds., Park Ridge. 1.0: 12.
- Abbott, T.A. and Shephard, R.G. (1997). Protection Against Penetrating Injury. Scientific Foundations of Trauma. G. J. Cooper, H. A. F. Dudley, D. S. Gann, R. A. Little and R. L. Maynard. Oxford, Reed Educaional and Professional Publishing Ltd: 83-100.
- Allsop, D. and Kennett, K. (2001). Skull and Facial Bone Trauma - A Review. Accidental Injury: Biomechanics and Prevention.
- Allsop, D., Warner, C.Y., Wille, M.G., Schneider, D. and Nahum, A.M. (1988). Facial Impact Response - A Comparison of the Hybrid III and Human Cadaver. 32nd Stapp Car Crash Conference. Atlanta, Society of Automotive Engineers, Inc.: 16.
- Allsop, D.L., Perl, T.R. and Warner, C.Y. (1991). Force / Deflection and Fracture Characteristics of the Temporo-Parietal Region of the Human Head. 35th Stapp Car Crash Conference, San Diego.
- Anctil, B., Bayne, T., Bourget, D., Pageau, G., Binette, J.-S., Rice, K. and Toman, A. (2008). An Alternative to Plastilina for Evaluating the Performance of Body Armours. Personal Armour Systems Symposium. Brussels, Belgium, PASS: 10.
- Anctil, B., Bourget, D., Pageau, G., Dionne, J.-P., Wonnacott, M., Rice, K. and Toman, A. (2008). The Development of a Ballistic Helmet Test Standard. Personal Armour Systems Symposium, Brussels, Belgium.
- Anctil, B., Bourget, D., Pageau, G., Rice, K. and Lesko, J. (2004). Evaluation of Impact Force Measurement Systems for Assessing Behind Armour Blunt Trauma for Undefeated Ballistic Helmets. Personal Armour Systems Symposium: 10.
- Anctil, B., Keown, M., Bourget, D. and Pageau, G. (2005). A Novel Test Method to Assess the Performance of Ballistic Helmets. 22nd International Symposium on Ballistics. Vancouver, Canada.
- Anctil, B., Keown, M., Bourget, D., Pageau, G., Rice, K. and Davis, G. (2006). Performance Evaluation of Ballistic Helmet Technologies. Personal Armour Systems Symposium.
- Arborelius, U.P., Tyrberg, A., Gustavsson, J., Malm, E., Gryth, D., Olsson, L.G., Skoglund, M. and Rocksén, D. (2012). Physiological Effects in Pig, and Mechanical Response in an Armour Test Rig, to Graded Chest Impacts using a Behind Armour Blunt Trauma (BABT) Simulator. Personal Armour Systems Symposium. Nuremburg, Germany: p.305.
- Arnold, C. and Akin, S. (2001). Mechanical Properties of Synthetic Bone Materials - A Comparison with Bovine Scapulae. DERA, University of Wales Swansea.
- Arnold, C. and Atkin, S. (1999). Development of Bone Analogue Material. DERA, University of Wales Swansea.

- Backaitis, S.H. and Mertz, H.J.E. (1994). "Hybrid III: The First Human –Like Crash Test Dummy PT-44." Society of Automotive Engineers, Inc. .
- Barnes-Warden, J. and Fenne, P. (2013). Development Report for Evaluation of Ballistic Helmets. Metropolitan Police Service, Operational Technology, Physical Protection Group: 22.
- Bass, C., Boggess, R., Bush, B., Davis, B., Harris, M., Rountree, R.S., Campman, S., Eklund, J., Monacci, W., Ling, G., Holborow, G., Sanderson, E. and Waclawik, S. (2003). Helmet Behind Armour Blunt Trauma. Joint RTO AVT/HFM Specialists Meeting. Koblenz, Germany, RTO-MP-AVT-097: 18.
- Bass, C., Bolduc, M. and Waclawik, S. (2002). Development of a Non-Penetrating, 9 mm, Ballistic Helmet, Trauma Test Method. Personal Armour Systems Symposium.
- Bass, C.R., Boggess, B. and Bush, B. (2000). Ballistic Helmet Backface Deformation Testing with a Dummy Subject. Personal Armour Systems Symposium. P. L. K. Gotts, P.M. Colchester, UK. 4.
- Bir, C., Viano, D. and King, A. (2004). "Development of Biomechanical Response Corridors of the Thorax to Blunt Ballistic Impacts." *Journal of Biomechanics*(37): 6.
- Bo, W.J., Meschan, M.D. and Krueger, W.A. (1980). Basic Atlas of Cross-Sectional Anatomy, W.B. Saunders Company.
- Bolduc, M. (2009). Better Test Methods for Better Protection: A Summary of Efforts to Develop More Biofidelic Tools for Evaluating Helmets and Body Armours. International Personal Armour Committee Workshop, Paris, France, .
- Bolduc, M. and Anctil, B. (2010). Improved Test Methods for Better Protection, a BAPT Protocol Proposal for STANAG 2920. Personal Armour Systems Symposium. Quebec City, Canada: 10.
- Budras, K.-D. and Habel, R.E. (2003). Bovine Anatomy. Hannover, Germany, Schlutersche GmbH & Co.
- Bullock, R. and Graham, D.I. (1997). Non-Penetrating Injuries of the Head. Scientific Foundations of Trauma. G. J. Cooper, H. A. F. Dudley, D. S. Gann, R. A. Little and R. L. Maynard. Oxford, Reed Educational and Professional Publishing Ltd: 101-126.
- Byers, S.N. (2008). Blunt Trauma. Introduction to Forensic Anthropology 3rd Edition: 21.
- Cantu, R.C. (1995). "Head and Spine Injuries in Youth Sports." *Clinical Sports Medicine* 14(3): 15.
- Carr, D.J., Lewis, E.L. and Horsfall, I. (2016). "A Systematic Review of Military Head Injuries." *J R Army Med Corps Online*: 8.
- Cheeseman, B. and Bogetti, T. (2003). "Ballistic Impact into Fabric and Compliant Composite Laminates." *Composite Structures* 61: 13.
- Cheng, J.S. and Reichert, K.W. (1998). Adult and Child - Head Anatomy Frontiers in Head & Neck Trauma; Biomedical and Health Research. N. Yoganandan, F. Pintar, S. J. Larson and J. A. Sances, IOS Press, Ohmsha. 21: 3-33.

- Clarke, G.M. and Cooke, D. (2004). A Basic Course In Statistics. 338 Euston Road, London, Arnold, a member of the Hodder Headline Group.
- Crawford, G.S. (2008). Biomechanical Response of the Human Frontal Bone and Zygoma to Blunt Ballistic Impacts. Doctor of Philosophy, Wayne State University.
- CSA-TC-Z613 (2008). Canadian Standards Association (CSA) Z613 Ballistic Helmets Test Standard - Test Standard Overview. Biokinetics and Associates Ltd.: 25.
- DE&S (2010). Fit, Care and Inspection of: Combat Assault Mk7 Helmet (5-Point Fixing Harness).[http://www.army.mod.uk/documents/general/20100705-Helmet\\_Mk7\\_Instruction.pdf](http://www.army.mod.uk/documents/general/20100705-Helmet_Mk7_Instruction.pdf). D. S. MOD. [www.army.mod.uk](http://www.army.mod.uk).
- Delye, H., Verschueren, P., Depreitere, B., Verpoest, I., Berckmans, D., Vander Sloten, J., Van Der Perre, G. and Goffin, J. (2007). "Biomechanics of Frontal Skull Fracture." Journal of Neurotrauma 24: 10.
- Ellis, S., Mansson, R., Craddock, L. and Helliker, M. (2013). Design and Analysis of Binary Trials. The Institute of Mathematics & its applications Conference - Mathematics in Defence QinetiQ, Malvern, UK.
- Evans-Pughe, C. (2014). New Designs, New Materials. Engineering and Technology Magazine, The Institute of Engineering and Technology. 9: 1.
- Finney, D.J. (1952). Probit Analysis. Cambridge, England, Cambridge University Press.
- Food Standards Agency (2005). BSE and Beef New Controls Explained. F. S. Agency. England, Food Standards Agency.
- Freitas, C.J., Gray, W.M., Mathis, J.T. and Weiss, C.E. (2010). Behind Helmet Blunt Trauma Experiments with a Human Head Surrogate. Personal Armour Systems Symposium Quebec Canada: 10.
- Freitas, C.J., Mathis, J.T., Scott, N., Bigger, R.P. and MacKiewicz, J. (2014). "Dynamic Response Due to Behind Helmet Blunt Trauma Measured with a Human Head Surrogate." International Journal of Medical Sciences 11(5): 14.
- Gadd, C.W., Nahum, A.M., Gatts, J. and Danforth, J.P. (1968). A Study of Head and Facial Bone Impact Tolerances. GM Automotive Safety Seminar, Detroit.
- Ganong, W.F. (2005). Review of Medical Physiology, Lange Medical Books/McGraw-Hill.
- GOM Optical measurement techniques (2009). ARAMIS. Braunschweig, Germany. Software, Version 6.1.
- GOM Optical measurement techniques (2011). ARAMIS. Braunschweig, Germany. Software, Version 6.2.
- Goodrich, S.G. (1885). The Animal Kingdom Illustrated. New York, A. J. Johnson & Co. 2015.
- Gray, H. (1973). Gray's Anatomy. Edinburgh, Longman Group Ltd.

- Hansen, U., Zioupos, P., Simpson, R., Curry, J.D. and Hynd, D. (2008). "The Effect of Strain Rate on the Mechanical Properties of Human Cortical Bone." *Journal of Biomechanical Engineering* 130: 8.
- Hisley, D., Gurgaus, J., Lee, J., Williams, S. and Drysdale, A. (2010). *Experimental Methodology Using Digital Image Correlation (DIC) to Assess Ballistic Helmet Blunt Trauma*. A. R. L. Survivability / Lethality Analysis Directorate, US. ARL: 23.
- Hodgson, V.R., Brinn, J., Thomas, L.M. and Greenberg, S.W. (1970). *Fracture Behaviour of the Skull Frontal Bone against Cylindrical Surfaces*. 14th STAPP Car crash Conference.
- Hodgson, V.R. and Thomas, L.M. (1971). *Comparison of Head Acceleration Injury Indices in Cadaver Skull Fracture*, SAE Technical Paper.
- HP White laboratories (1995). *Test Procedure - Bullet Resistant Helmet, Ballistic Resistance of Personal Body Armour*. Maryland, United States HPW. TP 0401.01B.
- Human Tissue Act (2004). *Human Tissue Act 2004*. H. T. Authority.
- imc Measurement and Control (2011). *FAMOS Signal analysis, Software, Version 6.1 Rev.7*.
- James, G.R. and Sedman, A.J. (2009). *Refinement of Skull Fracture Models*. Internal Dstl Report.
- Kent, R.W. and Funk, J.R. (2004). "Data Censoring and Parametric Distribution Assignment on the Development of Injury Risk Functions from Biochemical Data." *SAE International* 1: 10.
- Keown, M., Fournier, E., Williams, K., Taok, D. and Anctil, B. (2006). *Characterization of Helmet Energy Absorbing Liner Materials*. Personal Armour Systems Symposium.
- Kosmidis, I. (2013). *brglm: Bias Reduction in Binomial-Response Generalized Linear Models*, Computer Programme, R Package.
- Kosmidis, I. and Firth, D. (2010). "A Generic Algorithm for Reducing Bias in Parametric Estimation." *Electronic Journal of Statistics* 4: 15.
- Lewis, M.E. (2006). *Head Injury and Protection*. *Ernsting's Aviation Medicine*. D. J. G. Rainford, D.P., Edward Arnold (Publishers) Ltd: 179-188.
- Lindemulder, J.L. and Beugels, J. (1998). *Development of a Bullet and Fragment Resistant Dyneema UD helmet*. Personal Armour Systems Symposium. P. M. K. P.L. Gotts. Colchester, UK. 3: P.221 start.
- Lissner, H., Lebow, M. and Evans, F. (1960). "Experimental Studies on the Relation Between Acceleration and Intracranial Pressure Changes in Man." *Surgery, Gynecology & Obstetrics* 111: 329-338.
- Liu, H., Kang, J., Chen, J., Li, G., Li, X. and Wang, J. (2012). "Intracranial Pressure Response to Non-Penetrating Ballistic Impact: an Experimental Study Using a Pig Physical Head Model and Live Pigs." *International Journal of medical Sciences* 9(8): 10.

- Lucuta, V., Czeremuskin, G., Latreche, M., Samborsky, S. and A., T. (2014). Ballistic Limit and Dynamic Back-Face Deformation of Helmet Shell Composite Materials and Corresponding Deformation of the Projectiles. Personal Armour Systems Symposium.
- Maynard, R.L., Allen, I.V. and Hull, J.B. (1997). Penetrating Head Injury. Scientific Foundations of Trauma. G. J. Cooper, H. A. F. Dudley, D. S. Gann, R. A. Little and R. L. Maynard. Oxford, Reed Educational and Professional Publishing Ltd: 53-62.
- McCormick, N. and Lord, J. (2010). "Digital Image Correlation,." Materials Today 13(12): 52-54.
- Medical-Dictionary (2003). Oxford Concise Medical Dictionary, 6th Edition. Market House Books Ltd, Oxford University Press.
- Melvin, J.W. and Evans, F.G. (1968). A Strain Energy Approach to the Mechanics of Skull Fracture. 12th STAPP Car crash Conference. Detroit: 20.
- Merkle, A., Carneal, K., Wickwire, A., Ott, K., Freitas, C. and Tankard, S. (2010). Evaluation of Threat Conditions and Suspension Pad Configurations in Determining Potential for Behind Helmet Blunt Trauma. Personal Armour Systems Symposium. Quebec City, Canada: 10.
- Moore, K.L. and Dalley, A.F. (1999). Clinically Orientated Anatomy, Lippincott Williams & Wilkins.
- Moritz, A.R. (1943). "Mechanisms of Head Injury." Annals of Surgery 117(4): 14.
- Motherway, J.A., Verschueren, P., Van der Perre, G., Vander Sloten, J. and Gilchrist, M.D. (2009). "The Mechanical Properties of Cranial bone: The Effect of Loading Rate and Cranial Sampling Position." Journal of Biomechanics 42: 7.
- MPS DOI-MTD-03/010 (2003). Metropolitan Police Service Ballistic Helmet Test methodology
- Nahum, A.M., Gatts, J.D., Gadd, C.W. and Danforth, J. (1968). "Impact Tolerance of the Skull and Face." SAE Transactions 77: 17.
- National Research Council (2014). Review of Department of Defense test protocols for combat helmets. Washington (DC), National Academies Press.
- Neale, M. and Allanson-Bailey, L.S. (2012). Development of a BABT head model - Final report. DSTL.
- Neale, M. and Allanson-Bailey, L.S. (2013). Blunt Impact Injury Model System. DSTL. UK. 1: 20.
- NIJ 0106.01 (1981). U.S. Department of Justice, National Institute of Justice Standard for Ballistic Helmets National Institute of Justice: 16.
- Nusholtz, G.S., Lux, P., Kaiker, P. and Janicki, M.A. (1993). Head Impact Response - Skull Deformation and Angular Accelerations. Biomechanics of Impact Injury and Injury Tolerances of the Head-Neck Complex. S. H. Backaitis. Warrendale, US, Society of Automotive Engineers, Inc. PT-43: 34.

Nyman, J.S., Roy, A., Shen, X., Acuna, R.L., Tyler, J.H. and Wang, X. (2006). "The Influence of Water Removal on the Strength and Toughness of Cortical Bone." *Journal of Biomechanics* 39(5): 931-938.

Oldendorf, W.H. and Lisaka, Y. (1960). "Interference of Scalp and Skull with External Measurements of Brain Isotope Content: Part 1. Isotope Content of Scalp and Skull." *The Journal of Nuclear Medicine* 10(4): 7.

Ono, K., Kikuchi, A., Nakamura, M., Kobayashi, H. and Nakamura, N. (1993). Human Head Tolerance to Sagittal Impact - Reliable Estimation Deduced from Experimental Head Injury Using Subhuman Primates and Human Cadaver Skulls. *Biomechanics of Impact Injury and Injury Tolerances of the Head-Neck Complex*. S. H. Backaitis. Warrendale, US, Society of Automotive Engineers, Inc. PT-43.

Patrick, L.M., Mertz, H.J. and Kroell, C.K. (1993). Cadaver Knee, Chest and Head Impact Loads. *Biomechanics of Impact Injury and Injury Tolerances of the Head-Neck Complex*. S. H. Backaitis. Warrendale, US, Society of Automotive Engineers, Inc. PT-43: 10.

Protection of Human Subjects (2009). Protection of Human Subjects. Title 45 Public Welfare. U. D. o. H. a. H. Services. US Code of Federal Regulations. Part 46 Protection of Human Subjects.

R Core Team (2012). R: A Language and Environment for Statistical Computing. R Foundation for Statistical Computing, Vienna, Austria, Computer Program.

Raymond, D. (2008). Biomechanics of Blunt Ballistic Temporo-Parietal Head Impact. Doctor of Philosophy, Wayne State University.

Raymond, D., Crawford, G., Van Ee, C. and Bir, C. (2008). Biomechanics of Temporo-Parietal Skull Fracture from Blunt Ballistic Impact. ASME 2008 Summer Bioengineering Conference (SBC2008), Florida, USA, ASME.

Raymond, D., Crawford, G., Van Ee, C. and Bir, C. (2008). The Effect of Soft Tissue on the Biomechanics of Skull Fracture Due to Blunt Ballistic Impact: Preliminary Analysis and Findings. ASME 2008 Summer Bioengineering Conference (SBC2008) Florida USA, ASME.

Rustemeyer, J., Kranz, V. and Bremerich, A. (2007). "Injuries in Combat from 1982–2005 with Particular Reference to Those to the Head and Neck: A Review." *British Journal of Oral and Maxillofacial Surgery* 45(7): 556-560.

Sarron, J.-C., Caillou, J.-P., Da Cunha, J., Allain, J.-C. and Tramecon, A. (2000). "Consequences of Nonpenetrating Projectile Impact on a Protected Head: Study of Rear Effects of Protections." *The Journal of Trauma, Injury, Infection, and Critical Care* 49(5): 7.

Sarron, J.-C., Dannawi, M., Faure, A., Caillou, J.-P., Da Cunha, J. and Robert, R. (2004). "Dynamic Effects of a 9 mm Missile on Cadaveric Skull Protected by Aramid, Polyethylene or aluminium Plate: An experimental Study." *The Journal of Trauma, Injury, Infection, and Critical Care* 57: 7.

Schneider, D.C. and Nahum, A.M. (1972). Impact Studies of Facial Bones and Skull. 16th STAPP Car Crash Conference, New York, Society of Automotive Engineers.



- Shadrake, D. (2014). WW1: Combat Helmet Technology - The Brodie Steel Helmet. *Engineering and Technology Magazine*, The Institute of Engineering and Technology. 9.
- Slobodnik, B. (1982). Correlation of Head Injury with Mechanical Forces Based on Helmet Damage Duplication: 12.
- Sowry, P.J.B. (1998). An Investigation into Potential Composites for a Lightweight Helmet. *Personal Armour Systems Symposium*. P. M. K. P.L. Gotts. Cholchester, UK. 3: Start P.51.
- STANAG-2902 (2004). North Atlantic Treaty Organization Standardization Agency,. Criteria for a NATO Combat Helmet, NATO/PfP: 14.
- STANAG-2920 (2003). North Atlantic Treaty Organization Standardization Agency,. Ballistic Test Method for Personal Armour Materials and Combat Clothing, NATO/PfP.
- STANAG AEP 2920 (2015). North Atlantic Treaty Organization Standardization Agency,. Procedures for the Evaluation and Classification of Personal Armour, Bullet and Fragmentation Threats. NATO Standardization Office (NSO), NATO Standardization Office (NSO): 106.
- Strachan, D.S. (1993). *The Anatomy and Physiology of the Head and Neck Biomechanics of Impact Injury and Injury Tolerances of the Head-Neck Complex*. S. H. Backaitis. Warrendale, Society of Automotive Engineers, Inc.: 15-25.
- Sturdivan, L.M., Viano, D.C. and Champion, H.R. (2004). "Analysis of Injury Criteria to Assess Chest and Abdominal Injury Risks in Blunt and Ballistic Impacts." *Journal of Trauma and Acute Care Surgery* 56(3): 651-663.
- Taylor, D.E.M. and Whammond, J.S. (1997). The Possible use of Bove Scapula as an Analogue for the Human Skull in Experimental Blunt Trauma. DERA, Royal College of Surgeons, Lincoln's Fields, London, WC2A 3PN: 11.
- Tedeschi, C. (1977). "The Wound—Assessment by Organ Systems, I The head and spine." Tedeschi CG, Eckert WG, Tedeschi LG. *Forensic medicine*. Saunders: 29-75.
- Tortora, G.J. and Anagnostakos, N.P. (1990). *Principles of Anatomy and Physiology*. New York, Harper & Row.
- Tubbs, R.S., Murphy, R.L., Golden, J.B., Etheridge, B., Wellons, J.C., Blount, J.P., Salter, E.G. and Oakes, W.J. (2005). "The Results of Compression Forces Applied to the Isolated Human Calvaria." *Folia Morphol* 64(4): 5.
- Walker, L.B., Harris, E.H. and Pontius, U.R. (1973). Mass, Volume, Centre of Mass and Mass Moment of Inertia of Head and Head and Neck of Human Body. 17th Stapp Car Crash Conference, Oklahoma City, OK.
- Wallace, D. and Rayner, S. (2012). "Combat Helmets and Blast Traumatic Brain Injury." *Journal of Military and Veterans' Health* 20(1).
- Watson, C., Webb, A. and Horsfall, I. (2008). Assessment of Potential Blunt Trauma Under Ballistic Helmets. *Personal Armour Systems Symposium*.

Welch, B.L. (1947). "The Generalization of 'Student's' Problem When Several Different Population Variances Are Involved." *Biometrika* 34(1-2): 28-35.

Widmaier, E.P., Raff, H. and Strang, K.T. (2004). *Vander, Sherman, Luciano's Human Physiology: The Mechanisms of Body Function*. New York, McGraw-Hill.

Wilber, C.G. (1974). *Various Violent Deaths: Head Wounds*. Forensic Biology of the Law Enforcement Officer. Springfield, Charles C. Thomas Ltd.: 3.

Yoganandan, N. and Pintar, F. (2004). "Biomechanics of Temporal-Parietal Skull Fracture - A Review." *Clinical Biomechanics*(19): 14.

Yoganandan, N., Pintar, F.A., Sances, J.A., Walsh, P.R., Ewing, C.L., Thomas, D.J. and Snyder, R.G. (1995). "Biomechanics of Skull Fracture." *Journal of Neurotrauma* 12(4): 10.

Zhang, L., Yang, K.H. and King, A.I. (2004). "A Proposed Injury Threshold for Mild Traumatic Brain Injury." *Journal of Biomechanical Engineering* 126(2): 226-236.

## Appendix A: BSM Strain gauge data

### Data collection

Strain BSMs and DIC BSMs contained Vishay type 062UR tri-axial rosette strain gauges. Amplification of the strain gauge signals was achieved using one of six Endevco Model 136 DC 5 volt amplifiers, containing 4-pole anti-aliasing Butterworth filters. Cable lengths between the gauges and amplifiers were kept to a minimum by positioning the Endevco units on top of the target frame (Figure A). The amplified strain gauge outputs were collected simultaneously through multiple data channels using a Saturn Data Transient Recorder (SN: 1515-0506-0054-10).

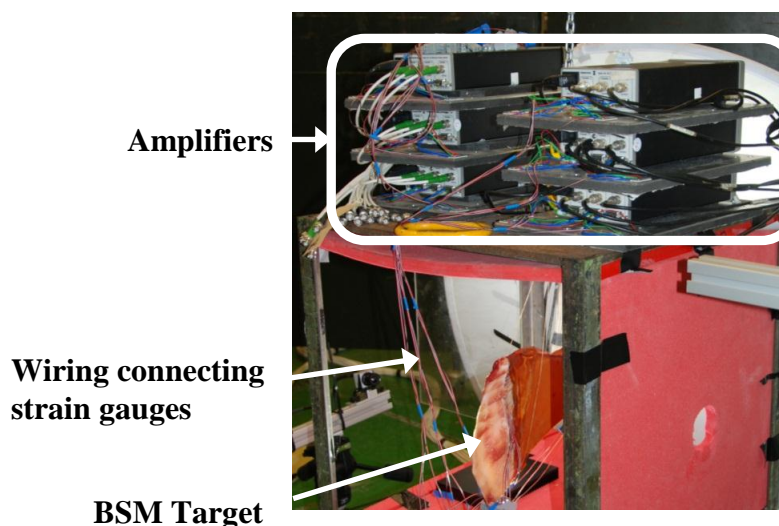


**Figure A:** Position of strain gauge amplifiers on top of target frame. This arrangement was used within the range set-up to investigate BSMs as fracture models of the cranium.

Settings were determined for the Saturn Data Transient Recorder (Table A). These were advised from previous strain data collection (J. Henshall, personal communication), in addition to optimising the input range following data collection from two BSM targets.

Input Parameter	Setting
Mode	Single
Impedance	1 Mohm
Range	40 V
Offset	0%
Input Range	-20 V ~ 20 V
Sample Rate	3 MHz
Trigger	1 V
Pre-Trigger	10%
Sample Time	-50 ms ~ 450 ms

Figure A: Saturn Data Transient Recorder settings for strain gauge data capture.

## Strain gauge data analysis

Using the formulas detailed in Equation A, principle strains and maximum shear strain for each tri-axial rosette strain gauge were calculated from the strain data. The calculated strains were filtered using a 4-pole Butterworth filter with a cut-off frequency of 4300 Hz; the same filter Raymond (2008) applied to the strain data obtained in the investigation of cadaveric specimens.

The peak values were identified for each strain gauge and the maximum shear strain for each impact recorded. This process was completed within FAMOS signal analysis software (imc Measurement and Control 2011). The peak values of principle strains 1, 2 and the maximum shear strain did not occur at the same time, highlighting that the change in strain field is not uniform due to the non-homogeneous nature of bone.

$$\text{Principle Strain 1: } \varepsilon_1 = \frac{1}{2}(\varepsilon_A + \varepsilon_C) + \left(\frac{1}{2}[(\varepsilon_A - \varepsilon_C)^2 + (2\varepsilon_B - \varepsilon_A - \varepsilon_C)^2]\right)^{\frac{1}{2}}$$

$$\text{Principle Strain 2: } \varepsilon_2 = \frac{1}{2}(\varepsilon_A + \varepsilon_C) - \left(\frac{1}{2}[(\varepsilon_A - \varepsilon_C)^2 + (2\varepsilon_B - \varepsilon_A - \varepsilon_C)^2]\right)^{\frac{1}{2}}$$

$$\text{Maximum Shear Strain: } \gamma_{max} = 2 \left(\frac{1}{2}[(\varepsilon_A - \varepsilon_C)^2 + (2\varepsilon_B - \varepsilon_A - \varepsilon_C)^2]\right)^{\frac{1}{2}}$$

**Equation A: Principle and maximum shear strain calculation where  $\varepsilon_A$ ,  $\varepsilon_B$  and  $\varepsilon_C$  represent the three individual gauges that form the rectangular rosette.**

## Strain gauge results

Strain measures were obtained from each gauge and filtered through post processing (Figure B). The strain values are individually reported within the trial data (Appendix E). The peak shear strains for Strain and DIC BSMs showed generally higher strains associated with fracture outcomes compared to non-fracture outcomes (Table B). This was as expected, with a large overlap due to biological variation across the scapula tested. The largest strain measured for fracture outcomes was double that of the maximum strain associated with non-fracture.

Where strain gauges were applied to the medial and lateral surfaces of the bone, non-fracture outcomes showed lower strain measures on the lateral (non-impact) surface of the bone when compared to the medial (impact) surface (Table C). For the fracture outcomes, the strain measures do not show a clear pattern; at the lower end of the scale the lateral (non-impact) surface has the lowest strains. However, at the top of the scale, the largest strains are also observed on the lateral surface. This variability is likely to be due to the mechanism of failure of the bone and the extent of the fracture caused.

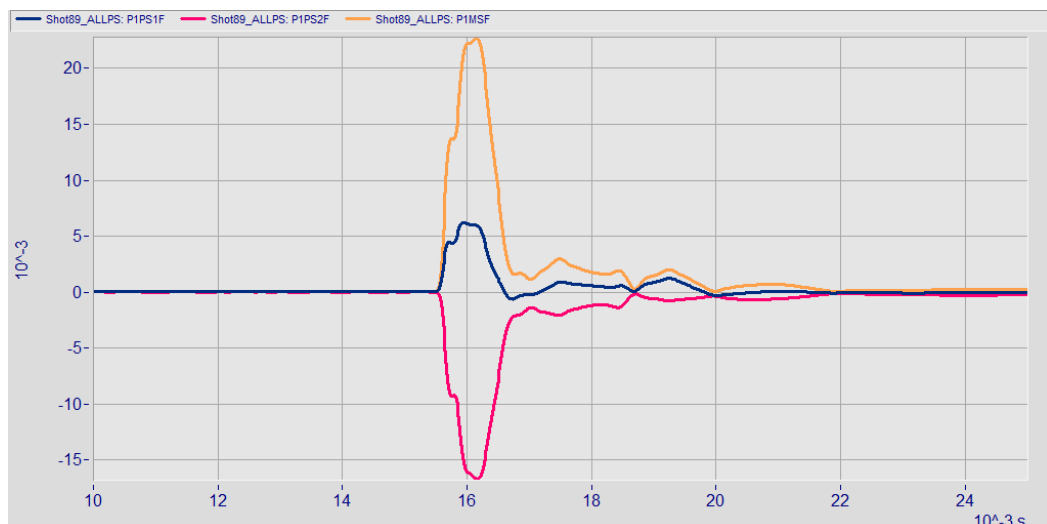


Figure B: Shot #89, Strain BSM #47 strain gauge one. Principle strain 1 shown in dark blue (Shot89\_ALLPS:P1PS1F), Principle strain 2 shown in red (Shot89\_ALLPS:P1PS2F) and the maximum shear strain represented by the yellow curve (Shot89\_ALLPS:P1MSF) extracted from FAMOS signal analysis software.

Group	Total number of models	No. 3 strain gauge models	No. 6 strain gauge models	Peak Shear Strain (microstrain)	
				Non-Fracture	Fracture
<b>B</b>	22	14	8	4296 - 15566	6006 - 34327
<b>C</b>	25	9	6	4273 - 12755	9858 - 29229

**Table B: Peak shear strain measures for Strain and DIC BSMs.**

Surface	Peak Shear Strain (microstrain)	
	Non-Fracture	Fracture
<b>Medial</b>	4274 - 15566	9863 - 24992
<b>Lateral</b>	3425 - 14496	7463 - 27894

**Table C: Comparison of medial and lateral shear strain measures for Strain and DIC BSM impacts.**

## **Appendix B: BSM Digital Image Correlation strain data**

### **Digital Image Correlation (DIC) data collection**

The DIC technique has previously been used to collect velocity, deformation and strain of a helmet material surface under impact (Hisley *et al.* 2010). The DIC software used in this study was developed by GOM Optical Measuring Techniques of Braunschweig, Germany, utilizing an ARAMIS software package v6.2.0-6 (GOM Optical measurement techniques 2011).

When testing the DIC BSMs, padding at the rear of the cuboid frame was removed and two Photron MC2 HSV cameras were placed behind the BSM target. The cameras collected images at 8000 frames per second to enable the surface of the bone to be stereoscopically tracked through the DIC analysis.

### **DIC data analysis**

The images collected by the two Photron MC2 HSV cameras were imported into ARAMIS Version 6.2.0-6 (GOM Optical measurement techniques 2011) software for post processing. The displacement of the bone and related strain measures were obtained from three-dimensional DIC analysis.

Calibration was required to determine the HSV camera positions relative to one another. This provided a measured volume within which the DIC BSMs could be visualised (GOM Optical measurement techniques 2011). The calibration process was achieved by moving National Institute of Standards and Technology (NIST) calibration panels through the imaging area, in a defined sequence. Using the 2D camera images, the ARAMIS software triangulated 3D coordinates of reference points to determine a local coordinate system or measured volume. The scapula surface was then imaged within this calibrated area.

## DIC results

Three-dimensional DIC was completed for 24 of the 25 DIC BSMs impacted. The ARAMIS software was able to track the dynamic displacement of the tattooed bone (Figure C), producing a plot of peak percentage strain for the impact (Figure D).

Peak strains in the range of 3.8% to 17.8% were identified for samples which fractured under impact. This related to a maximum deformation of the bone in the range of 5 mm to 10 mm. DIC measurements were disrupted as soon as the high contrast pattern became damaged, either by removal of the tattoo from the bone surface or due to fracture.

Non-fracture impacts showed strain measures in the range of 1 to 9.8%, relating to displacements in the range of 3 mm to 6 mm. An error of 0.8% was identified for the strain measures and 0.8 mm for the displacement. The reported error of 0.8% strain relates to an 8000 microstrain.

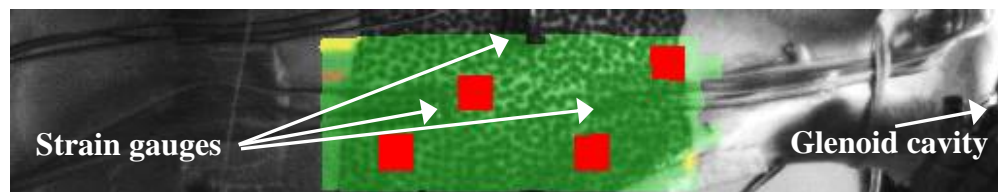


**Figure C: Shot #110 HSV image of the lateral surface of BSM #49 within ARAMIS (GOM Optical measurement techniques 2011), with the area identified for tracking highlighted in green and tracking points in red.**



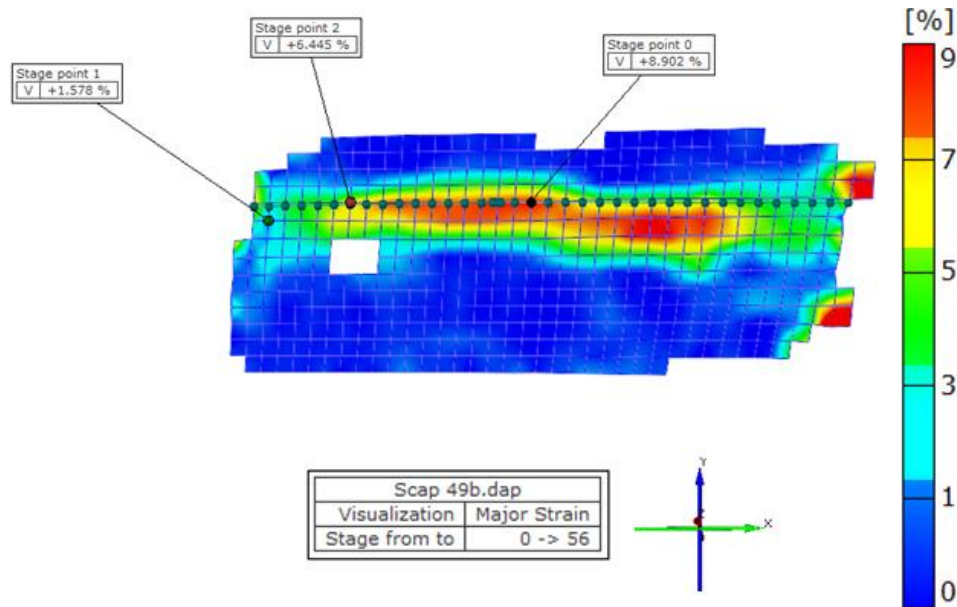


**Figure D:** Post processing image of Figure (Shot #110, BSM #49) within ARAMIS (GOM Optical measurement techniques 2011). The colour scale represents the strain observed; red being the greatest areas of strain (9% strain) and blue showing low levels of strain (0% strain) within the lateral surface of the bone. Three points within the plot have been identified with associated values of strain.

The DIC BSMs showed that DIC can be achieved on the surface of bone. DIC may be a technique which is used in future testing to observe the response of bone throughout impact, developing understanding of the failure mechanism.

Using the DIC technique, higher strains were observed for fracture outcomes when compared to non-fracture impacts, as would be expected. However, the percentage strains calculated within ARAMIS were an order of magnitude higher than those obtained from the strain gauges. Reporting by Raymond (2008) and Freitas *et al.* (2014) on strain measures from impacts to the cranium aligns with the BSM strain gauge measures, indicating the gauge data to be representative of the expected magnitude of strain for the cranium. Further investigation of the ARAMIS percentage strain calculation process and the relationship between the DIC and gauge strain measures would enable determination of the reasons for the differences between strain measures from DIC and gauge techniques.

## Appendix C: Probit curve calculation script for projectile velocity

The R (R Core Team 2012) script (R. Mansson) used to determine the probit curve for binary output trials.

```
require(brglm)

require(MASS)

test.df = read.csv("test-data.csv")

mod1 = brglm(Outcome ~ V, data = test.df, family = binomial(link = probit))

dose.p(mod1, p = c(0.001, 0.002, 0.005, 0.01, 0.05, 0.10, 0.15, 0.20, 0.25, 0.30, 0.35, 0.40,
0.45, 0.50, 0.55, 0.60, 0.65, 0.70, 0.75, 0.80, 0.85, 0.90, 0.95, 0.99, 0.995, 0.998, 0.999))

Vp.values = dose.p(mod1, p = c(0.001, 0.002, 0.005, 0.01, 0.05, 0.10, 0.15, 0.20, 0.25,
0.30, 0.35, 0.40, 0.45, 0.50, 0.55, 0.60, 0.65, 0.70, 0.75, 0.80, 0.85, 0.90, 0.95, 0.99, 0.995,
0.998, 0.999))

Vp.table = data.frame(

  Probability = c(0.001, 0.002, 0.005, 0.01, 0.05, 0.10, 0.15, 0.20, 0.25, 0.30, 0.35,
0.40, 0.45, 0.50, 0.55, 0.60, 0.65, 0.70, 0.75, 0.80, 0.85, 0.90, 0.95, 0.99, 0.995, 0.998,
0.999),

  Vp = as.numeric(Vp.values),

  Vp.SE = as.numeric(attr(Vp.values, "SE"))

Vp.table$Lower.CI = Vp.table$Vp - 1.96 * Vp.table$Vp.SE

Vp.table$Upper.CI = Vp.table$Vp + 1.96 * Vp.table$Vp.SE

  Vp.table

summary(mod1)
```

## Appendix D: BSM construction post-trial statistical analysis script

The R (R Core Team 2012) script used to investigate the BSM constructions and cadaveric data (L. Craddock).

```
require(brglm)

require(MASS)

require(ggplot2)

theme_set(theme_bw())

require(lattice)

##### Data Processing

data2=read.csv("20140109-data2.csv") ## reading data from csv file

head(data2) ## view first 6 rows of data

data2$group= factor(data2$group, levels= c("R","A","B","C")) ### setting order of
groups, first is used as a baseline of model, this should be what you want to compare to

##### Fit Model

##help(brglm)

## view help page

frac.mod4 = brglm(Fracture~ OEHLER.Velocity * thickness.average * Mass * group,
data=data2, family = binomial(probit), method = "brglm.fit")

### full brglm model

summary(frac.mod4) ### View model results

confint.default(frac.mod4) ### View 95% Confidence Intervals

##### Fit Reduced Model

frac.mod3=brglm(Fracture~ OEHLER.Velocity+Mass + group, data=data2, family =
binomial(probit), method = "brglm.fit") ### Reduced brglm model (remove highest
order interaction with highest non sig p-value, and repeat till best model is achieved)

summary(frac.mod3) ### View model results

confint.default(frac.mod3) ### View 95% Confidence Intervals

plot(frac.mod3) ### View model assumptions - check 2nd graph

##### Create 3D plot
```

```

frac.mod3.fitR = expand.grid(OEHLER.Velocity = seq(5, 60, length.out=50), Mass =
seq(1, 8, length.out=50), group="R")

###choose min and max for variables (velocity and mass) and number of points between
wanted (how smooth?) and state which group

frac.mod3.fitR$Fit = predict(frac.mod3, newdata = frac.mod3.fitR, type = "response")
###Create data for group R based on model

frac.mod3.fitA = expand.grid(OEHLER.Velocity = seq(5, 60, length.out=50), Mass =
seq(1, 8, length.out=50), group="A")

###choose min and max for variables (velocity and mass) and number of points between
wanted (how smooth?) and state which group

frac.mod3.fitA$Fit = predict(frac.mod3, newdata = frac.mod3.fitA, type = "response")
###Create data for group A based on model

frac.mod3.fitB = expand.grid(OEHLER.Velocity = seq(5, 60, length.out=50), Mass =
seq(1, 8, length.out=50), group="B")

###choose min and max for variables (velocity and mass) and number of points between
wanted (how smooth?) and state which group

frac.mod3.fitB$Fit = predict(frac.mod3, newdata = frac.mod3.fitB, type = "response")
###Create data for group B based on model

frac.mod3.fitC = expand.grid(OEHLER.Velocity = seq(5, 60, length.out=50), Mass =
seq(1, 8, length.out=50), group="C")

###choose min and max for variables (velocity and mass) and number of points between
wanted (how smooth?) and state which group

frac.mod3.fitC$Fit = predict(frac.mod3, newdata = frac.mod3.fitC, type = "response")
###Create data for group C based on model

frac.mod3.fit= rbind( frac.mod3.fitR, frac.mod3.fitA, frac.mod3.fitB, frac.mod3.fitC)
### Combine the 4 new datasets

wireframe(Fit~OEHLER.Velocity*Mass|group,      data=frac.mod3.fit,      drape=TRUE,
colorkey=FALSE)

### Produce 3D plot

##### Create 2D plot

frac.mod3=brglm(Fracture~ OEHLER.Velocity + group, data=data2, family =
binomial(probit), method = "brglm.fit")

##### Model with only 2 variables explaining variation in fracture summary(frac.mod3)

frac.mod3.fitR = expand.grid(OEHLER.Velocity = seq(5, 60, length.out=50), group="R")

###choose min and max for variable (velocity) and number of points between wanted (how
smooth?) and state which group

```

```

frac.mod3.fitR$Fit = predict(frac.mod3, newdata = frac.mod3.fitR, type = "response")
####Create data for group R based on model

frac.mod3.fitA = expand.grid(OEHLER.Velocity = seq(5, 60, length.out=50), group="A")
####choose min and max for variable (velocity) and number of points between wanted (how
smooth?) and state which group

frac.mod3.fitA$Fit = predict(frac.mod3, newdata = frac.mod3.fitA, type = "response")
####Create data for group A based on model

frac.mod3.fitB = expand.grid(OEHLER.Velocity = seq(5, 60, length.out=50), group="B")
####choose min and max for variable (velocity) and number of points between wanted (how
smooth? )and state which group

frac.mod3.fitB$Fit = predict(frac.mod3, newdata = frac.mod3.fitB, type = "response")
####Create data for group B based on model

frac.mod3.fitC = expand.grid(OEHLER.Velocity = seq(5, 60, length.out=50), group="C")
####choose min and max for variable (velocity) and number of points between wanted (how
smooth?)and state which group

frac.mod3.fitC$Fit = predict(frac.mod3, newdata = frac.mod3.fitC, type = "response")
####Create data for group C based on model

ggplot(data2, aes(x = OEHLER.Velocity, y = Fracture, colour= group)) + geom_point() +
#### Draws 2D graph

geom_line(aes(x = OEHLER.Velocity, y = Fit), data = frac.mod3.fitR)+
geom_line(aes(x = OEHLER.Velocity, y = Fit), data = frac.mod3.fitA)+
geom_line(aes(x = OEHLER.Velocity, y = Fit), data = frac.mod3.fitB)+
geom_line(aes(x = OEHLER.Velocity, y = Fit), data = frac.mod3.fitC)

```

## Appendix E: Data for the investigation of BSM variants as a fracture analogue of the cranium

BSM Construction	Scapula No.	Avg. Bone Thickness (mm)	Model Mass (kg)	Velocity (m·s <sup>-1</sup> )	Outcome	Fracture Index	Peak Medial Strain Gauge Data			Peak Lateral Strain Gauge Data		
							Principle Strain 1 (microstrain)	Principle Strain 2 (microstrain)	Max Shear strain (microstrain)	Principle Strain 1 (microstrain)	Principle Strain 2 (microstrain)	Max Shear strain (microstrain)
Original	9	4.8	3.9	22.1	Non-fracture	1	-	-	-	-	-	-
Original	21	3.4	3.9	23.0	Non-fracture	1	-	-	-	-	-	-
Original	5	6.4	5.9	29.7	Non-fracture	1	-	-	-	-	-	-
Original	16	5.9	5.0	40.9	Non-fracture	1	-	-	-	-	-	-
Original	15	4.6	4.3	45.0	Fracture	2	-	-	-	-	-	-
Original	6	4.0	4.7	45.2	Non-fracture	1	-	-	-	-	-	-
Original	8	4.1	4.7	51.0	Fracture	2	-	-	-	-	-	-
Original	13	3.4	5.0	47.8	Fracture	3	-	-	-	-	-	-
Original	18	4.0	3.6	48.2	Fracture	4	-	-	-	-	-	-
Original	2	4.6	5.9	46.4	Non-fracture	1	-	-	-	-	-	-
Original	10	6.2	4.4	49.3	Fracture	3	-	-	-	-	-	-
Original	22	2.8	3.6	48.0	Fracture	4	-	-	-	-	-	-
Original	11	3.5	4.5	47.9	Fracture	4	-	-	-	-	-	-
Original	32	3.5	3.6	41.8	Non-fracture	1	-	-	-	-	-	-
Original	28	3.8	3.8	43.1	Fracture	3	-	-	-	-	-	-
Original	35	6.3	3.9	44.8	Fracture	2	-	-	-	-	-	-
Original	29	3.5	3.6	45.9	Fracture	3	-	-	-	-	-	-
Original	34	3.6	4.3	42.1	Non-fracture	1	-	-	-	-	-	-
Original	33	4.1	3.8	41.1	Non-fracture	1	-	-	-	-	-	-
Original	45	3.6	3.6	40.9	Fracture	4	-	-	-	-	-	-
Original	46	4.5	4.1	48.1	Fracture	2	-	-	-	-	-	-
Original	44	5.5	4.5	40.0	Non-fracture	1	-	-	-	-	-	-

BSM Construction	Scapula No.	Avg. Bone Thickness (mm)	Model Mass (kg)	Velocity (m·s <sup>-1</sup> )	Outcome	Fracture Index	Peak Medial Strain Gauge Data			Peak Lateral Strain Gauge Data		
							Principle Strain 1 (microstrain)	Principle Strain 2 (microstrain)	Max Shear strain (microstrain)	Principle Strain 1 (microstrain)	Principle Strain 2 (microstrain)	Max Shear strain (microstrain)
Strain +3	19	2.9	4.1	47.6	Fracture	4	2517	-3880	6006	-	-	-
Strain +3	17	6.4	4.0	42.6	Fracture	2	4790	-4394	9178	-	-	-
Strain +3	1	4.0	3.4	43.3	Non-fracture	1	3086	-6813	9899	-	-	-
Strain +3	20	4.1	4.5	39.0	Fracture	2	-	-	-	-	-	-
Strain +3	12	4.5	3.9	44.0	Fracture	2	27972	-6355	34327	-	-	-
Strain +3	14	3.3	3.6	36.9	Non-fracture	1	34580	-8601	43154	-	-	-
Strain +3	4	5.3	4.4	37.5	Non-fracture	1	3507	-2079	5586	-	-	-
Strain +3	7	6.4	3.9	37.6	Non-fracture	1	1958	-4120	6064	-	-	-
Strain +3	3	4.5	3.5	37.8	Non-fracture	1	7799	-7426	9419	-	-	-
Strain +3	41	3.4	3.4	43.3	Fracture	2	7532	-5791	13227	-	-	-
Strain +3	31	4.4	3.8	43.7	Fracture	2	6123	-2405	7867	-	-	-
Strain +3	39	6.2	3.6	42.9	Non-fracture	1	3032	-3097	4269	-	-	-
Strain +3	43	3.0	4.1	50.5	Fracture	3	8393	-11068	18766	-	-	-
Strain +6	57	3.8	3.5	43.4	Fracture	3	7510	-6496	13402	-	-	-
Strain +6	42	6.3	3.6	51.6	Fracture	2	-	-	-	-	-	-
Strain +6	40	4.0	4.1	49.0	Fracture	4	5856	-4585	9863	1094	-6370	7463
Strain +6	36	4.4	3.6	38.1	Non-fracture	1	8793	-6823	15566	10412	-5692	10353
Strain +6	30	4.5	4.3	41.0	Non-fracture	1	7769	3482	10159	6152	-8345	14496
Strain +6	38	3.4	3.6	41.7	Fracture	4	18853	-6242	24992	11437	-6673	18084
Strain +6	37	3.6	3.6	41.9	Fracture	2	5643	-5894	11003	8131	-5562	13399
Strain +6	47	3.3	4.2	40.4	Fracture	3	8452	-10186	18528	22118	-5820	27894
Strain +6	48	4.3	4.4	42.3	Fracture	2	6255	-16814	22795	7003	-5759	12411

BSM Construction	Scapula No.	Avg. Bone Thickness (mm)	Model Mass (kg)	Velocity (m·s <sup>-1</sup> )	Outcome	Fracture Index	Peak Medial Strain Gauge Data			Peak Lateral Strain Gauge Data		
							Principle Strain 1 (microstrain)	Principle Strain 2 (microstrain)	Max Shear strain (microstrain)	Principle Strain 1 (microstrain)	Principle Strain 2 (microstrain)	Max Shear strain (microstrain)
DIC	62	4.2	2.2	41.7	Fracture	2	-	-	-	-	-	-
DIC	66	6.6	1.8	40.6	Fracture	3	-	-	-	-	-	-
DIC	55	4.4	1.9	41.3	Fracture	2	-	-	-	-	-	-
DIC	67	4.4	1.9	39.9	Fracture	5	-	-	-	-	-	-
DIC	65	2.8	1.4	41.6	Fracture	5	-	-	-	-	-	-
DIC	56	4.6	2.3	37.5	Non-fracture	1	-	-	-	-	-	-
DIC	68	3.8	1.8	37.0	Fracture	4	-	-	-	-	-	-
DIC	69	5.5	1.6	35.6	Non-fracture	1	-	-	-	-	-	-
DIC	61	3.2	1.8	37.7	Fracture	5	-	-	-	-	-	-
DIC	60	4.1	1.5	33.4	Non-fracture	1	-	-	-	-	-	-
DIC +3	27	4.3	1.9	38.7	Non-fracture	1	5312	-9199	12756	-	-	-
DIC +3	23	4.8	1.8	50.1	Fracture	5	5938	-10982	13417	-	-	-
DIC +3	24	4.1	1.9	41.9	Non-fracture	1	3375	-6423	9674	-	-	-
DIC +3	26	3.9	1.6	40.0	Fracture	1	24299	-5124	29229	-	-	-
DIC +3	63	3.4	1.7	34.5	Fracture	2	5364	-4574	9858	-	-	-
DIC +3	64	5.2	1.5	41.4	Fracture	3	8377	-7317	15667	-	-	-
DIC +3	59	4.1	1.3	39.7	Fracture	2	7277	-7489	14730	-	-	-
DIC +3	58	6.5	2.0	39.5	Non-fracture	1	4083	-844	4274	-	-	-
DIC +3	25	4.4	1.8		Double impact	-	-	-	-	-	-	-
DIC +6	53	4.7	1.6	31.4	Non-fracture	1	7913	-4632	11492	1608	-5557	6431
DIC +6	51	4.9	1.7	39.9	Fracture	2	8928	-4696	10924	8219	-3606	10517
DIC +6	52	6.7	2.2	38.0	Non-fracture	1	3903	-1800	5138	3552	-8129	3425
DIC +6	50	4.0	1.7	35.9	Fracture	2	4435	-7350	11603	5522	-6686	12105
DIC +6	54	3.7	1.7	36.2	Fracture	2	5083	-11641	16718	7529	-6381	13756
DIC +6	49	4.6	1.7	35.4	Fracture	2	5141	-5750	10602	14963	-4795	19647



## Appendix F: Helmet Deformation DIC Analysis Data

Shot No.	Helmet Type	Helmet No.	Location	Shot Order	Max depth (mm)	Time to max depth ( $\mu$ s)	Max velocity ( $m \cdot s^{-1}$ )	Time to max velocity ( $\mu$ s)	5 mm Stand-off			10 mm Stand-off			15 mm Stand-off		
									Deformation Area ( $\times 10^3 \text{ mm}^2$ )	Max velocity at Stand-off ( $m \cdot s^{-1}$ )	Radius of Curvature (mm)	Deformation Area ( $\times 10^3 \text{ mm}^2$ )	Max velocity at Stand-off ( $m \cdot s^{-1}$ )	Radius of Curvature (mm)	Deformation Area ( $\times 10^3 \text{ mm}^2$ )	Max velocity at Stand-off ( $m \cdot s^{-1}$ )	Radius of Curvature (mm)
1	Mk6A	1	front	1	57.7	860	234	80	0.9	212.1	16.7	1.8	251.5	17.2	2.9	259.2	12.3
2	Mk6A	1	back	2	39.9	720	170	60	1.0	146.4	16.5	2.1	207.1	24.2	3.8	173.1	31.8
3	Mk6A	1	right	3	42.7	700	180	60	0.8	160.7	32.3	1.5	180.1	43.0	3.2	159.1	47.7
4	Mk6A	1	left	4	40.7	640	168	80	1.0	151.8	52.0	1.5	163.8	53.9	2.8	153.1	50.5
5	Mk6A	1	crown	5	45.5	800	176	80	0.6	83.8	24.8	1.7	175.8	30.9	2.8	143.2	
6	Mk7	13	right	1	53.9	760	190	80	0.4	77.1	34.5	2.0	19.0	32.1	2.5	17.0	32.5
7	Mk7	13	left	2	45.2	860	177	60	0.7	141.4	31.2	1.3	177.1	28.0	3.1	145.8	33.7
8	Mk7	13	front	3	44	820	181	60	0.5	83.3	36.0	2.0	180.7	35.2	3.5	151.0	42.1
9	Mk7	13	back	4	45.2	940	182	60	1.1	173.0	24.2	1.7	182.2	26.0	2.6	172.3	22.1
10	Mk7	13	crown	5	57	1220	186	40	0.9	186.0	22.1	1.5	181.1	27.8	2.8	154.0	27.6
11	Mk7	11	crown	1	41.9	680	190	60	0.7	175.2	15.2	1.4	200.8	23.3	2.9	167.3	23.8
12	Mk7	11	back	2	44.9	820	185	60	0.7	138.6	22.2	1.4	180.9	20.6	2.7	148.2	22.1
13	Mk7	11	right	3	43.7	920	169	60	1.0	178.0	24.0	1.5	178.0	23.6	3.2	155.4	29.2
14	Mk7	11	left	4	43.2	920	167	60	1.5	173.1	25.2	2.0	170.4	24.7	3.4	150.7	32.1
15	Mk7	11	front	5	45.3	880	174	60	0.5	80.5	23.1	1.7	173.8	21.9	3.3	150.9	28.6
16	Mk6A	10	crown	1	40.9	700	176	60	0.5	114.1	23.4	1.7	174.1	30.7	2.8	163.3	33.1
17	Mk6A	10	left	2	40.9	700	176	60	0.8	136.5	23.0	1.3	176.0	25.2	2.8	156.4	32.3
18	Mk6A	10	front	3	40.9	780	168	60	0.8	154.1	25.3	1.8	167.9	26.8	3.0	152.0	29.2
19	Mk6A	10	right	4	44.2	780	178	60	0.8	145.0	20.6	1.4	177.9	24.8	2.8	156.1	30.3
20	Mk6A	10	back	5	45.2	960	175	60	0.9	162.1	24.2	1.6	175.1	22.5	3.2	155.4	31.3

Shot No.	Helmet Type	Helmet No.	Location	Shot Order	Max depth (mm)	Time to max depth ( $\mu$ s)	Max velocity ( $m \cdot s^{-1}$ )	Time to max velocity ( $\mu$ s)	5 mm Stand-off			10 mm Stand-off			15 mm Stand-off		
									Deformation Area ( $\times 10^3 mm^2$ )	Max velocity at Stand-off ( $m \cdot s^{-1}$ )	Radius of Curvature (mm)	Deformation Area ( $\times 10^3 mm^2$ )	Max velocity at Stand-off ( $m \cdot s^{-1}$ )	Radius of Curvature (mm)	Deformation Area ( $\times 10^3 mm^2$ )	Max velocity at Stand-off ( $m \cdot s^{-1}$ )	Radius of Curvature (mm)
21	Mk6A	9	right	1	41.5	720	175	60	0.9	159.9	26.9	1.5	174.8	26.2	2.9	149.1	30.2
22	Mk6A	9	back	2	42.4	780	170	60	0.6	85.7	30.9	1.8	170.1	29.8	3.4	150.0	39.2
23	Mk6A	9	left	3	42.9	740	172	60	0.9	149.9	26.1	1.3	172.3	26.8	2.9	161.6	32.4
24	Mk6A	9	front	4	40.2	760	153	60	1.3	144.8	28.2	1.9	152.8	27.6	3.3	133.8	30.4
25	Mk6A	9	crown	5	51.4	1100	182	60	0.4	122.9	17.6	0.9	182.2	19.5	2.2	169.4	33.4
26	Mk6A	2	left	1	52.1	940	190	60	0.5	92.0	20.2	1.7	189.5	21.4	2.4	176.1	25.7
27	Mk6A	2	crown	2	50.2	960	201	60	0.7	176.1	20.2	1.2	200.7	21.7	2.6	178.1	28.3
28	Mk6A	2	back	3	54	1160	178	60	1.1	165.8	22.3	1.6	178.3	23.2	3.5	153.8	24.1
29	Mk6A	2	right	4	54.2	1120	174	80	0.3	131.3	21.8	1.5	173.8	21.9	2.6	168.1	24.2
30	Mk6A	2	front	5	52.7	1120	168	80	0.5	102.6	19.0	1.6	167.8	23.2	3.2	147.3	25.4
31	Mk6A	4	front	1	44.9	860	171	60	0.7	128.8	22.0	2.1	164.3	23.5	2.8	155.0	27.0
32	Mk6A	4	right	2	40.6	660	169	60	0.9	141.9	23.6	1.6	168.6	20.7	2.8	162.5	28.8
33	Mk6A	4	crown	3	37.1	700	154	60	-	-	-	-	-	-	-	-	-
34	Mk6A	4	back	4	44.9	860	170	80	-	-	-	-	-	-	-	-	-
35	Mk6A	4	left	5	42.9	720	164	60	0.3	40.5	19.6	1.6	163.5	22.5	2.8	152.4	27.4
36	Mk6A	5	left	1	44.5	720	167	80	0.7	154.6	18.9	1.1	168.3	17.8	2.9	157.6	20.1
37	Mk6A	5	back	2	39.8	720	175	60	0.6	114.8	21.2	1.4	170.3	26.8	3.1	144.0	32.0
38	Mk6A	5	front	3	54.8	1140	185	80	0.5	88.2	21.4	1.8	184.8	20.7	2.5	176.4	24.1
39	Mk6A	5	crown	4	48	1020	163	80	0.4	106.2	28.7	1.8	157.7	29.3	3.0	154.7	26.4
40	Mk6A	5	right	5	53.4	960	182	80	0.6	115.6	19.9	1.8	181.7	20.4	3.7	179.7	21.9

Shot No.	Helmet Type	Helmet No.	Location	Shot Order	Max depth (mm)	Time to max depth ( $\mu$ s)	Max velocity ( $m \cdot s^{-1}$ )	Time to max velocity ( $\mu$ s)	5 mm Stand-off Max			10 mm Stand-off Max			15 mm Stand-off Max		
									Deformation Area ( $\times 10^3 mm^2$ )	velocity at Stand-off ( $m \cdot s^{-1}$ )	Radius of Curvature (mm)	Deformation Area ( $\times 10^3 mm^2$ )	velocity at Stand-off ( $m \cdot s^{-1}$ )	Radius of Curvature (mm)	Deformation Area ( $\times 10^3 mm^2$ )	velocity at Stand-off ( $m \cdot s^{-1}$ )	Radius of Curvature (mm)
41	Mk6A	8	right	1	48.1	820	181	60	0.9	160.9	22.6	1.6	181.3	23.8	3.0	165.0	24.6
42	Mk6A	8	front	2	48.7	820	186	80	0.5	84.8	20.3	1.6	185.5	19.7	2.2	179.6	20.9
43	Mk6A	8	back	3	44.7	860	174	80	0.6	99.8	16.2	1.7	174.1	20.0	2.3	160.3	23.8
44	Mk6A	8	crown	4	49.4	960	180	80	0.7	161.0	23.4	1.2	178.4	20.3	2.5	165.2	23.3
45	Mk6A	8	left	5	46.8	840	173	60	1.1	160.1	19.9	1.5	173.3	22.6	2.8	159.5	24.5
46	Mk6A	3	back	1	39.6	720	158	80	0.8	135.6	24.2	2.2	158.2	22.7	3.7	150.7	29.8
47	Mk6A	3	left	2	44.6	780	173	60	0.6	86.9	16.8	1.7	173.3	24.3	3.4	153.8	26.7
48	Mk6A	3	right	3	45.7	740	180	60	0.6	92.2	19.2	1.6	179.9	21.9	2.3	169.1	23.8
49	Mk6A	3	crown	4	50.2	1000	166	60	0.6	155.0	23.2	1.6	166.3	22.5	3.2	152.6	29.7
50	Mk6A	3	front	5	52.2	940	202	60	0.9	140.0	19.9	1.6	201.6	21.2	3.4	163.1	25.0
51	Mk6A	6	crown	1	53.9	920	187	60	0.6	137.1	12.5	1.0	187.0	17.0	2.6	167.7	20.9
52	Mk6A	6	front	2	53.1	1260	182	60	0.4	89.6	21.9	2.2	182.0	23.0	2.5	173.8	24.2
53	Mk6A	6	left	3	51.2	960	170	60	0.6	116.2	14.2	1.1	182.6	18.0	2.5	168.4	19.3
54	Mk6A	6	right	4	54.1	1040	178	60	0.9	161.9	19.7	1.3	177.6	23.5	2.9	160.0	24.8
55	Mk6A	6	back	5	50.6	1080	158	80	0.7	96.4	22.1	1.9	158.4	24.3	3.3	145.2	31.0
56	Mk6A	7	left	1	45.5	800	172	80	0.8	154.5	23.0	1.4	170.3	22.1	2.9	158.6	25.6
57	Mk6A	7	back	2	49.6	880	184	60	0.8	142.7	11.4	1.2	183.9	16.1	2.9	170.4	22.2
58	Mk6A	7	crown	3	52.2	1020	176	80	0.7	142.8	27.3	1.1	162.8	16.3	2.3	169.2	18.9
59	Mk6A	7	front	4	56.7	1080	191	80	0.6	147.7	18.5	1.3	176.8	17.2	3.2	185.0	19.6
60	Mk6A	7	right	5	51.5	880	179	80	0.5	117.5	24.8	1.8	178.7	18.0	2.5	168.3	25.7

Shot No.	Helmet Type	Helmet No.	Location	Shot Order	Max depth (mm)	Time to max depth ( $\mu\text{s}$ )	Max velocity ( $\text{m}\cdot\text{s}^{-1}$ )	Time to max velocity ( $\mu\text{s}$ )	5 mm Stand-off			10 mm Stand-off			15 mm Stand-off		
									Deformation Area ( $\times 10^3 \text{ mm}^2$ )	Max velocity at Stand-off ( $\text{m}\cdot\text{s}^{-1}$ )	Radius of Curvature (mm)	Deformation Area ( $\times 10^3 \text{ mm}^2$ )	Max velocity at Stand-off ( $\text{m}\cdot\text{s}^{-1}$ )	Radius of Curvature (mm)	Deformation Area ( $\times 10^3 \text{ mm}^2$ )	Max velocity at Stand-off ( $\text{m}\cdot\text{s}^{-1}$ )	Radius of Curvature (mm)
61	Mk7	12	right	1	43.1	820	179	60	1.0	172.4	18.3	1.7	178.9	23.6	3.2	145.2	27.7
62	Mk7	12	front	2	42.9	740	187	40	0.5	83.8	19.7	1.8	182.5	20.5	2.3	169.1	22.7
63	Mk7	12	back	3	45	700	189	60	0.6	140.3	21.6	1.1	189.3	23.5	2.8	171.4	23.5
64	Mk7	12	crown	4	47.8	840	190	60	0.8	179.9	19.5	1.3	189.7	20.8	2.3	173.5	31.6
65	Mk7	12	left	5	55.3	1040	179	60	0.6	164.2	22.0	1.3	178.7	21.8	3.1	165.1	26.4
66	Mk7	14	crown	1	39.9	700	185	80	0.5	107.2	16.3	1.7	185.1	24.6	2.3	166.7	23.2
67	Mk7	14	right	2	47.8	800	178	80	0.7	143.3	26.3	1.9	177.5	27.1	2.7	169.2	27.0
68	Mk7	14	left	3	49	900	179	60	1.1	174.8	23.5	1.7	179.4	23.9	3.2	160.3	28.3
69	Mk7	14	front	4	44.1	840	186	60	0.8	179.9	27.3	1.7	185.9	27.7	3.0	156.6	34.4
70	Mk7	14	back	5	50.8	1360	186	60	1.0	168.3	20.2	1.5	186.4	26.9	2.4	173.7	23.8
71	Mk7	15	left	1	38.2	680	181	40	1.3	181.3	26.9	2.3	170.6	29.0	4.1	143.5	33.6
72	Mk7	15	front	2	42.6	720	183	60	0.6	143.9	17.8	1.1	182.5	17.9	2.8	164.9	33.7
73	Mk7	15	crown	3	40.3	720	177	60	0.6	168.3	21.2	1.3	176.5	23.6	2.0	165.0	28.1
74	Mk7	15	back	4	48.9	2040	181	60	0.6	87.9	16.2	1.9	180.3	26.3	3.4	155.3	34.5
75	Mk7	15	right	5	43.5	760	179	80	0.7	143.4	23.5	1.9	178.3	29.5	3.0	162.6	28.7
76	Mk7	16	back	1	48.3	1000	183	60	1.0	171.6	23.3	1.6	183.2	25.1	3.4	152.0	29.5
77	Mk7	16	crown	2	53.4	1280	179	60	0.4	164.8	22.6	1.6	172.9	26.7	2.2	158.9	28.6
78	Mk7	16	right	3	50.5	840	175	80	1.1	162.0	27.7	1.9	174.7	23.5	3.2	169.2	27.7
79	Mk7	16	left	4	56.6	1020	180	80	0.4	144.1	22.7	2.0	179.8	27.6	2.7	173.0	31.9
80	Mk7	16	front	5	47.4	1060	183	40	0.4	77.2	13.2	1.7	177.7	23.6	2.6	172.8	34.5

## Appendix G: Post processing of projectile accelerometer data

FAMOS (imc Measurement and Control 2011) script (M. Gant) .

```
FileResetAll()
```

```
directory=boxtext?("File path","C:\",0) ;enter the file path where the data is stored
```

```
ldir <directory>
```

```
sdir <directory>
```

```
file=boxtext?("File Name","XXX.csv",0);enter the file name including the extension
```

```
ID=boxtext?("Test Name","test001",0) ;enter a test name
```

```
Mass=boxvalue?("Mass of Projectile / g",100,0) ;enter the mass of the projectile in grams
```

```
file=fileopenxls(file,0)
```

```
timebase=filexlscolumnread(file,1,30,100000,0) ;reads the first column of the data starting at the 30th row and stores it as the timebase
```

```
timebase=timebase/1000 ;corrects the timebase so it is measured in seconds
```

```
Acceleration=filexlscolumnread(file,2,30,100000,0) ;reads the second column of the data starting at the 30th row and stores it as acceleration
```

```
Acceleration=xy(timebase,Acceleration);creates a plot of the acceleration and timebase data
```

```
Acceleration=Acceleration*9.81 ;converts the acceleration data from g to m/s2
```

```
xunit Acceleration "s" ;defines the units for the plot
```

```
yunit Acceleration "m/s2"
```

```
Force=Acceleration*Mass/1000 ; uses the projectile mass to calculate the force
```

```
yunit force "N"
```

```
AccelerationFiltered=filtlp(Acceleration,0,0,4,4300) ;filters the acceleration and force plots
```

```
ForceFiltered=filtlp(Force,0,0,4,4300)
```

```
PeakAcceleration=max(AccelerationFiltered); finds the maximum acceleration and force
```

```
PeakForce=max(ForceFiltered)
```

```
<ID>=GrNew() ;creates a group and adds the data
```

```
GrChanAppend(<ID>,Acceleration)
```

```
GrChanAppend(<ID>,AccelerationFiltered)
```

```
GrChanAppend(<ID>,Force)
```

```
GrChanAppend(<ID>,ForceFiltered)
```

```
GrChanAppend(<ID>,PeakAcceleration)
```

```
GrChanAppend(<ID>,PeakForce)
```

```
fileclose(file)
```

## Appendix H: Post processing of DIC analysis data

FAMOS (imc Measurement and Control 2011) script (M. Gant).

```
FileResetAll()
```

```
directory=boxtext?("File path","C:\",0) ;enter the file path where the data is stored
```

```
ldir <directory>
```

```
sdir <directory>
```

```
file=boxtext?("File Name","XXX.xlsx",0);enter the file name including the extension
```

```
ID=boxtext?("Test Name","test001",0);enter a test name (must contain alphabetic characters)
```

```
Mass=boxvalue?("Mass of Projectile / g",100,0) ;enter the mass of the projectile in grams
```

```
file=fileopenxls(file,0)
```

```
timebase=filexlscolumnread(file,4,7,100000,0) ;reads the first column of the data starting at the 30th row and stores it as the timebase
```

```
timebase=timebase/1000 ;corrects the timebase so it is measured in seconds
```

```
Position=filexlscolumnread(file,5,7,100000,0) ;reads the second column of the data starting at the 30th row and stores it as acceleration
```

```
Position=Position/1000
```

```
Position=xy(timebase,Position);creates a plot of the acceleration and timebase data
```

```
xunit Position "s" ;defines the units for the plot
```

```
yunit Position "m"
```

```
Velocity=diff(Position)
```

```
Acceleration=diff(Velocity)
```

```
AccelerationFiltered=filtp(Acceleration,0,0,4,4300); filters the acceleration and force plots
```

```
Force=AccelerationFiltered*Mass/1000; uses the projectile mass to calculate the force
```

```
yunit force "N"
```

```
PeakAcceleration=max(AccelerationFiltered); finds the maximum acceleration and force
```

```
PeakForce=max(Force)
```

```
<ID>=GrNew() ;creates a group and adds the data
```

```
GrChanAppend(<ID>,Position)
```

```
GrChanAppend(<ID>,Velocity)
```

```
GrChanAppend(<ID>,Acceleration)
```

```
GrChanAppend(<ID>,AccelerationFiltered)
```

```
GrChanAppend(<ID>,Force)
```

```
GrChanAppend(<ID>,PeakAcceleration)
```

```
GrChanAppend(<ID>,PeakForce)
```

```
fileclose(file)
```

## Appendix I: BSM impact data investigating a range of flat face diameters and curvatures delivered by instrumented projectile

Group	Impact diameter (mm)	Impact radius of curvature (mm)	Scapula number	Avg. bone thickness (mm)	BSM mass (kg)	Projectile mass (g)	Impact velocity ( $\text{m}\cdot\text{s}^{-1}$ )	Fracture outcome (1-fracture or 0-non-fracture)	Fracture index (1-5)	BDAS peak acceleration ( $10^3\text{m}\cdot\text{s}^{-2}$ )	BDAS Peak force (kN)	BDAS time to peak force ( $10^{-6}\text{s}$ )
1	38	$\infty$	1	5.3	3.5	104.1	45.6	1	3	75.2	7.3	0.45
1	38	$\infty$	15	2.9	4.3	104.1	42.5	1	4	60.9	6.3	0.31
1	38	$\infty$	5	4.4	3.4	104.1	36.5	1	2	70.2	7.3	0.46
1	38	$\infty$	13	4.3	4.3	104.1	32.0	1	2	51.1	5.3	0.50
1	38	$\infty$	17	3.0	4.0	104.1	27.7	0	1	43.4	4.5	0.60
1	38	$\infty$	18	6.6	5.0	104.1	29.3	0	1	57.0	5.9	0.62
1	38	$\infty$	9	3.6	3.7	104.1	32.5	0	1	47.0	4.9	0.57
1	38	$\infty$	14	2.9	3.4	104.1	18.8	0	1	-	-	-
1	38	$\infty$	10	3.2	3.5	104.1	29.1	1	4	62.2	6.5	0.48
1	38	$\infty$	2	5.3	3.8	104.1	29.1	0	1	53.3	5.6	0.50
1	38	$\infty$	20	4.2	4.6	104.1	28.1	0	1	68.3	7.1	0.48
1	38	$\infty$	19	3.1	4.1	104.1	40.3	1	2	-	-	-
1	38	$\infty$	7	2.8	3.7	104.5	28.5	1	3	50.0	5.2	0.49
1	38	$\infty$	16	2.3	3.6	104.5	31.6	1	3	67.1	7.0	0.46
1	38	$\infty$	4	4.4	3.0	104.5	32.8	0	1	52.5	5.5	0.53
1	38	$\infty$	12	3.3	4.5	104.5	33.7	1	4	66.6	7.0	0.42
1	38	$\infty$	6	4.3	2.7	104.5	29.3	0	1	57.0	6.0	0.52
1	38	$\infty$	11	2.6	3.5	104.5	31.6	0	1	75.5	7.9	0.50
1	38	$\infty$	21	2.4	4.2	104.9	32.4	1	2	72.0	7.6	0.40
1	38	$\infty$	35	2.9	4.6	104.9	28.8	1	2	43.8	4.6	0.58
1	38	$\infty$	26	3.9	4.9	104.9	32.1	1	2	62.4	6.5	0.48
1	38	$\infty$	34	3.4	4.9	104.9	32.8	1	3	56.6	5.9	0.50
1	38	$\infty$	23	6.0	4.2	104.9	29.3	0	1	47.5	5.0	0.51
1	38	$\infty$	31	2.9	4.2	104.9	26.5	0	1	46.9	4.9	0.56
1	38	$\infty$	32	4.8	4.4	104.9	25.4	0	1	43.4	4.6	0.57
1	38	$\infty$	38	5.3	4.6	104.9	31.5	0	1	51.1	5.4	0.47
1	38	$\infty$	25	3.1	4.9	104.9	23.9	0	1	32.6	3.4	0.71
1	38	$\infty$	39	4.7	3.8	104.9	26.2	1	3	40.6	4.3	0.51

Group	Impact diameter (mm)	Impact radius of curvature (mm)	Scapula number	Avg. bone thickness (mm)	BSM mass (kg)	Projectile mass (g)	Impact velocity ( $\text{m}\cdot\text{s}^{-1}$ )	Fracture outcome (1-fracture or 0-non-fracture)	Fracture index (1-5)	BDAS peak acceleration ( $10^3\text{m}\cdot\text{s}^{-2}$ )	BDAS Peak force (kN)	BDAS time to peak force ( $10^{-6}\text{s}$ )
2	32	$\infty$	160	2.8	4.5	103.9	33.7	1	4	51.6	5.4	0.48
2	32	$\infty$	149	3.7	5.0	103.9	20.9	0	1	36.2	3.8	0.60
2	32	$\infty$	152	1.9	4.9	103.9	31.6	1	3	50.0	5.2	0.51
2	32	$\infty$	144	3.2	5.1	103.9	27.4	1	2	51.0	5.3	0.55
2	32	$\infty$	142	2.5	4.4	103.9	28.6	1	3	51.4	5.3	0.54
2	32	$\infty$	146	4.0	4.9	103.9	13.8	0	1	22.7	2.4	0.89
2	32	$\infty$	145	3.2	4.8	103.9	16.2	0	1	24.1	2.5	0.98
2	32	$\infty$	155	5.3	3.9	103.9	21.0	0	1	36.2	3.8	0.60
2	32	$\infty$	156	4.6	4.0	103.9	24.0	0	1	48.0	5.0	0.68
2	32	$\infty$	148	3.4	4.9	103.9	25.1	0	1	50.6	5.3	0.63
2	32	$\infty$	176	5.2	4.2	103.9	23.4	0	1	41.5	4.3	0.64
2	32	$\infty$	169	3.5	3.6	103.9	26.2	0	1	57.1	5.9	0.55
2	32	$\infty$	164	3.0	4.4	103.9	28.8	1	3	44.7	4.6	0.55
2	32	$\infty$	179	4.1	3.8	103.9	32.3	1	2	55.0	5.7	0.54
2	32	$\infty$	168	2.9	4.2	103.9	27.8	1	3	40.2	4.2	0.72
2	32	$\infty$	173	2.7	4.2	103.9	32.6	1	3	71.1	7.4	0.70
2	32	$\infty$	165	3.5	4.1	103.9	26.6	0	1	53.7	5.6	0.55
2	32	$\infty$	161	4.7	4.8	103.9	20.7	0	1	40.0	4.2	0.62
2	32	$\infty$	170	3.6	4.7	103.9	19.0	0	1	38.3	4.0	0.80
2	32	$\infty$	177	4.0	4.8	103.9	28.5	0	1	57.1	5.9	0.68
2	32	$\infty$	163	2.5	4.3	103.9	33.6	1	4	42.2	4.4	0.48
2	32	$\infty$	178	3.2	4.1	103.9	39.4	1	3	83.9	8.7	0.42
2	32	$\infty$	172	2.7	4.4	103.9	29.9	1	4	44.2	4.6	0.53
2	32	$\infty$	180	2.7	4.1	103.9	24.4	1	3	46.2	4.8	0.71
2	32	$\infty$	171	3.7	3.9	103.9	27.5	0	1	59.8	6.2	0.62
2	32	$\infty$	162	5.6	4.2	103.9	23.9	0	1	46.2	3.3	0.85
2	32	$\infty$	167	3.8	4.4	103.9	31.1	1	2	61.1	6.3	0.55
2	32	$\infty$	175	4.7	3.6	103.9	21.3	0	1	42.8	4.4	0.69
2	32	$\infty$	174	4.0	5.0	103.9	21.7	0	1	47.4	4.9	0.69
2	32	$\infty$	166	4.2	4.1	103.9	26.0	0	1	47.5	4.9	0.61



Group	Impact diameter (mm)	Impact radius of curvature (mm)	Scapula number	Avg. bone thickness (mm)	BSM mass (kg)	Projectile mass (g)	Impact velocity ( $m \cdot s^{-1}$ )	Fracture outcome (1-fracture or 0-non-fracture)	Fracture index (1-5)	BDAS peak acceleration ( $10^3 m \cdot s^{-2}$ )	BDAS Peak force (kN)	BDAS time to peak force ( $10^{-6}s$ )
3	26	$\infty$	138	3.5	4.9	102.8	20.3	0	1	27.5	2.8	0.82
3	26	$\infty$	133	3.3	4.9	102.8	21.5	0	1	38.8	4.0	0.55
3	26	$\infty$	136	3.8	4.7	102.8	30.0	1	3	52.8	5.4	0.43
3	26	$\infty$	123	2.6	4.3	102.8	26.2	1	3	36.1	3.7	0.76
3	26	$\infty$	129	4.9	4.4	102.8	29.6	1	2	58.2	6.0	0.49
3	26	$\infty$	132	2.9	4.3	102.8	25.6	1	2	45.0	4.6	0.67
3	26	$\infty$	124	4.8	5.0	102.8	26.8	0	1	52.2	5.4	0.59
3	26	$\infty$	126	5.0	4.9	102.8	28.8	1	2	63.6	6.5	0.43
3	26	$\infty$	139	4.4	4.7	102.8	22.9	0	1	40.0	4.1	0.54
3	26	$\infty$	122	5.6	5.1	102.8	22.0	0	1	41.9	4.3	0.63
3	26	$\infty$	137	2.5	4.1	102.8	21.8	1	3	32.1	3.3	0.61
3	26	$\infty$	131	2.7	5.8	102.8	20.2	1	2	30.9	3.2	0.76
3	26	$\infty$	130	4.5	4.0	102.8	19.2	0	1	21.6	2.2	0.68
3	26	$\infty$	134	3.3	4.1	102.8	13.5	0	1	16.5	1.7	0.71
3	26	$\infty$	125	4.3	4.1	102.8	19.1	0	1	32.7	3.4	0.85
3	26	$\infty$	128	3.4	4.6	102.8	26.1	0	1	47.7	4.9	0.72
3	26	$\infty$	140	3.1	5.0	102.8	23.1	1	2	34.4	3.5	0.70
3	26	$\infty$	121	6.5	5.8	102.8	14.7	0	1	31.3	3.2	1.00
3	26	$\infty$	135	3.4	3.7	102.8	25.1	1	2	44.7	4.6	0.59
3	26	$\infty$	128	3.4	4.6	102.8	28.0	1	3	55.1	5.7	0.49
3	26	$\infty$	159	2.6	4.0	103.9	24.2	1	3	33.9	3.5	0.60
3	26	$\infty$	147	4.0	4.8	103.9	27.9	0	1	47.1	4.9	0.57
3	26	$\infty$	150	3.8	4.4	103.9	29.2	1	2	62.5	6.5	0.50
3	26	$\infty$	153	3.6	4.2	103.9	33.8	1	3	63.6	6.6	0.49
3	26	$\infty$	151	3.6	4.2	103.9	22.7	1	2	37.0	3.8	0.93
3	26	$\infty$	157	5.2	4.2	103.9	26.5	0	1	58.8	6.1	0.61
3	26	$\infty$	154	4.8	4.3	103.9	19.4	0	1	38.4	4.0	0.66
3	26	$\infty$	143	3.4	4.8	103.9	27.0	1	2	55.5	5.8	0.54
3	26	$\infty$	141	4.2	3.2	103.9	25.7	0	1	53.2	5.5	0.55

Group	Impact diameter (mm)	Impact radius of curvature (mm)	Scapula number	Avg. bone thickness (mm)	BSM mass (kg)	Projectile mass (g)	Impact velocity ( $m \cdot s^{-1}$ )	Fracture outcome (1-fracture or 0-non-fracture)	Fracture index (1-5)	BDAS peak acceleration ( $10^3 m \cdot s^{-2}$ )	BDAS Peak force (kN)	BDAS time to peak force ( $10^{-6}s$ )
4	20	$\infty$	70	7.0	4.4	104.6	22.4	0	1	-	-	-
4	20	$\infty$	66	4.7	4.1	104.6	20.7	0	1	30.8	3.2	0.55
4	20	$\infty$	77	2.5	4.2	104.6	27.0	1	5	20.1	2.1	0.39
4	20	$\infty$	65	2.9	4.8	104.6	21.5	1	2	27.8	2.9	0.65
4	20	$\infty$	64	2.0	4.3	104.6	22.9	1	3	27.0	2.8	0.63
4	20	$\infty$	69	5.4	4.9	104.6	23.9	0	1	33.3	3.5	0.59
4	20	$\infty$	63	3.4	4.7	104.6	27.8	1	4	32.8	3.4	0.52
4	20	$\infty$	67	3.3	4.8	104.6	23.7	1	4	24.7	2.6	0.41
4	20	$\infty$	72	3.9	3.5	104.6	22.1	0	1	26.8	2.8	0.76
4	20	$\infty$	71	7.0	5.0	104.6	19.7	0	1	34.6	3.6	0.73
4	20	$\infty$	68	3.2	2.9	104.6	18.0	1	2	21.8	2.3	0.78
4	20	$\infty$	75	3.7	5.1	104.6	16.3	0	1	24.2	2.5	0.89
4	20	$\infty$	62	4.6	5.2	104.6	20.5	0	1	30.8	3.2	0.59
4	20	$\infty$	79	4.3	4.5	104.6	17.0	0	1	32.5	3.4	0.75
4	20	$\infty$	76	2.9	4.1	104.6	23.6	1	3	36.6	3.8	0.57
4	20	$\infty$	61	3.4	5.0	104.6	18.0	0	1	32.7	3.4	0.73
4	20	$\infty$	78	2.1	3.1	104.6	19.6	1	3	24.4	2.5	0.80
4	20	$\infty$	80	2.6	4.7	104.6	21.3	1	3	30.7	3.2	0.73
4	20	$\infty$	73	3.3	4.3	104.6	21.3	1	3	32.9	3.4	0.66
4	20	$\infty$	74	2.8	4.2	104.6	19.5	1	3	21.4	2.2	0.66
4	20	$\infty$	81	4.4	4.1	104.5	15.2	0	1	21.5	2.2	0.85
4	20	$\infty$	87	2.7	4.8	104.5	26.5	1	4	35.0	3.7	0.59
4	20	$\infty$	82	2.9	4.8	104.5	36.3	1	5	37.6	3.9	0.45
4	20	$\infty$	98	4.7	3.4	104.5	18.0	0	1	35.4	3.7	0.72
4	20	$\infty$	86	3.5	3.8	104.5	24.3	1	3	38.3	4.0	0.62
4	20	$\infty$	84	4.8	5.0	104.5	19.6	0	1	38.7	4.0	0.64
4	20	$\infty$	97	4.0	5.0	104.5	22.2	1	3	42.3	4.4	0.69
4	20	$\infty$	92	3.6	4.3	104.5	18.5	0	1	37.9	4.0	0.75
4	20	$\infty$	96	4.5	5.0	104.5	19.2	0	1	31.3	3.3	0.74
4	20	$\infty$	93	3.6	4.4	104.5	20.8	1	2	34.6	3.6	0.67

Group	Impact diameter (mm)	Impact radius of curvature (mm)	Scapula number	Avg. bone thickness (mm)	BSM mass (kg)	Projectile mass (g)	Impact velocity ( $\text{m}\cdot\text{s}^{-1}$ )	Fracture outcome (1-fracture or 0-non-fracture)	Fracture index (1-5)	BDAS peak acceleration ( $10^3\text{m}\cdot\text{s}^{-2}$ )	BDAS Peak force (kN)	BDAS time to peak force ( $10^{-6}\text{s}$ )
5	38	19	30	3.3	3.4	105.8	26.4	0	1	49.2	5.2	0.67
5	38	19	33	3.6	4.3	105.8	37.7	1	4	45.2	4.8	0.45
5	38	19	37	2.2	5.1	105.8	32.9	1	4	37.3	3.9	0.49
5	38	19	40	2.3	4.3	105.8	28.7	1	3	-	-	-
5	38	19	27	5.7	3.7	105.8	25.4	1	2	40.3	4.3	0.62
5	38	19	24	2.9	4.3	105.8	23.7	0	1	48.4	5.1	0.73
5	38	19	22	2.6	4.0	105.8	24.2	1	2	38.5	4.1	0.63
5	38	19	36	4.1	5.1	105.8	25.5	1	3	36.7	3.9	0.56
5	38	19	29	4.5	4.1	105.8	24.1	1	2	44.3	4.7	0.57
5	38	19	51	3.4	4.0	105.8	17.5	0	1	-	-	-
5	38	19	46	2.6	4.7	105.8	20.5	1	5	-	-	-
5	38	19	49	4.1	4.6	105.8	14.6	0	1	-	-	-
5	38	19	56	3.4	4.1	105.8	21.9	1	2	31.7	3.4	0.66
5	38	19	60	4.6	4.2	105.8	21.3	0	1	42.7	4.5	0.65
5	38	19	53	3.0	4.8	105.8	22.4	1	2	33.8	3.6	0.74
5	38	19	41	3.5	4.2	105.8	23.1	1	3	34.1	3.6	0.62
5	38	19	44	3.7	5.2	105.8	14.2	0	1	21.4	2.3	0.81
5	38	19	55	2.8	4.6	105.8	18.1	1	2	24.9	2.6	0.73
5	38	19	54	1.9	4.5	105.8	22.5	1	4	20.1	2.1	0.70
5	38	19	47	5.6	4.9	105.8	20.8	0	1	35.1	3.7	0.81
5	38	19	59	2.0	4.7	105.8	18.8	1	4	18.8	2.0	0.82
5	38	19	50	2.9	3.5	105.8	20.3	1	2	27.9	2.9	0.77
5	38	19	42	3.8	4.6	105.8	16.7	0	1	25.8	2.7	0.69
5	38	19	48	5.0	3.6	105.8	11.8	0	1	-	-	-
5	38	19	45	3.0	3.2	105.8	18	0	1	29.7	3.1	0.69
5	38	19	52	5.0	4.2	105.8	17.8	0	1	30.6	3.2	0.71
5	38	19	57	2.6	3.9	105.8	15.8	1	2	21.8	2.3	0.84
5	38	19	43	3.7	4.3	105.8	18.4	0	1	28.8	3.1	0.73
5	38	19	58	2.5	4.2	105.8	14.1	0	1	19.5	2.1	1.07

Group	Impact diameter (mm)	Impact radius of curvature (mm)	Scapula number	Avg. bone thickness (mm)	BSM mass (kg)	Projectile mass (g)	Impact velocity ( $\text{m}\cdot\text{s}^{-1}$ )	Fracture outcome (1-fracture or 0-non-fracture)	Fracture index (1-5)	BDAS peak acceleration ( $10^3\text{m}\cdot\text{s}^{-2}$ )	BDAS Peak force (kN)	BDAS time to peak force ( $10^{-6}\text{s}$ )
6	38	30	90	2.1	3.9	106.1	24.1	1	3	32.5	3.5	0.70
6	38	30	91	3.2	5.0	106.1	26.0	1	2	47.2	5.0	0.55
6	38	30	95	3.7	5.1	106.1	21.5	0	1	33.8	3.6	0.69
6	38	30	94	3.5	5.4	106.1	19.3	0	1	45.9	4.9	0.74
6	38	30	99	4.3	4.8	106.1	23.9	0	1	38.9	4.1	0.64
6	38	30	85	2.3	4.6	106.1	20.9	1	3	23.7	2.5	0.86
6	38	30	83	7.0	5.3	106.1	21.8	0	1	52.0	5.5	0.67
6	38	30	88	3.5	4.1	106.1	31.2	1	2	55.6	5.9	0.55
6	38	30	100	2.9	4.4	106.1	24.0	1	2	31.9	3.4	0.66
6	38	30	117	4.5	4.9	106.1	18.3	0	1	33.8	3.6	0.84
6	38	30	120	2.6	5.1	106.1	14.2	0	1	19.4	2.1	0.84
6	38	30	103	2.7	4.2	106.1	18.2	0	1	29.4	3.1	0.69
6	38	30	119	4.4	3.7	106.1	16.2	0	1	21.8	2.3	0.95
6	38	30	112	3.8	4.5	106.1	26.9	1	2	49.8	5.3	0.58
6	38	30	111	3.8	4.6	106.1	19.9	0	1	26.5	2.8	0.82
6	38	30	113	3.1	5.1	106.1	18.7	0	1	29.2	3.1	0.71
6	38	30	116	4.1	3.7	106.1	22.6	0	1	42.8	4.5	0.72
6	38	30	114	2.9	4.5	106.1	21.1	0	1	20.3	2.2	0.67
6	38	30	102	4.9	4.7	106.1	29.0	1	2	28.2	3.0	0.43
6	38	30	105	4.5	4.8	106.1	27.2	1	2	23.6	2.5	0.49
6	38	30	115	2.5	4.9	106.1	16.4	1	2	21.3	2.3	0.79
6	38	30	107	3.6	4.9	106.1	6.7	0	1	-	-	-
6	38	30	110	2.8	5.1	106.1	16.7	0	1	20.3	2.2	0.75
6	38	30	108	2.5	5.0	106.1	24.8	1	2	42.0	4.5	0.55
6	38	30	118	3.2	3.7	106.1	26.4	1	3	41.7	4.4	0.49
6	38	30	101	3.8	4.6	106.1	25.0	0	1	55.6	5.9	0.59
6	38	30	106	2.5	4.8	106.1	34.8	1	3	58.4	6.2	0.47
6	38	30	109	3.0	5.1	106.1	28.2	1	4	43.8	4.6	0.57

Group	Impact diameter (mm)	Impact radius of curvature (mm)	Scapula number	Avg. bone thickness (mm)	BSM mass (kg)	Projectile mass (g)	Impact velocity ( $\text{m}\cdot\text{s}^{-1}$ )	Fracture outcome (1-fracture or 0-non-fracture)	Fracture index (1-5)	BDAS peak acceleration ( $10^3\text{m}\cdot\text{s}^{-2}$ )	BDAS Peak force (kN)	BDAS time to peak force ( $10^{-6}\text{s}$ )
7	38	40	199	4.0	4.5	103.7	20.7	0	1	28.0	2.9	0.81
7	38	40	184	1.8	4.7	103.7	34.8	1	4	44.2	4.6	0.54
7	38	40	198	5.5	4.7	103.7	25.0	0	1	53.4	5.5	0.60
7	38	40	193	4.5	5.4	103.7	28.8	0	1	57.3	5.9	0.49
7	38	40	191	3.4	4.9	103.7	18.0	0	1	30.6	3.2	0.70
7	38	40	186	2.4	4.8	103.7	34.2	1	4	46.2	4.8	0.47
7	38	40	195	3.9	5.2	103.7	31.4	1	2	52.5	5.4	0.49
7	38	40	197	4.0	4.6	103.7	28.5	0	1	52.9	5.5	0.52
7	38	40	182	2.0	3.5	103.7	33.3	1	4	42.9	4.5	0.49
7	38	40	183	2.5	3.8	103.7	30.6	1	3	59.3	6.1	0.55
7	38	40	192	3.7	4.2	103.7	31.4	1	2	62.7	6.5	0.50
7	38	40	181	3.0	4.3	103.7	27.6	1	3	45.7	4.7	0.48
7	38	40	200	3.4	3.8	103.7	31.4	0	1	65.3	6.8	0.54
7	38	40	185	4.3	3.1	103.7	18.5	0	1	27.2	2.8	0.79
7	38	40	188	3.6	3.9	103.7	24.2	0	1	42.9	4.5	0.77
7	38	40	196	4.1	3.6	103.7	23.2	0	1	41.8	4.3	0.69
7	38	40	187	3.1	4.1	103.7	10.9	0	1	-	-	-
7	38	40	194	2.1	3.5	103.7	34.7	1	4	39.9	4.1	0.52
7	38	40	189	3.5	4.0	103.7	32.0	1	2	58.7	6.1	0.57
7	38	40	190	2.1	5.0	103.7	18.3	1	3	30.7	3.2	0.71
7	38	40	215	3.1	5.1	103.9	34.2	1	3	55.7	5.8	0.49
7	38	40	219	2.8	4.5	103.9	24.3	0	1	42.0	4.4	0.55
7	38	40	216	5.6	4.8	103.9	30.7	0	1	63.1	6.6	0.45
7	38	40	205	4.5	4.3	103.9	30.5	0	1	52.5	5.5	0.49
7	38	40	201	4.0	4.4	103.9	30.3	1	3	52.3	5.4	0.41
7	38	40	204	5.2	5.5	103.9	26.5	0	1	44.5	4.6	0.72
7	38	40	217	3.6	4.3	103.9	25.2	0	1	41.3	4.3	0.55
7	38	40	220	3.5	4.7	103.9	51.2	1	4	70.8	7.4	0.35
7	38	40	218	2.8	4.0	103.9	39.4	1	3	65.5	5.6	0.65
7	38	40	203	2.1	4.0	103.9	32.2	1	3	49.2	5.1	0.51

Group	Impact diameter (mm)	Impact radius of curvature (mm)	Scapula number	Avg. bone thickness (mm)	BSM mass (kg)	Projectile mass (g)	Impact velocity ( $m \cdot s^{-1}$ )	Fracture outcome (1-fracture or 0-non-fracture)	Fracture index (1-5)	BDAS peak acceleration ( $10^3 m \cdot s^{-2}$ )	BDAS Peak force (kN)	BDAS time to peak force ( $10^{-6} s$ )
8	38	50	209	4.3	4.3	103.9	26.0	0	1	48.8	5.1	0.59
8	38	50	214	4.2	5.4	103.9	38.8	1	2	68.9	7.2	0.40
8	38	50	210	2.3	4.1	103.9	28.9	1	4	36.9	3.8	0.45
8	38	50	208	2.2	3.6	103.9	28.9	1	3	49.6	5.2	0.53
8	38	50	206	3.8	3.7	103.9	20.9	1	2	29.6	3.1	0.62
8	38	50	202	3.0	4.3	103.9	29.7	1	4	51.6	5.4	0.49
8	38	50	213	4.6	4.2	103.9	23.9	0	1	43.8	4.5	0.56
8	38	50	207	6.3	4.9	103.9	26.9	0	1	51.4	5.3	0.72
8	38	50	212	3.6	4.2	103.9	13.6	0	1	23.9	2.5	0.70
8	38	50	211	7.8	4.8	103.9	15.0	0	1	24.8	2.6	0.71
8	38	50	233	3.7	4.3	103.9	33.6	0	1	53.5	5.6	0.56
8	38	50	226	3.8	4.3	103.9	33.5	1	2	62.8	6.5	0.47
8	38	50	236	4.2	5.4	103.9	36.8	1	2	69.5	7.2	0.49
8	38	50	225	3.8	3.8	103.9	35.6	1	3	54.8	5.7	0.52
8	38	50	235	3.8	4.1	103.9	32.6	1	2	49.9	5.2	0.50
8	38	50	229	3.4	4.2	103.9	28.5	0	1	47.9	5.0	0.66
8	38	50	224	3.1	4.2	103.9	28.4	1	2	49.9	5.2	0.58
8	38	50	239	3.6	4.2	103.9	22.5	0	1	39.1	4.1	0.65
8	38	50	227	3.8	4.4	103.9	23.7	0	1	41.1	4.3	0.59
8	38	50	237	4.2	4.8	103.9	16.3	0	1	25.8	2.7	0.75
8	38	50	234	5.5	4.2	103.9	30.4	0	1	54.9	5.7	0.67
8	38	50	232	2.5	3.9	103.9	32.2	1	3	44.8	4.7	0.49
8	38	50	240	3.2	3.9	103.9	24.7	1	2	31.9	3.3	0.61
8	38	50	221	5.2	4.7	103.9	18.1	0	1	28.5	3.0	0.68
8	38	50	238	1.8	3.4	103.9	30.0	1	3	42.1	4.4	0.55
8	38	50	230	3.2	4.3	103.9	25.5	0	1	42.8	4.4	0.73
8	38	50	223	3.9	4.6	103.9	16.3	0	1	24.5	2.5	0.78
8	38	50	231	2.6	4.6	103.9	31.8	1	3	39.0	4.1	0.57
8	38	50	222	3.2	4.6	103.9	31.8	1	3	45.4	4.7	0.53
8	38	50	228	3.1	4.3	103.9	27.5	1	3	42.1	4.4	0.66

# Annex A: Dstl Bovine Scapula Model (BSM) production

## Introduction

Bovine Scapula Models (BSMs) were constructed using a method based on the reporting by James *et al.* (2009). The scapula were obtained from a local butcher<sup>1</sup> and delivered frozen.

## Method

1. Frozen bovine scapulae were thawed and hydrated in Hartman's solution at room temperature. Hartmann's is a saline solution (Table 1) used for rehydrating biological tissues. The scapulae were hydrated within 80 litre bins (Figure 1A) for a total of 24 hours. In addition, standard 61 cm square chamois leathers<sup>2</sup> were soaked in distilled<sup>3</sup> water (Figure 1B) for 24 hours prior to use, ensuring complete saturation. Any chamois leathers with holes or thinning of the surface were discarded.

Chemical	Calculation of content	Unit of Measurement	Example
Distilled H <sub>2</sub> O	1	Litres	50
CaCl <sub>2</sub> .2H <sub>2</sub> O	1 x 0.17	Grams	8.5
KCl	1 x 0.3	Grams	15
NaCl	1 x 6	Grams	300
C <sub>3</sub> H <sub>5</sub> NaO <sub>3</sub>	1 x 3.17	Millilitres	158.5

**Table 1: Chemical content and concentrations within Hartmann's solution.**

<sup>1</sup>Supplied by R. Ownton Butchers, Southampton.

<sup>2</sup>Described as 'Genuine Chamois Leathers', 'graded for fragment assessment', supplied by Russells in Hertfordshire.

<sup>3</sup> Distilled water was obtained from an Elix Millipore deioniser (SN: KJQ0001704).

2. Within the rehydration period, as soon as the bones had thawed, the scapulae were individually removed from the solution. Any flesh attached to the medial and lateral surfaces of the target area was removed using a PM40 knife (Figure 2A). Considerable care was taken to ensure that the periosteum membrane was not damaged. Where damage to the bone was observed or caused as a result of the butchering and cleaning processes the scapula was removed from testing and discarded.

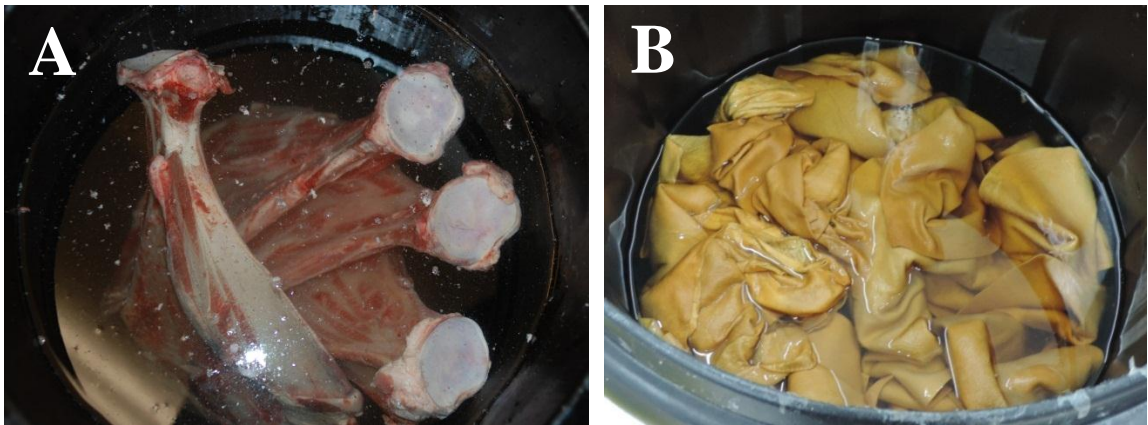


**Figure 1: A) Hydration and thawing of bovine scapulae in Hartmann's solution. B) Soaking of chamois leathers in distilled water.**

3. Following this preparation the average thickness of the target area was calculated from measurements taken at three random points using a Mitutoyo 0-25 mm micrometer, accurate to 0.01 mm (Figure 2B). The variation in thickness across the impact area has previously been less than 1 mm. The scapula was then labelled before being placed back into the Hartman's solution for the remainder of the rehydration period.



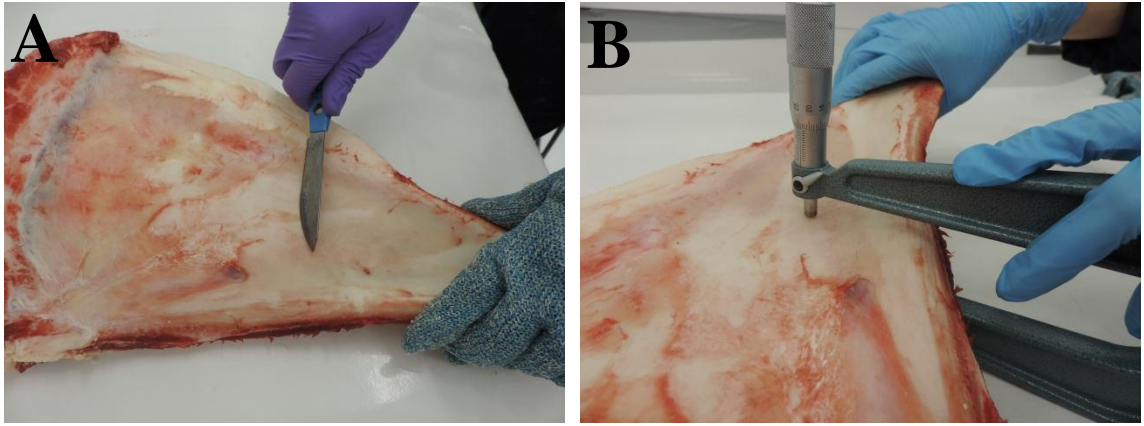


**Figure 2: Removal of excess flesh material from the bovine scapula (A) and measurement of the bone thickness in the target region using a micrometer (B).**

4. Twenty percent ballistic grade gelatin was produced by using an electric whisk to dissolve gelatin granules in distilled water at a temperature between 60 and 70 °C. The mixture was then left for an hour to rest. Any air bubbles were scraped off the surface and discarded, leaving the remaining liquid for use in the next stages of model construction.
5. Slices of 10 mm thick 20% ballistic gelatin were formed using a mould<sup>4</sup> (Figure 3A) filled with liquid gelatin (Figure 3B). The mould was left to set for at least 12 hours.

Once set, the mould was dismantled to extract the 10 mm thick gelatin layers. Each square of gelatin was cut across the diagonal<sup>5</sup>, producing material for the construction of two BSMs.

---

<sup>4</sup> This was a smaller more rigid version of the original mould developed by James *et al.* (2009), optimised for the production of twelve gelatin slices. The new mould required a smaller volume of gelatin and enabled easier extraction once the gelatin had set. This did not compromise the construction of the 10 mm gelatin slices but reduced the resourcing requirement.

<sup>5</sup> The original construction documented by James *et al.* (2009) proposed use of a whole slice per model, however the gelatin extended beyond the borders of the scapula. The gelatin had to be cut away and discarded. Division of each slice into two triangles produced an area of gelatin which fitted within the borders of the scapula without compromising the structure of the model. It was determined to be a more efficient use of the gelatin slices, requiring fewer to be moulded and simplifying further stages of construction.

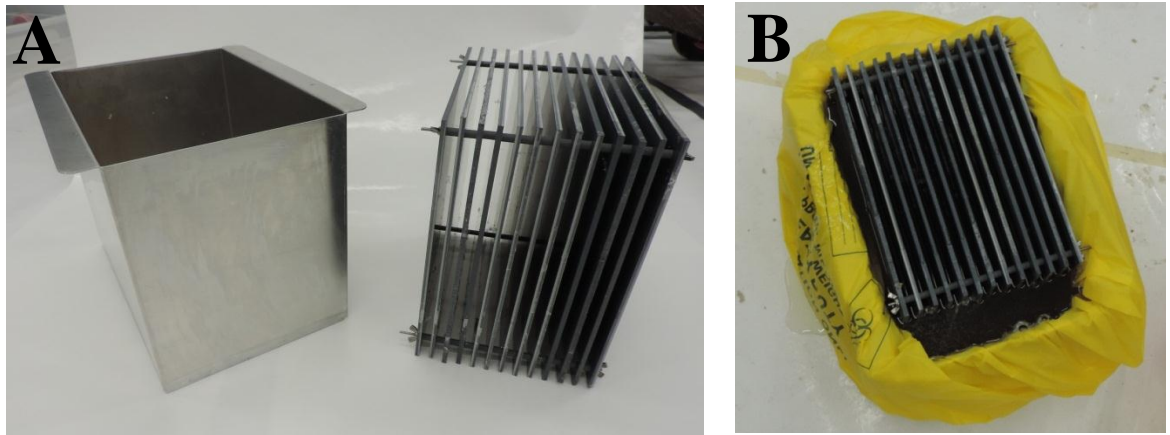


**Figure 3: A) Construction mould for 10 mm thick slices of 20% ballistic gelatin, filled with liquid gelatin (B) and left to set for use in BSM construction.**

6. Representation of the scalp over the impact area was constructed by placing a 10 mm thick triangle of gelatin over the target area of the scapula (Figure 4A). A single<sup>6</sup> chamois leather was then submerged in a fresh batch of 20% liquid gelatin and excess gelatin removed, ensuring a thin layer of gelatin coated the chamois surface. The chamois was then folded in half diagonally before being placed over the gelatin slice (Figure 4B). The surface was carefully smoothed to remove any air bubbles, taking care not to cause undesired folds in the chamois leather over the impact area. The chamois leather extending beyond the borders of the scapula was wrapped around the bone.

---

<sup>6</sup> The original construction documented by James *et al.* (2009) proposed use of two whole chamois leathers to achieve the desired two layers over the gelatin slice. However, it was identified that the two layers could be achieved by folding a single chamois leather in half. This reduced the chamois material wrapped around the bone, without compromising the mechanical properties of the model. This resulted in a reduction in the number of chamois leathers required.

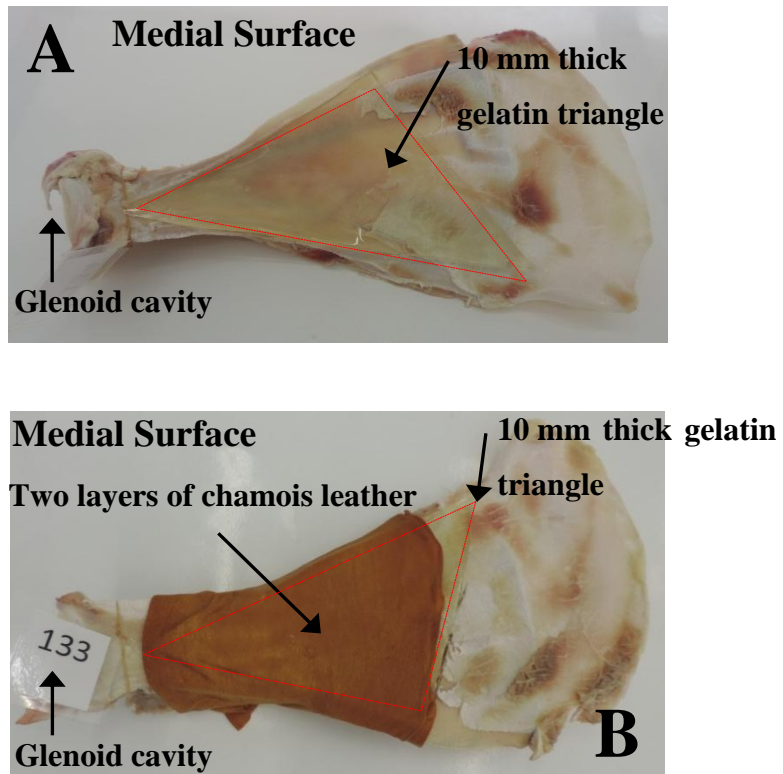
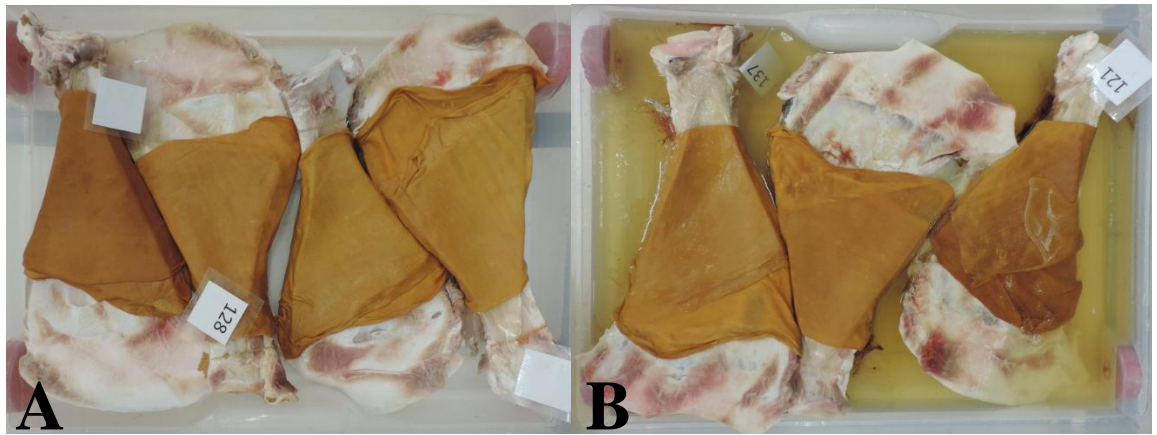


Figure 4: A) Application of a 10 mm thick, 20% ballistic gelatin slice over the target area on the medial side of the bone. B) Addition of two layers of gelatin soaked chamois leather, combined with the 10 mm thick gelatin, to form representation of the scalp over the BSM impact area.

7. Finally, a backing of 20% ballistic gelatin between 30 and 60 mm in depth was achieved by laying the models in plastic trays (Figure 5A), with the prepared impact area facing upwards. Liquid gelatin was poured in around the models (Figure 5B) to as great a depth as possible without breaching the top of the scapula and flooding the target area. The scapulae were gently moved to release any air bubbles, ensuring contact between the gelatine and lateral bone surface.
8. Once set, the models were extracted from the tray mould and cut apart, completing the BSM construction (Figure 6). Prior to use, each BSM was weighed using D. Brash and Sons Ltd scales, accurate to  $\pm 1$  g.

Ideally, the models would be tested the same day they are completed to ensure the bone and gelatin remained hydrated.



**Figure 5: Medial view of scapula models laid in a plastic tray (A) with 20% ballistic gelatin poured in (B) to form a backing.**

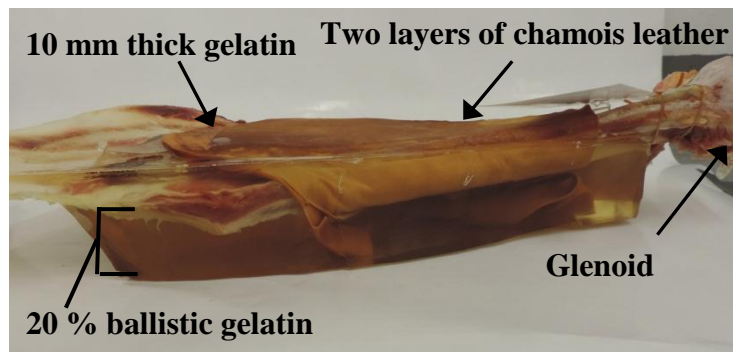


**Figure 6: Side view of the Dstl BSM, showing a depth of 20% ballistic gelatin set on the lateral surface of the bone.**

Reference:

James, G.R. and Sedman, A.J. (2009). Refinement of Skull Fracture Models. Internal Dstl Report. Dstl/CR35477.

## Annex B: Development of an instrumented projectile

### 1 Introduction

To undertake comparative impact testing to the studies by Raymond (2008) and Crawford (2008), an instrumented projectile commensurate with the Raymond and Crawford system, was required. The projectile used by Raymond and Crawford (Figure 1) was a tethered system, recording uniaxial acceleration data throughout flight. The impact face was a flat fronted 38 mm diameter cylinder, made from solid aluminium. An Endevco (model 7270) 20,000 g accelerometer was attached to the rear of the impact head, with a tail piece to protect the data capture cables (Figure 1).

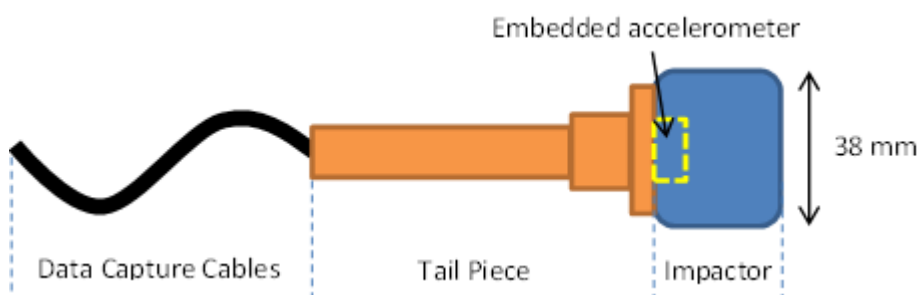


**Figure 1: Instrumented projectile used by Raymond (2008) and Crawford (2008) to conduct impact studies on cadaveric specimens..**

Personal communication with Dr Cythia Bir, supervisor to Raymond and Crawford at Wayne State University, reported a number of limitations associated with the tethered projectile:

- The firing system was complex. It was designed to enable the tether to be attached to the projectile whilst maintaining a closed chamber to achieve enough pressure to fire the projectile. This made the process of loading the firing system time consuming;

- The tether would often become detached from the body of the projectile due to the severe loading conditions during firing and impact with the target. Data for these shots would be lost at the point of tether failure; and,
- The mass or effect imparted to the target as a result of the tether following the projectile was unknown.

After consideration of these limitations it was decided that an un-tethered instrumented projectile should be developed, avoiding the limitations associated with tethered systems and providing a projectile that could be used with the current firing set-up at Dstl.

## 2 Requirements

A number of requirements were identified for the untethered instrumented projectile (Table 1). These were based on the projectile and test set-up used by Raymond (2008) and Crawford (2008), in conjunction with the compressed air firing system available at Dstl.

Factors		Requirement
Loading conditions	Maximum acceleration to withstand	20,000 g
	Pulse duration of impact	~1 ms
	Frequency Response	~10 kHz
Complete Projectile Properties	Mass	103 ±1 g
	Dimensions	Impact face flat circular 38 mm Diameter
	Shell Material	Aluminium
Instrumentation	Sampling Rate	≥ 100 kHz
	Output	Time history for acceleration
	Software Outputs	Numerical and Graphical
Dstl Firing System	Barrel Diameter	38 mm
	Barrel Length	50 cm
	Propulsion Method	Compressed Air
	Velocity Range	20 – 70 ms <sup>-1</sup>

**Table 1: Requirements determined for the untethered instrumented projectile, capable of collecting acceleration throughout impact.**

### **3 Developmental Approach**

Investigation of commercially available data capture systems determined that there was no off-the-shelf projectile solution which could meet all of the requirements. Therefore, two commercial partners with expertise in instrumentation for ballistic environments were identified. They were approached individually and tasked to develop a bespoke projectile solution. The commercial partners were Cranfield University at Shrivenham (UK) and Med-Eng (a brand of the Safari-land Group and previously Allen Vanguard, Canada).

To ensure the projectiles would meet the requirements, a collaborative approach was taken with each of the commercial partners. Whilst the internal electronic components were developed solely by the commercial partner, the outer shell was designed collaboratively and manufactured at Dstl. In addition, testing of the systems was undertaken by Dstl, using numerical modelling and physical impact trials to evaluate the capability of each projectile solution.

### **4 Test and evaluation**

#### **4.1 Numerical modelling**

Each of the shells housing the electronic components was initially produced as an engineering drawing. As part of this process the mass of the shell was determined to ensure it was below the total system requirement of  $103 \pm 1$  g (Table 1).

In conjunction with the Dstl structural dynamics team, the shell was then numerically modelled within Hypermesh software (Altair Engineering 2008) to create a Finite Element (FE) model. The projectile geometry FE model was then imported to LS-DYNA software (Livermore Software Technology Corporation 2009) to conduct an impact simulation. An initial velocity of  $70 \text{ m}\cdot\text{s}^{-1}$  was applied to the projectile, after  $0.1 \text{ m}\cdot\text{s}^{-1}$  a deceleration of

20,000 g applied to the front face. This was expected to be the worst case impact in the physical test environment.

Outputs showing strain were used to determine permanent damage to the projectile shell. A strain above 10% was determined to highlight an area of failure for a single impact. As the unit was required to withstand multiple impacts in the physical environment, a strain of 2% was determined to be acceptable. This was based on the aluminium material of the shell and considering that the simulation represented the most severe impact event.

Following completion of the simulation, the strain levels throughout the shell were identified and modifications were made to reduce the levels of strain observed. Improvements to the construction, such as the numbers and locations of screws, were also investigated within this model. Once the shell design was finalised, several units were manufactured for inclusion of the electronic components to enable physical testing.

## **4.2 Physical Testing**

### **4.2.1 Experimental Set-Up**

Physical testing of the prototype projectiles was undertaken within the 100 meter ballistic range at Dstl Porton Down. Each projectile was required to successfully complete a minimum of 20 impacts.

The range set-up, schematically shown in Figure 2, used a Honed Tube Pressure Housing (HTPH)<sup>1</sup> system to fire the projectiles. The system was combined with a 40 mm diameter smooth bore proof barrel<sup>2</sup>, using an obturator<sup>3</sup> to improve projectile fit and achieve

---

<sup>1</sup> Within the Dstl indoor range facility WASP tracking system, the HTPH was number 92.

<sup>2</sup> Within the Dstl indoor range facility WASP tracking system, the proof barrel was number 117.

<sup>3</sup> An obturator is a plastic device placed behind the projectile (in front of the air cartridge), which expands under the force of the compressed air to fit the barrel. Therefore, the majority of the air pressure is transferred to moving the projectile as less is able to escape down the sides of the barrel around the projectile.



repeatable velocities. Firing was achieved using compressed air delivered from an Airmunition cartridge (SN04663).

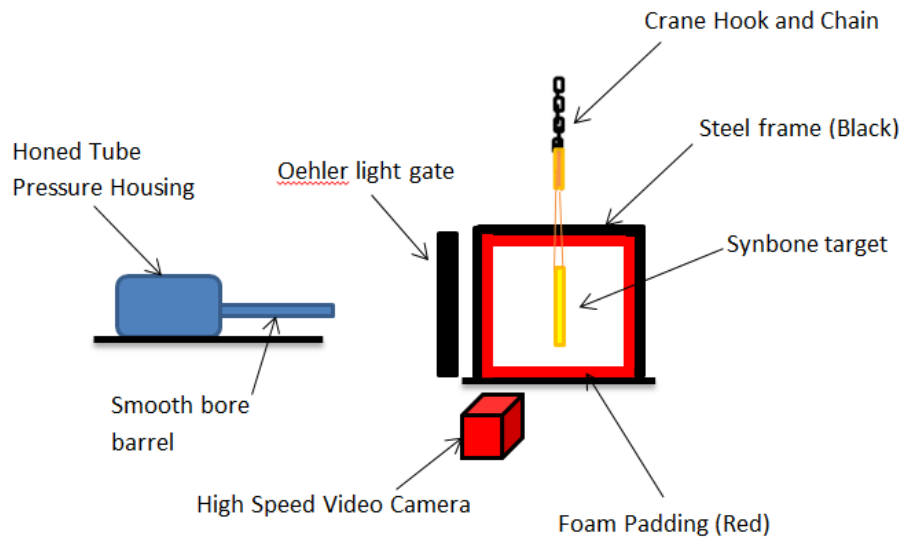


**Figure 2: Experimental set-up used to evaluate instrumented projectile prototypes.**

Each projectile was tested at a range of velocities between 20 to 70  $\text{m}\cdot\text{s}^{-1}$ , measured using calibrated High Speed Video (HSV) images. Images were collected at 100,000 frames per second, with calibration achieved by placing a rule in the field of view so the actual distance travelled could be measured. The time taken to travel a specific distance enabled calculation of the projectile velocity. The HSV camera was placed perpendicular to the shot line of the projectile, focused on the target and final stage of projectile flight pre-impact.

Raymond (2008) and Crawford (2008) conducted cadaveric testing using their instrumented projectile. Therefore, a target with a similar response to impacting bone was required to test the durability of the instrumented projectile solutions. Although synthetic materials do not closely replicate biological tissues (Arnold *et al.* 2001) they are frangible systems<sup>4</sup>, which are affordable, readily available and do not require a significant

---

<sup>4</sup> Frangible is a term used to describe a model which is expected to be damaged beyond repair as a result of a single impact. Generally, biological targets are described as frangible models.

construction time. Therefore, a synthetic bone model target was identified to support assessment of the instrumented projectile solutions.

The target was made from synthetic bone sheets of 250 mm square and 5 mm thickness, obtained from Synbone™. Due to biological variability in bone thickness, the sheets were used singly or combined together to produce a thickness of 10 mm. Silicone squares of 10 mm thickness and approximately 10 cm square were positioned in the centre of the front and rear of the bone sheets, held in place using plastic cable ties (Figure 3).

The synthetic bone target was suspended from the gantry crane using a string cradle (Figure 3) and aligned with the barrel to ensure impact was achieved at the centre of the target. The target was positioned as close to the barrel end as possible, at a distance of 65 cm. This allowed for the target assembly and inclusion of an Oehler light screen to trigger the HSV data capture, to be placed between the barrel end and the target.

The target assembly (Figure 4) consisted of an outer steel frame with padding on the internal surfaces to reduce post impact damage to the projectiles. The sides of the frame were covered with transparent Perspex sheeting to enable observation of the target during impact using the HSV camera, whilst shielding the camera from the projectile and any fragments produced from the target.

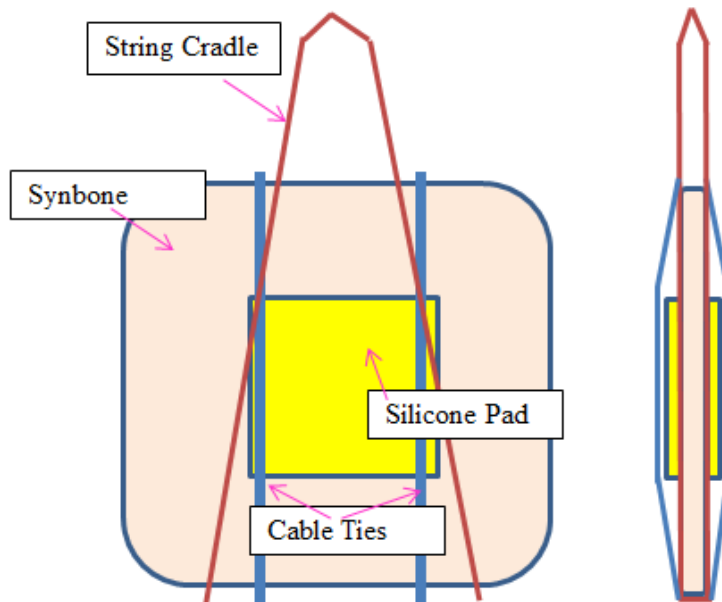


Figure 3: Front (left) and side view (right) of the Synbone target construction used to assess the durability of instrumented projectile prototypes.

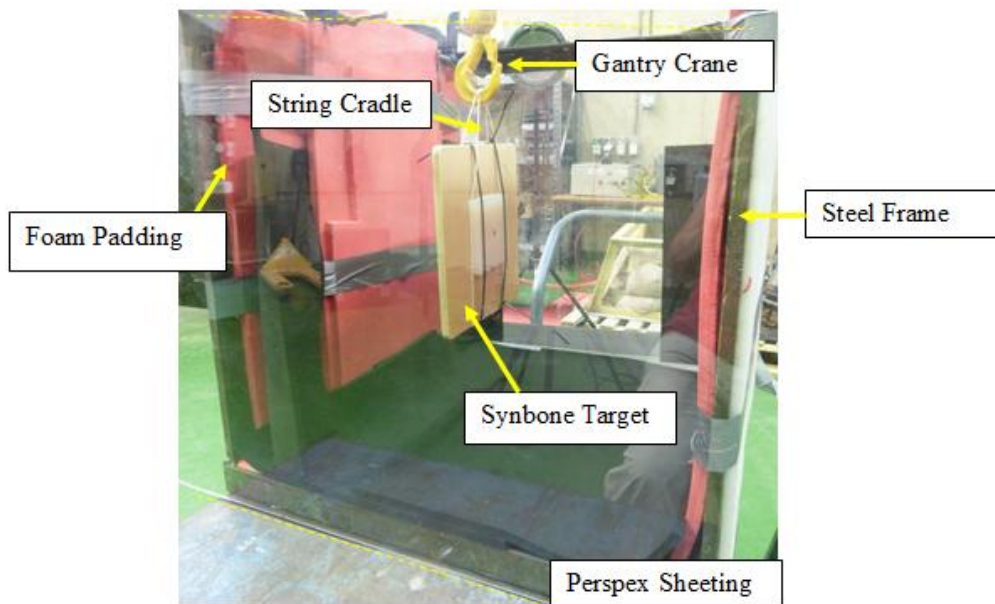


Figure 4: Target assembly within the range set-up used to assess the durability of instrumented projectile prototypes.

Finally, information relating to range temperature and humidity, shots per projectile, air-munition pressure, projectile serial number and projectile accelerometer data file were

recorded to ensure consistency and storage of the impact data for comparison between test series.

#### **4.2.2 Data Analysis**

The data collected by the projectile electronics was downloaded to a computer via a simple software interface. In each case this software was designed by the commercial partner to enable communication with the projectile. Battery charging, selection of data collection settings and data download post firing was completed via this interface. The acceleration profile was visualised within the software or exported to Microsoft Excel; noise spikes and large offsets in the data were used to indicate potential failure of the electronic components.

### **4.3 Projectiles**

#### **4.3.1 Option 1 – Instrumented Projectile Acceleration Logger**

The Acceleration Logger was developed in conjunction with Cranfield University. As a starting point, 75% (77/103 g) of the available mass was assigned to the shell construction. Estimation of the shell mass was required due to initial uncertainty regarding the weight of the electronic components. Minor alterations were made at a later stage when an accurate weight of the electronics was determined.

The shell consisted of two parts, an impact face and a hollow cylinder, held together with a number of small screws (Figure 5). The outer shell maintained the impact face diameter of 38 mm throughout its length, with the inside of the impact face shaped to enable attachment of an accelerometer. The rear section of the projectile was a simple cylinder design with one end enclosed. A wall thickness of 2 mm was maintained throughout its length. This helped to ensure stable flight due to equal distribution of the aluminium

material, whilst providing enough space and protection for the electronics inside. Holes in the rear face of the shell enabled connection to the electronics pre and post firing.

The internal electronics consisted of a Printed Circuit Board (PCB) containing the data acquisition system, with rechargeable battery attached to the rear surface. The PCB was connected to a Type 4374 Brüel & Kjær Charge Accelerometer and a 3.5 mm stereo socket, enabling connection to an interface unit via a stereo jack plug. The circuit board also contained a yellow Light Emitting Diode (LED), which could be seen at the rear of the projectile shell. This indicated connection to a power supply and the state of the projectile in terms of being pre or post trigger.



**Figure 5: Option 1, Instrumented Projectile Acceleration Logger casing, impact face on the left and hollow cylinder housing to contain the instrumentation, shown on the right.**

The system was able to collect data at a sampling rate of 100 kHz, capturing 4095 data points over the duration of 41 milliseconds. A 48 kHz filter was applied to the signal prior to storage of the data.

The projectile was connected to a Personal Computer (PC) interface via a Universal Serial Bus (USB), running from the interface unit. Once connected, the projectile was switched on and a number of parameters were made available for pre-firing adjustment within a bespoke software package. Trigger delay, trigger threshold and peak acceleration could all be selected to optimise data collection for an individual impact.

The internal components of the projectile were potted into the aluminium shell and fixed in place using expanding foam (Figure 6). The accelerometer was rigidly fixed to the frontal impact surface using a thin layer of adhesive combined with a stiff material, acting as a mechanical damper. Once held inside, the electronic components were sealed within the shell by attachment of the impact face, and secured with the screws.

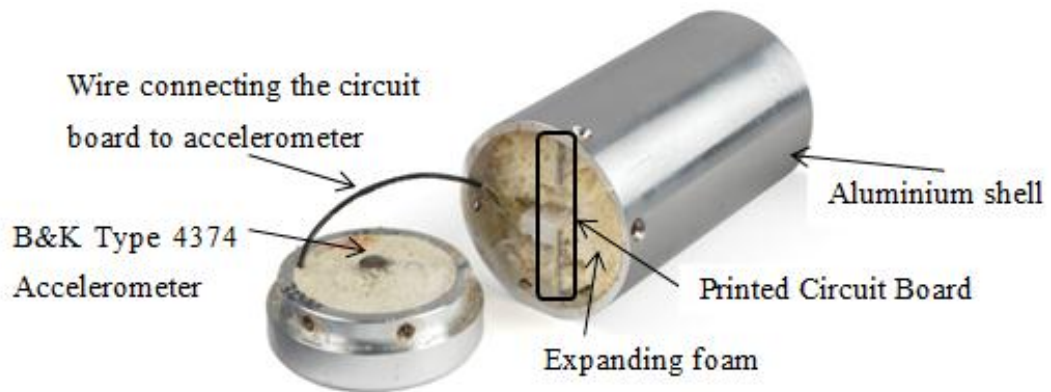


**Figure 6: Instrumented Projectile Acceleration Logger electronics mounted within the aluminium shell and fixed in place using expanding foam.**

#### **4.3.2 Option 2 - Ballistic Data Acquisition System**

The Ballistic Data Acquisition System (BDAS) was developed in conjunction with Med-Eng. The shell consisted of 5 parts, with a number of screws throughout its length to hold the sections together (Figure 7).

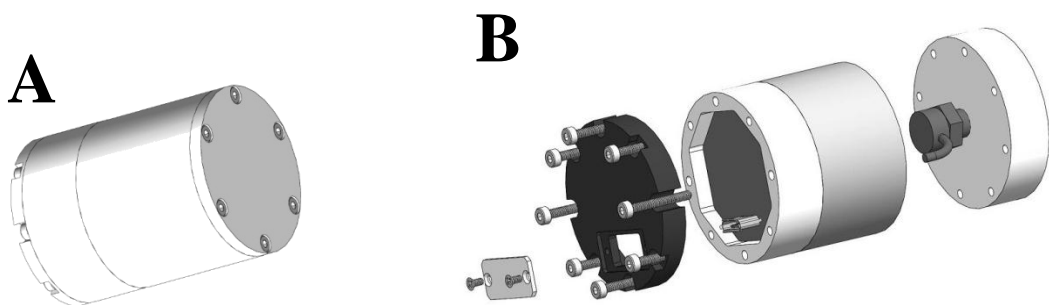


**Figure 7: Ballistic Data Acquisition System shell design; a constructed shell with impact face visible (A) and an exploded view with representation of the electronic components (B).**

© Copyright Med-Eng (2015), reproduced with permission from Robert Lukshis (Med-Eng).

The internal electronics consisted of a PCB, rechargeable Lithium-Polymer battery, a PCB Piezotronics accelerometer (Type 3501A1220KG) and a mini USB connector port. The electronic system for each projectile was manufactured by Med-Eng and combined with the off-the-shelf accelerometer. The system was capable of collecting data at 103.4 kHz, recording 6448 samples over a 62.4 ms duration. The signal was filtered using a four-pole anti-aliasing Bessel filter, with a cut-off frequency of 15 kHz. Finally, the memory was non-volatile; any data collected prior to a power failure within the unit was stored, reducing the risk of data loss post impact.

## **5. Results**

### **5.1 Option 1 – Instrumented Projectile Acceleration Logger**

Through the use of numerical modelling of the Acceleration Logger design, shell failure was observed in the centre of the rear and front faces. The rear face showed significant movement after impact. Therefore, increased wall thickness improved the strength in these areas of the shell design.

Other stress concentrations were observed around the screw points connecting the two shell sections together. An increased number of screws, with longer thread lengths, were included to reduce the likelihood of failure in this area. It was also determined that use of an aircraft grade Aluminium (Type 7025) would provide increased material strength to the shell without a significant increase in weight. A revised numerical model determined these changes to improve the strength of the shell design, reducing the strain observed within the shell below the 2% threshold (Figure 8).

Following incorporation of the findings from the numerical modelling assessment and development of the electronic components, a prototype Acceleration Logger was produced (Figure 9).

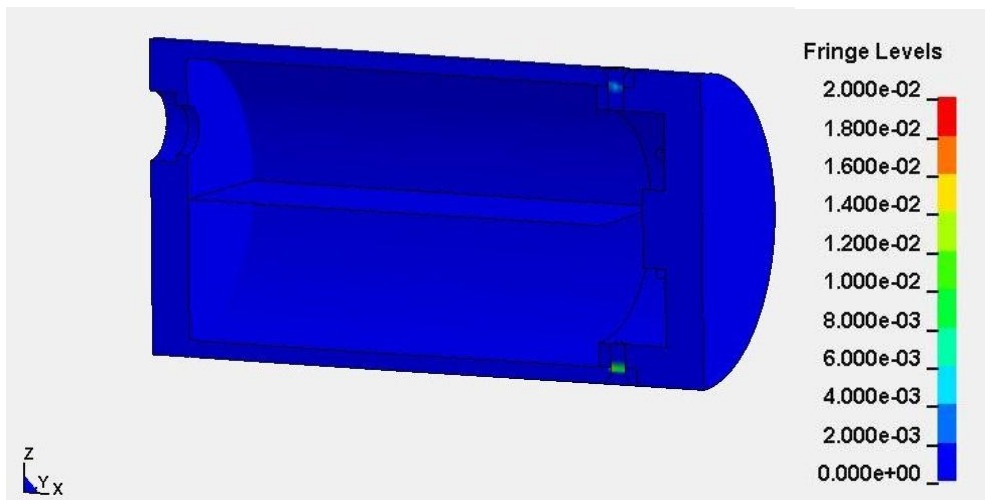


**Figure 8: Numerical model output for final Acceleration Logger shell design, with strain represented by colour variations. Image exported from LS-DYNA (Livermore Software Technology Corporation 2009).**



**Figure 9: Rear view of the prototype Acceleration Logger. The connector and LED viewing hole are visible on the rear in conjunction with the projectile serial number.**

A total of 53 impacts were completed using seven different Acceleration Logger units (Table 2). Testing was completed over five sessions due to a number of catastrophic system failures, which had to be rectified and improved prior to further testing. The common causes of system failure were the battery and accelerometer, with other electronic components also failing in some of the units (Table 2).



Test Series	Number of Projectiles	Total Firings	Maximum no. of successful firings with a single projectile	Notes
1	1	4	3	Trigger Level error
2	3	29	16	Battery failure, accelerometer detachment and physical damage, connector failure
3	1	1	0	Battery failure
4	3	9	4	Large post impact offsets observed and accelerometer failure
5	2	10	6	Accelerometer and battery failure

**Table 2: Impact test results using the Acceleration Logger, developed in collaboration with Cranfield University, Shrivenham.**

The projectile shell showed minor damage in the form of indentations to the edges of the front and rear surfaces (Figure 10). These occurred due to ricochet, resulting in impact with other structures of the target assembly. The shell did not show any significant plastic deformation after a number of impacts, although loosening of the screws caused shearing of the screw heads. In these cases the shell had to be cut apart to access the internal electronics.

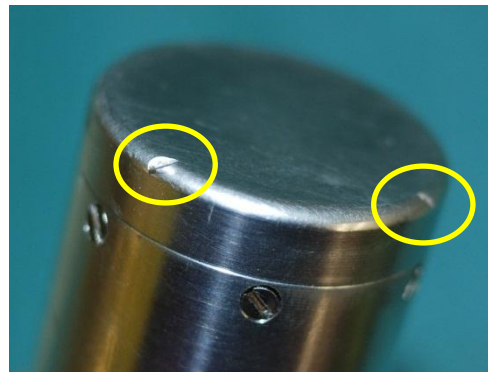


**Figure 10: Acceleration Logger shell damage post impacts, highlighted by yellow circles.**

## 5.2 Option 2 - Ballistic Data Acquisition System

Numerical analysis of the BDAS shell design (Figure 11) did not identify any areas of plastic deformation under the applied loads. Although, peak stresses were observed in the housing around the bolts on the impact surface and in the bolts themselves. In addition there were concerns regarding the exposed screw heads on the impact surface, and the effect these may have on contact with a target. Therefore, increased thickness of the front and rear shell sections, combined with a change to the screw locations attaching the impact face to the rest of the shell were proposed to improve the design. The final shell design (Figure 12) had a continuous flat impact face, with increased wall thickness to the front and rear sections.

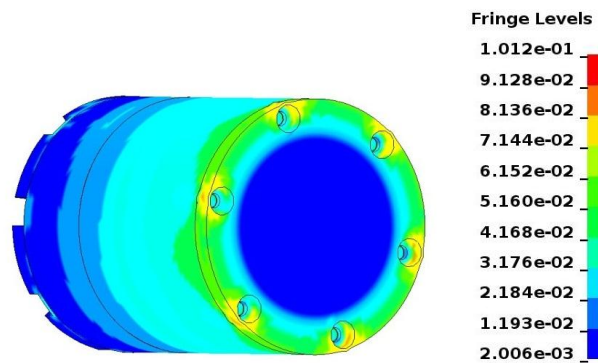


Figure 11: Strain measures obtained through numerical evaluation of the initial shell design for the Ballistic Data Acquisition System. Image exported from LS-DYNA (Livermore Software Technology Corporation 2009).



Figure 12: Ballistic Data Acquisition System final shell design with impact face on the right of the image and rear section to the left.

A total of 39 impacts were completed using two BDAS units, over two trial sessions (Table 3). Initial testing resulted in system failure due to disconnection of the accelerometer wires from the PCB. On visual inspection the casing did not show any plastic deformation and the screws were successfully removed to enable investigation of the internal components. Following further development to improve the robustness of the connections between the accelerometer wires and PCB, the prototype system successfully completed 20 impacts (Table 3).

Test Series	Number of Projectiles	Total Firings	Maximum no. of successful firings with a single projectile	Notes
1	2	10	7	Accelerometer disconnected from PCB
2	2	29	20	No failures

**Table 3: Impact test results of the Ballistic Data Acquisition System developed in collaboration with Med-Eng.**

Acceleration data was collected for each successful impact. The profiles showed the projectile acceleration up the barrel, and the deceleration experienced on contact with the target (Figure 13). As the focus of the signal was the deceleration due to impact, deceleration was reported in the positive axis.

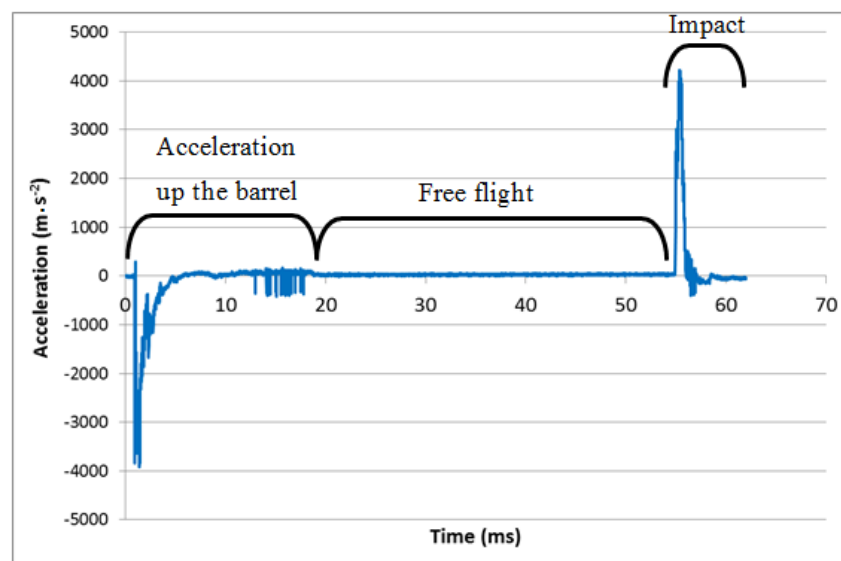


**Figure 13: Acceleration profile obtained from a Ballistic data Acquisition System accelerating up to a velocity of 26.2 m.s<sup>-1</sup>, prior to impacting a synthetic bone target.**

## **6 Discussion**

### **6.1 Option 1 – Instrumented Projectile Acceleration Logger**

Although the Acceleration Logger was not able to meet the requirements outlined in section 2, there were a number of positive aspects of the design identified within the durability assessment:

- The shell provided a robust housing for the electronic components, with the ability to modify the impact face if desired;
- Identification of the loosening of the screws holding the two shell sections together was remedied by using a mild adhesive to hold the screw threads in place; and,
- The electronics were easily inserted, although securing the contents with expanding foam made it difficult to observe and extract the shell contents during post firing investigation.

The limiting factor of the Acceleration Logger was the ability of the electronic components to withstand the high accelerations experienced when impacting the target, including further ricochet impacts. There was no common point of failure, with several different components failing during the development of the system.

### **6.2 Option 2 - Ballistic Data Acquisition System**

The BDAS successfully collected impact acceleration data for the required 20 impacts. The systems were not able to be tested to failure due to a lack of resources. Therefore, it is unknown how many impacts these projectiles could withstand prior to system failure. This is a risk associated with using the system for complex trials without undertaking further durability testing. However, the risk could be reduced with the use of more BDAS units, instead of relying on one or two prototype systems.

Overall, the BDAS projectile system met all of the requirements. In addition:

- The shell was robust, showing minimal physical damage as a result of target impact and ricochet. Damage to the shell was likely to be reduced by having the padded target assembly to catch the projectile post impact;
- The interface software was easy to use, with clear indication of the projectile state. It also enabled the accelerometer offset to be adjusted prior to impact, ensuring the accelerometer reading was zero prior to firing the projectile;
- The on-board data capture system was able to record the entire projectile flight, recording the acceleration up the barrel and the deceleration profile during impact; and,
- The non-volatile nature of the data storage system was essential to capturing the impact event in case catastrophic damage occurred to the system post impact.

Learning from experience with the Acceleration Logger, a low resistance adhesive was used on each screw. The screws were checked between impacts to determine any loosening, which may have resulted in further damage to the system if loose shell components were able to impact each other.

There were concerns regarding the potential cutting effect of the sharp edge of the impact face (90 degrees between the flat face and the shell side). This resulted in the addition of a 2 mm radius of curvature applied to the edge of the impact face; the same curvature used on the Raymond (2008) and Crawford (2008) projectile impact face.

The in-built filtering of the instrumented projectile was not the same as that used by Raymond (2008) and Crawford (2008); the BDAS had a filtering cut off frequency of 15kHz, compared to the 4.3kHz used by Raymond and Crawford. However, as the BDAS

filter has a higher cut off frequency, the data collected by the projectile can be filtered in post processing to align it to the filtering applied by Raymond and Crawford.

### **6.3 Test and evaluation methods**

Numerical simulation provided a low cost, rapid assessment of the shell designs with the ability to test and evaluate modifications. Areas of weakness were identified and a range of modifications investigated, without the need for physical testing until the final system was determined.

The ballistic test method enabled firing of the instrumented projectiles at a range of velocities, against a representative target model. The high number of failures seen throughout projectile development suggests this to be a challenging environment for untethered data collection. The primary cause is likely to be the high shock received on impact.

Evaluation of a number of prototypes identified different points of failure within the Acceleration Logger, whereas there was a common point of failure for the BDAS. The consistent test method enabled comparison between testing sessions, so improvements could be identified as well as testing for other failure mechanisms.

## **7 Conclusions**

The aim of this work was to produce an untethered, instrumented projectile to enable the collection of acceleration data throughout an impact event. The projectile was required to enable comparison with previous impact investigations reported by Raymond (2008) and (Crawford (2008)), whilst overcoming the limitations identified with a tethered system.

In collaboration with Med-Eng, an untethered instrumented projectile has been developed, consisting of a BDAS housed in a five part aluminium shell. The system has been

evaluated using numerical modelling and physical impact tests; it is robust for a minimum of 20 impacts against a synthetic bone target. The system was not tested to failure; therefore it is unknown how many impacts an individual projectile system can withstand.

## **References**

Altair Engineering (2008). Hypermesh. HyperWorks.

Arnold, C. and Akin, S. (2001). Mechanical Properties of Synthetic Bone Materials - A Comparison with Bovine Scapulae. DERA, University of Wales Swansea.

Crawford, G.S. (2008). Biomechanical Response of the Human frontal Bone and Zygoma to Blunt Ballistic Impacts. Doctor of Philosophy, Wayne State University.

Livermore Software Technology Corporation (2009). LS-DYNA 971 R4. LS-DYNA.

Raymond, D. (2008). Biomechanics of Blunt Ballistic Temporo-Parietal head Impact. Doctor of Philosophy, Wayne State University.